The Application of Polarization as a Magnetic Field Diagnostic.

by

Victorino Ameijenda B.Sc.

Thesis
submitted to the
University of Glasgow
for the degree of
Ph.D.

Astronomy and Astrophysics Group,
Department of Physics and Astronomy,
University of Glasgow,
Glasgow, G12 8QQ.

July 1998

ProQuest LLC.
789 East Eisenhower Parkway
P.O. Box 1346
Ann Arbor, MI 48106 – 1346

Acknowledgements

First and foremost, my thanks and gratitude are extended to my co-supervisors Dr. David Clarke and Dr. Colette Hunt. During the past three years I have had the opportunity to divide my time between the Glasgow University Observatory and the UKAEA research site at Culham, Oxfordshire. At times this constant coming and going was rather stressful but throughout Dr. Hunt has been supportive, patient and inspirational. I am also indebted to the entire COMPASS-D group for their contribution, I would like to particularly thank Trevor Pinfold and Trevor Edlington for their assistance and many useful discussions.

It is a great pleasure to acknowledge Dr. David Clarke for his excellent guidance, patience, inspiration and for the opportunity to travel to conferences, workshops and research meetings to discuss work and ideas. The many useful discussions and comments on the dissertation have been invaluable and have greatly assisted me in the preparation of this manuscript. I would like to take this opportunity to thank him for his friendship and those rather amusing anecdotes.

Thanks go to Colin Hunter, the technician at the Observatory, for constructing the double-beam polarimeter (a number of times!!!) and for chatting about Rangers F.C. and football in general producing lively conversations during the dreary winter months. I am also grateful to Richard Smith for his many amusing stories and friendship during the last three years, Steve Owens and David Scott for ideas, chat and generally keeping me sane in the loneliness of the Observatory! Special thanks go to Jaber Naghizadeh-Khouei for introducing me to the Starlink packages and the Unix machines and also for his friendship and the unswerving ability to make me laugh. I am indebted to John Powton for his proof reading of the manuscript and for his friendship over the past seven years. Also thanks go to the many other members of the Astronomy department past and present, and to the other friends I have made since my arrival in Glasgow.

A special thank you to my parents and family for their love, encouragement and continuing support in many ways during my years at the University of life.

Finally I would like to thank Noelle Daly for her love and support during the last year.

Summary

The aim of this thesis is to explore the application and development of polarization diagnostics as a means of determining magnetic field structures in plasmas. It comprises two main themes: (1) an exploration of the center-to-limb Hα polarization variation in the solar polar and equatorial regions and (2) an investigation of the Faraday rotation effect on the COMPASS-D tokamak. The former deals with the application of the Hanle effect in determing solar magnetic field structures while the latter is a means for diagnosing the magnetic field profile and hence the distribution of the current density in a tokamak plasma. Other solar features exhibiting polarization are also presented and the corresponding magnetic fields investigated.

First an investigation of the center-to-limb linear polarization variation was conducted utilising an instrument capable of performing high precision polarimetry with a narrow band (FWHM $\Delta\lambda = 0.3$Å) Hα filter tunable by $\pm$ 0.33Å. A double beam imaging polarimeter was designed and constructed to measure the differential polarization between the center of the Sun and the limb at an angular resolution of 4 arcseconds per CCD pixel, with an expected polarimetric accuracy of $\pm$ 0.02%. Other solar features exhibiting linear polarization such as prominences and areas of the quiet chromosphere are presented and the related magnetic fields determined. The radiation under investigation is engendered by coherent scattering processes associated with spectral lines and is modified by weak magnetic fields. This process is called the Hanle effect and involves a depolarization and a rotation of the plane of polarization. The second major part of the thesis relates to the results of the double diagnostic, namely an interferometer and a proposed polarimeter system operated at COMPASS-D. The interferometric part of the diagnostic serves as a tool to determine the electron density in the plasma. Once this is known, the polarimetric data may be analysed to give the cross-section distribution of the poloidal magnetic field, or, equivalently, the current density. The major limitation of the diagnostic is the line-integrated nature of the measurement. Since measurements are performed under one viewing angle only, assumptions related to plasma symmetry are essential for a proper interpretation of the data.

This thesis focuses on the development and evaluation of the polarimetric aspects of the

combined diagnostic. Plasma birefringence, resulting from the presence of a magnetic field component along the propagation direction of the beam, causes the linear or elliptical polarization of an incident probing wave to rotate. The rotation angle can be determined via a measurement of the polarization state of the emerging wave, hence the term polarimetry. A conventional but robust technique measures the relative intensity of two orthogonal linear polarization components separately after passing through or reflected from a polarizer. Alternatively, single detector techniques have been developed, where the incident polarization is modulated to generate an amplitude-modulation on the detected signal, from which the Faraday rotation can be derived.

The work in this thesis was carried out by the author at the University of Glasgow and at the UKAEA Culham research site during the period 1995-1998. Two-thirds of the time was spent at Glasgow under the supervision of Dr. David Clarke developing and observing with the double beam imaging polarimeter. The remaining time was spent at Culham working on the COMPASS-D tokamak under the supervision of Dr. Colette Hunt. The original work of this thesis appears in Chapters 2, 4 and 5.

The opening chapter reviews the two main fields of interest. It starts with a discussion of the basic concepts and terminology of polarimetry introducing the Stokes and Jones vector formalism. The polarigenic processes in the Sun and their suitability as magnetic field diagnostic are considered, followed by a review of recent studies with particular attention paid to the Hanle effect phenomenon. The Faraday rotation effect is then described with the existing techniques for measurement and interpretation of the poloidal magnetic field in a tokamak plasma reviewed. The remainder of the chapter serves to introduce the reader to the basic principles of fusion.

Chapter 2 starts with a review of the current imaging techniques used in astronomical polarimetry followed by a discussion of the factors that adversely affect any measurement. A prototype solar imaging polarimeter is described with an explanation of the instrumental techniques which have been used, and the optical system specially designed to observe the small levels of polarization in the solar light. The reduction techniques required to ascertain a polarimetric measurement are also discussed and developed. A novel technique to determine the polarimeter's instrumental polarization utilising a monochromatic depolarizer is experimentally evaluated for the first time.

A comprehensive overview of the theory of electromagnetic wave propagation in an magnetised plasma including the theories of Faraday rotation and birefringence is introduced in Chapter 3. The inversion techniques necessary to obtain the poloidal magnetic field from the

Faraday rotation measurements are also discussed. Finally an analytical solution is presented that details the expected Faraday rotation angle for COMPASS-D and the birefringence introduced due to the presence of the toroidal magnetic field.

Chapter 4 outlines the two polarimetric techniques being considered for commissioning on the COMPASS-D tokamak and discusses the suitability, accuracy and reliability of each in turn. The second part of the chapter is devoted to the design and development of a polarimetric test bench in order to experimentally ascertain the feasibility of the amplitude method and its suitability for operation on COMPASS-D. The chapter concludes with a thorough discussion of all the results and a recommendation for possible implementation of a polarimetric technique on the experiment.

The Hα observations taken with the solar imaging polarimeter of the solar disk in Glasgow during the summer of 1997 are presented in Chapter 5, commencing with a discussion of the techniques used to determine the instrumental polarization of the experimental setup. This is followed by the center-to-limb observations taken at three distinct wavelengths centered on Hα. The final part of the chapter presents the polarization map of two prominences recorded during the observing run.

Chapter 6 offers a brief overview of the results and conclusions of the whole of the work providing, in a digestible form, a summary of achievements by the various studies described in this thesis. It also proposes new avenues of research and makes suggestions of how the various methods used in this thesis may be improved.

Contents

List of Tables

List of Figures

Chapter 1

Introduction

Polarimetry has been an important observational tool for solar and plasma physicists since 1908 when George Ellery Hale first detected circular polarization in the wings of a Fraunhofer line in the light from a sunspot. Zeeman had earlier discovered that polarized light is emitted and absorbed by atoms in a magnetic field and Hale used his measurements to estimate the magnetic fields in the sunspots. The measurement of magnetic fields remains today a primary motivation for most solar polarimetry. Recent observations by Stenflo and Keller (1997), using a high precision polarimeter, have revealed a polarization spectrum that looks very different to the ordinary, unpolarized solar spectrum and also contains an astounding wealth of spectrum structures. It has therefore been referred to as the "second solar spectrum". Fields as strong as one or two thousand gauss are common on the Sun and these interact strongly with solar plasmas either to produce or to infiuence profoundly the nature of many solar features such as sunspots, prominences, flares, plages and the corona. Fusion in solar type plasmas may be a long-term candidate for energy production with the most promising magnetic confinement device a toroidal shaped donut called a "tokamak". The physical processes in tokamaks are dominated by magnetic fields and their understanding is vital for future research.

This chapter starts with a discussion of the basic concepts of polarization introducing the Stokes and Jones vector formalism. The polarigenic processes in the Sun and their suitability as magnetic field diagnostic are then considered. A review of past and current work in this area is presented. The Faraday rotation effect is described, which can be used as a diagnostic for the poloidal magnetic field in a plasma. The existing techniques for the measurements of the Faraday effect are reviewed. The remainder of this chapter serves to introduce the reader to the basic principles of fusion. Magnetic confinement is introduced as a means to control and stabilise a plasma. The relevance of the poloidal magnetic field to confinement in a toroidal geometry is discussed. The research, presented in this thesis, is placed in relation

to this work.

1.1 Polarimetric Definitions

The polarization of electromagnetic waves may be uniquely defined in terms of four Stokes parameters formulated by G. G. Stokes (1852), (more modern descriptions may be found in Shurcliff, 1962 and Clarke and Grainger, 1971). A beam of radiation containing an assembly of waves may first be considered in terms of a single classical wave, formally described by the components of its electric vector in two orthogonal planes perpendicular to the direction of propagation of the wave. For a wave of arbitrary polarization **E** propagating along the z axis of a Cartesian coordinate system, these components may be written at a time t as,

$$\begin{aligned} E_x &= E_{xo}e^{i(\omega t - kz + \delta_x)} \\ E_y &= E_{yo}e^{i(\omega t - kz + \delta_y)} \end{aligned} \tag{1.1}$$

where E_{xo} and E_{yo} are the amplitude of the x- and y-components, δ_x and δ_y are the phases at $z = 0$, ω is the angular frequency of the electromagnetic wave and k the wavenumber. In general, the tip of the electric vector will trace out an ellipse through time in the x-y plane. There are two special cases of interest:

1. Linear polarization, where the phase difference $\delta_y - \delta_x = m\pi$
2. Circular polarization, where the phase difference $\delta_y - \delta_x = \pm\frac{\pi}{2}$, and the amplitudes are equal.

In general the electric field behaviour associated with radiation from a source is more complicated, comprising a mixture of classical waves whose amplitudes, directions of vibration and phases are varying in some way.

The polarization associated with a beam of waves can be related to the electric field vectors by the Stokes parameters, I, Q, U and V, which are defined as

$$\begin{aligned} I &= < E_{xo}^2 > + < E_{yo}^2 > \\ Q &= < E_{xo}^2 > - < E_{yo}^2 > \\ U &= < 2E_{xo}E_{yo}\cos(\delta_y - \delta_x) > \\ V &= < 2E_{xo}E_{yo}\sin(\delta_y - \delta_x) > \end{aligned} \tag{1.2}$$

where the expectation values ($< >$) are determined over the experimental time and over all the wavelengths included in the passband of the experiment. The term I represents the total

intensity of the waves, Q and U the intensities associated with linear polarization, and V the intensity associated with circular polarization with its sign describing the sense of the handedness. The V parameter is rarely determined in astronomical optical polarimetry due to very low signal-to-noise levels. The Stokes parameters describing a mixture of incoherent beams of light are the sum of the respective Stokes parameters describing the component beams.

The quantities Q and U are determined with respect to a set of chosen reference axes for a particular observing system. For astronomical measurements, the Equatorial co-ordinate frame is normally chosen such that positive Q corresponds to a direction of vibration parallel to the N/S direction or Declination; a negative value for Q refers to the vibration being parallel to the E/W direction. A polarization measurement with zero Q component but with positive U describes a vibration set along the projection of north east on the sky. The degree of polarization, p, is defined by

$$p = \frac{\sqrt{(Q^2 + U^2 + V^2)}}{I}. \tag{1.3}$$

with $V = 0$ for linear polarization. The direction of vibration of the electric field, known as the position angle, may be expressed as an angle running from 0° to 180° measured anti-clockwise with respect to the positive Q-axis. The angle θ relating the direction of vibration of the linear polarization to the frame may be defined by

$$\tan 2\theta = \frac{U}{Q}. \tag{1.4}$$

The parameters Q and U may also be normalised as q and u, such that

$$q = \frac{Q}{I} \qquad\qquad u = \frac{U}{I}. \tag{1.5}$$

The degree of linear polarization may now be written as

$$p = \sqrt{(q^2 + u^2)} \tag{1.6}$$

where $p = 0$ corresponds to unpolarized light and $p = 1$ to complete linear polarization of the light. The position angle, θ, can be expressed in terms of the normalised Stokes parameters where

$$\begin{aligned} q &= p\cos 2\theta \\ u &= p\sin 2\theta \\ \theta &= \frac{1}{2}\arctan\left(\frac{u}{q}\right). \end{aligned} \tag{1.7}$$

When a beam of light propagates through an optical element the Stokes parameters will be affected, implying that the polarization of the light has been altered. This transformation can be represented analytically with the application of Mueller calculus whereby optical components are represented by a 4×4 matrix and the Stokes parameters are expressed as a 4-vector. The affect of a light beam transversing several optical components can be represented by the multiplication of the appropriate Muller matrices where

$$I_{out} = \begin{pmatrix} I \\ Q \\ U \\ V \end{pmatrix}_{out} = [M] \cdot I_{in} = \begin{pmatrix} M_{11} & M_{12} & M_{13} & M_{14} \\ M_{21} & M_{22} & M_{23} & M_{24} \\ M_{31} & M_{32} & M_{33} & M_{34} \\ M_{41} & M_{42} & M_{43} & M_{44} \end{pmatrix} \begin{pmatrix} I \\ Q \\ U \\ V \end{pmatrix}_{in} . \tag{1.8}$$

The application of Mueller calculus allows the effects of the polarizing optics or modulator in a simple polarimeter to be investigated. The polarization of the emergent light may be determined with the incorporation of the appropriate optical components in the polarimeter. The fast axis of an optical component, such as a half-wave plate, can be aligned at an arbitrary angle, ψ, with respect to the Cartesian coordinate system of the instrument. Therefore, to evaluate its effect on the incoming light, the coordinate frame is first rotated through an angle ψ, $[+R(\psi)]$, the Mueller matrix $[M]$ of the optic is applied and the frame is then rotated back through ψ, $[R(-\psi)]$ to its original position. This procedure is summarised by:

$$I_{out} = [R(-\psi)\,[M]\,R(+\psi)] \cdot I_{in}. \tag{1.9}$$

The Mueller matrix for an ideal half-wave plate is

$$[M] = \begin{pmatrix} 1 & 0 & 0 & 0 \\ 0 & 1 & 0 & 0 \\ 0 & 0 & -1 & 0 \\ 0 & 0 & 0 & -1 \end{pmatrix} . \tag{1.10}$$

The coordinate rotation matrix $R(\psi)$ can be expressed by

$$[R(\psi)] = \begin{pmatrix} 1 & 0 & 0 & 0 \\ 0 & \cos 2\psi & \sin 2\psi & 0 \\ 0 & -\sin 2\psi & \cos 2\psi & 0 \\ 0 & 0 & 0 & 1 \end{pmatrix} . \tag{1.11}$$

The final element in a polarimeter is an analyser which separately transmits two of the orthogonal polarization components. The linear polarizer is aligned to the reference axis of

the instrument to produce a constant vibration of polarization such that

$$[P] = \frac{1}{2}\begin{pmatrix} 1 & \pm 1 & 0 & 0 \\ \pm 1 & 1 & 0 & 0 \\ 0 & 0 & 0 & 0 \\ 0 & 0 & 0 & 0 \end{pmatrix}. \tag{1.12}$$

Incorporating matrix $[P]$ into Equation 1.9 enables the determination of the Stokes parameters, Q and U from the output of the polarimeter. The form of the light emerging can be represented by

$$I_{out} = [P] \cdot [R(-\psi)\,[M]\,R(+\psi)] \cdot I_{in}. \tag{1.13}$$

Evaluating Equation 1.13 with the appropriate matrices yields

$$\begin{pmatrix} I \\ Q \\ U \\ V \end{pmatrix}_{out} = \frac{1}{2}\begin{pmatrix} I \pm Q\cos 4\psi \pm U \sin 4\psi \\ I \pm Q\cos 4\psi \pm U \sin 4\psi \\ 0 \\ 0 \end{pmatrix}. \tag{1.14}$$

The above equation is the general form of a double beam polarimeter where the $\pm$ signs refer to orthogonal polarized states. For reference these will be termed the Ordinary and Extraordinary rays with a $+$ and $-$ sign accordingly. A more detailed discussion of this type of polarimeter is presented in Section 2.2. In terms of the measured signal, it is the output intensity which is monitored and this may be expressed by

$$I(\psi) = \frac{1}{2}(I \pm Q\cos 4\psi \pm U \sin 4\psi). \tag{1.15}$$

Evaluating Equation 1.15 for various values of ψ allows the parameters Q and U to be determined.

The Stokes and Mueller matrix formalism may only be utilised when dealing with an incoherent beam of waves. However, when the phase of a polarized wave relative to some other polarized wave is important, the Stokes parameters cannot be used since they deliberately ignore phase (except in a relative sense within each signal, as needed to specify the state of polarization). However, there are situations (such as when combining the beams of an interferometer) when phase does matter, (see Section 4.1.1). Under such circumstances Jones vectors and matrices, first introduced by R. C. Jones (1941) are utilised. These represent the electric fields (and their transformation) of two orthogonal polarization forms, including absolute phase if desired. However, it is important to know when it is necessary to use Jones rather than Mueller calculus (i.e. when the absolute phase is important). The notation used

for Jones calculus is the complex notation for sinusoidally varying quantities. This notation is explained clearly in Born and Wolf (1964). Jones represents a fully polarized signal as the vector sum of two electric fields at right angles, written in column matrix

$$\mathbf{E} = \begin{pmatrix} E_x \\ E_y \end{pmatrix}. \tag{1.16}$$

Any optical component modifying the state of polarization is represented by a 2×2 matrix operator or the column matrix in an analogous way to the Mueller calculus.

1.2 Solar Polarimetry

Polarization associates with radiation emerging from the Sun is engendered by a variety of processes in the photosphere and chromosphere and its detection is a well established diagnostic in understanding surface phenomena. From studies of specific regions of the Sun, linear polarization has been observed both in the continuum spectrum and within spectral lines. Continuum polarization may originate from Rayleigh scattering (by atoms, mainly by neutral hydrogen), Thompson scattering (by electrons) or by radiative transfer processes. Within solar spectral lines, either the Zeeman effect or coherent resonance scattering can produce polarization. The versatility and relative ease of the Zeeman effect has made it the mainstay of observational investigations of solar magnetism (e.g. magnetograms, see Baur, 1981), in particular strong magnetic fields organised into networks, active-region plages and sunspots. The Zeeman effect suffers, however, from a lack of sensitivity to intrinsically weak fields and to fields with mixed polarities or random orientations at small scales (turbulent fields).

A promising alternative for field investigation is the Hanle effect (see Hanle (1924), Moruzzi and Strumia (1991) and Stenflo (1994)). This phenomena enables certain spectral lines to be sensitive to very weak fields and exhibit polarization, thus allowing the magnetic field strength and direction to be determined. The Hanle effect has been employed to deduce the magnetic structure of solar prominences (see Leroy et al. (1977), Sahal-Bréchot et al. (1977), Bommier (1980), Degl'Innoncenti (1982) and Querfeld et al. (1985)), to investigate turbulent fields in the solar photosphere (see Stenflo (1982), Faurobert-Scholl (1993) and Faurobert-Scholl et al. (1995)) and to explore magnetic canopies in the chromosphere (see Faurobert-Scholl, 1992 and Faurobert-Scholl, 1994). However, its application is relatively rare. The problem has largely been an observational one, since the full diagnostic of the Hanle effect requires observations that combine both high spectral resolution and high polarimetric accuracy.

It is convenient to describe four distinct observed polarization phenomena relevant to the work presented here, viz:

- Limb polarization
- Resonance or fluorescence scattering
- Polarization from differential saturation with the Zeeman effect
- Hanle Effect

and these will be described briefly below.

1.2.1 Limb Polarization

Light from the solar limb is polarized with its azimuth in a tangential direction. The gradient of the growth of the polarization from the solar center to the limb, the center-to-limb variation (CLV), has been well documented by Leroy (1972), Dollfus (1974) and Mickey and Orrall (1974). Dollfus made radial scans from the center of the solar disk out to about 20 arcseconds from the limb in a range of wavelength bands; the results of such measurements are shown in Figure 1.1. These graphs not only show clearly the CLV of polarization, but also highlight the wavelength dependence as the magnitude of p decreases by a factor of about 2 at the limb itself between the measurements of 0.41μm and 0.60μm. According to Stenflo et al. (1983b) and Leroy (1990) the solar limb broadband polarization is well understood in terms of theory developed by Dumont and Pecker (1971). This states that the variation of p with μ (where μ is the cosine of the angle between the solar radius vector to the scatterer, and the line of sight) depends on the variation of scattering particle densities with height. Typically the value of p may be $\sim 0.2\%$ within a few arcseconds of the limb, reducing to $\sim 0.01\%$ at 20 arcseconds. At $\sim$ 5 arcseconds from the limb, the measured component of linear polarization with electric vector tangent to the limb is at least 50 times greater than the measured circular polarization, and at least 15 times greater than the measured net u linear polarization. Figure 1.2 illustrates empirical and continuum polarizations as a function of wavelength at a limb distance of 10 arcseconds, illustrating that the continuum polarization varies from $\geq 0.1\%$ below 4200Å to $\leq 0.01\%$ above 6000Å.

Resonance scattering and Zeeman effects may also play important roles in the generation of limb polarization. In addition, polarization effects also result from radiative transfer processes, from scattering by electrons and Rayleigh scattering. Leroy (1972) has shown how a plage can alter the smooth behaviour of the CLV and he suggested that the CLV may have

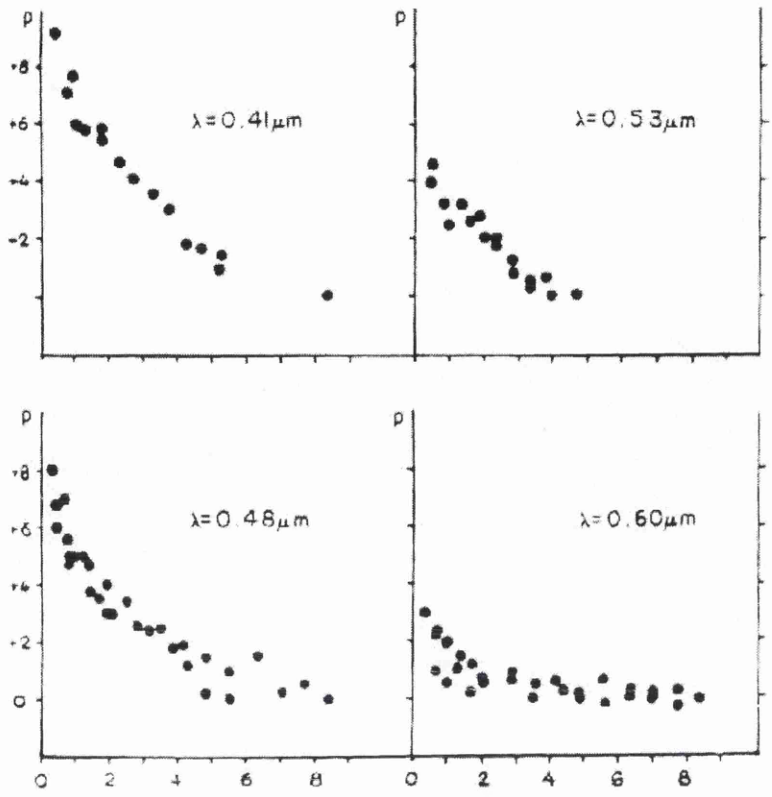

Figure 1.1: Polarization p (in units of 10^{-4}) as a function of distance, d, inside the solar limb (in arcminutes) at four wavelengths (Taken from Dollfus, 1974).

different gradients along equatorial and polar radii, with the equator displaying 10% larger polarization than the pole (see Figure 1.3). Outside of solar active regions with large magnetic fields, it is not possible to measure line polarizations due to the Zeeman effect. However, resonant and fluorescent scattering does generate polarization all over the solar disk, with increasing amplitude near the solar limb. Near the edge of the solar disk, all these processes generate polarizations with the predominant electric vector tangential to the limb.

1.2.2 Resonance and Fluorescent Scattering

Lord Rayleigh, circa 1922, first discovered that by exciting gaseous mercury by polarized radiation, the emitted resonance line at 2527Å will exhibit linear polarization. This resonance polarization effect was also detected in the Ca I 4227Å line in light from the solar limb by Redman (1941). Since then, such effects have been explored in a variety of lines (see Stenflo (1974), Wiehr (1978), Stenflo et al. (1980), Wiehr (1981) and Bianda et al. (1998)). Recently the CLV of polarization for many resonance spectral and the investigations have been extended to the detection of the Hanle effect (resonance scattering in the presence of a weak magnetic field).

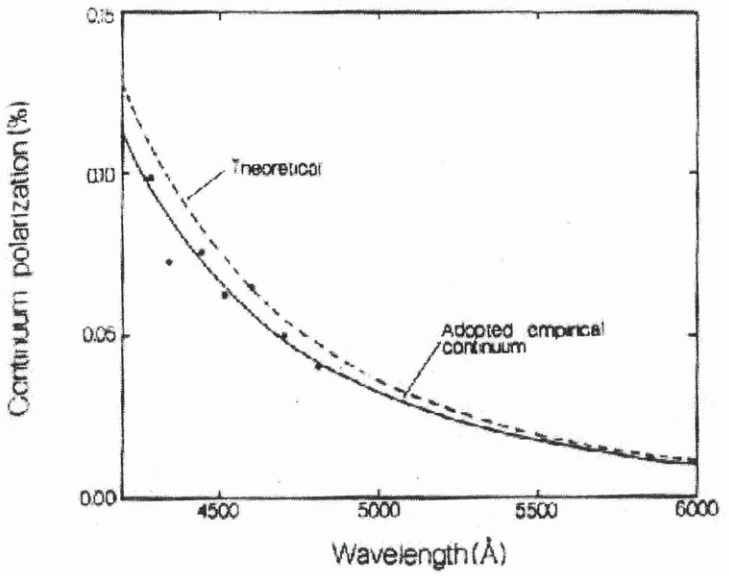

Figure 1.2: Empirical and theoretical continuum polarization as a function of wavelength. The filled circles represent determinations from scatter-plot diagrams. The solid curve, 84% of the theoretical curve, represents a fit to these points (Taken from Stenflo, 1983b).

The generated polarization for each resonance line increases towards the solar limb with the observed level of effects depending on a variety of influences. The scattered radiation will be polarized only if there is an anisotropy in the incident radiation field. This global anisotropy is provided by the solar limb darkening. Polarization arises because the incident radiation, being anisotropic, induces a net dipole moment in the scattering particle. If the particle does not suffer a collision before it re-radiates, the phase between the vector components of the dipole moment are preserved and remain imprinted on the scattered radiation, a phenomena known as coherent scattering. Most of the scattering in the solar atmosphere is incoherent due to the high collision rate, but the fraction of coherent scattering increases rapidly with height in the atmosphere due to the decrease in density and thus in collision rate. The anisotropic illumination makes the scattering polarization increase from zero at disk center to a maximum at the solar limb. Due to decreasing limb darkening, the magnitude of the polarization generally decreases towards the blue end of the spectrum. Stenflo et al. (1980) measured polarized line profiles of 10 non-magnetic resonance lines (including Ca II H and K and Ca I 4227Å) and their center to limb variation. They showed that in strong lines with pronounced dampening in the wings, the polarization had a maxima in the wings, typically about 0.6Å from the line-center, and a few strong lines such as Ca II K and Ca I had narrow polarization peaks in the Doppler core, as illustrated in Figure 1.4, whereas the absence of core polarization in some resonance lines is likely to be connected with magnetic

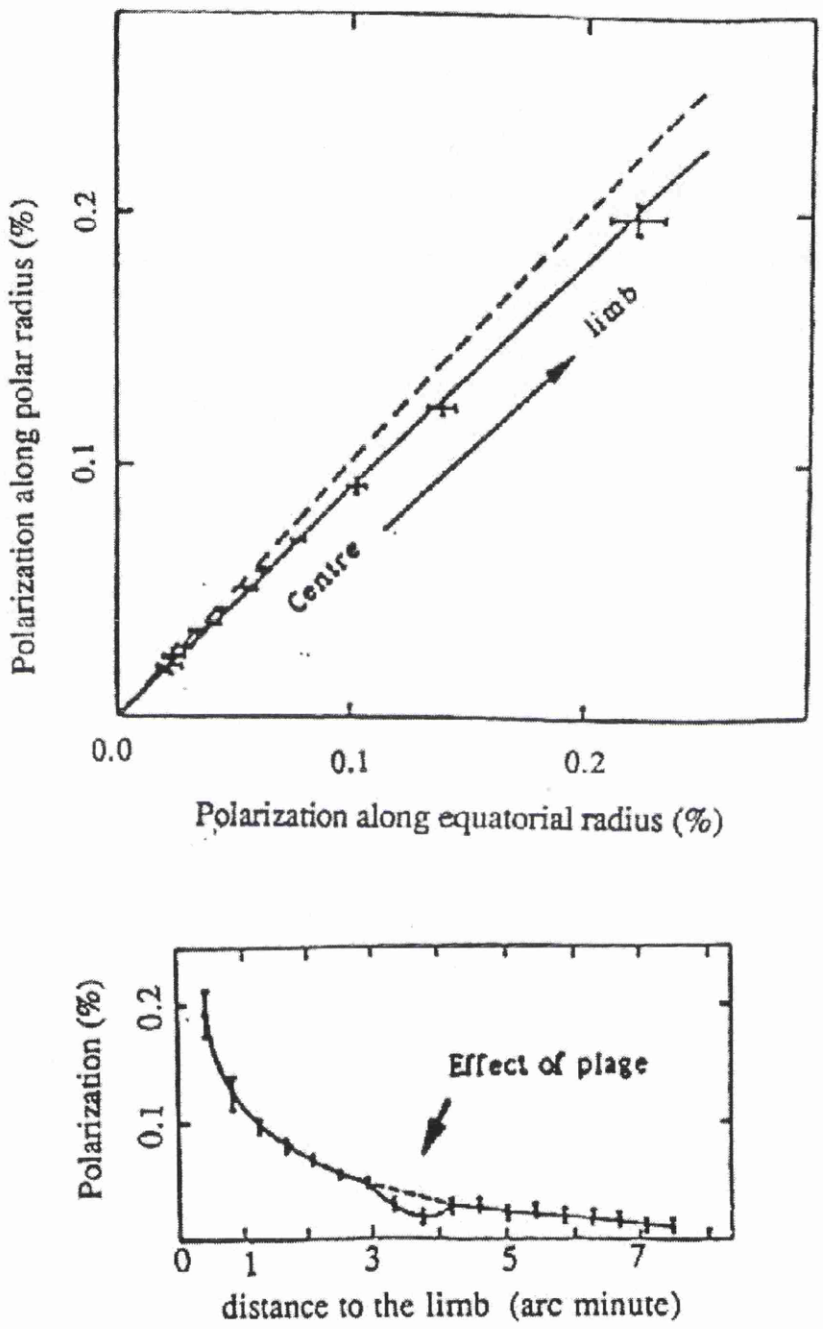

Figure 1.3: Upper- A diagram of polarization measured along an equatorial radius and a polar radius. The dashed line represents the condition of the polarization being identical along the two radii. Lower- A scan along a solar radius including a plage. (Taken from Leroy, 1972).

depolarization, see Section 1.2.4. The existence of maxima in the wings may be explained in qualitative terms. Firstly, the polarization must decrease out in the far wings because the ratio of the line to continuum opacities decreases and the continuum is less polarized than the line. Secondly, the polarization must decrease when moving close to the core since the large opacities there make the radiation field more isotropic leading to reduced polarization. These effects have been reproduced in radiative transfer calculations by Dumont et al. (1973). Later Rees and Saliba (1982) and Saliba (1985) showed how the presence of a narrow polarization peak in the Doppler core together with the separate peaks in the wings could be understood as an effect of partial frequency redistribution in polarized radiative transfer for strong lines. This means that the depolarization dip between the core and wing polarization maxima is perhaps the clearest signature of the transition from complete non-coherent scattering in frequency in the Doppler core to coherent scattering in the dampening wings of a resonance line. In addition it was found that the polarization is very sensitive to temperature gradients, indicating that linear polarization profile analysis may offer an important new way of modelling the temperature distribution in the solar atmosphere. Typical maximum values are about $p \sim 3\%$ with the direction of vibration tangential to the limb.

Stenflo et al. (1983a,b) recorded the linear polarization spectrum of 10 arcseconds inside the solar limb at the heliographic north pole across the wavelength ranges 3165–4230Å and 4200–9950Å in order to explore the physics of scattering in spectral lines. A result of particular interest to this work was the polarization in two Balmer lines Hα and Hβ, p_{max} = 0.17% and 0.20% respectively, a case of fluorescent scattering in which emission of an Hα photon seems to be preceded by excitation by a Lyβ photon, and similarly photons scattered in Hβ representing scattering of Lyγ photons, see Figure 1.5. The Balmer lines should represent a clear case of fluorescent scattering, when the initial and final levels are different. The population of the hydrogen ground level dominates greatly in the solar atmosphere over the population of the first excited level. When for instance Hα is emitted by a transition from n = 3 to n = 2, it seems more likely that the preceding radiative excitation of level n = 3 has occurred from the ground state, i.e. by a Lyβ photon.

Recent observations by Stenflo and Keller (1997) of the "second solar spectrum" have revealed a highly unexpected and surprising feature, the prominence of molecular contributions, particularly the C_2 and MgH lines as illustrated in Figure 1.6. The polarization of molecular lines provides a new source of information on the temperature and pressure structure of the solar atmosphere. A number of spectral lines have been observed, by Stenflo et al. (1997), at two different limb distances (μ = 0.1 and 0.2) in order to compare the steepness

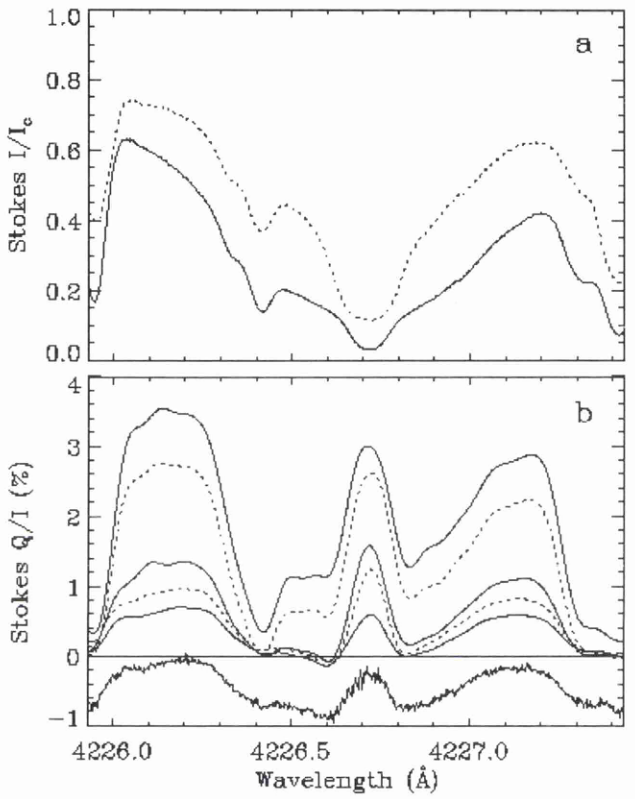

Figure 1.4: (a) Stokes I/I_c spectra of Ca I 4227Å , where I_c is the continuum intensity. The solid profile was observed at $\mu = 1$, the dotted profile at $\mu = 0.1$. (b) Stokes Q/I spectra. The top 5 spectra were obtained at (from top to bottom) $\mu = 0.1$, 0.15, 0.2, 0.3, 0.4. The noisy spectrum at the bottom of the frame is the same as the spectrum at $\mu = 0.4$, but prior to Fourier smoothing (Taken from Bianda et al. 1998).

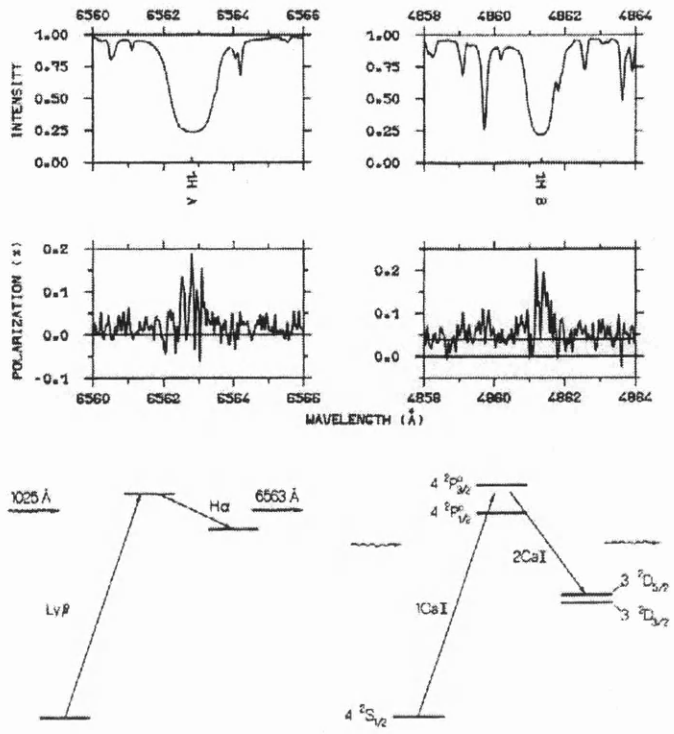

Figure 1.5: Top: Polarization in Hα and Hβ. Bottom: Principles of fluorescent scattering in Lyβ $\rightarrow$ Hα (left) and 1 Ca II H and K $\rightarrow$ 2 Ca II infrared triplet (right) (Taken from Stenflo et al. 1983b).

of the CLV of their polarization amplitudes. The spectral lines with the steepest CLV are molecular lines, the Ca II infrared triplet (8542Å and 8662Å), Hα, and Na I 8195Å where the polarization declines by about a factor of 3 when going the 15 arcsecond distance from $\mu = 0.1$ to $\mu = 0.2$, as compared with a factor of 6 for the continuum polarization and 1.38 for a purely dipole-scattering atmosphere, see Figure 1.7. In contrast the Sr I 4607Å and Ba II 4554Å lines have only moderately steeper CLVs than that of the purely scattering atmosphere. The CLV of the Sr I 4607Å has received most attention, see Figure 1.8, since this line lends itself well to detailed modelling with numerical radiative transfer (see Faurobert-Scholl, 1993 and Faurobert-Scholl et al., 1995). This modelling has been performed mainly for the purpose of diagnosing "hidden" turbulent magnetic fields. Such fields that are tangled or turbulent on scales that are beyond the attainable spatial resolution are invisible in any regular magnetogram.

The shapes and slopes of the CLV curves are sensitive functions of the atmosphere structure, and as such they may serve as new constraints on models of the temperature density stratification of the Sun's atmosphere. A semi-analytical expression provides a good fit to

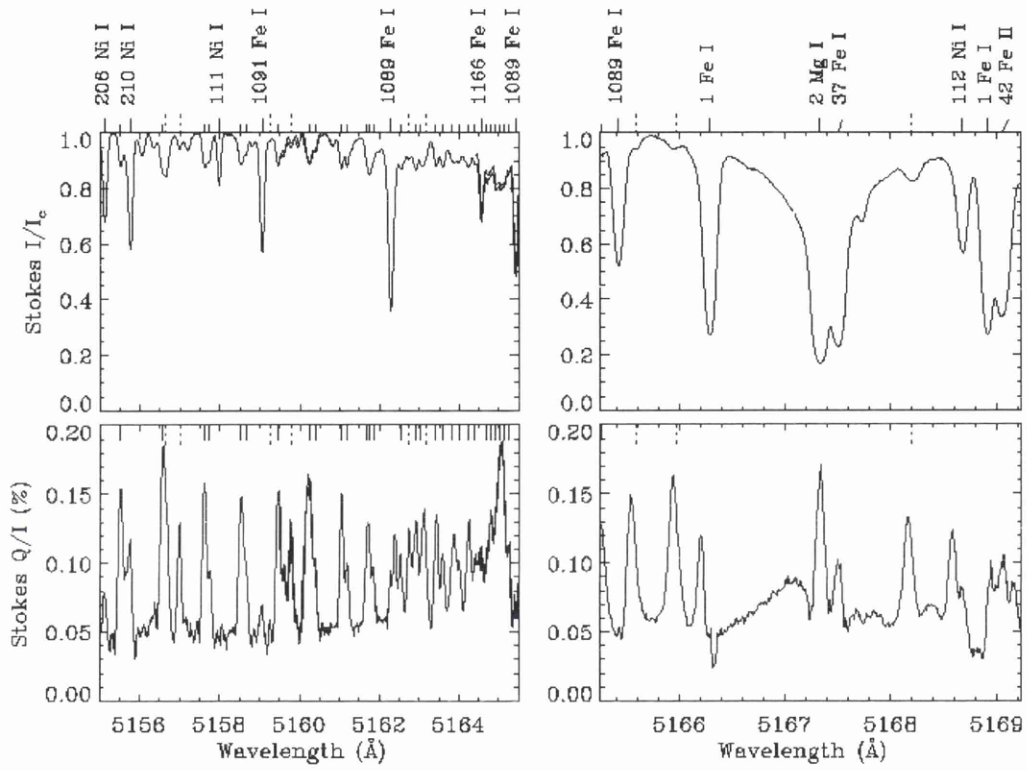

Figure 1.6: Examples of molecular features in the second solar spectrum. The wavelength of identified lines of C_2 molecule are marked by solid, unlabelled tick marks, those of MgH by dashed tick marks a the top of both the upper and lower panels (Taken from Stenflo and Keller, 1997).

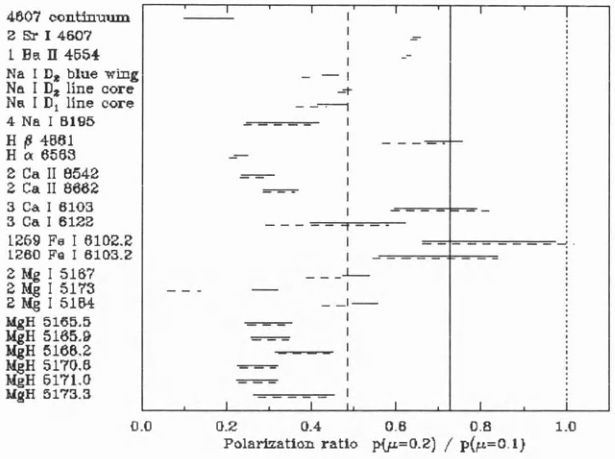

Figure 1.7: Overview of the slopes of the CLV for a number of lines. The slopes are represented by the ratio between Q/I polarizations observed at $\mu = 0.2$ and $\mu = 0.1$. The horizontal lines represent error bars. The ratio of 0.726 for a purely scattering atmosphere is given by the solid vertical line, while the corresponding ratio of 0.485 for the analytical function $(1 - \mu^2)/\mu$ is given by the vertical dashed line. For any optically thin scattering layer the CLV function at 5000Å gives a polarization ratio of 0.37 (Taken from Stenflo et al. 1997).

the observed values of the polarization maximum of the Sr I line:

$$\frac{Q}{I} = \frac{a(1-\mu^2)}{(\mu + b)}, \tag{1.17}$$

with the parameters values $a = 0.3\%$ and $b = 0.07$ fitting the data. The choice of this functional form, first introduced by Stenflo and Keller (1997), is based on two main considerations. Firstly, in the case of a plane-parallel stratification, the path length of an optically thin layer scales as $1/\mu$. Secondly, the source function of Stokes Q scales as $(1 - \mu^2)$. Combining these two dependences yields the form $(1-\mu^2)/\mu$, which gives a good description for optically thin lines. In order to approximate the CLV of optically thick lines the free parameters a and b are introduced. Parameter b accounts for the breakdown of the plane-parallel approximation when approaching the limb. However, while these considerations provide a good explanation for the steep CLV of optically thin lines like the molecular lines, they are not very applicable to optically thick lines whose CLV will be governed by more complex radiative-transfer effects, like Hα and the Ca II infrared triplet.

To understand the scattering physics on the Sun and to exploit it for various diagnostic purposes it is imperative to observe systematically the CLV behaviour of many more lines in a similar, rather complete way as has been done for the Sr I line. The CLV of the scattering

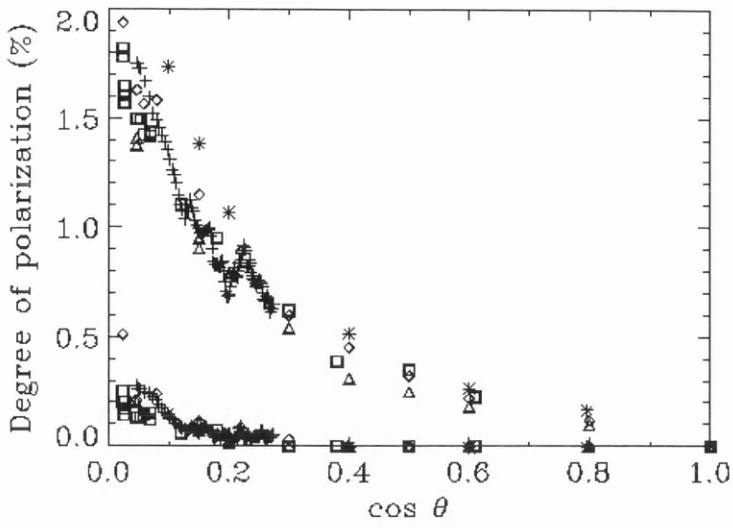

Figure 1.8: Center-to-limb polarization (Q/I) amplitude variation of the Sr I 4607Å line (upper set of points) and continuum polarization (lower set of points) (Taken from Stenflo et al. 1997).

polarization is a sensitive function of the height variations of temperature and density in the upper photosphere, temperature minimum, and chromosphere, and it thus provides novel constraints for atmospheric modelling.

1.2.3 The Magnetic Zeeman Effect and Magnetic Intensification

The Zeeman effect in a magnetic field is a well known phenomenon and is the basis of measurement of solar magnetic fields by means of standard magnetographs. The energy levels of atomic electrons in an external magnetic field are split into several components according to their total magnetic dipole moment, μ, due to the orbital and spin magnetic dipole moments. For a magnetic field strength, B, of less than several tenths of 1T (i.e. a few thousand Gauss) the splitting is proportional to B and given by

$$\Delta E = -\mu \cdot \mathbf{B}. \tag{1.18}$$

The polarization properties of the radiation depends on the direction of observation relative to the magnetic field.

For observation along the poloidal field there are only two σ components which are right- and left-handed circularly polarized. For observation perpendicular to the magnetic field there are two σ lines polarized perpendicular to $\mathbf{B}$ and a π line polarized parallel to $\mathbf{B}$.

Considering a transition from a singlet state to a higher energy level, the spectral line will be split into 3 components. The central component has the same energy as the single zero-field line, is twice the intensity of the two components displaced in energy by ΔE and is of orthogonal polarization to them. The separation of the Zeeman components may be calculated from the expression, viz

$$\Delta\lambda = \pm 5.89 \times 10^{-19} g \mathrm{B} \lambda^2 \tag{1.19}$$

where $\Delta\lambda$ is the Zeeman displacement, λ is the undisturbed wavelength, B is the magnetic strength strength (gauss) and g is the Landé factor. In order to detect this effect, the magnetic field should be strong enough to introduce a measurable displacement greater than the natural width. If the magnetic field is weak, Zeeman splitting will be too small for detection. However the presence of the weak field might be investigated through the Hanle effect and resonance scattering polarization.

1.2.4 The Hanle Effect

The Hanle effect concerns the modification of polarized resonance line scattering by solar magnetic fields and it can thus be used as a diagnostic of magnetic fields. It provides a different diagnostic of magnetic fields, operating for a lower range of field strengths than does the Zeeman effect. The current status of the theory and observations of the Hanle effect in solar studies are discussed in several contributions to a workshop on solar polarization, (see Stenflo and Nagendra, 1996).

The consequences of the Hanle effect for resonance line scattering polarization can be described in terms of the classical damped oscillator model for the scattering of radiation by an atom, Mitchell and Zemansky (1961). In the classical model, the absorption of light will induce oscillations of the atom in two orthogonal directions. The basic physics of the Hanle effect is that the components of the electron motion that are transverse to the magnetic field will be made to precess at the Larmour frequency ω_L, owing to the $\mathbf{v} \times \mathbf{B}$ Lorentz force on the electron emitting circular polarized light along the magnetic field and linearly polarized light normal to the field. The results are a decrease of the degree of polarization and a rotation of its plane, depending on the strength and the direction of the magnetic field. In terms of the linear polarization with the dominant vector parallel to the solar limb, the Hanle effect reduces the polarization, and rotates the direction of vibration through an angle Θ. Breit (1925) derived expressions for the percentage polarization, p, and the angle of rotation, Θ.

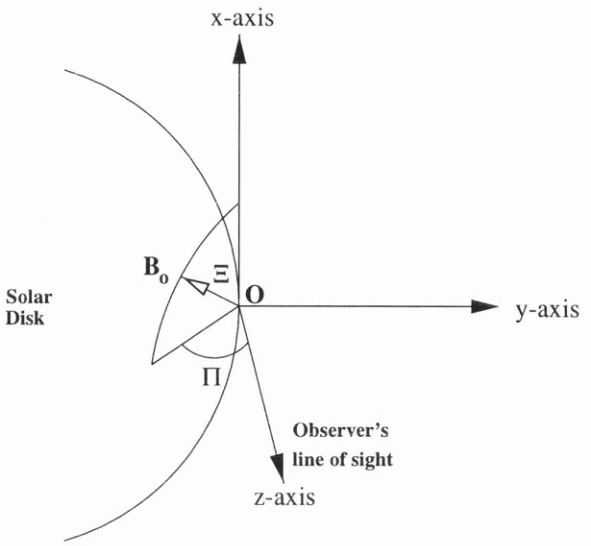

Figure 1.9: Co-ordinate system for describing the Hanle effect on the solar limb.

For polarization observed along the magnetic field of strength B, the polarization is

$$p = \frac{p_o}{\sqrt{1 + (g\omega_L\tau)^2}}, \tag{1.20}$$

where p_o is the percentage polarization for the field-free case, $\omega_L = \frac{eB}{2m_e c}$, τ is the mean radiative lifetime (or the reciprocal of the Einstein transition rate A_{ul} with upper and lower levels u and l), e is the electron charge, g is the Landé correction factor, c is the speed of light and m_e is the electron mass. The rotation Θ of the polarization is given by

$$\Theta = \frac{1}{2}\arctan(g\omega_L\tau). \tag{1.21}$$

The effect of the magnetic field on the linear polarization can be explained by considering Figure 1.9 and Figure 1.10. As radiation travels from the Sun to the observed point O (lying along the y-axis) the scattered light exhibits polarization p_o with plane of polarization parallel to the x-axis. If a weak magnetic field is present at the region of scattering, p will be modified, depending on the direction of the magnetic field with respect to the observer. The magnetic field vector is characterized by $\mathbf{B_o}$. This latter vector is at angle Ξ with respect to the x-axis and its projection onto the zy-plane is at angle Π with respect to the line of sight.

In the case of a longitudinal magnetic field (along z-axis, $\Xi = 90°$ and $\Pi = 0°$) an observer sees radiation that is polarized in the x-direction. Figure 1.10 shows the motion of the atomic oscillator as viewed by an observer on the z-axis looking along the magnetic field, with positive

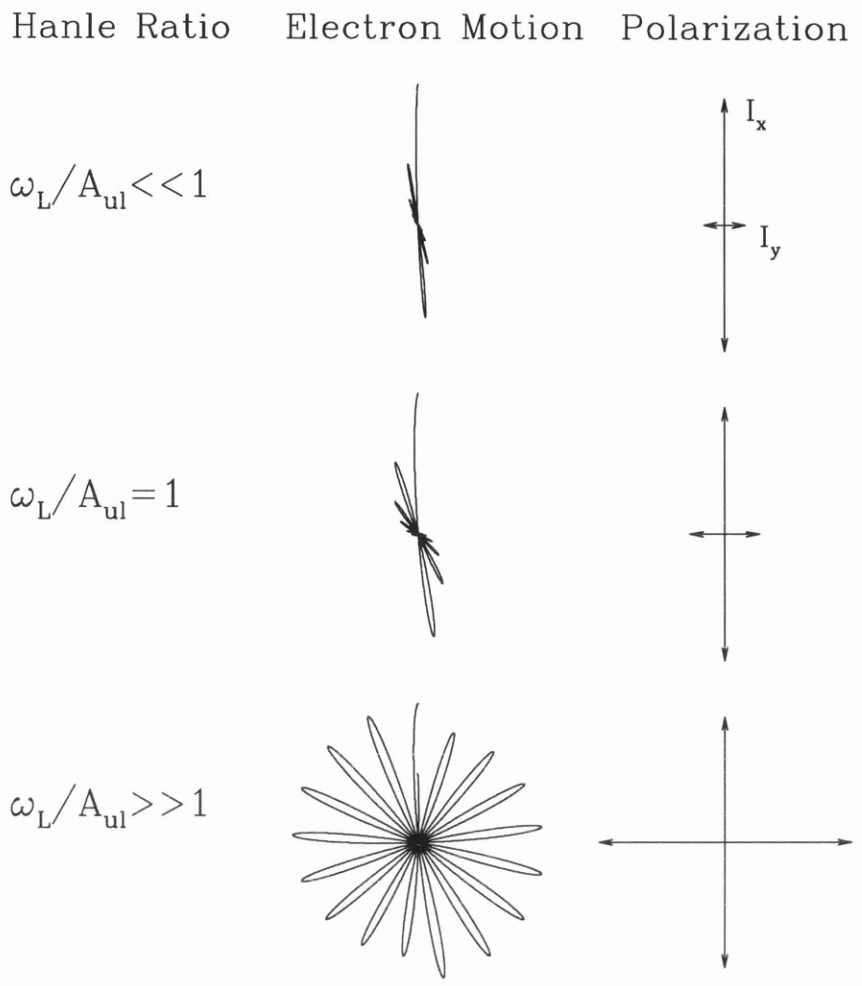

Figure 1.10: The Hanle effect as seen by an observer looking along the magnetic field. Three cases are shown for the ratio of the precession rate ω_L to the radiative rate A_{ul}. The left hand column gives the ratio A_{ul}; the middle column shows the classical electron motion; and the right column indicates the intensities of the scattered light in two orthogonal directions. The cases shown are for the scattering of unpolarized light that is incident from the negative y-direction at the left with the magnetic field along the viewing line-of-sight on the z-axis. For weak magnetic fields, $I_x \gg I_y$, the scattered light is nearly 100% polarized along the x-direction. For large fields with $\omega_L/A_{ul} \gg 1$, the Hanle precession completes an entire rotation before much damping of the oscillator can occur, so the scattered light is emitted evenly at all position angles (known as "saturation"), such that $I_x \approx I_y$ and the polarization drops toward zero. When $\omega_L/A_{ul} = 1$, the optimal Hanle effect sensitivity to the magnetic field is observed. Note that an observer on the y-axis (forward scattering) would see $I_x = I_z$ in the absence of a magnetic field. However, as I_y increases owing to the Hanle effect, I_x will decrease and I_z becomes greater than I_x, thus the Hanle effect can actually produce polarization in the case of forward-scattering.

x- up and positive y- right. There are three cases of ω_L/A_{ul} shown as indicated in the left hand column. For each case the middle column shows the Hanle precession and the rightmost column indicates the scattered light in terms of the orthogonal intensities I_x and I_y. In the absence of a magnetic field, the observer sees the scattered light as 100% polarized, because the transverse oscillator emits at a single fixed position angle and the parallel oscillator is viewed along the axis of oscillation, so it scatters no light into the viewing direction. As the magnetic field increases, the dipole oscillator in the x-direction is caused to precess about the z-axis, hence a depolarization of the scattered beam is observed, yet the intensity of light is not diminished. In contrast, an observer who is situated to see forward scattering would measure zero polarization in the zero field case, but with a magnetic field, a net polarization is observed along the direction of the magnetic field. So, the Hanle effect can create or destroy polarization depending on the magnetic and scattering geometries. As the field strength increases to large values, the depolarization becomes nearly complete when $\omega_L \gg A_{ul}$ (c.f. the bottom row of Figure 1.10). In this case the depolarization is said to be "saturated", because larger magnetic fields can produce no discernible change in the observed polarization. The saturated case is still of interest because it indicates the presence of a magnetic field and can be assigned a lower limit of the field strength, but an accurate determination of the field strength is best made when $\omega_L \simeq A_{ul}$ (c.f. the middle row of Figure 1.10), for which the depolarization is significant but not complete. Therefore a longitudinal magnetic field will cause both a reduction of the degree of the polarization and a rotation of its direction of vibration by an angle Θ.

If the magnetic field direction is normal to the photosphere (along the x-axis, $\Xi = 0°$) the scattered light is completely polarized along OZ when there is no magnetic field. However, the Hanle effect results in a depolarization with an increase in total intensity. Alternatively, a transverse magnetic field (along the y-axis, $\Xi = 90°$ and $\Pi = 90°$) will decrease the degree of polarization without altering its plane of polarization which is still parallel to the x-axis.

Due to the precession of the damped oscillator in the presence of the magnetic field, the direction of vibration will deviate from the original direction, and this causes the plane of vibration of the emitted light to rotate. The oscillator describes a rosette when viewed along the magnetic field, and the shape of the rosette - and therefore the nature of the polarization - will depend on the ratio between the angular velocity of precession, ω_L, and the radiative damping constant, A_{ul} $(1/\tau)$, of the oscillator. If $\omega_L/A_{ul} \gg 1$ the rosette will be axially symmetric, since the atom will have ample time to precess before it is damped out. Consequently, there is no polarization observed along the magnetic field if the field

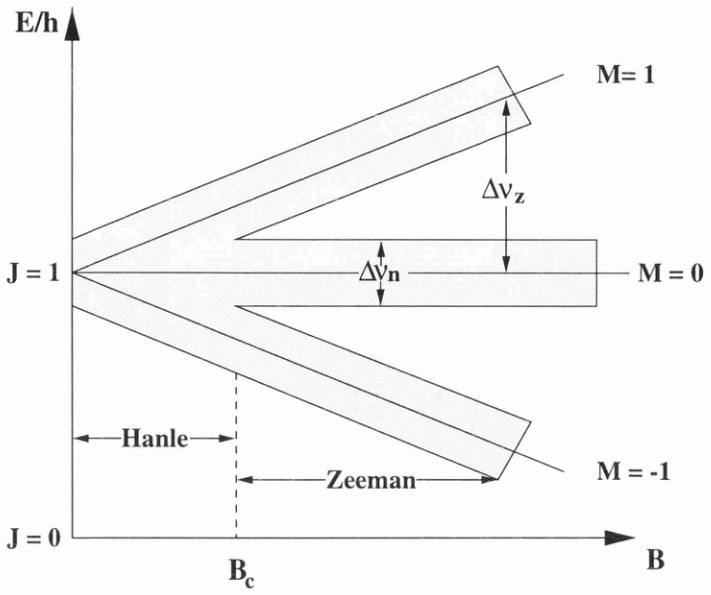

Figure 1.11: Energies of naturally broadened excited state sublevels of a Zeeman triplet as functions of magnetic field strength B. M-state interference occurs for $B \leq B_c$.

is strong enough to make the inequality hold. If $\omega_L/A_{ul} \simeq 1$ the oscillator describes an asymmetrical rosette, which means that the degree of polarization is reduced relative to the value of the field-free case with the direction of polarization rotated with respect to the direction of polarization of the exciting beam. Finally if $\omega_L/A_{ul} \ll 1$, the oscillator hardly has time to precess before it is damped out, which explains the weak-field results.

Considering the Hanle effect in quantum mechanical terminology provides a useful insight into its applicability for different magnetic field strengths. The effect applies when the magnetic sublevels of a line transition are sufficiently close in frequency that the natural line widths of the sublevels overlap significantly. As a consequence, coherence effects result in interference of the wave functions between these levels, and the interference causes changes in the polarization of the scattered light. At larger field strengths, the sublevels will be distinctly separated, and the Zeeman effect will dominate over the Hanle effect, because the phase coherences are lost. This alternative picture is given in Figure 1.11 where the classical oscillator is identified with a normal Zeeman triplet. The lower level (J = 0) is assumed to have infinite lifetime; the three upper state (J = 1) sublevels are broadened, revealing that the Hanle effect occurs in the region of overlapping sublevels, or the so-called M-state interference. Denoting $\Delta\nu_Z$ as $\nu - \nu_0$ for a normal Zeeman triplet and $\Delta\nu_N$ as the natural

line width, the following summarises the different magnetic effects for atomic scattering of light:

$$\begin{cases} \Delta\nu_{\rm Z} \ll \Delta\nu_{\rm N} & \Longrightarrow \text{Non} - \text{Magnetic}, \\ \Delta\nu_{\rm Z} \approx \Delta\nu_{\rm N} & \Longrightarrow \text{Hanle} \qquad \text{(weak field regime)}, \\ \Delta\nu_{\rm Z} \gg \Delta\nu_{\rm N} & \Longrightarrow \text{Zeeman} \qquad \text{(strong field regime)}. \end{cases}$$

The Zeeman splitting for a normal triplet is just the Larmor precession frequency, ω_L, and the natural line width is the radiative transition rate, A_{ul}, hence it is useful to consider the ratio

$$\frac{\Delta\mu_{\rm Z}}{\Delta\mu_{\rm N}} = \frac{\omega}{A_{ul}} = \frac{e\,{\rm B}}{2\,m_{\rm e}\,c\,A_{ul}}. \tag{1.22}$$

The first observation of the Hanle effect on the solar disk was made by Stenflo (1981). By using a frame of reference parallel to the limb, the polarization by ordinary resonance scattering would be described by the value of Q only, with $U = 0$. However, Stenflo's observations of the core of the Ca I 4227Å line in the spectrum of a plage clearly indicate that U has a non-zero value, which means that the plane of polarization is not parallel to the limb. Calculation from the Stokes parameters, Q and U, shows that the direction of vibration of the linear polarization in the Doppler core has been rotated by 33°. The polarization in the wings is unaffected. Based on these observations Faurobert-Scholl (1992) and Faurobert-Scholl (1994) deduced that there is a magnetic field of 20-100G at heights between 700 and 1200km above the continuum-forming level, if it is assumed that the field is in the form of a magnetic canopy, i.e. a horizontal magnetic field overlying a field-free atmosphere.

Stenflo (1982) attempted to interpret the observed polarization amplitudes of Sr I 4607Å, and led to an estimated value of 10-100G for the strength of the turbulent field in the photosphere. This approach has been refined by Faurobert-Scholl (1993), who carried out detailed radiative-transfer calculations to fit the CLV of the polarization profiles of the Sr I 4607Å line, allowing the admitted range of turbulent field strengths (assuming an isotropic distribution) to be narrowed down to 0-20G (see Faurobert-Scholl et al., 1995).

Observations of the CLV of Sr I 4607Å line Q/I amplitude, by Stenflo and Keller (1997), show a very pronounced kink near $\mu = 0.2$, as illustrated in Figure 1.8. Closer to the limb the amplitudes from November 1994 are considerably larger than those from June 1994, but the agreement is good for $\mu \geq 0.2$. The most natural explanation for the kink is that for the June 1994 observations the slit happened to cut across a region that had more Hanle-depolarizing magnetic fields inside the 20 arcsecond limb zone as compared with the case for the November 1994 observations.

In the presence of a weak magnetic field, with mixed polarities over the resolution element of the telescope, there is no preferred direction for the rotation of the polarization plane, but the depolarization is not cancelled out. This provides a diagnostic tool for weak fields with mixed polarities. This was first pointed out by Stenflo (1982) and confirmed by Stenflo et al. (1998), who suggested that such weak magnetic fields, although hidden from magnetograms, could carry a significant part of the solar magnetic flux.

The indirect diagnostic of magnetic fields, based on the Hanle effect, requires detailed non-LTE radiative transfer calculations including polarization. The first step of the diagnostic method is to compute as accurately as possible the resonance polarization which would be observed in the absence of a magnetic field. Resonance polarization is very sensitive to the non-LTE processes which contribute to the line formation, such as frequency redistribution, depolarizing collisions, velocity fields and multiple scattering. It is obviously highly sensitive to the anisotropy of the line radiation field, which depends on the atmospheric structure. The results are then compared with the observed polarization and the discrepancy is interpreted in terms of the Hanle effect. The Hanle effect does not affect the polarization in the line wings and does not change the intensity profiles, since very weak magnetic fields do not significantly modify the line absorption profile. This allows the constraint, at least partly, of the first step of the calculations by requiring that the CLV of the line intensity profile should be well reproduced. Until now this has been done essentially for two resonance lines, namely the Ca I 4227Å and the Sr I 4607Å lines. Both are normal triplets which show relatively high linear polarization rates outside active regions. The sensitivity of a line to the Hanle effect is unique, for Sr I and Ca I this is 20G, the useful range being approximately 5-100G.

Another area where the Hanle effect has been much applied in the past is the diagnostics of magnetic fields in solar prominences. Most of this work has focused on the He I D_3 5876Å line, which, being optically thin, allows direct interpretation without involving radiative-transfer calculations. In this case not only the Hanle depolarization, but also the rotation of the plane of polarization can be observed and studied in detail. However, interpretations that are based on observations of a single spectral line are sensitive to the model used for the solar atmosphere and the atomic physics. As in the Zeeman effect diagnostics one can suppress such model dependence by using the differential rather than the absolute polarization effects, which are seen in combinations of lines with different sensitivities to the Hanle effect. The combinations of spectral lines for differential Hanle diagnostics must be chosen carefully since the different lines may not sample the same magnetic fields.

1.3 Polarization Measurements in Fusion Plasmas

Fusion in thermonuclear plasmas is a long-term candidate for providing the world with a large fraction of its energy demands. In a fusion process, two relatively light atomic nuclei are fused together into a single heavier nucleus, thereby transferring some of the mass into energy. In order to sustain fusion processes inside a medium, which may be the solar core or a magnetically confined plasma, the temperature not only has to reach a sufficiently high level, but also it has to remain at this level. Hence the ratio of energy production inside the medium to energy loss of the medium to the world outside has to be balanced. Obviously, the amount of energy produced is determined by the number of reactions, and hence by the number of particles per unit of volume. Energy loss is determined by the quality of confinement, and is usually expressed via an energy confinement time τ_E, i.e. the time it would take a plasma without a heating source to cool down. Although there has been steady progress towards breakeven (where energy output exceeds energy input), many puzzling issues related to plasma instabilities and energy/particle confinements remain.

1.3.1 Magnetic Confinement Schemes

The requirement of a high temperature environment implies that little thermal contact may exist between the fusion medium and the outside world. In many schemes, this situation is obtained by applying a sufficiently large magnetic field, which causes the charged particles to gyrate around the field lines as a result of the Lorentz force. The gyro-motion reduces heat and particle transfer perpendicular to the direction of the magnetic field. Confinement along the field lines is obtained either by squeezing the magnetic field at the edges of the device, thus obtaining high magnetic field values from which the particles are bounded, or by avoiding end effects in a toroidal geometry, where the field lines close on themselves. However, drift effects caused by the toroidal curvature lead to increased losses across the field lines in an up- and downward direction. To avoid this, a second, weaker field is applied poloidally, that causes the field lines to become helical and the drift effects to cancel to first order. As a result of this poloidal field, the field lines no longer close on themselves but lie on a nested toroidal surface of equal flux, the so-called "magnetic surface". Only for certain ratios of poloidal to toroidal field strength are the field lines themselves closed, in which case the magnetic surfaces are called "rational". Because of the geometrical resonance, plasma instabilities are often located on rational surfaces. At present, most experiments in the field of magnetic confinement fusion make use of a toroidal geometry in a device called a "tokamak".

The tokamak is a toroidally shaped device, as shown in Figure 1.12. The major radius of

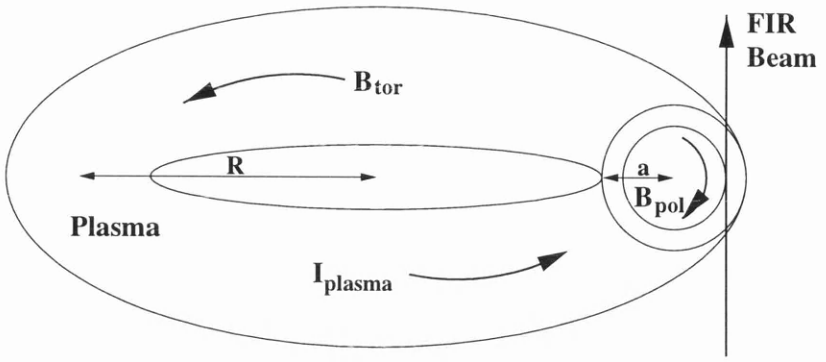

Figure 1.12: Basic magnetic field configuration for a tokamak.

the torus is usually designated R and the minor radius a. The main confining magnetic field is in the toroidal direction and is typically 1–10T. Because of particle drifts caused by the curved magnetic field, the plasma cannot be confined by the toroidal field alone; an additional poloidal field (B_{pol}) in the range of 0.1–1.0T is required. A unique feature of the tokamak is that this poloidal field is produced by current flowing in the plasma itself. A transformer coil running through the center of the torus induces a toroidal electric field which drives the plasma current I_{plasma}. The plasma current not only provides the stabilising poloidal field required to eliminate charged particle drifts, but also provides I^2R ohmic heating of the plasma, and plays a role in pressure balance through the relation $\nabla \mathbf{p} = \mathbf{J} \times \mathbf{B}$. An additional small vertical field is needed for plasma position control. The combination of the plasma polodial field with the larger toroidal field B_{tor} produces field lines that follow a helical path around the torus. A measure of this helicity is given by the safety factor $q_s = rB_{tor}/(RB_{pol})$ which represents the number of toroidal rotations per polodial rotation for a field line on a given flux surface. The radial profile of $q_s(r)$, or equivalently $B_{pol}(r)$ or J(r), had been shown to be a key parameter in transport models as well as the magnetohydromagnetic (MHD) stability theory of tearing modes, sawteeth, and disruptions. Thus a knowledge of the poloidal field profile is absolutely essential to an advanced understanding of the complex phenomena that governs the behaviour of a tokamak confined plasma.

1.3.2 Current Density Measurements

Progress in magnetic confinement fusion depends on improvements of the quality of the plasma confinement. To determine this quality in a specific situation, measurement of the

relevant plasma parameters with sufficient accuracy and resolution (spatial and temporal) is extremely important. One of the key parameters governing the confinement is the distribution of the poloidal magnetic field over a cross-section, since this field is responsible for a significant reduction of drift effects. The poloidal magnetic field in a tokamak is determined by the poloidal distribution of the current density. Accurate measurement of this parameter is therefore highly desirable. The quality of confinement can be evaluated e.g. through measurement of the electron temperature and electron density profile, from which information on heat and particle transport in the plasma can be deduced.

Measurement of the poloidal field shape at the plasma edge is fairly easy, and is done on virtually every tokamak by means of a set of magnetic (Mirnov) coils. Measurement of the distribution of the poloidal magnetic field in the plasma interior, however, is much more complicated. In this area, polarimetry has become an important technique, since it has enabled rather accurate measurements with a relatively simple geometry. A good review of such polarimetric techniques is presented by Donné (1995). In this type of measurement, the polarization of a beam probing the plasma is rotated as a result of the presence of the poloidal field. Polarimetry is inherently line-integrated, because the amount of rotation of the emerging beam is determined by all local magnetic field values that the wave has experienced along the beam trajectory. Other techniques, mainly spectroscopic, involve measurement of the splitting of atomic energy levels as a result of the Zeeman effect (see Feldman et al., 1984 and Wróbleski et al., 1988) or, in the case of hydrogenic emission from high-energy neutral beams, as a result of the motional Stark effect (see Wróbleski and Lao, 1992). These methods have the advantage of directly measuring the local field pitch angle with no required inversion of chord averaged data, but they all suffer from limitations in time response, radial resolution, and the range of plasma parameters over which they can operate.

The Faraday rotation effect offers a means to measure the poloidal field that has some advantages over the methods described above. The spatial and temporal resolution can be quite good, and the range of plasma parameters that can be measured is large. Consider a linearly polarized far-infrared (FIR) laser beam passing vertically through the plasma cross section as shown in Figure 1.12. As will be derived in Chapter 3, the plasma causes a rotation of the polarization given by

$$\Psi = 2.63\times10^{-13}\lambda^2 \int \mathrm{B}_{||}(r) n(r) dr \tag{1.23}$$

where $\mathrm{B}_{||}(r)$ is the component of the poloidal field parallel to the FIR beam and $n(r)$ is the plasma density.

Passing several chords through the plasma (or equivalently sending a continuous beam imaged onto an array of detectors), the Faraday rotation profile may be determined. Knowing the density $n(r)$ from another diagnostic (usually interferometry), the above equation can be inverted to give the poloidal field profile. The Faraday rotation effect has been measured on other tokamaks; however, it is a notoriously difficult measurement because of the small rotation angle (1° and 15°) and other complicating effects such as beam refraction. In addition, the measurement must be made simultaneously on many different chords passing through the plasma to determine the poloidal field profile accurately.

1.3.3 Previous Faraday Rotation Work

The theoretical basis for Faraday rotation measurements was development by Marco and Segre (1972) and Segre (1978). First-order analytical solutions to the polarization propagation equation were presented. The polarization propagation model, as it applies to this experiment, will be discussed in detail in Chapter 3.

The first proof-of-principle Faraday rotation experiment was done by Kunz and Dodel (1978) on TFR using a single probe beam. In this experiment, the FIR beam polarization was modulated using a ferrite disk immersed in an oscillating magnetic field. A lock-in amplifier was then used to detect the signal, giving an improved signal-to-noise ratio. These single-chord results were important in establishing the validity of Faraday rotation, but did not allow inversion of the line integrated signal which is necessary to determine the poloidal field. The earliest experimental technique for performing polarimetry employed two relatively slow detectors per line of sight. Good mutual calibration of these detectors was vital to the quality of the measurements.

Since the original work, several interferometer/polarimeter systems have been built for various experiments. The first polarimeter system to operate routinely, with sufficient chords to obtain the poloidal field profile, was constructed by Soltwisch (1986) on TEXTOR . This system utilises 9 chords and performs interferometry and polarimetry simultaneously measuring the change in orthogonal polarization before and after passage through the plasma. A schematic drawing of the optical system for a single probe beam is shown in Figure 4.7. The FIR source is an HCN laser with an output of 150mW and a wavelength of 337μm. The beam is incident on a splitter providing reference and plasma beams. The reference beam is shifted in frequency by a rotating grating so that heterodyne detection can be used, as is the standard in modern-day interferometers. After passing through the plasma, the plasma

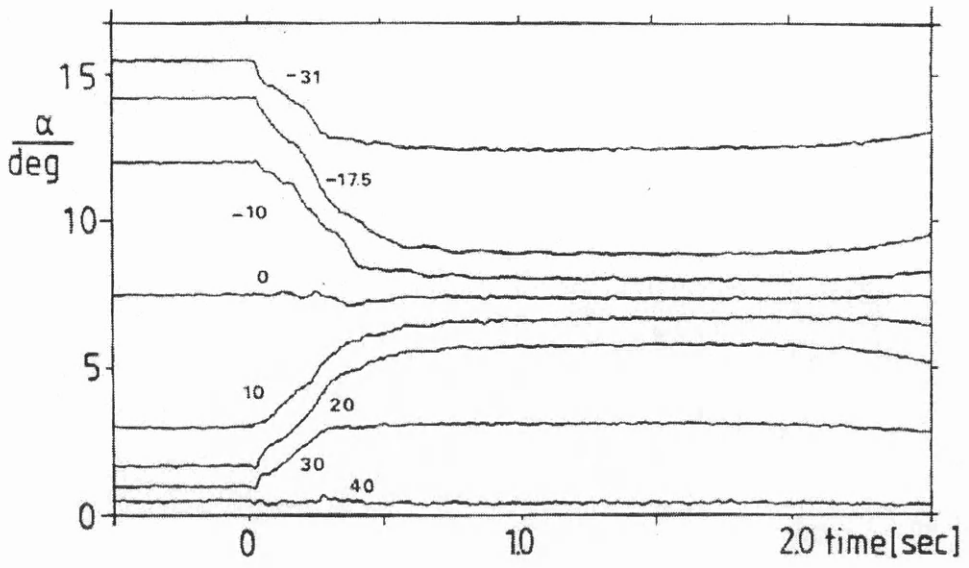

Figure 1.13: Faraday rotation profile data from TEXTOR (Taken from Soltwisch, 1987).

beam experiences a phase shift Φ and polarization rotation Ψ. In addition, the linearly polarized plasma beam picks up a small ellipticity ϵ. The plasma and reference beams are then recombined using a polarizing grid and projected onto two detectors. The interferometer signal is nearly constant in amplitude, with the phase being the usual interferometry phase shift that is proportional to the line integrated density. The polarimetry signal is essentially proportional to the Faraday rotation angle. The beam intensities are not necessarily constant, they can vary due to changes in source power or due to refraction. However, since the intensities show up in both signals, this dependence may be removed from the polarimeter signal by appropriate processing, see Section 4.2.1 for details. The ellipticity complicates the interpretation of the data but for most experiments it is a small (a few percent) correction. An example of the polarimeter data and the inverted profiles for TEXTOR is shown in Figure 1.13. Recently, a six-chord interferometer on JET has been converted by Braithwaite et al. (1989) to polarimetry using essentially the same TEXTOR configuration.

A technique first proposed by Dodel and Kunz (1978) and developed by Rice (1992) on the MTX tokamak transforms the polarization measurement into a phase rather than amplitude measurement. This simultaneously increases the temporal resolution and requires only one detector per line of sight. The method requires two lasers to produce the standard plasma and reference beams, separated by a difference frequency of typically 1MHz. The plasma beam is passed through a quartz quarter-wave plate rotated through a fixed angle to generate an elliptically polarized beam. This is followed by a rapidly rotating quartz half-wave plate that rotates the polarization at four times the plate frequency. After passing through the plasma,

the beam is incident on a polarizing grid followed by a detector. The detected signal is then a sine wave with a frequency of 1MHz which is amplitude modulated at the rotating ellipse frequency. A simulated time history of the signals is shown in Figure 1.14. As the plasma density and poloidal field build up, the axis of the ellipse is rotated due to the Faraday effect, and the phase of the modulation envelope is shifted. Thus by measuring the phase shift of the modulation envelope relative to a reference detector, the Faraday rotation angle is determined; the phase of the high-frequency carrier (or IF) signal is used to obtain the density data. Both the interferometer and polarimeter measurements can now be made independent of signal amplitude, provided the signal remains large enough to stay above the noise level. A similar diagnostic has successfully been commissioned onto the TEXT-Upgrade tokamak by Brower et al. (1997). Details of this technique, along with an analysis of possible errors, is presented in Chapter 4.

The phase method described above is limited by an additional time-varying phase term which is superimposed on the required interferometer data, see Equation 4.19. This term does not represent a plasma effect but is an artifact of the rotating polarization ellipse technique itself. Barry et al. (1996) proposed a modification to this method which does not suffer from the inherent error in the interferometer phase measurement but still preserves the overall robustness of Rice's approach. In the modified method, the rotating elliptically polarized probing beam is replaced by the combination of a rotating linearly polarized beam and a plain linearly polarized beam. Part of this beam combination is altered as it traverses the plasma, and is superimposed with a frequency shifted linearly polarized reference beam on the plasma detector. The other part passes through free space before also being combined with the reference beam on the reference detector. Currently the design is at the test bench phase and is being developed for commissioning onto a tokamak. It retains the major advantages of the original method with the additional benefit that the interferometer data is not disturbed by the extra time-dependent phase term.

On the RTP tokamak a new experimental technique has been developed by Rommers et al. (1997), requiring still only one detector per line of sight, that is inherently capable of measurements with much higher temporal resolution. This makes the method ideal for polarimetric measurements when both high temporal and high spatial resolution are required. Modulation of the wave polarization, either mechanically or through other means, is no longer necessary. Moreover, the method has some fundamental implications, since it has abandoned the physical picture of an actual rotation of the polarization, but instead probes the cause of this rotation, i.e. plasma birefringence, directly. The problem of crosstalk from

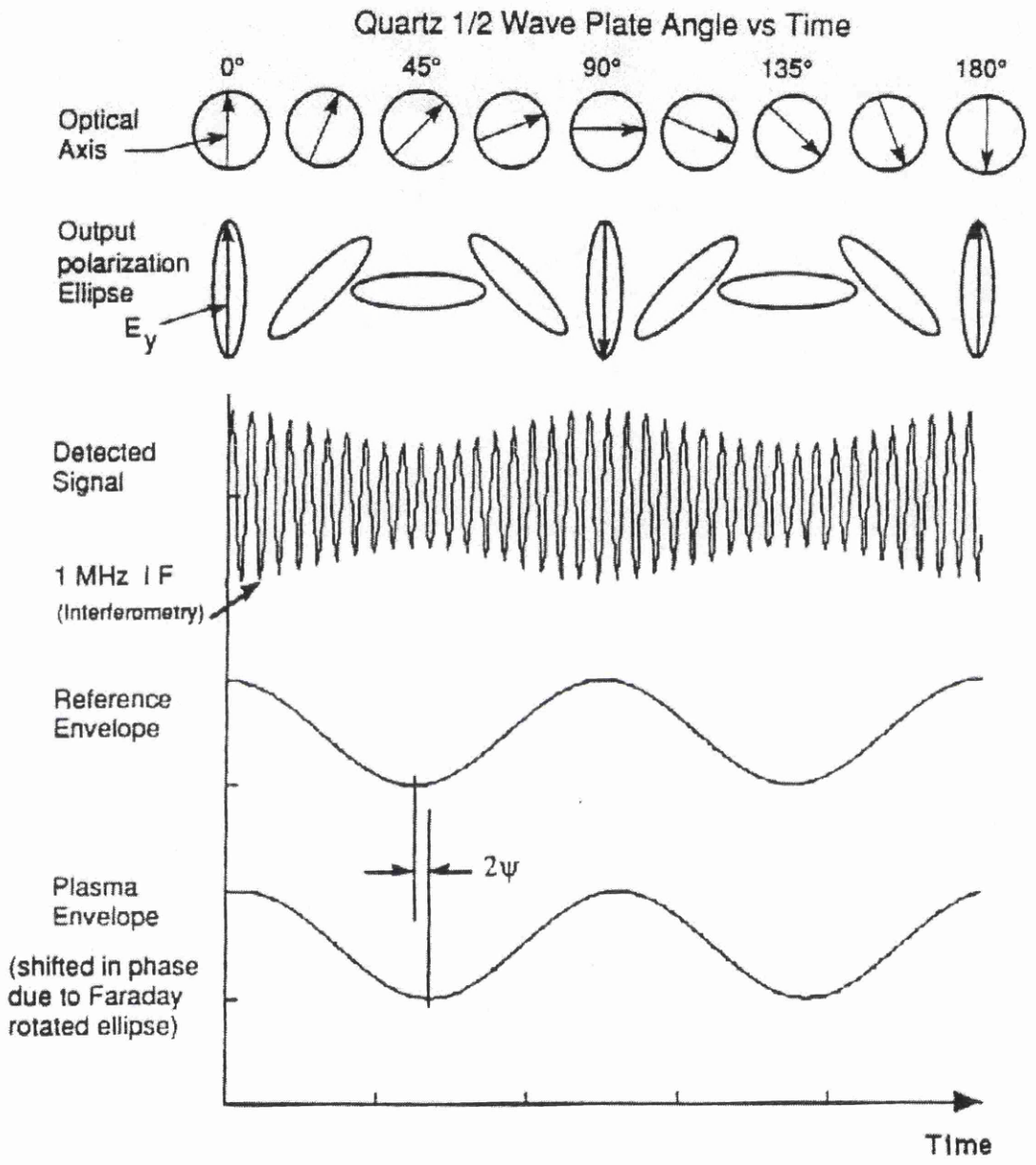

Figure 1.14: Simulated time history of the polarimeter waveforms for a 180° rotation of the quartz half-wave plate. The polarization ellipse is Faraday rotated by the plasma, resulting in the phase shift of the lower waveform (Taken from Rice, 1992).

the polarimeter into the interferometer data, which existed in previous experiments is now eliminated, and in principle a very high temporal resolution can be obtained.

A total of three infrared lasers are applied. Two of the lasers are used for probing the plasma, while the third one acts as a local oscillator. A slight frequency difference between all three lasers is introduced such that after detection three frequency multiplexed beat signals are obtained. Because of circular birefringence, the beams will experience a different value of the refractive index during propagation through the plasma. Due to the frequency offsets, the information on the two refractive indices is spectrally resolved and can be retrieved by separating the carriers after detection and performing a separate phase measurement on each. This difference in refractive index is related to the Faraday rotation angle, whereas their average is related to the density induced phase shift. However, the system suffers from a systematic measurement error in the detected Faraday angle, $\sim 0.3°$. This results from the diffractive distortion of the phase front, caused by a significant beam truncation at the tokamak vacuum vessel window, therefore preventing the necessary inversion to obtain the current density profile.

1.3.4 COMPASS-D Overview

The COMPASS-D (compact assembly) tokamak is a highly flexible, medium-sized device that has been specifically designed to address the key physics issues associated with magnetic confinement fusion. Some important parameters are given in Table 1.1. The programme of experimental research on COMPASS-D is divided into related topic areas:

- Control of instabilities: this is vital to tokamak development, as instabilities reduce the confinement properties of the plasma and/or create disruptive plasma behaviour
- Impurity control: low impurity levels and control of plasma exhaust are critical prerequisites for efficient tokamak operation
- "H-mode" (i.e. High energy confinement mode) operation: the characterisation and control of Edge Localised Modes (ELMs), which are a feature of H-mode operation, are important for power exhaust and impurity control optimisation.

These themes can be investigated in a small device as well as in a large one because the fundamental physical processes are identical. The extensive facilities on COMPASS-D include a set of magnetic perturbation coils for correcting internal instabilities and for modifying the plasma edge region. A 2MW 60GHz microwave system is utilised for precise, localised heating and current drive, for bulk heating and instability control. A 1.3GHz lower hybrid system for

Quantity	Symbol	Value
Major radius	R	0.557m
Minor radius	a	0.232m
Aspect ratio	R/a	2.53
Plasma current	I_{plasma}	$\leq$ 400kA
Pulse duration (without current drive) (with RF current drive)		approx 600ms approx 2s
Central toroidal field	B_{tor}	2.1T
Effective ion charge	Z_{eff}	1.5–3.0
Central electron density	n_e	$1\times10^{20}m^{-3}$
Central electron temperature	T_e	0.5–2.0keV
Confinement time	τ_e	5–25ms

Table 1.1: Main COMPASS-D sizes and indicative discharge parameters.

bulk current drive and current profile control is also available. The tokamak has a real-time electronic neural network for feedback control of the plasma equilibrium position and shape. The COMPASS device has the same magnetic geometry as JET (Joint European Torus) and the planned Next Step device, ITER (International Thermonuclear Experimental Reactor) and is therefore ideally suited for modelling future design parameters.

A series of instruments is available on COMPASS-D for plasma diagnostics, amongst them is an interferometer which will be modified to incorporate a polarimetric measurements, one of the topics of this thesis.

1.4 Outline of this thesis

As previously stated, this thesis comprises two main themes. The following chart illustrated the progressive structure of the thesis (with numerals indicating the chapter numbers):

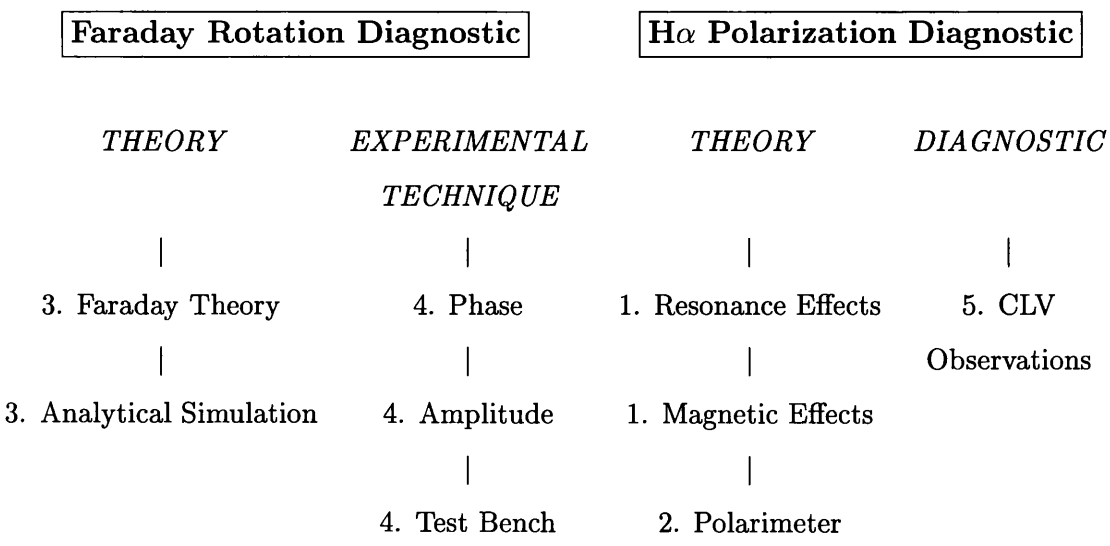

In the present chapter, an introduction to basic polarimetric concepts has been given, followed by a discussion on the predominant polarization processes occurring in the Sun. The engendered polarization is typically a non-LTE phenomena, induced in the solar atmosphere by the radiation field anisotropy or, alternatively by collisions with oriented beam of fast particles. An introduction to nuclear fusion and magnetic confinement was also given, followed by a discussion of the relevance of the present work. In Chapter 2, the prototype solar imaging polarimeter will be introduced and some of the basic reduction techniques required to ascertain a polarimetric measurement will be discussed. A novel technique to determine the polarimeter's instrumental polarization using a monochromatic depolarizer will also be presented. Starting from the theory of electromagnetic wave propagation in an magnetised plasma, the theories of Faraday rotation and birefringence will be reviewed in Chapter 3. The inversion techniques necessary to obtain the poloidal magnetic field from the Faraday rotation measurements are also discussed. An analytical solution is presented that details the expected Faraday rotation angles for COMPASS-D and the birefringence introduced due to the presence of the toroidal magnetic field. Chapter 4 starts with an outline of the two polarimetric techniques being considered for commissioning on the COMPASS-D tokamak and discusses the suitability, accuracy and reliability of each in turn. The second part of Chapter 4 is devoted to test bench results and data analysis of each method. Chapter 5 deals with the Hα observations taken with the solar imaging polarimeter. Finally, the thesis is concluded with a chapter to summarise the findings of this thesis work, and to give some recommendations towards future improvements and extensions.

Chapter 2

Instrumental and Observational Polarimetry

Astronomical systems with asymmetric configurations will exhibit linear or circular polarization. The non-spherical distribution of scattering material around a star, the alignment of non-spherical grains by a magnetic field, or the acceleration of charged particles in a preferred plane are all such examples. The two most important polarizing processes are scattering (which gives rise to linear polarization) and magnetic fields (resulting in circular polarization through the Zeeman effect). Therefore a determination of the polarization of the radiation from a celestial source will yield invaluable geometric insight, unique to this type of measurement. The basic concepts of polarimetry and the construction and types of polarimeter are reviewed. An investigation of the polarimeter's instrumental polarization using a monochromatic depolarizer, first suggested by Billings (1951), is experimentally tested for the first time. In addition, the reduction techniques required to ascertain a polarimetric measurement are presented.

2.1 Introduction to Polarimetric Methods

Polarimeters may generally be divided into two parts; the optical components which transform the state of incident polarization into the appropriate intensities and the detector component which measures the intensities. The incident light beam will pass through a polarimetric modulator, such as a half-wave plate and polarizer, before encountering the imaging optics necessary before the detector. A whole range of optical and spectroscopic devices may be placed between these two components in order to enhance the capabilities of the polarimeter. The element prior to the detector is commonly an analyser such as a perfect polarizer which

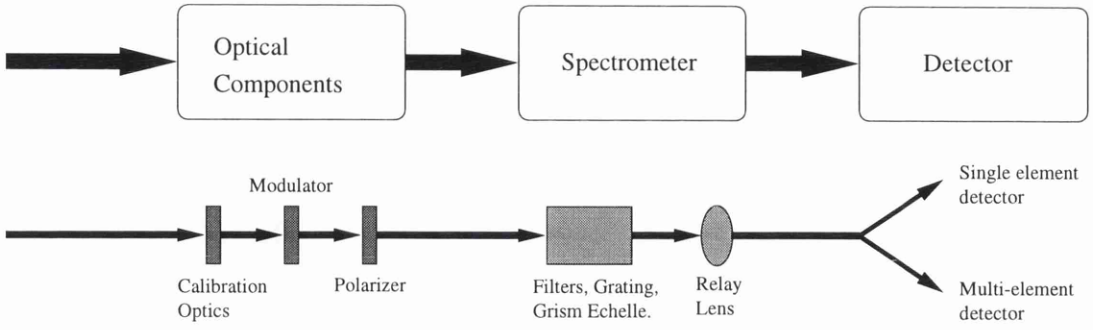

Figure 2.1: Schematic outline of a typical polarimeter indicating the type and position of the components.

completely polarizes the light along its principal axes. For a single beam polarimeter a Polaroid or a Glan prism is utilised, whereas a Wollaston or maybe a Savart plate is encountered in a double beam polarimeter. By rotating the polarimetric modulator in a pre-determined fashion the intensity of the incident light will be modulated allowing a measurement of the polarization.

There are currently three types of preferred modulator:

- a superachromatic half-wave plate which rotates or is set at preferred orientations – essentially a mechanical operation.
- electro-optic cells, such as a pockell cell, whose state may be altered electronically.
- photo-elastic birefringent crystals whose birefringence may be controlled by the application of stress.

In order to reduce or eliminate polarimetric noise caused by atmospheric effects or incorrect telescope guidance, rapid modulation of the signal is necessary for a single channel instrument (see Stenflo and Povel, 1985). Electro-optic and photo-elastic devices are capable of high modulation frequencies but their efficiencies must be calibrated for different wavelengths. Double beam instruments utilise a modulating device to rotate the electric vector with respect to the orientation of a stationary analyser between integrations, in order that the Stokes Q and U parameters may be determined. However, by taking the ratio of the intensity of the ordinary to extraordinary beams the atmospheric effects upon the incident radiation during the integration can be cancelled, (see Serkowski, 1974a).

Two types of detector are commonly utilised in polarimetry; a single element integrating detector such as photomultipler and multi-element imaging detectors such as a Charged Coupled Device (CCD). Integrating detectors are capable of very high precision, of the order 0.001%, whereas imaging devices operate with lower precision of the order 0.1%. Imaging

detectors can simultaneously observe many objects during one integration and do not suffer from the drawback of dead-time corrections, (see Clarke and Naghizadeh-Khouei, 1994). However, dead time problems are replaced by non-linearity near saturation as explained in Section 2.4.1.

2.1.1 Polarimetric Precision

For many astronomical objects the observed polarization is very small, making high precision essential. Theoretically, uncertainties on the order of $\pm 0.001\%$ may be achieved for bright sources. The main sources of noise in a polarimetric measurement may be expressed under the following categories

- Instrumental noise.
    1. Systematic error – instrumental polarization.
    2. Random noise – thermal background.
- Atmospheric noise.
- Photon noise.

Instrumental noise due to the influence of optical elements in the light path, such as the modulator itself, may be removed by the implementation of a suitable diagnostic routine as outlined in Section 2.3. This noise will be instrument dependent and individual calibration will be required. A further instrumental complication is the gain table or flatfield noise. This arises when two images that represent orthogonal polarization states fall on different detecting areas, as in the case of beam splitter systems. Photocharges are generated by elements with differing photosensitivity. This noise may be avoided by implementing a technique known as "flatfielding", (see Buil, 1991).

Scintillation and seeing are the main sources of atmospheric noise. Scintillation is caused by the passage of light through the Earth's atmosphere producing intensity variations in the image of the source. However, since air is not birefringent, scintillation is the same for both perpendicular polarized components of light from an astronomical object. Therefore the ratio of intensities of two such beams emerging from a double beam polarimeter may be free of the effects of atmospheric scintillation and will not be affected by the presence of thin clouds. Extinction by clouds is nearly neutral in the visible region (see Serkowski, 1970), and the accuracy of polarimetry through clouds is reduced only because of fluctuations in sky background and the smaller number of photons received. Rapid modulation of the light

beam, on time scales smaller than atmospheric oscillation typically $\sim$ 10ms, will have the same desired effect for a single beam polarimeter. Atmospheric seeing, i.e, the fluctuations and spread in direction of the stellar light as it propagates through the air, affects the ratio of signals from two beams emerging from a beam splitting prism and causes the image of the source to move around the detector. Such movement may also be introduced by bad tracking of the telescope or, if a rotating optical element is not perfectly aligned with the optical axis causing "image wobble", affecting point sources and extended objects alike.

The ultimate limitation in determining the polarimetric precision of an astronomical source results from quantum photon noise, i.e. the fluctuations in the number of arriving photons at the detector. The effect of the fluctuation may be analysed with the application of Poisson statistics as follows.

Consider M repeated photometric observations of a non-variable star with μ as the mean number of detected photon counts per observation. The expected root mean square (rms) noise level will be $\sqrt{\mu}$. The fluctuations over the individual measures, x_i, can be expressed as

$$\mathrm{rms(x_i)} = \sqrt{\frac{1}{M}\sum_{i=1}^{M}(x_i - \mu)^2}. \tag{2.1}$$

Assuming a signal level of $\mu = 10^6$ detected photons, the corresponding Poisson fluctuation will be $\sqrt{\mu} = 1000$. The signal-to-noise level, $\frac{S}{N}$, may be expressed by $\frac{\mu}{\sqrt{\mu}} = \frac{10^6}{10^3} = 1000$ which corresponds to an accuracy of (0.1%). This is the statistical photometric limit for a given photon count, i.e. the highest precision attainable.

For low levels of polarization, simple error analysis provides uncertainty estimates for the normalised Stokes parameters dependent solely on the number of detected photons. The normalised Stokes parameters q and u are directly related to the difference between intensities measured at the appropriate settings of a half-wave plate. For instance, q, may be determined from two intensity measurements such that,

$$q = \frac{I_{\updownarrow} - I_{\leftrightarrow}}{I_{\updownarrow} + I_{\leftrightarrow}} \tag{2.2}$$

where $I_{\updownarrow}$ and $I_{\leftrightarrow}$ are the intensity values (photon counts) determined in a specific time interval. Therefore, $I_{\updownarrow} = n_{\updownarrow}$ and $I_{\leftrightarrow} = n_{\leftrightarrow}$ in a time t, yielding

$$\frac{\delta q}{\delta n_{\updownarrow}} = \frac{2n_{\leftrightarrow}}{(n_{\updownarrow} + n_{\leftrightarrow})^2} \qquad \textit{and} \qquad \frac{\delta q}{\delta n_{\leftrightarrow}} = \frac{-2n_{\updownarrow}}{(n_{\updownarrow} + n_{\leftrightarrow})^2}. \tag{2.3}$$

Error analysis of Equation 2.2 provides

$$(\Delta q)^2 = \left(\frac{\delta q}{\delta n_{\updownarrow}}\right)^2 (\Delta n_{\updownarrow})^2 + \left(\frac{\delta q}{\delta n_{\leftrightarrow}}\right)^2 (\Delta n_{\leftrightarrow})^2 \tag{2.4}$$

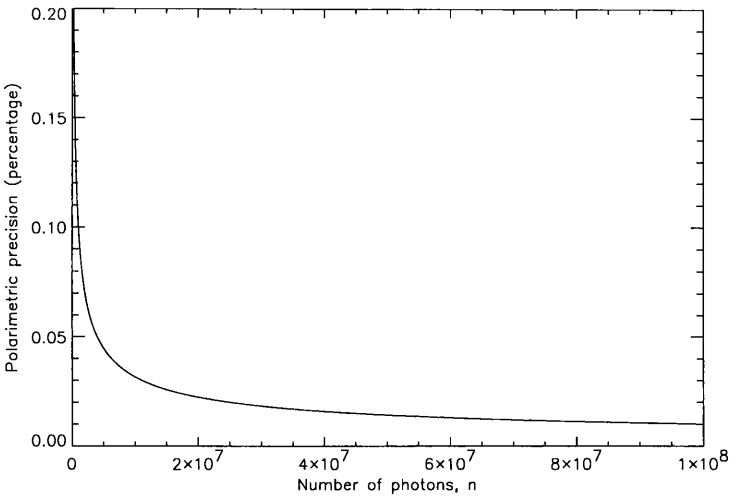

Figure 2.2: The expected polarimetric precision as a function of the detected photons.

with $\Delta n_{\updownarrow} = \sqrt{n_{\updownarrow}}$ and $\Delta n_{\leftrightarrow} = \sqrt{n_{\leftrightarrow}}$, therefore

$$(\Delta q)^2 = \frac{4 n_{\updownarrow} n_{\leftrightarrow}}{(n_{\updownarrow} + n_{\leftrightarrow})^3}. \tag{2.5}$$

A double beam polarimeter simultaneously measures orthogonal polarization intensities. Therefore, defining the photon count as $n = n_{\updownarrow} + n_{\leftrightarrow}$ and with $n_{\updownarrow} \cong n_{\leftrightarrow}$ yields

$$\sigma_q = \sqrt{\frac{1}{n}} \tag{2.6}$$

for a double beam polarimeter. Similar treatment may be applied to the u Stokes parameter with

$$\sigma_u = \sqrt{\frac{1}{n}}. \tag{2.7}$$

Consequently as the number of detected photons increases the polarimetric precision will improve meaning that σ_q and σ_u will decrease in value, as illustrated in Figure 2.2. Photon noise can be suppressed only by increasing the integration time of an observation. In solar observations, polarimetric noise as low as 0.01% to 0.001% was achieved by Baur (1981). From studies of polarization of the whole solar disk, Clarke (1991) reported measurements with a precision of the order of 0.003%.

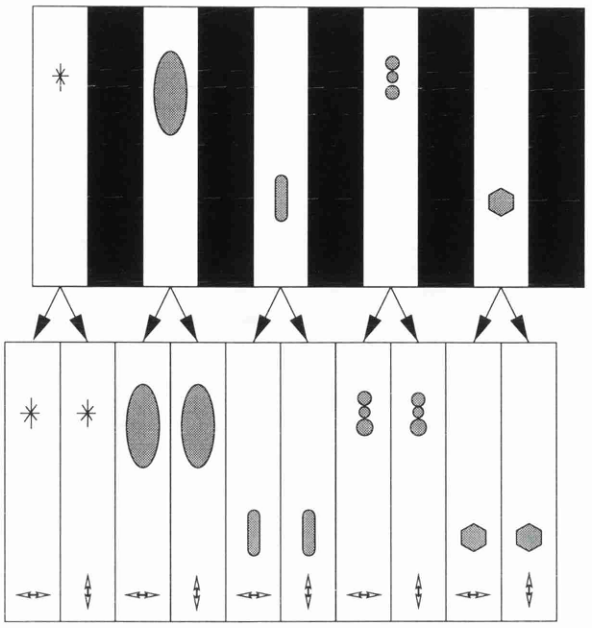

Figure 2.3: View of the sky as seen through the polarimeter. Top - in the focal plane of the telescope. Bottom - as recorded on the detector after passing through the polarization optics (Taken from Scarrott, 1983).

2.2 The Double Beam Imaging Polarimeter

The inherent limitation of imaging polarimetry is the variation in atmospheric transparency and scintillation, during an integration, affecting the polarization measurement. However, the optical system comprising the imaging polarimeter first suggested by Pickering (1873) and improved by Öhman (1939) has overcome this atmospheric limitation. Numerous polarization maps of reflection nebulae and galaxies have been recorded by Scarrott (1983) and Scarrott (1991) utilising a similar double beam imaging polarimeter. Such a system incorporates a polarizing prism which splits incoming radiation into orthogonally resolved polarized beams (the ordinary($\parallel$) and extraordinary ($\perp$)). For such polarizing polarimeters, a Savart plate is an excellent beam splitter as it provides identical path lengths for the two beams resulting in unique focussing, but at the expense of producing half the separation possible by the bulk of calcite used. A series of parallel obscuring strips, constituting the masking grid as illustrated in Figure 2.3, is placed in the focal plane of the telescope. By using an appropriate lens system, an image of the focal plane through the calcite crystal can be produced onto the detector. By design, the Savart plate will produce two images of orthogonal polarization with

a separation of one half grid spacing. Prior to the fixed prism, a rotating superachromatic half-wave plate provides the polarimetric modulation. Figure 2.4 illustrates an exposure of the Orion nebula as a series of strip pairs of orthogonal polarization.

2.2.1 Theory

The output of the double beam polarimeter can be represented by Equation 1.14. Incorporating atmospheric transparency, seeing and detector responsivity into Equation 1.14 the intensities of the two beams may be expressed as

$$\begin{aligned} I_{\parallel}(\psi) &= \frac{1}{2}T(t)G_{\parallel}(I + Q\cos 4\psi + U\sin 4\psi) \\ I_{\perp}(\psi) &= \frac{1}{2}T(t)G_{\perp}(I - Q\cos 4\psi - U\sin 4\psi) \end{aligned} \tag{2.8}$$

where $T(t)$ describes the atmospheric transparency at time t, and $G_{\parallel}$ and $G_{\perp}$ refer to the detector pixel sensitivity to the polarized light for ordinary($\parallel$) and extraordinary($\perp$) beams respectively. The Stokes parameters I, Q and U are defined in the instrumental frame, this being described by the orientation of the principal axis of the analyser. In order to determine the normalised Stokes parameters, four exposures are taken with the plane of polarization of the incident light rotated through a sequence of four steps with respect to a reference direction. This can be achieved by rotating a half-wave plate in front of an analyser in multiples of 22.5°, (see Appenzeller, 1967). Initially the half-wave plate is orientated with its fast axis parallel to the direction of vibration of the ordinary beam in the stationary analyser, where $\psi = 0°$

$$\begin{aligned} I_{\parallel}(0°) &= \frac{1}{2}T_{0°}(t)G_{\parallel}(I + Q) \\ I_{\perp}(0°) &= \frac{1}{2}T_{0°}(t)G_{\perp}(I - Q). \end{aligned} \tag{2.9}$$

The half-wave plate is then rotated such that $\psi = 45°$, yielding

$$\begin{aligned} I_{\parallel}(45°) &= \frac{1}{2}T_{45°}(t)G_{\parallel}(I - Q) \\ I_{\perp}(45°) &= \frac{1}{2}T_{45°}(t)G_{\perp}(I + Q). \end{aligned} \tag{2.10}$$

The four intensities outlined in Equation 2.9 and 2.10 are required to determine the Stokes parameter Q. In order to measure the Stokes parameter U, the half-wave plate is set such that $\psi = 67.5°$, yielding

$$\begin{aligned} I_{\parallel}(67.5°) &= \frac{1}{2}T_{67.5°}(t)G_{\parallel}(I - U) \\ I_{\perp}(67.5°) &= \frac{1}{2}T_{67.5°}(t)G_{\perp}(I + U) \end{aligned} \tag{2.11}$$

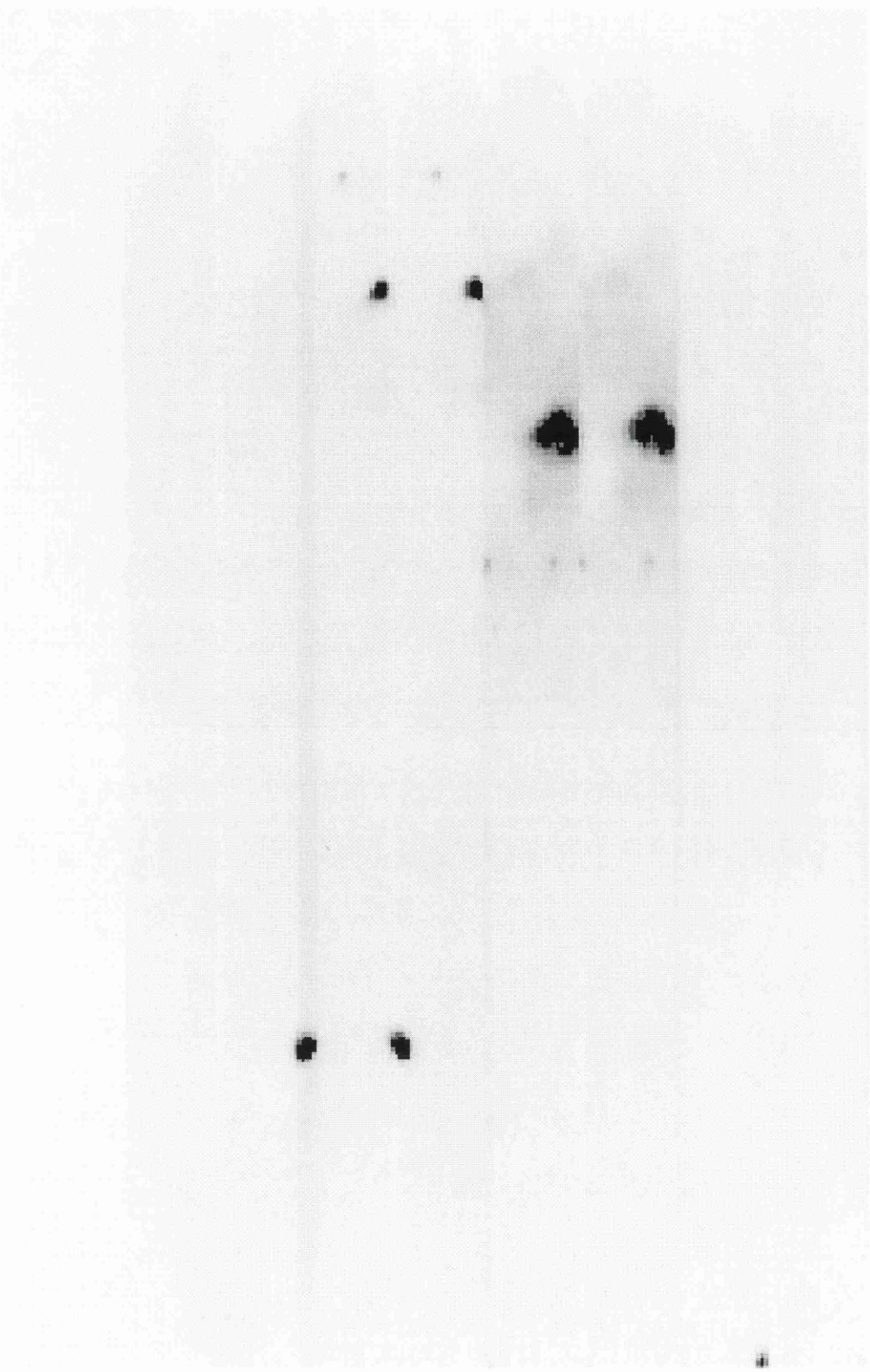

Figure 2.4: A CCD image of the Orion Nebula recorded with the prototype double beam imaging polarimeter in the visible during the winter 1996/1997.

and then rotated so that $\psi = 112.5°$, where

$$\begin{aligned} I_{\|}(112.5°) &= \frac{1}{2}T_{112.5°}(t)G_{\|}(I+U) \\ I_{\perp}(112.5°) &= \frac{1}{2}T_{112.5°}(t)G_{\perp}(I-U). \end{aligned} \tag{2.12}$$

In order to remove the dependence of atmospheric transparency, $T(t)$, the ratio of the two intensity measurements at $I(0°)$, Equation 2.9, and $I(45°)$, Equation 2.10, can be taken giving

$$R(0°) = \frac{\frac{1}{2}T_{0°}(t)G_{\|}(I+Q)}{\frac{1}{2}T_{0°}(t)G_{\perp}(I-Q)} = \frac{G_{\|}(I+Q)}{G_{\perp}(I-Q)} \tag{2.13}$$

and

$$R(45°) = \frac{\frac{1}{2}T_{45°}(t)G_{\|}(I-Q)}{\frac{1}{2}T_{45°}(t)G_{\perp}(I+Q)} = \frac{G_{\|}(I-Q)}{G_{\perp}(I+Q)}. \tag{2.14}$$

The dependence on the detector sensitivity, $G_{\|}$ and $G_{\perp}$, may be eliminated by taking a further ratio

$$R_q = \frac{R(0°)}{R(45°)} = \frac{\frac{G_{\|}(I+Q)}{G_{\perp}(I-Q)}}{\frac{G_{\|}(I-Q)}{G_{\perp}(I+Q)}} = \left(\frac{I+Q}{I-Q}\right)^2 \tag{2.15}$$

giving

$$q = \frac{R_q^{0.5}-1}{R_q^{0.5}+1}. \tag{2.16}$$

Similarly extending this treatment to the normalised Stokes parameter u yields

$$u = \frac{1-R_u^{0.5}}{1+R_u^{0.5}} \tag{2.17}$$

where

$$R_u = \frac{R(67.5°)}{R(112.5°)} = \left(\frac{I+U}{I-U}\right)^2. \tag{2.18}$$

The polarization state of any beam may be determined uniquely with exposures at four half-wave plate positions. In summary, this technique removes the effects of variations in atmospheric transparency and is self calibratory, avoiding the need for undertaking flatfielding routines, (see Section 2.4.3).

2.2.2 The Telescope

A Meade 25cm model 2080 reflecting telescope of Schmidt-Cassegrain design was utilised for observational work. Light entering the telescope encounters a thin lens with two sided aspheric correction, a correcting plate, proceeding a spherical primary before being incident upon and a convex aspheric secondary mirror. The convex secondary mirror multiplies the effective focal length of the primary mirror to 250cm. The Meade telescope is itself attached to the frame of the 51cm diameter telescope at the Cochno station of the University of Glasgow

in order to improve vibrational stability, and also to take advantage of the superior tracking capabilities. This observational site is situated some 15km from the city at an elevated site (150m).

The polarimeter has two operating modes:

- Night-time observation in white light, or with a series of colour band filters, using the entire 25cm diameter primary mirror for light collection.
- Solar observation utilising an 7.5cm energy rejection filter at the 12 o'clock position to work in conjunction with the Hα filter described in Section 2.2.3.

2.2.3 The Daystar Hα Filter

The Daystar Hα filter is an interference filter centered on the Hydrogen Balmer-alpha line at 6562.8Å, as described by Chou (1991). The filter consists of a "sandwich" made up of an anti-reflection coated optical window, a narrow-band birefringent blocking filter, an etalon window, a Fabry-Perot solid spacer crystal, another etalon window, a broadband trimming filter and an anti-reflection coated window. Figure 2.5 is a photograph of the filter components.

Filtering is solely dependent on the thickness of the optical components and is therefore sensitive to thermal expansion. By varying the ambient temperature of the operating environment the transmission band of the filter can be adjusted. A temperature difference of one degree shifts the maximum transmission in the birefringent material such as quartz by 0.74Å and in calcareous spar by 0.42Å. Therefore, within certain limitations, the transmission band of the filter may be shifted to observe structures whose radiation is not exactly in the Hydrogen alpha core.

The Daystar filter utilised was calibrated for on-band operation with a resolution of 0.3Å on either side of the central frequency. There are certain prerequisites for use: the path of the rays entering the filter must be as parallel as possible ($\geq$ f/30) and an energy rejection filter must be used. The Hα filter operates in an off-axis configuration and introduces a large undefined instrumental polarization to all measurements. This will be considered in Section 2.3.

2.2.4 The Instrument

The complete double-beam imaging polarimeter design is illustrated in Figure 2.6. It comprises a reflecting telescope, an Hα filter, a light-tight optically sealed unit and a Charged Coupled Device (CCD) detector. The sealed unit held the polarizing modulator comprising

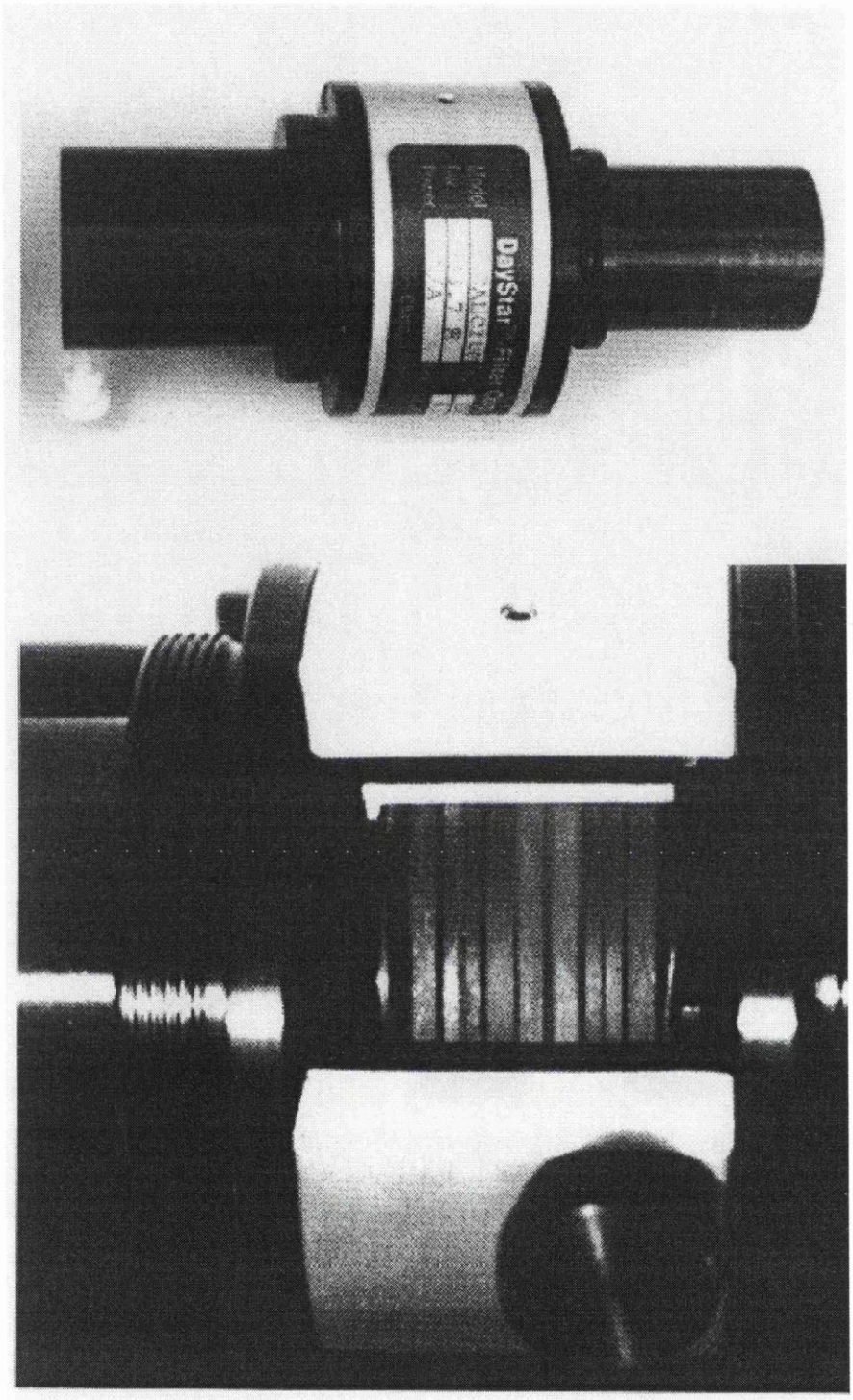

Figure 2.5: Top: A complete Daystar Filter. Bottom: The "insides" of a Daystar Filter consisting of (left to right): 1) an anti-reflection coated optical window, 2) a narrow-band birefringent blocking filter, 3) an etalon window, 4) a Fabry-Perot solid spacer crystal, 5) another etalon window, 6) a broad-band trimming filter, and 7) an anti-reflection coated window.

a half-wave plate, a Savart prism, a grid and a series of lenses. The half-wave plate and the Savart prism were placed in between a field lens-camera lens combination, which reimages the telescope focal plane on to the CCD with a reduction factor of about 2.6; the field lens reimages the telescope aperture on the half-wave plate and the light reaches the camera lens with minimum vignetting.

The light entering the polarimeter was focussed such that the focal plane of the telescope coincided with the first optical component, the masking grid. This comprised a black dielectric material to avoid edge polarizing effects, (see Pospergelis, 1965). The grid itself was a 20mm by 15mm perspex rectangle mounted within a precision rotator, with five alternate parallel obscuring and clear strips 1mm wide and 14mm long as illustrated in Figure 2.3. This resulted in a field of view of 14mm by 10mm in the focal plane of the telescope. Utilising a 25cm telescope, this corresponded to a 18 arcminute by 10 arcminute field of view with a 2 arcsecond resolution for night-time work and 4.5 arcsecond resolution for solar work. The grid spacing was chosen to minimise the effects of variations in the detector and chromatic dispersion in the Savart plate.

Immediately after the grid an achromatic f/4 16mm diameter relay lens re-imaged the telescope aperture on the superachromatic 10mm diameter half-wave plate. This was set strictly in the plane perpendicular to the optical axis and placed as close as possible to the Cassegrain focus. This prevents and minimises instrumental polarization and also reduces prismatic effects, a cause of image wobble due to rotation of the half-wave plate, (see Serkowski, 1974b). The plate itself was placed within a cylindrical housing with a ball race attached to allow rotation. An RS Components stepper motor controlled the rotation with 400 steps per revolution. Incorporating a three-spur gear system allowed a final ratio of 4:1 resulting in a rotation in discrete steps of 0.15°. A previewing system was installed to precede the half-wave plate. It comprised a prism and a 10mm focal length lens both housed in an extractable periscope. This enabled the prism to be inserted into the optical axis of the polarimeter and present a view of the grid and the object under consideration.

The next component in the optical path was a 20mm square by 20mm long Savart plate held within a precision rotatable holder. Each component of the Savart plate was cut with its optical axis at 45° to the faces and cemented with the axes crossed. This arrangement, giving rise to simultaneous focussing of the ordinary and extraordinary rays, minimises the astigmatism and colour which are present when a single calcite block is used, (see Röser, 1981). The Savart plate was placed immediately after the half-wave plate and orientated such that the two emerging beams are set perpendicular to the bars of the grid. This ensures

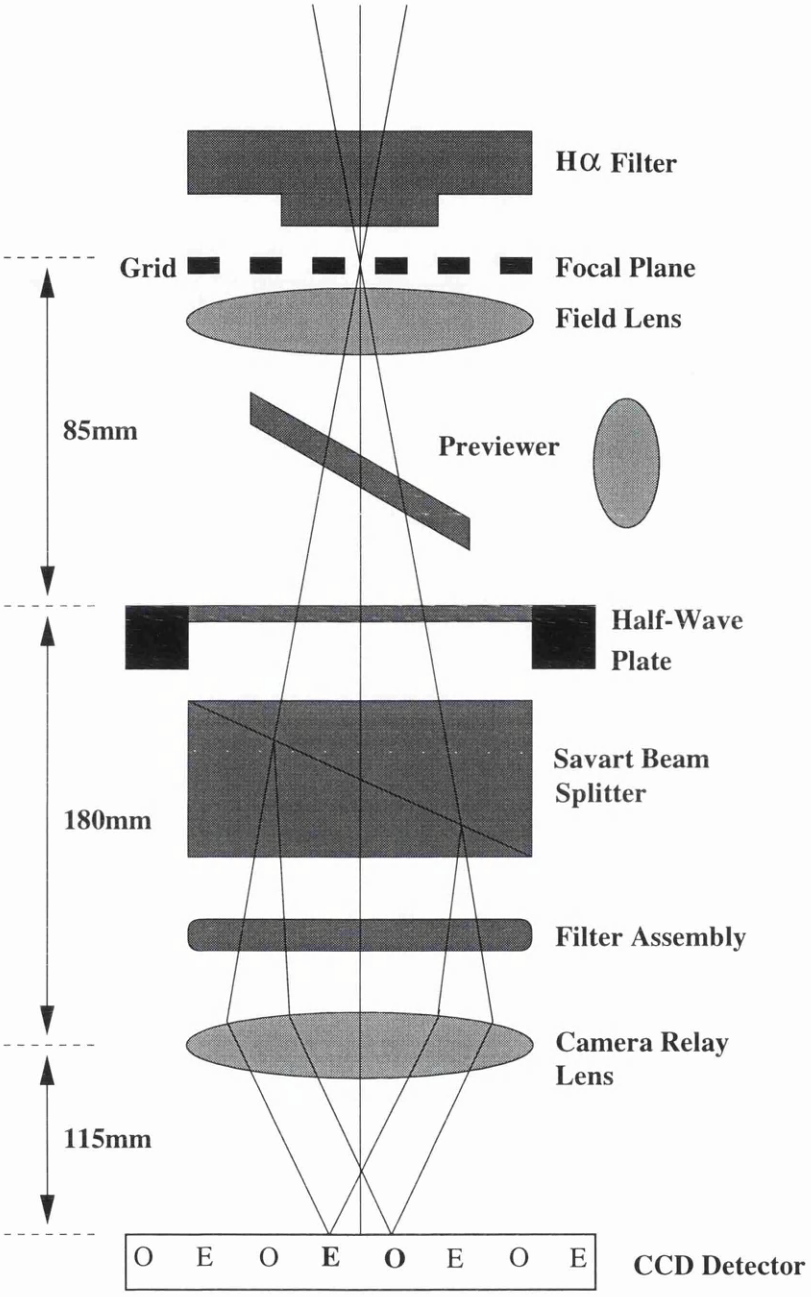

Figure 2.6: Schematic representation of the double beam imaging polarimeter, with O representing the ordinary rays and E the Extraordinary rays.

Component	Source	Description
Field lens	Comar	⊘16mm, eff. FL 100mm, achromatic
Half-wave plate	Bernard Halle	superachromatic magnesium fluoride, 20mm clear aperture, AR coated
Savart plate	Halbo Optics	quartz, 20mm by 20mm clear aperture, 30mm long
Camera lens	Pentax	eff. FL 28-80mm, f/3.5-f/4.5
Hα filter	Daystar Filter Corporation	$\frac{1}{3}$Å resolution off the central frequency
Filters	Oriel	⊘30mm B, V, R and neutral density, 5mm thick, image quality
Previewer	Oriel	40mm by 40mm prism, 10mm eff. FL lens, ⊘20mm

Table 2.1: Optical components utilised in the imaging polarimeter

that the polarization analysis occurs in planes 0° and 90° to the reference direction. A filter assembly into which coloured filters may be inserted follows the Savart plate. A neutral density filter is inserted into the filter assembly whilst observing the Sun in order to avoid saturating the CCD detector.

Since the incident light beam was not collimated but an expanding light cone of ratios f/10 and f/32 for night and solar observations respectively, a telephoto relay lens was required after the filter assembly. This reimaged the grid and the focal plane of the telescope onto the CCD detector. The dispersion of the beam emerging from the telescope was small and hence collimation was unnecessary. The CCD used was an SBIG ST-6 detector situated at the rear of the instrument. A more thorough discussion of this detector is presented in Section 2.4. Table 2.1 lists the optical components used in the imaging polarimeter.

The tracking of the 51cm telescope was inadequate for long exposures of night sky objects, therefore it was necessary to incorporate a commercially available CCD guidance system. The 51 cm telescope was meticulously aligned with the main 25cm telescope so that both had identical fields of view. An SBIG ST-4 CCD attached to the 51cm telescope enabled the tracking to be better than 5 arcseconds over long exposure periods. However, tracking of the Sun required the construction and installation of a finderscope alongside the 25cm telescope. The whole solar disk was imaged onto a 5.9mm by 5.1mm commercial black and white CCD chip. Several filters were installed in order to diminish the solar intensity. The solar disk appeared between certain equidistant markers on a display monitor, thus allowing manual adjustments of the tracking to be made in order to keep the image fixed between

these markers.

2.2.5 Data Acquisition and Instrument Control

A mixture of digital and analogue electronics were developed to perform the instrument control and data-acquisition operations. The electronics assembly of the instrument consisted of three parts:

- The positioning system for the half-wave plate.
- The tracking CCD camera and associated electronics.
- The main CCD camera with its own control and host computer (IBM compatible PC 486) for exposure and data acquisition.

A block schematic of the control system is shown in Figure 2.7. The half-wave plate was positioned at four specific angles using a stepper motor controlled by an in-house dedicated hard-wire electronic setup. By depressing one of four buttons on a control box the half-wave plate was positioned at the desired orientation. The principles behind the control system are reviewed thoroughly by Clarke (1989a) and Clarke (1989b). A red LED indicated that the half-wave plate had completed a revolution and returned to its starting position.

The tracking CCD was an SBIG (Santa Barbara Instruments Group) ST-4 detector. The camera has a controller unit which executed specific tasks and was connected directly to the 51cm telescope drive motor. Therefore any movement in the star's position on the CCD chip was immediately corrected by sending corrective commands to the drive unit's right ascension and declination motors. During solar observations the tracking was controlled manually with exposures generally several seconds in length. However, the tracking was not considered important on these timescales. The main CCD camera used for data acquisition was an SBIG ST-6 detector. The CCD central processing unit was connected to a laptop computer via an RS 232 port. The software provided by the SBIG group was utilised to capture and archive the image pixel data.

The observational routine may be outlined as follows:

- The PC, CCD and half-wave plate electronics were switched on. The CCD was shuttered and an image readout was produced in order to clean the chip. The temperature was set $-50°$ Celcius below the ambient temperature at least 15 minutes prior to observations.
- The target was located in the previewer system.

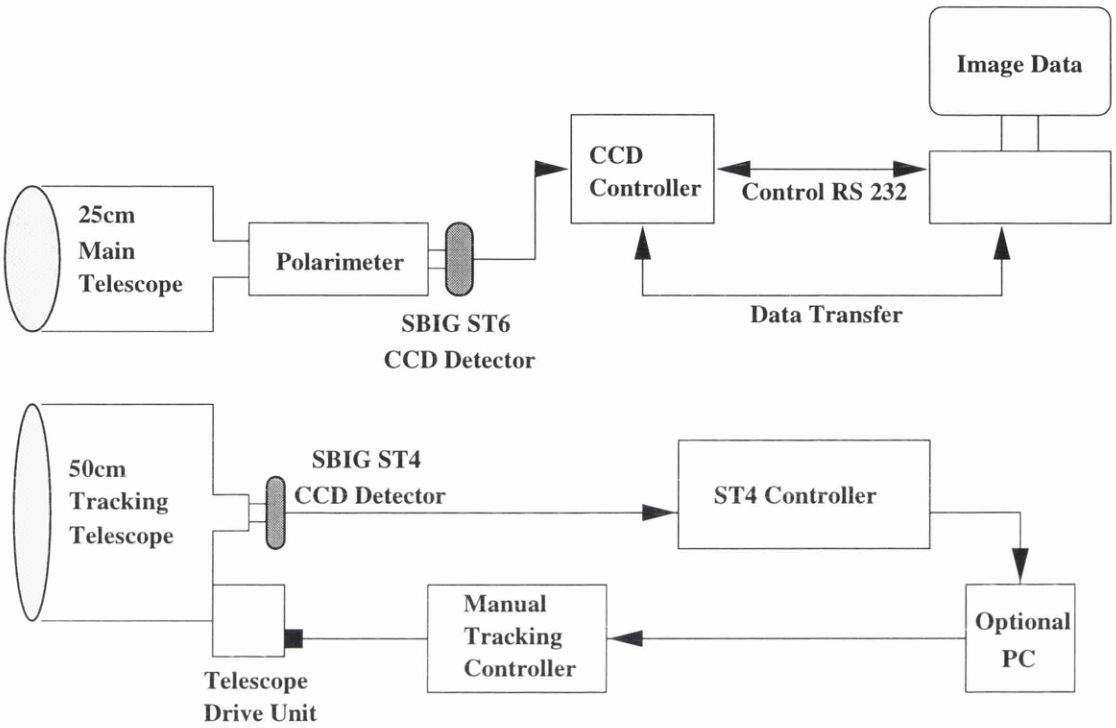

(a) Electronic and hardware arrangement for night-time observations.

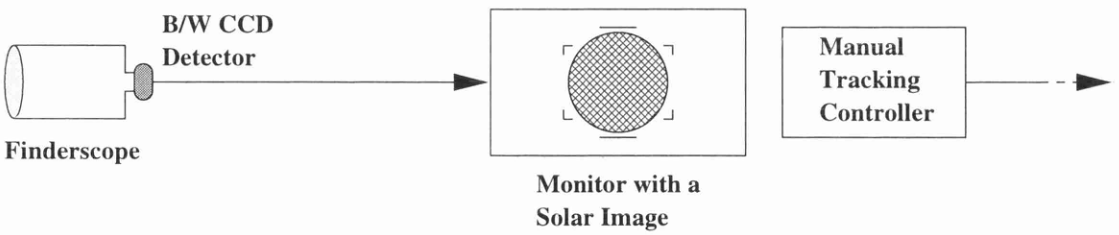

(b) Modified tracking arrangements for solar observations.

Figure 2.7: Block diagrams of the instrument and data acquisition control system.

- The ST-4 CCD attached to the 51cm telescope was programmed to track the target.
- The photometric brightness was tested with the half-wave plate at 0°.
- An integration time was selected in order that the CCD is not saturated.
- Dark and bias exposures were taken with the 25cm aperture covered.
- Exposures were then taken with half-wave plate setting at 0°, 45°, 67.5° and 112.5°.

At the end of each run, four source and three calibration images are automatically archived in FITS (Flexible Image Transport System) format. Since a grid of parallel obscuring strips is placed at the telescope focal plane, only less than half the field is seen by the detector during any observation. Once a set of exposures has been taken for all four positions of the half-wave plate, the telescope orientation is slightly changed to ensure that readings are taken of the previously obscured field of view. Alternatively in the case of stellar fields with slowly changing background (i.e. intensity and polarization) the grid may be removed during observations provided the field is not too crowded.

2.2.6 Distortions in Polarization

Any measurements recorded depend on detecting changes in the polarization vector caused by rotating the half-wave plate. Consequently, any small instrumental polarization or shift in images on the detector must be eliminated. The retardance introduced by the half-wave plate may deviate from 180° either due to the finite angle of incidence or because of chromatic effects. If the incident light makes an angle i with the normal to the surface of the half-wave plate and the plane of incidence makes an angle ϖ with the optical axis of the crystal, then according to Serkowski (1974b) the retardance may be expressed by

$$\Delta \cong \pi \left[1 - \frac{i^2}{2n_o}\left(\frac{\cos^2 \varpi}{n_o} - \frac{\sin^2 \varpi}{n_e}\right)\right]. \tag{2.19}$$

The maximum change in retardance may be given by

$$\sigma_\Delta \approx \pi \frac{i^2}{4n_o}\left(\frac{1}{n_o} - \frac{1}{n_e}\right) \tag{2.20}$$

where n_o and n_e are the refractive indices of the material for ordinary and extraordinary rays respectively.

For the aperture used, the maximum angle of incidence corresponding to the cone angle of the bundle of rays is about 5° implying that $\sigma_\Delta \leq 0.01$rad. The chromatic effects give $\sigma_\Delta \leq 0.18$rad for the wideband. It can be shown that the depolarization σ_p due to an

uncertainty of σ_p rad in the retardance is, to lowest order, given by $\sigma_p \simeq p\sigma_\Delta^2$, where p is the fractional polarization. Furthermore, circular polarization in the incident light is converted to a linear polarization of magnitude $V\sigma_\Delta$, where V is the Stokes circularity parameter. For wideband observations, conversion to linear polarization would be $0.18V$, but in typical observations this does not pose a serious problem since the circular polarization in the incident light is usually much less than the linear polarization.

Another chromatic effect is the change in position of the half-wave plate fast axis with wavelength. Although this will not produce any error in the measurement of the polarization p, it will render the measurement of the position angle θ subject to systematic error. The superachromatic half-wave plate used did not produce any appreciable dispersion in its fast axis position angle over the wavelength range of interest.

The uncertainty involved in the positioning of the half-wave plate leads to an error in the measurement of the polarization. The positioning uncertainty σ_α produces a maximum error in the measurement of linear polarization given by $\sigma_{pl} \simeq p\sigma_\alpha$, (see Ramaprakash et al., 1997). Thus an error of 0.1° in the positioning of the half-wave plate results in $\sigma_{pl} \simeq 0.002p$.

2.2.7 Performance of the Instrument

The commissioning of the polarimeter involved two levels of tests. Firstly laboratory tests were conducted on an optical bench in order to determine various parameters such as linearity, gain and readout noise of the detector. Vignetting and instrumental polarization were also investigated. Measurements were carried out with a tungsten lamp focussed onto the masking grid. A Polaroid was introduced into the optical train in order to determine the polarimeter's performance in analysing completely polarized light. The half-wave plate was then removed and the Polaroid adjusted until it was accurately crossed with one of the beams emerging from the Savart plate. The half-wave plate was replaced and rotated until a minimum signal was obtained from the extraordinary beam and a maximum signal was produced from the ordinary beam. A further rotation of 45° resulted in a maximum intensity for the extraordinary beam. At an angle of 22.5° the two intensities were equal. Rotation of the half-wave plate clearly indicated the expected $\cos 4\theta$ intensity variation. The retarder was then clamped into the rotatable gear system of the instrument. The instrumental polarization of the polarimeter may be estimated under laboratory conditions by the introduction of a Lyot depolarizer in front of the light source. By taking multiple exposures and the addition of pixel elements, the polarization was demonstrated to be less than 0.04% for white light as illustrated in Figure 2.8.

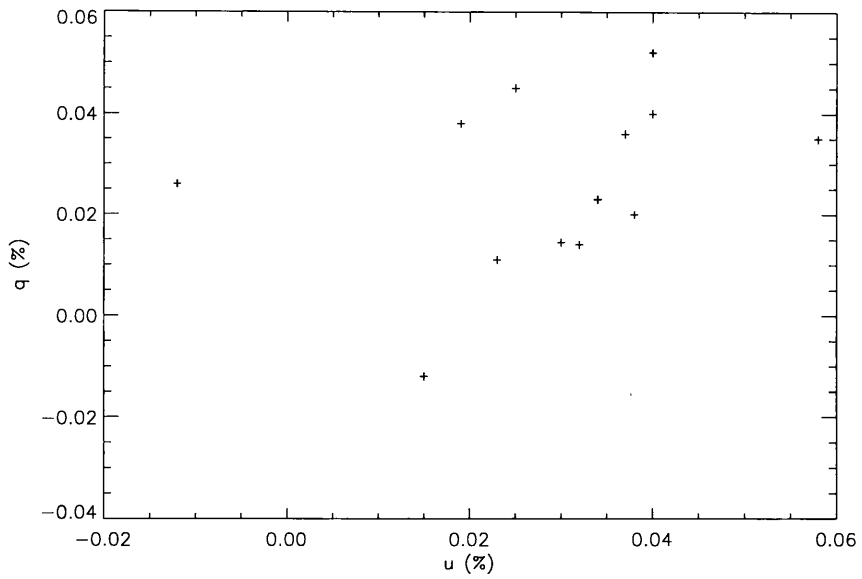

Figure 2.8: Normalised Stokes parameters q plotted against u for a tungsten light source. The correlation coefficient of the points is about 0.05 and the average values of q and u give a value of $p = 0.04\%$.

The second stage of the testing programme was conducted during the winter 1996/1997 at the Cochno observatory with the 25cm telescope. Several standard polarized and unpolarized stars were observed over a succession of nights. Since the standard stars were quite bright, having visual magnitudes in the range 4 to 7, the instrument was slightly defocussed to avoid the saturation of the detector pixels in reasonable exposure times and to increase the count rates. Table 2.2 contains the results of the observations using white light. Columns(1–2) gives the identification number of the star and the time of observation. Columns(3–4) contain the measured values of the polarization p and position angle θ. Column(5) gives the estimated error σ_{photon} based on photon statistics alone as derived in Section 2.1.1. The final two numbered columns lists the published values of p_p and θ_p.

The first star in the table, HD 36384, also known as χ Auriga, is a polarized standard star while the second star HD 31964, ϵ Auriga, exhibits variability with a period of 27.1 years, (see Coyne, 1974). Unfortunately, since ϵ Auriga's polarization varies by approximately 0.5% over a four year period beginning at a phase of 0.4, it is not a perfect candidate as a polarized standard. Nevertheless by extrapolating its variability, observations were made at a phase of 0.505 and the polarization determined with a rather large uncertainty as indicated in Table 2.2. The final star, β Cassiopeia, is an unpolarized star. Comparing the measured and published results for the polarized stars it is apparent that there is no indication of depolarization. Reviewing columns (3) and (4) for the unpolarized star indicates that the

Star	Date	p	θ	σ_{photon}	p_p	θ_p	
(1)	(2)	(3)	(4)	(5)	(6)	(7)	Reference
HD	JD	%	°	%	%	°	
	245						
36384	0512.5	1.99	134	0.05	2.019	177	[a]
	0515.5	2.03	132	0.06			
31964	0512.5	2.08	97	0.06	1.94–2.05	144–147	[b]
	0515.5	2.01	99	0.05			
432	0511.5	0.02	166	0.05	0.009	32	[c]
	0515.5	0.03	167	0.06			

[a]Serkowski (1974)
[b]Coyne (1974)
[c]Appenzenller (1966)

Table 2.2: Observations of standard stars.

errors in the measured polarization are comparable with the expected values on the basis of photon statistics alone. Comparing the measured values of θ with those quoted in the literature it is apparent that the instrumental reference axis is offset by $45° \pm 1°$, within the expected errors, with respect to the equatorial reference frame, the standard frame in the literature.

The instrumental polarization introduced by the telescope mirrors may be determined by observing unpolarized standard stars and then eliminating this bias from the final measurement. Uniformly aluminised mirrors viewing an on-axis point source will introduce small amounts of polarization as various parts of the curved surface present differing angles of incidence with reflection coefficients which are sensitive to polarization. A detailed theoretical argument is presented by Almeida and Pillet (1992). The observations indicate that for accuracies $\tilde{>}$ 0.05% in the measurement of polarization the performance of the polarimeter is still limited by photon noise and the instrument polarization floor has not yet been reached.

Unfortunately, as illustrated in Figure 2.4, overlapping of the extraordinary and ordinary beams is prominent in one of the five obscuring strips. This occurs due to a flaw in the manufacture of the masking grid. This marginally reduces the available working area of the final polarization images.

2.3 Investigation into Instrumental Polarization

From the design of the polarimeter, working in Hα, with the telescope operating off-axis it is inevitable that there will be an instrumental polarization which will add to all measured

polarizations. It must be compensated for and the zero point of the polarization scale determined. It is imperative that the instrumental offset be known with an uncertainty much smaller than the random errors associated with the q and u measurements.

In the case of stellar work the most common method of determining the instrumental polarization is the measurement of one or more standard stars with either zero or a known polarization. This procedure is outlined in Section 2.2.7. However, this approach is impossible with the Hα filter incorporated in the instrument since it actively reduces the incident intensity by a factor of 10^6 making the standard stars too faint to observe and with no comparable object available. The instrumental polarization may also be estimated in laboratory conditions with the introduction of a Lyot depolarizer, see Lyot (1928), in the optical path of the polarimeter. However, this approach is only effective in an instrument which examines a large wavelength region simultaneously. In the case of an instrument observing a small wavelength region, such as with an Hα filter, a monochromatic depolarizer is required. A design for such an instrument was first suggested by Billings (1951) but it has never been explored experimentally. It was decided to construct such an instrument and this is outlined in Section 2.3.1.

For reasons of symmetry and scattering geometry the polarization should generally be zero at the solar disk center with a sharp, rapid rise at the limb reaching a maximum value of $p \sim 1\%$. Therefore, making recordings at the disk center allows the instrumental offset to be estimated, (see Section 5.2). This procedure was followed in order to complement the monochromatic depolarizer approach.

2.3.1 Optical Arrangement for a Monochromatic Depolarizer

A combination of rotating wave plates may be devised which will act as a complete depolarizer for monochromatic light. A quarter-wave plate rotating at one speed followed by a half-wave plate rotating at twice the speed will give a device which is a perfect depolarizer and will operate on any state of polarization, provided that there are many rotations over the experimental time.

Consider the case of two wave plates with retardance Δ_1 and Δ_2, rotating at $\omega_1 = \frac{d\psi_1}{dt}$ and $\omega_2 = 2\omega_1 = \frac{d\psi_2}{dt}$ respectively. Using the Muller calculus introduced in Section 1.1 their effect may be expressed by

$$I_{out} = [R(-\psi_2)\,[M(\Delta_2)]\,R(+\psi_2)] \cdot [R(-\psi_1)\,[M(\Delta_1)]\,R(+\psi_1)] \cdot I_{in} \tag{2.21}$$

with the coordinate rotation matrix $R(\psi)$ expressed by Equation 1.11. The general Mueller

matrix for a wave plate of retardance Δ may be expressed by

$$[M(\Delta)] = \begin{pmatrix} 1 & 0 & 0 & 0 \\ 0 & 1 & 0 & 0 \\ 0 & 0 & \cos(\Delta) & \sin(\Delta) \\ 0 & 0 & -\sin(\Delta) & \cos(\Delta) \end{pmatrix}. \tag{2.22}$$

Evaluating Equation 2.21 with the appropriate Mueller matrices and the following approximations

$$\begin{aligned} < \sin 2\psi_1 > &= < \cos 2\psi_1 >= 0 \\ < \sin 2\psi_2 > &= < \cos 2\psi_2 >= 0 \\ < \sin^2 2\psi_1 > &= < \cos^2 2\psi_1 >= \frac{1}{2} \\ < \sin^2 2\psi_2 > &= < \cos^2 2\psi_2 >= 1 \end{aligned} \tag{2.23}$$

yields

$$I_{out} = \begin{pmatrix} I \\ \frac{Q}{2}(1+\cos\Delta_1)(1+\cos\Delta_2) \\ \frac{U}{2}(1+\cos\Delta_1)(1+\cos\Delta_2) \\ V\cos\Delta_1\cos\Delta_2 \end{pmatrix}. \tag{2.24}$$

Incorporating Equation 2.24 into Equation 1.3 will yield an expression for the resulting degree of polarization, p,

$$p = \frac{\sqrt{\left(\frac{Q^2}{4}+\frac{U^2}{4}\right)(1+\cos\Delta_1)^2(1+\cos\Delta_2)^2 + V^2\cos^2\Delta_1\cos^2\Delta_2}}{I}. \tag{2.25}$$

Clearly $p = 0$ in the case where the $\Delta_1 = 90°$ and $\Delta_2 = 180°$, confirming that the combination of a rotating quarter- and half-wave plate will act as a perfect monochromatic depolarizer.

However, it is of interest to investigate the depolarizing efficiency as the wavelength moves off center. The retardance, Δ, of each wave plate may be defined as

$$\Delta = \frac{2\pi}{\lambda}(N_o - N_e)d \tag{2.26}$$

where d is the thickness of the retarder, and N_o and N_e are the refractive indices of the ordinary and extraordinary waves respectively. To first order the retardance of each wave plate is inversely dependent on wavelength, and as the birefringence, $N_o - N_e$, usually displays little dispersion this may be neglected in the analysis. Figure 2.9 illustrates the quarter- and half-wave plate dependence with wavelength.

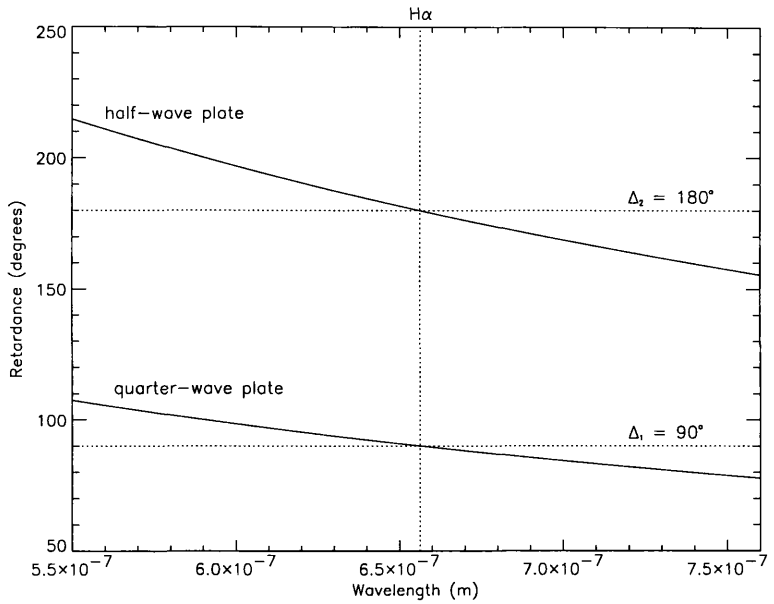

Figure 2.9: The dependence of the quarter- and half-wave plates retardance with wavelength. The vertical dashed line refers to the Hα wavelength.

Incorporating the wavelength dependence of the two retarders into the preceding analysis and specifically into Equation 2.25 it is possible to determine the effectiveness of the depolarizer for a range of wavelengths. This is shown in Figure 2.10 with three distinct incident polarizations. At Hα, the arrangement is completely effective as a depolarizer but at different wavelengths the effectiveness decreases, this is especially the case for any incident circular polarization. It is also obvious that the component wave plates should be manufactured to have the correct values for the selected wavelengths.

The imaging polarimeter described in Section 2.2 has been constructed primarily for solar observations in and around the Hα wavelength. The Daystar filter, by its design, will inevitably introduce additional instrumental polarization to the instrument which may be investigated and measured by the use of the monochromatic depolarizer arrangement. It is therefore important to explore the efficiency of the components if they are not exact or if the selected wavelengths depart from Hα.

2.3.2 Experimental Implementation

A test bench was assembled, as illustrated in Figure 2.11, in order to test the monochromatic depolarizer arrangement. A single He-Ne laser of wavelength 6328Å producing a vertically

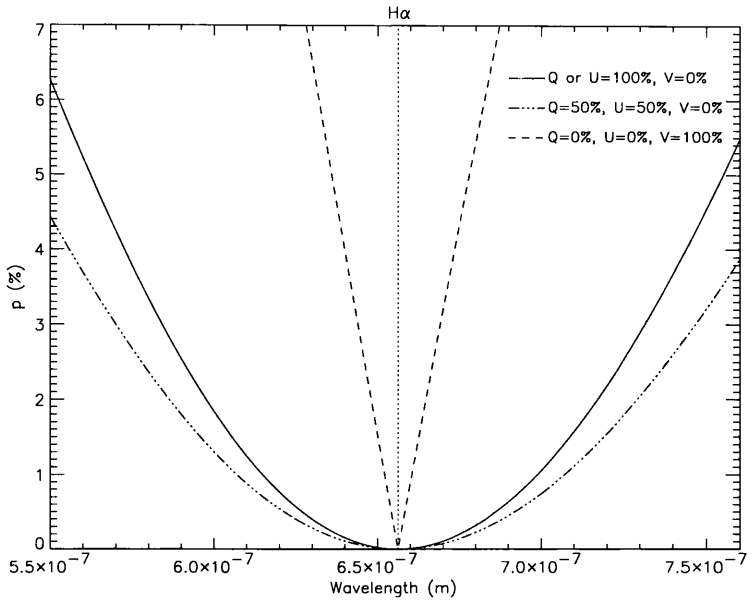

Figure 2.10: The theoretical effectiveness of the depolarizer arrangement with wavelength for three distinct incident polarizations.

polarized TEM_{00} Gaussian mode at a power level of 2mW was utilised as the linearly polarized light source. A Polaroid ensured that the laser beam was 100% polarized before encountering the wave plate combination. The two wave plates were made of mica encased in crown glass for protection. The quarter- and half-wave plates, each 80mm in diameter, were held in place in a hollow bearing driven by a synchronous A.C. motor, with a rated speed of 1500 rpm, through a series of gears. This enabled the quarter- and half-wave plates to be driven at a frequency of 7Hz and 14Hz respectively. These wave plates were set strictly in the plane perpendicular to the optical axis in order to minimise the instrumental polarization and also reduce any prismatic effects. The laser beam then entered the polarimeter, excluding the Hα filter, and was focussed onto the CCD detector. A polarimetric measurement was then determined for the depolarizing setup utilising the data acquisition system outlined in Section 2.2.5.

2.3.3 Results

The laser beam's polarization was first checked, without the depolarizer arrangement in the beam, in order to confirm its high degree of polarization. Figure 2.12a illustrates the profile of the laser beam for the four positions of the half-wave plate. The Savart plate in

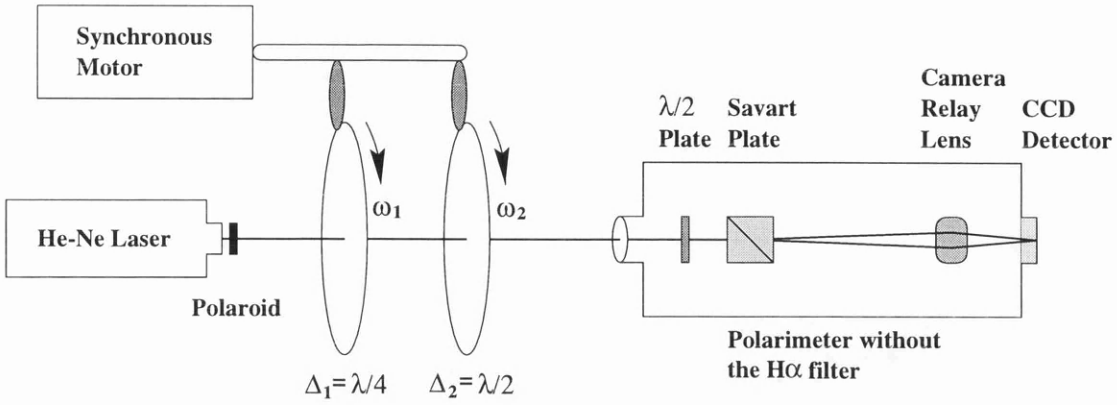

Figure 2.11: Schematic depiction of the test bench setup for the monochromatic depolarizer.

the polarimeter ensures that the beam is split into two orthogonally polarized beams. The laser beam was found to have a polarization, $p = 100.08\% \pm 0.03\%$. The stability of the laser's power output was tested over an extended period and found not to drift significantly (about 5% over an hour). However, the double beam approach to polarimetry completely compensates for any such power fluctuations. The two wave plates were then replaced and rotated at their optimum speed. The profile of the laser beam with this configuration is shown in Figure 2.12b. The inclusion of the rotating wave plates unfortunately broadens the beam's profile so that the two orthogonal polarizations overlap resulting in the polarization measurement being fraught with additional uncertainties. The beam profile also demonstrates a speckled pattern which may be explained by imperfections in the mica wave plates.

The half- and quarter-wave plates were designed for use at the Hα wavelength while the test bench utilises a He-Ne laser with a wavelength of 6328Å. According to the analysis in Section 2.3.1, there should be a residual p of 0.32%, owing to the wavelength dependence of the mica wave. Numerous exposures of several seconds were taken with the wave plates rotating and the polarization determined, shown in Figure 2.13. The measured polarization was $p = 1.01\%$, three times the expected amount. This discrepancy between theory and experimental results may be explained by a variety of factors. The wave plates may not have been manufactured perfectly for use at Hα causing erroneous phase shifts to the propagating laser beam. The rotation of the wave plates at high speed introduces a broadening and wobbling of the profile of the laser beam. This wobbling is caused by the non-parallelism of the wave plates with respect to each other and the incoming beam, essentially a prismatic

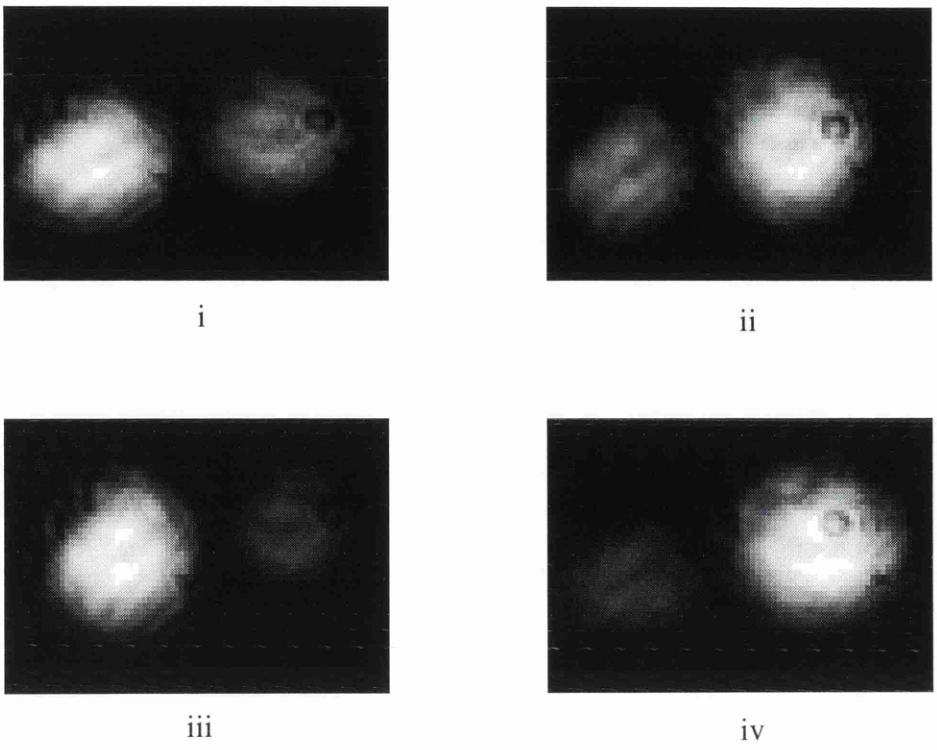

(a) Laser beam profile without the wave plates in the optical path

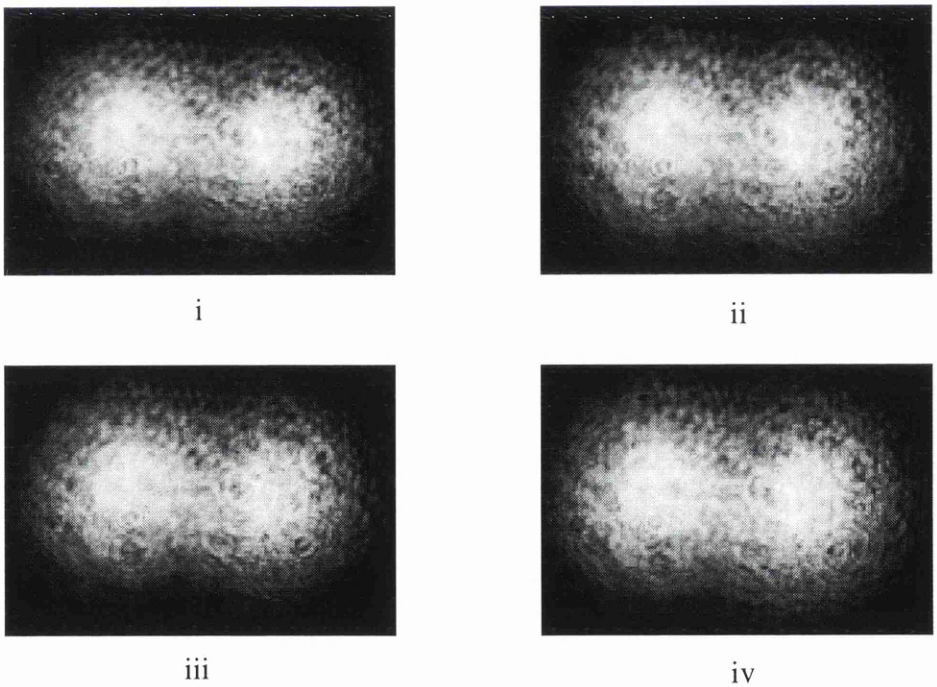

(b) Laser beam profile for the depolarizer arrangement

Figure 2.12: Laser beam profile at (i) 0°, (ii) 45°, (iii) 67.5° and (iv) 112.5° half wave plate positions for two different configurations.

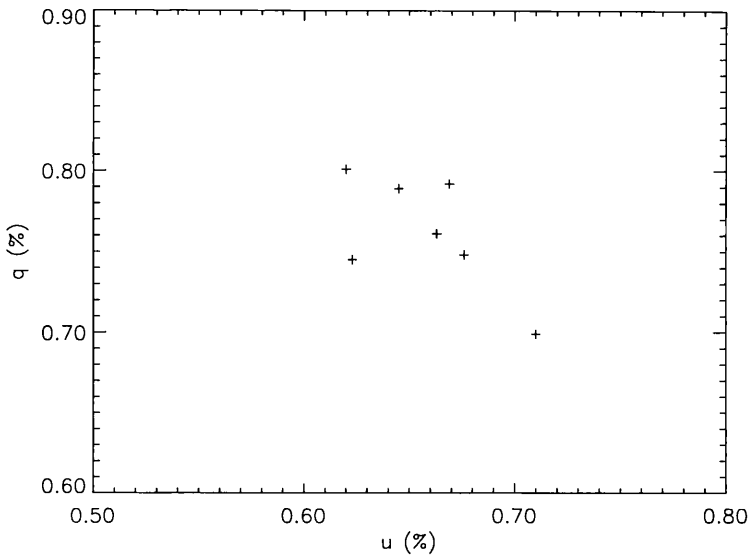

Figure 2.13: Normalised Stokes parameters q plotted against u for a tungsten light source. The average values of q and u give a value of $p = 1.01\%$.

effect, and the rather inexpensive bearing and gear system used. Utilising air bearings and materials with a higher degree of manufacturing tolerance would greatly improve matters. Better results would be apparent if quartz wave plates were to be used rather than the optically poorer material mica. The mica plates were encased in crown glass by the use of an adhesive which may cause phase shifts to the beam as it propagates through, reducing the efficiency of the wave plates. An additional complication is determining whether the laser is exactly at the prescribed wavelength. Any wavelength drift will influence the effectiveness of the depolarizer as demonstrated in Figure 2.10.

Considering the practical difficulties and the equipment used, the results obtained clearly demonstrate that the Billings proposed depolarizer is effective when dealing with monochromatic linearly polarized light. Unfortunately this approach cannot be used to determine the prototype imaging polarimeter instrumental polarization to a sufficient accuracy due to the problems discussed previously.

Parameters	Details
CCD Make	TC-241
CCD Chip Size	375(H) $\times$ 242(V)
Pixel Size	23μm by 27μm
Active Area	8.6mm by 6.5mm
No. of Amplifiers	1
Quantum Efficiency	blue 25%
	red 65%
Readout Speed	22μs per pixel
Acquisition and Display Time	20s for a full frame
Readout Noise	104e^- RMS
Gain	10e^-/ADU
Full-Well Capacity	$\sim 5 \times 10^5$ electrons

Table 2.3: The parameters of the SBIG ST-6 CCD Camera

2.4 The CCD Detector and its Calibration

Multi-element detector arrays such as charged coupled devices have introduced a new dimension to astronomical instrumentation. They inherently have a high quantum efficiency, low readout noise, small pixel size (10-22μm) and are affordably priced. A CCD comprises of a photosensitive array of MOS (Metal Oxide Semiconductor) capacitors which generate photoelectric charged carriers by the absorption of photons. This mechanism is known as the photoelectric effect. The charged carriers are transferred in discrete time increments from one potential well to the next by a sequence of voltage changes called clocking. This vertical transfer process delivers entire rows of the array to a horizontal shift register for transmission to the video output port. During the transfer from one stage of the register to another, a certain number of charges are left behind. For modern CCD's this quantity may be defined by the Charge Transfer Efficiency (CTE) which is typically 99.999%, (see Buil, 1991). The information from the array is stored in discrete signal packets, appearing at the output as sampled signals, with each sample representing a packet of charge. This packet of charge is then converted into an analogue to digital unit (ADU) by the electronics of the CCD and stored.

The CCD detector utilised was an SBIG ST-6 with an array of 375 by 242 pixels. The pixel size was 23μm by 27μm with a total area of 8.6mm by 6.5mm; for further details consult Table 2.3.

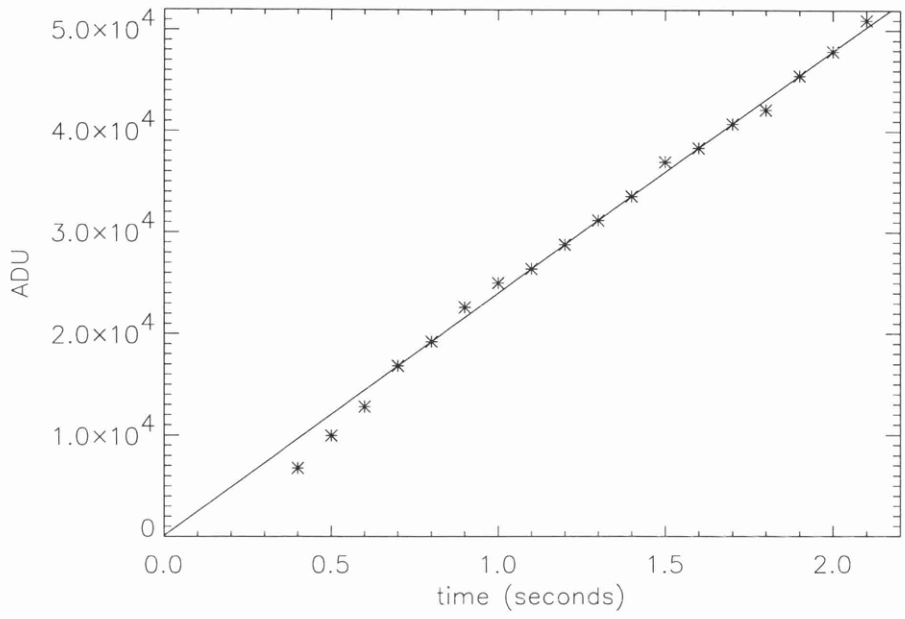

Figure 2.14: Measurement of the linearity of the ST-6 detector and the associated electronics.

2.4.1 Linearity

CCD systems are dominated by several different noise regimes which correspond to differing illumination levels, (see Mackay, 1986). At the lowest illumination level, the readout noise dominates. However, as increasing signal is readout, the shot noise of the signal charge is added in quadrature with the intrinsic readout noise. Eventually this readout noise will become negligible and the signal-to-noise ratio will thus be proportional to the square root of the signal level. This is the working regime of the detector where recorded events are directly related to the arriving photons. At higher illumination levels the signal-to-noise ratio increases slowly which can be attributed to the onset of non-linearity near saturation.

The linearity of the detector was determined by illuminating the CCD with a stable luminous source connected to a uniformly regulated power supply. The integration time of the detector was varied whilst keeping the intensity of illumination constant throughout. Five frames were taken at each integration time including dark and bias exposures. A test area of 10 by 10 pixels on the CCD was selected to evaluate the response of the detector. A least squares line fitted to the data points illustrates the excellent linearity of the detector within the linear noise regime. Figure 2.14 clearly illustrates the linearity of the ST-6 detector. The

CCD saturates at an illumination level of 65535 ADU but experimentation demonstrates that it is linear between 100 ADU and 50000 ADU.

2.4.2 Noise and Gain

The CCD images are recorded initially in analogue digital units (ADU), each corresponding to a fixed number of electrons (i.e. detected photons). The ADU are generated by the electronics with a 16-bit capacity giving a possible (2^{16}) 65535 units. It is imperative to determine the gain of the system, that is, the number of electrons corresponding to an ADU.

In order to determine the system gain and noise concurrently, a calibration method proposed by Janesick et al. (1984) was followed. This technique known, as the photon transfer or variance method, is outlined below.

Photon Transfer Technique

A transfer equation may be written to represent the output signal of the electronic converter in terms of ADU

$$S((\text{ADU}) = \mathcal{G}N \tag{2.27}$$

where N is the number of electrons and $\mathcal{G}$ is the gain of the amplifier expressed in ADU per electron. The signal noise may be expressed in terms of ADU

$$\sigma_s(\text{ADU}) = \mathcal{G}\sqrt{N} \tag{2.28}$$

with the variance expressed by

$$\sigma_s^2(\text{ADU}) = \mathcal{G}^2\sqrt{N}. \tag{2.29}$$

Taking the ratio of the variance to the measured signal yields

$$\frac{\sigma_s^2(\text{ADU})}{S(\text{ADU})} = \frac{\mathcal{G}^2\sqrt{N}}{\mathcal{G}\sqrt{N}} = \mathcal{G}. \tag{2.30}$$

Rearranging this equation further gives

$$\sigma_s^2(\text{ADU}) = \mathcal{G}S(\text{ADU}). \tag{2.31}$$

The RMS system noise may also be obtained by following a similar argument. Provided that the signal and noise are not coherent the following is true

$$\sigma_s^2 = \mathcal{G}S(\text{ADU}) + \sigma_{noise}^2. \tag{2.32}$$

This equation has the form of a straight line equation with the inverse of the gradient $\frac{1}{\mathcal{G}}$ directly yielding the number of electrons corresponding to an ADU. The intercept of the line allows a determination of the RMS noise, σ_{noise}^2, of the system.

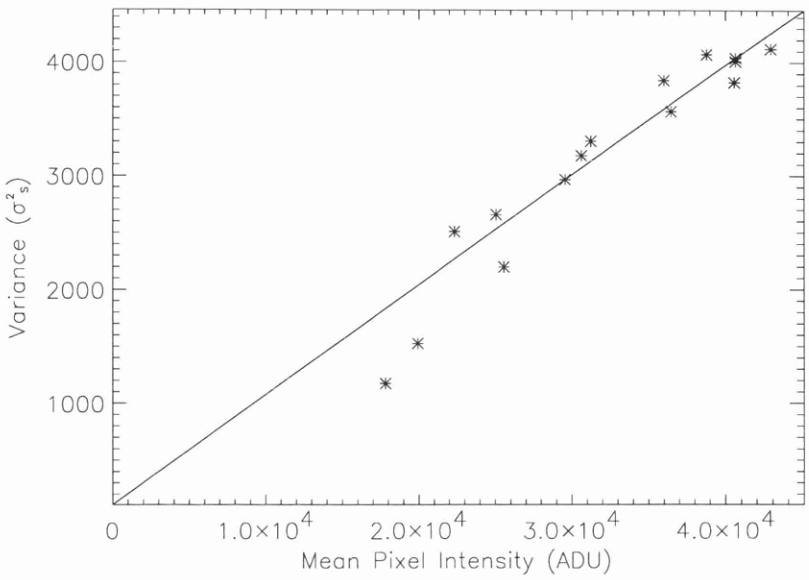

Figure 2.15: The transfer curve of the ST-6 CCD detector with the variance σ_s^2 plotted as a function of the mean signal for a 10 by 10 pixel area of the chip.

Experimental Determination of Noise and Gain

In order to determine the gain and noise of the ST-6 CCD detector the following calibration procedure was followed. The CCD was illuminated by a flat illumination source connected to a uniformly regulated power supply and a variable resistor in order to vary the illumination intensity.

Twenty exposures were taken at numerous illumination levels with an accompanying dark exposure. A test area of 10 by 10 pixels on the detector was selected and the procedure outlined below was followed.

Introducing $\mathcal{X}_{i,j,k}$ as the measured signal for row i, column j and exposure k with the corresponding dark value $\mathcal{D}_{i,j}$. Taking M number of exposures and introducing P as the number of pixels in the sub-area, the mean signal level may be expressed by

$$\overline{\mathcal{X}}_{i,j} = \sum_k \frac{\mathcal{X}_{i,j,k}}{M}. \tag{2.33}$$

The pixel deviation from the mean may be expressed as

$$d_{i,j,k} = \mathcal{X}_{i,j,k} - \overline{\mathcal{X}}_{i,j}. \tag{2.34}$$

Expressing the variance of the signal by

$$\sigma^2_{signal} = \frac{\sum_{i,j,k} d^2_{i,j,k}}{MP} \tag{2.35}$$

the mean signal level may be defined by

$$\overline{S}_{signal} = \frac{\sum_{i,j}(\overline{\mathcal{X}}_{i,j} - \mathcal{D}_{i,j})}{P}. \tag{2.36}$$

For each illumination level the signal mean and variance were determined. Figure 2.15 illustrates the transfer curve with a least squares regression fit also plotted. This yields a gradient of 0.0967 with an intercept of 108.487. The inverse of the gradient is defined as the gain of the system and within uncertainties this yields 10 electrons per ADU. The RMS of the system may be expressed by $\sigma_s \times$ gain, yielding 104 electrons. A typical CCD pixel may hold $\leq$ 500000 electrons before saturation. This translates to an uncertainty of 0.15% in the determination of the normalised Stokes parameters. This may further be degraded by observing faint stars at long integration times in the presence of strong and generally polarized sky background.

2.4.3 Flatfielding and Vignetting

The sensitivity of a CCD is not uniform across its surface. Different pixels have different quantum efficiencies resulting from small structural variations on the chip. These variations in sensitivity can reach 1% to 2% over the array and are far from negligible when observing faint objects for polarimetry. This multiplicative error is, in principal, completely removable by division with an exposure of an uniformly illuminated surface (commonly referred to as a flatfield) in a process known as flatfielding. However, in determining the Stokes parameters in the procedure outlined in Section 2.2, the dependence on the detector sensitivity is clearly eliminated and the cumbersome flatfielding technique is not required.

Due to the nature of the light cone entering the polarimeter and the physical size of the optical components, spatial vignetting (shadowing) from the instrument must be considered. During the course of solar observations the masking grid's field of view exceeded 16 arcminutes with an f/32 light cone entering the instrument resulting in spatial vignetting of the image. For night time work this effect is compounded by the wider f/10 light cone transversing through the system. In order to determine the amount of vignetting, an exposure of the quiet Sun was taken. This produced an exposure of uniform intensity enabling a calibration routine to remove the dependence on vignetting. Figure 2.16 illustrates the vignetting contour map.

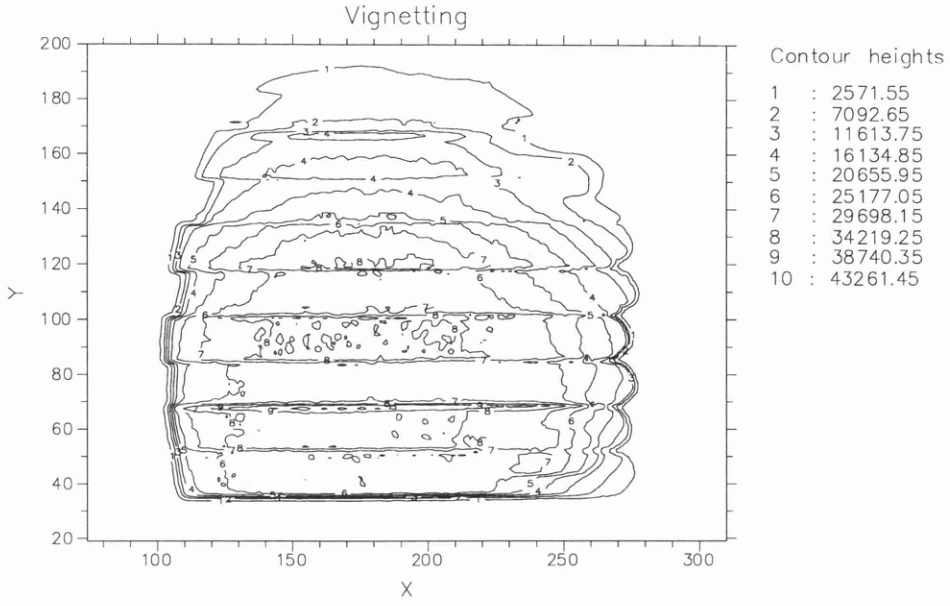

Figure 2.16: The contour map demonstrating the optical vignetting.

2.5 Data Reduction Procedures

The images collected by the data acquisition computer during observations were transferred via disks to UNIX-based workstations. The raw data was archived in the standard astronomical FITS (Flexible Image Transfer System) format. Conversion of the files to an NDF (Extensible N-Dimensional Data Format) format allowed data manipulation by the Starlink environment. The packages utilised were a combination of KAPPA, GAIA, DAOPHOT, PHOTOM and FIGARO with several C-shell scripts written to automate the data reduction. A further non-Starlink package, IDL, was employed in order to analyse the data with specific routines not available elsewhere.

Two distinct approaches were followed for the data reduction depending on the object observed; a stellar point source as outlined in Section 2.5.1 or an extended source such as the Sun or the Orion nebula as reviewed in Section 2.5.2. Certain instrumental parameters must be considered before any analysis can be undertaken. The instrumental polarization and the coordinate frame of the instrument must be determined by suitable calibration procedures and the results incorporated into the analysis.

2.5.1 Stellar Analysis

In order to improve the accuracy of the polarization measurement, a stellar source was slightly defocussed onto the detector and the intensity dispersed over a large number of pixel elements. Four exposures were taken at the appropriate half-wave plate positions during a three minute interval for a 5^{th} magnitude star. Any movement of the source on the detector due to image wobble caused by the half-wave plate rotation or poor tracking by the telescope may be corrected during the data analysis. Furthermore, a bias exposure is taken in order to determine the readout noise and also a dark exposure of similar length to the light exposure is taken to ascertain the inherent thermal background of the detector. The sky background can show strong temporal variations in both its intensity and its degree of polarization. It is therefore important to eliminate or compensate for its effects on the final measurement. A commonly used method is to take separate measurements of the sky background before and after each observation and to subtract this from the stellar (plus sky) measures. However, a background exposure was deemed unnecessary since the imaging polarimeter has an extended field of view and thus both source and background may be measured simultaneously.

The following analysis routines were carried out:

- Images are subjected to preliminary steps of bias and dark removal, cosmic ray and bad pixel detection.
- PSF fitting tasks of the DAOPHOT package are then used to determine accurately the centroids of the stellar images. The intensity estimates are, however, made using aperture photometry covering a diameter greater than 2×FWHM (full width at half maximum transmission) so as to integrate more than 90% of the signal. Any temporal drift on the detector is also eliminated.
- The gain factor of the system ($10e^{-}$/ADU) is applied.
- The sky background may be subtracted from the stellar exposures.
- The normalised Stokes parameters q and u are determined, with the instrumental polarization corrections incorporated in the measurement.
- The position angle, θ, is determined and corrected to the equatorial coordinate frame.

The degree of polarization p and position angle θ may thus be determined for any stellar source.

2.5.2 Extended Image Analysis

The analysis procedure for extended sources is similar to that discussed in the previous section with several additional complications. In order to improve the polarimetric accuracy, multiple exposures of an extended source are undertaken with the frames co-added thus increasing the total number of detected photons. The expected precision for one set of exposures (i.e. at the four half-wave plate positions) is of the order 0.1% per pixel. Taking ten sets of exposures and co-adding frames and detector pixels improves the accuracy of the polarization to 0.02%. However, this observational technique amounts to recording over forty exposure frames in a time period of approximately 45 minutes. Unfortunately, mistracking by the telescope introduces drifts between different exposures requiring alignment corrections. Mutual alignment of the digital images to allow intercomparison is dependent on the positional determination of the solar limb or some appropriate surface structure such as a sunspot or granulation, in the case of the Sun, as reference markers. Certain imperfections in the grid construction also provide excellent reference markers.

One of the main aims of this thesis is the study of the center-to-limb polarization gradient along the equatorial and polar directions. It is therefore imperative to determine the exact position of the solar limb consistently in all exposures. The center-to-limb intensity variation, illustrated in Figure 5.2, is explored and the median intensity value along the limb gradient is used as a positional marker for the limb position. It is also important to consider the effect of refraction in the Earth's atmosphere when reducing the data.

Differential Refraction of the Sun

In undertaking the exercise related to CLV of the East/West and North/South sections of the solar surface, the effect of refraction on the relative plate scales needs to be considered. When observing celestial sources, refraction due to the Earth's atmosphere must be considered and the following section presents a simple analysis of this effect. Therefore, taking the Earth's atmosphere to consist of a large number of thin parallel layers of differing densities, see Figure 2.17. A ray of light from a source meets the topmost layer of the atmosphere at B, at an angle of incidence i, and is therefore refracted in successive layers until it reaches the observer at O. Since the direction of increasing density is downwards, the refractive index also increases in that direction, so that the source is displaced towards the zenith along the great circle through Z and X, where X is the true position and A the apparent position of the source, as illustrated in Figure 2.17.

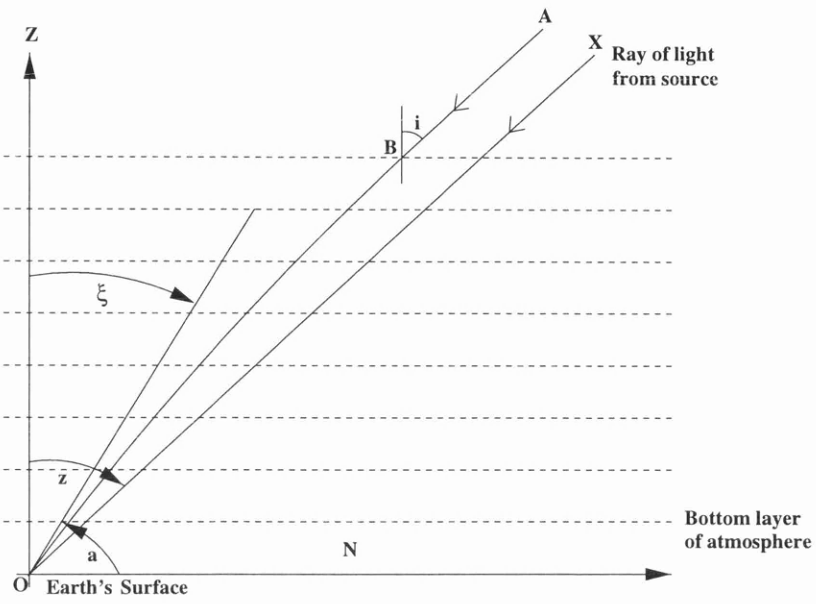

Figure 2.17: The coordinate system for refraction in the Earth's atmosphere.

Defining N as the refractive index of the bottom layer yields,

$$\sin z = N \sin \xi. \tag{2.37}$$

Let R, defined by

$$R = z - \xi \tag{2.38}$$

be the angle of refraction, the correction that has to be applied to the apparent zenith distance ξ to obtain the true zenith distance z. Eliminating z from equation 2.37 and 2.38 and with the small angle approximation yields

$$R_1 = k \tan \xi \tag{2.39}$$

where k is 60.3 arcseconds when the surface atmospheric pressure is 760mm of mercury and the temperature is 0°C (values of k for other pressures and temperatures can be found from tables, see Allen, 1973) and R_1 expressed in arcseconds. The equation above is valid for zenith distances less than 45° and is a fairly good first approximation up to 70°. Beyond that, a more accurate formula taking into account the curvature of the Earth's surface is required. For altitudes of 15° or more, the refraction R_2 in degrees, can be calculated from the following equation, (taken from Ridpath, 1989),

$$R_2 = \frac{0.00452 p_a}{(273 + T) \tan a} \tag{2.40}$$

where p_a is the atmospheric pressure in millibars, T is the temperature in degrees Celsius, and a is the altitude in degrees. For altitudes below 15° the simple formula becomes increasingly inaccurate, and the following more precise formula, R_3 also in degrees, must be used

$$R_3 = \frac{p(0.1594 + 0.0196a + 0.00002a^2)}{(273 + T)(1 + 0.505a + 0.0845a^2)}. \tag{2.41}$$

The amount of refraction ranges from just over half a degree at the horizon to zero at the zenith.

The Sun is an extended source subtending an angle of 0.533° in the sky from limb to limb. In the direction of increasing altitude or decreasing zenith distance, i.e southern to northern limb, the Sun's diameter will appear to be reduced due to the differential refraction caused by the Earth's atmosphere. The rays from the top of the Sun will be refracted more than the rays emanating from the bottom and hence the apparent "squashing" from pole to pole. However, there is no differential refraction along the equatorial direction, i.e. western limb to eastern limb, since this is a direction of constant zenith distance and hence not refraction dependent.

One of the aims of this thesis is to determine whether there is a significant difference in the center-to-limb variation in Hα polarization between the polar and equatorial regions of the Sun. A contributory factor may be the different scale length in the polar direction caused by the differential refraction. It is therefore imperative to quantify this effect for the observations taken. Applying Equation 2.38 to both the northern and southern limb of the Sun yields,

$$\begin{aligned} R_n &= z_n - \xi_n \\ R_s &= z_s - \xi_s. \end{aligned} \tag{2.42}$$

The apparent angular change of the Sun's diameter from the northern to the southern limb due to differential refraction in the atmosphere may be expressed by the following expression,

$$(z_n - z_s) + (\xi_s - \xi_n) = R_n - R_s \tag{2.43}$$

where R_n and R_s may be determined using one of the three approximations outlined in Equations 2.39–2.41 and $z_n - z_s = 0.533°$. Figure 2.18a illustrates the altitude of the Sun at Glasgow at midday during the year while Figure 2.18b shows the corresponding variation in the Sun's diameter between the northern and southern limbs due to the differential refraction caused by the Earth's atmosphere. Evidently if the Sun's altitude is greater than 30° the differential refraction effect is less than 4 arcseconds. This is smaller than the angular resolution of the polarimeter and corresponds to 0.2% change in the Sun's apparent scale

length. All observations of the Sun were conducted during the months of July and August within two hours of midday and only approximately a fifth of the solar surface was observed at any one time for the CLV analysis, therefore the refractive effects of the atmosphere may be neglected. This means that the non-linear plate scale North/South relative to the linear scale East/West in not important.

Image Reduction Technique

Several exposures of the Orion Nebula (M42) taken during the winter 1996/1997 are shown in Figure 2.19 illustrate the required observational reduction routines:

- An image of the extended source is taken with the Savart plate, half-wave plate and grid removed as shown in Figure 2.19a.
- A set of exposures of the source is taken through the polarization optics producing a series of strip pairs of orthogonal polarization. Since the grid of parallel obscuring strips ensures only half the field of view is visible, the telescope orientation is slightly changed to ensure that data is taken of the previously obscured view. Figure 2.19b and Figure 2.19c are two such examples.
- Images are subjected to bias and dark removal with the gain factor of the system applied. Bad pixel detection and sky background subtraction is applied where appropriate.
- The ordinary and extraordinary strips of the region under consideration are extracted from the exposure by the Kappa analysis package. This is demonstrated in Figure 2.19d and Figure 2.19e for both exposures.
- The degree of polarization and angle of polarization are determined. Figure 2.19f is a contour plot of degree of polarization. Conventionally the two quantities are superimposed in one plot.

2.6 Summary

An optical polarimeter has been constructed based on the use of a Savart plate to split the telescope image into two polarized components. The instrument has a field of view of about 16 arcminutes for a 7.5cm diameter f/32 telescope and 8 arcminutes for a 25cm diameter f/10 telescope. Combined with the use of a two dimensional cooled CCD detector, this allows the mapping of linear polarization in extended astronomical objects with a spatial

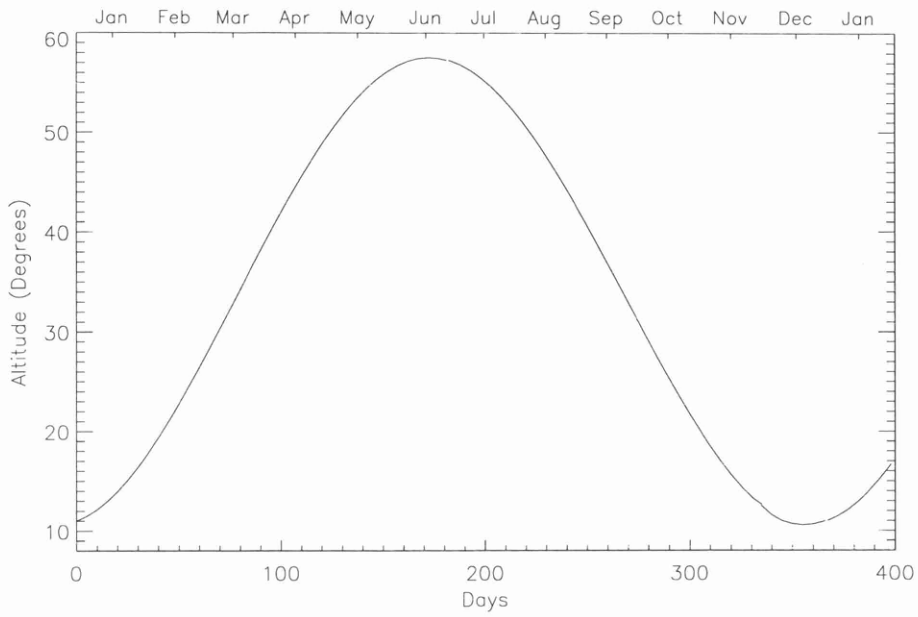

(a) The altitude of the Sun above the horizon at Glasgow at midday during the year.

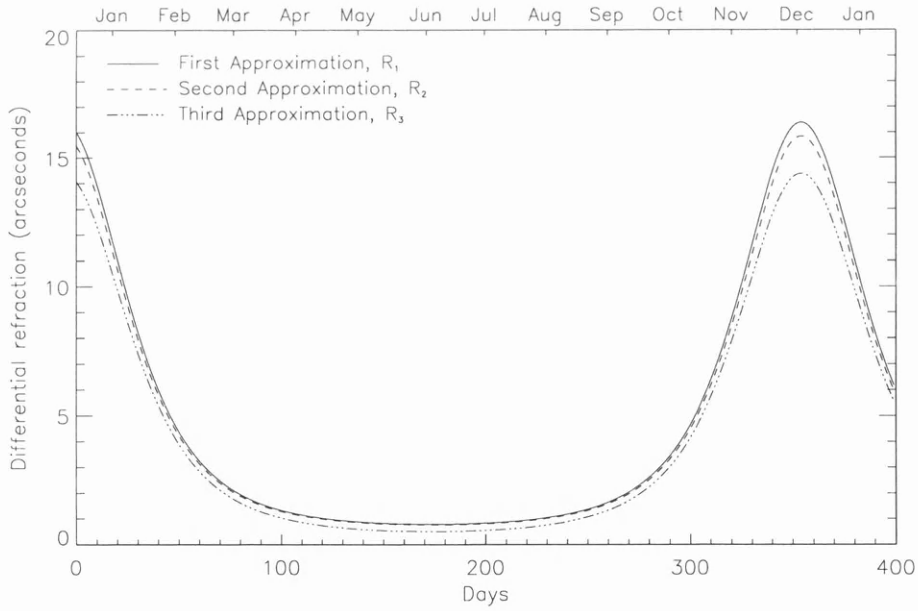

(b) The apparent change in the Sun's diameter from the northern to the southern limb, in arcseconds, caused by the differential refraction in the atmosphere.

Figure 2.18: The effect of differential refraction on the center to pole measurement.

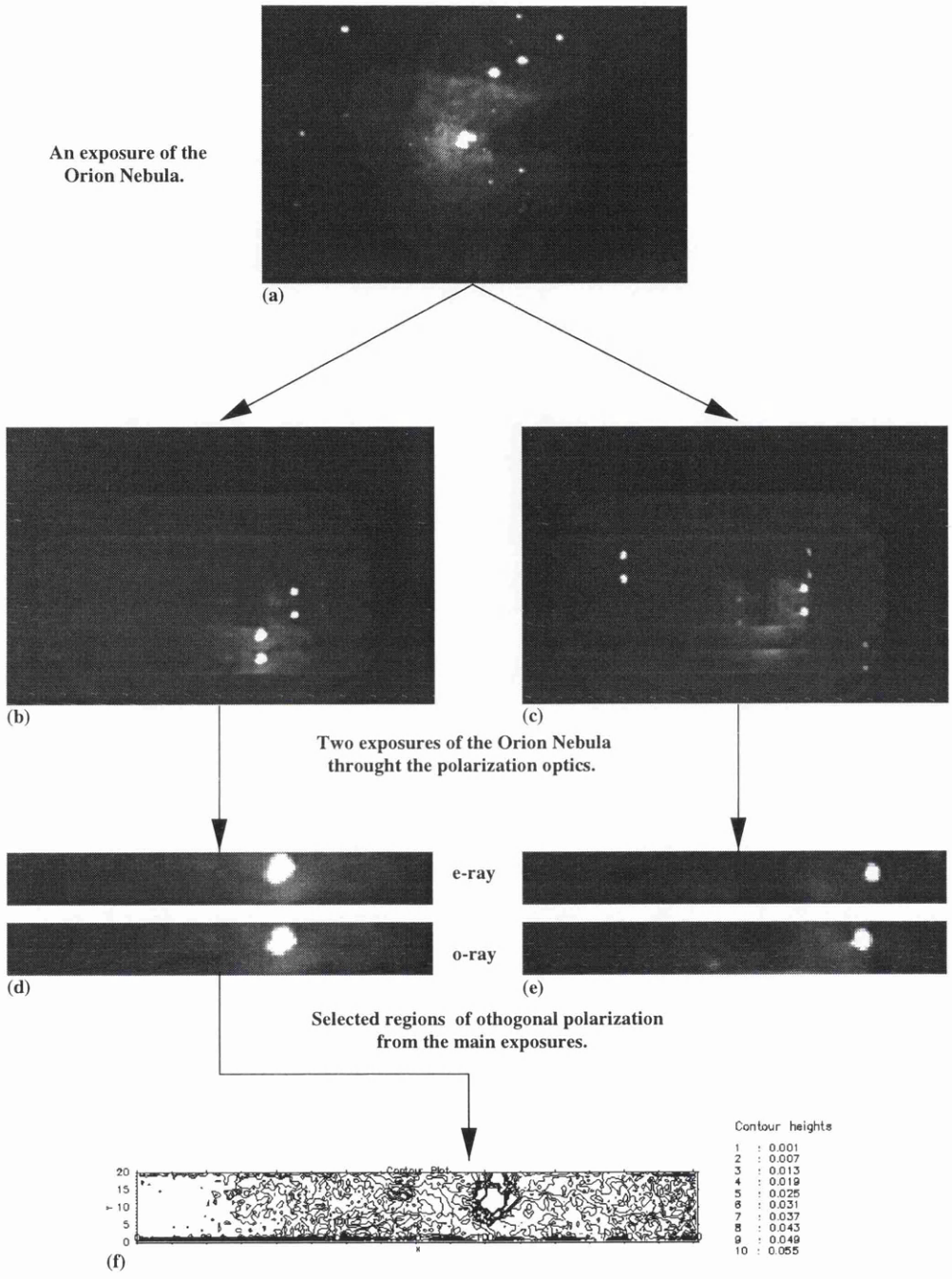

Figure 2.19: Diagrammatic representation of the extended image analysis routine.

resolution that can match the limit set by the atmospheric seeing, which at Glasgow is 5 arcseconds at best. An off-axis guidance system was implemented enabling the tracking of faint objects such that the corresponding image on the CCD face is kept stationary to within one half pixel. Instrumental polarization, excluding the Hα filter, was calculated to be of the order of 0.04% during test bench calibration. Observations of nearby standard polarized and unpolarized stars show that for wideband observations there is no discernible depolarization and the instrumental polarization is less than 0.05%.

Chapter 3

Faraday Rotation Theory

A plasma permeated by a magnetic field can be considered an anisotropic medium with properties such as birefringence, optical activity, and dichroism. These occur due to the difference in the electron dynamics between motions parallel and perpendicular to the magnetic field. In addition, due to electron density gradients, plasmas are refractive. Starting from the theory of electromagnetic wave propagation in an magnetised plasma, the theories of Faraday rotation and birefringence are reviewed. The inversion techniques necessary to obtain the poloidal magnetic field from the Faraday rotation measurements are discussed. Finally, an analytical solution is presented that details the expected Faraday rotation angles for COMPASS-D and the birefringence introduced due to the presence of the toroidal magnetic field.

3.1 Fundamental Frequency Parameters in Tokamak Plasmas

An electrically charged particle in the presence of a magnetic field will exhibit a cyclotron gyration along the field line. The angular rotation frequency ω_c is fundamental to the analysis of electromagnetic wave propagation through a plasma, and is defined by

$$\omega_c = \frac{|q|\mathrm{B}}{m} \tag{3.1}$$

where q is the charge of the particle, m is its mass, and B the magnetic field strength. The cyclotron frequency for COMPASS-D with $\mathrm{B}_{tor} \leq 2.10\mathrm{T}$ on axis for electrons is in the 30-60GHz range, and for ions in the MHz range. If an electromagnetic wave with a frequency in one of these ranges propagates into the plasma, most of the wave power will be resonantly absorbed by the plasma. This may also occur at a few higher harmonics of the ion or electron cyclotron frequencies.

A charged particle displaced from its equilibrium position in a quasi-neutral plasma will experience electrostatic oscillations, where the restoring force is due to charge separation.

This oscillatory motion by the charged particle is defined as the plasma frequency. Since ions are very much heavier than electrons, to a first approximation, it is possible to consider them to be at rest. The plasma angular frequency ω_p is given by

$$\omega_p = \sqrt{\frac{n_e e^2}{\epsilon_o m_e}} \tag{3.2}$$

where n_e is the electron density, e the elementary charge of the electron, m_e the electron mass, and ϵ_o the dielectric vacuum constant. The density regime on COMPASS-D lies between $5\times10^{18}\mathrm{m}^{-3}$ and $1\times10^{20}\mathrm{m}^{-3}$, yielding plasma frequencies between 20 and 90GHz.

In many plasmas it is unsatisfactory to use material probes to determine internal plasma parameters and nonperturbing methods for diagnostics are required. The most successful and accurate of these use electromagnetic waves as a probe into the plasma. Provided their intensity is not too great, such waves cause negligible perturbations to the plasma and are valuable diagnostic tools. Given the applied wave frequency, ω, it is interesting to consider the density for which it equals the plasma frequency. This critical density n_c is, by inversion of Equation 3.2, defined as

$$n_c = \frac{\epsilon_o m_e \omega^2}{e^2}. \tag{3.3}$$

For a probing wave frequency of 693GHz the critical density equals $5.96\times10^{21}\mathrm{m}^{-3}$ which is two orders of magnitude larger than typical plasma densities in COMPASS-D discharges.

3.2 Wave Propagation in a Homogeneous Magnetised Plasma

In this section, the theory of electromagnetic wave propagation in a cold, homogeneous Lorentz plasma will be considered. A Lorentz plasma is one for which the ions can be considered as being at rest, acting as a continuous stationary fluid through which the electrons move. The electron thermal velocity is also assumed to be much less than the wave phase velocity. It will be shown that a wave propagating in the plasma can be described by two orthogonally polarized characteristic waves, each experiencing a different refractive index N. To describe fully the interaction between the electromagnetic wave and the Lorentz plasma it is necessary to derive these refractive indices.

The derivation can be done by determing Ohm's law from both the equation of motion and from Maxwell's equations. The requirement that these two different expressions for the conductivity of the plasma be self-consistent leads to the Appleton-Hartree formula, (see Appleton, 1932).

Consider a plane electromagnetic wave propagating along the z-axis at an angle θ to the external magnetic field $\mathbf{B_o}$, which lies in the y-z plane (see Figure 3.1). The interaction of

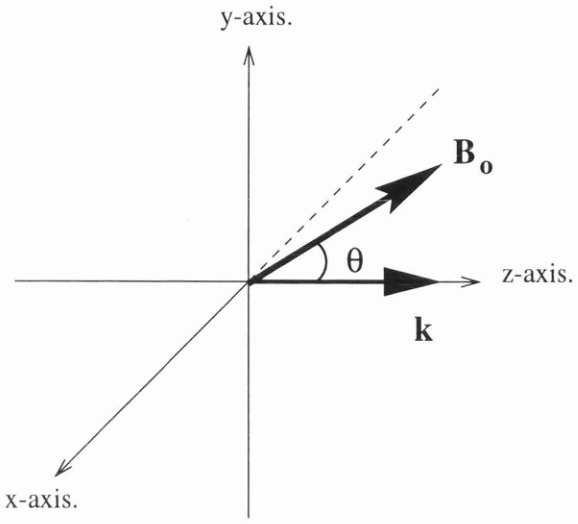

Figure 3.1: Coordinate frame for wave propagation in an arbitrary direction to the external magnetic field $\mathbf{B_o}$. Parameter θ is the angle between the direction of propagation $\mathbf{k}$ and $\mathbf{B_o}$.

the wave with the plasma occurs via the electric field of the wave $\mathbf{E}$, with the equation of motion of the electrons given by

$$m_e \frac{d\mathbf{v}}{dt} = -e\mathbf{E} - e\mathbf{v} \times \mathbf{B_o} \tag{3.4}$$

where $\mathbf{v}$ is the electron velocity. All interactions with other particles are neglected. In some texts, a collisional term $-\nu m_e \mathbf{v}$, where ν is the collisional frequency for momentum transfer, is included in the analysis. However for small amplitude waves this collisionality term is negligible in practice. The wave magnetic field is also neglected with respect to its electric field since the magnetic field compares to the electric field as $\frac{|\mathbf{v}|}{c}$ in a non-relativistic plasma.

Expressing the temporal and spatial dependence of a plane monochromatic electromagnetic wave as $e^{i(\omega t - kz)}$ and defining the current density $\mathbf{J}$ as

$$\mathbf{J} = -en_e\mathbf{v} \tag{3.5}$$

it is possible to rewrite the equation of motion, Equation 3.4, in the form of Ohm's Law

$$\bar{\rho} \cdot \mathbf{J} = \mathbf{E} \tag{3.6}$$

where the resistivity tensor $\bar{\rho}$ is given by

$$\bar{\rho} = \frac{1}{\epsilon\omega_p^2} \begin{pmatrix} i\omega & \omega_{ce}\cos\theta & -\omega_{ce}\sin\theta \\ -\omega_{ce}\cos\theta & i\omega & 0 \\ \omega_{ce}\sin\theta & 0 & i\omega \end{pmatrix} \tag{3.7}$$

and ω_{ce} denotes the angular cyclotron frequency for electrons.

The second stage in the theory is to derive Ohm's law with a conductivity tensor $\bar{\sigma}$, namely

$$\mathbf{J} = \bar{\sigma} \cdot \mathbf{E}. \tag{3.8}$$

The dispersion relation for wave propagation then follows from the requirement that Equations 3.6 and 3.8 are self-consistent.

The conductivity tensor is obtained by considering the Maxwell equations:

$$\nabla \times \mathbf{E} = -\frac{\delta \mathbf{B}}{\delta t} \tag{3.9}$$

$$\nabla \times \mathbf{B} = \mu_0 \mathbf{J} + \frac{1}{c^2}\frac{\delta \mathbf{E}}{\delta t} \tag{3.10}$$

$$\nabla \cdot \mathbf{B} = 0 \tag{3.11}$$

$$\nabla \cdot \mathbf{E} = \frac{\rho_f}{\epsilon}. \tag{3.12}$$

where ρ_f is the column density of free charge and $\mathbf{J}$ the net current density.

Combining Equations 3.9 and 3.10 yields the equally well known electromagnetic wave equation

$$\nabla \times \nabla \times \mathbf{E} = -\frac{1}{c^2}\frac{\delta^2 \mathbf{E}}{\delta t^2} - \mu_o \frac{\delta \mathbf{J}}{\delta t}. \tag{3.13}$$

re-writing Equation 3.12 in the shape of Ohm's law yields

$$\bar{\sigma} \cdot \mathbf{E} = \mathbf{J} \tag{3.14}$$

and taking $k = N\omega/c$, with N being the refractive index and c the velocity of light, this yields an expression for the plasma conductivity

$$\bar{\sigma} = i\omega\epsilon_o \begin{pmatrix} N^2-1 & 0 & 0 \\ 0 & N^2-1 & 0 \\ 0 & 0 & -1 \end{pmatrix}. \tag{3.15}$$

For Equations 3.8 and 3.14 to be self-consistent they must satisfy

$$(\bar{\rho} \cdot \bar{\sigma} - \bar{\mathbf{I}}) \cdot \mathbf{E} = 0 \tag{3.16}$$

where $\bar{\mathbf{I}}$ is the unit tensor. This equation represents a set of three simultaneous equations which upon substitution of Equations 3.7 and 3.15 can be expressed as

$$\frac{i\omega}{\omega_p^2} \begin{pmatrix} i\omega(N^2-1) + i\frac{\omega_p^2}{\omega} & \omega_{ce}(N^2-1)\cos\theta & \omega_{ce}\sin\theta \\ -\omega_{ce}(N^2-1)\cos\theta & i\omega(N^2-1) + i\frac{\omega_p^2}{\omega} & 0 \\ \omega_{ce}(N^2-1)\sin\theta & 0 & -i\omega + i\frac{\omega_p^2}{\omega} \end{pmatrix} \cdot \mathbf{E} = 0. \tag{3.17}$$

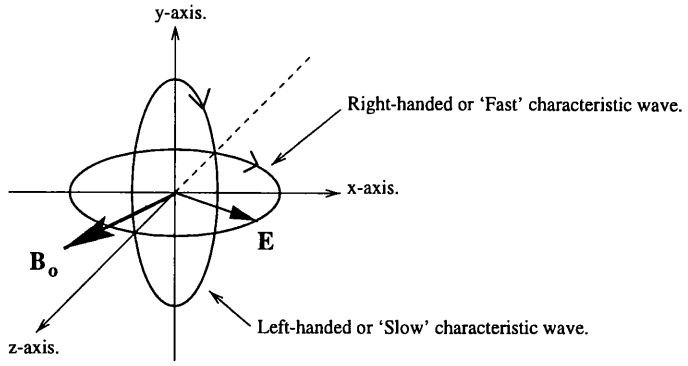

Figure 3.2: The general polarization state of the characteristic waves.

The determinant of the matrix coefficients must be zero for a non-trivial solution to exist. This results in a dispersion relation for wave propagation that can be solved for the refractive index N, (see Heald and Wharton, 1965 and Segre, 1978),

$$N^2 = 1 - \frac{\frac{\omega_p^2}{\omega^2}}{1 - \frac{\omega_{ce}^2}{\omega^2}\frac{\sin^2\theta}{2(1-\omega_p^2/\omega)} \pm \frac{\omega_{ce}^2}{\omega^2}\frac{\sin^2\theta}{2(1-\omega_p^2/\omega^2)}[1+F^2]^{1/2}} \tag{3.18}$$

where

$$F = \frac{2\omega}{\omega_{ce}}(1 - \frac{\omega_p^2}{\omega^2})\frac{\cos\theta}{\sin^2\theta}. \tag{3.19}$$

This expression is called the Appleton-Hartree formula for the refractive index. For a given plasma, described by the parameters ω_p and ω_{ce}, Equation 3.18 will, in general, yield two different positive values for the refractive index. For each of these values, Equation 3.17 can be solved giving the particular state of polarization. Waves can only travel through the plasma in one of these two characteristic polarization states. They are the normal modes of electromagnetic oscillation in the plasma and, as they propagate through the plasma, these characteristic waves do not change their state of polarization, as long as the plasma properties do not change. They are generally elliptically polarized, orthogonal with their major axes at 90° to each other and with the same ellipticity but opposite handedness, (see Figure 3.2). Any polarized wave can be resolved into two waves with orthogonal polarization. However, the refractive indices that the two waves experience are in general different, and therefore their propagation velocities will also differ. As a consequence, the polarization of the resultant wave will change.

The polarization states of any electromagnetic wave can be fully described by three convenient parameters; the electric field ratios $\kappa_{x,y}$, $\kappa_{z,y}$, $\kappa_{z,x}$

$$\kappa_{x,y} = \frac{E_x}{E_y} = i\frac{N^2 - 1 + \frac{\omega_p^2}{\omega^2}}{\frac{\omega_{ce}}{\omega}(N^2-1)\cos\theta} \tag{3.20}$$

$$\kappa_{z,y} = \frac{E_z}{E_y} = \frac{(N^2 - 1 + \frac{\omega_p^2}{\omega^2})\tan\theta}{1 - \frac{\omega_p^2}{\omega^2}} \tag{3.21}$$

$$\kappa_{z,x} = \frac{E_z}{E_x} = -i\frac{\frac{\omega_{ce}}{\omega}(N^2-1)\sin\theta}{1 - \frac{\omega_p^2}{\omega^2}}. \tag{3.22}$$

Considering purely transverse electromagnetic waves the electric field ratio $\kappa_{x,y}$ is important. By substituting Equation 3.18, N can be eliminated in the above expression to yield

$$\kappa_{x,y} = \frac{i}{\cos\theta}\left[\frac{\frac{\omega_{ce}}{\omega}sin^2\theta}{2[1-\frac{\omega_p^2}{\omega^2}]} \mp \sqrt{\cos^2\theta + \left(\frac{\frac{\omega_{ce}}{\omega}\sin^2\theta}{2[1-\frac{\omega_p^2}{\omega^2}]}\right)^2}\right]. \tag{3.23}$$

3.2.1 The Principal Characteristic Waves

There are two directions in the plasma which are of special interest. These are parallel and perpendicular to the external magnetic field lines, called the principal directions. The refractive indices and state of polarization of these characteristic waves for these directions are considered.

Propagation Parallel to the Magnetic Field

For the case of wave propagation parallel to the external magnetic field, $\theta = 0°$, it is possible to simplify equation 3.18 to yield two refractive indices N_L and N_R

$$N_L^2 = 1 - \frac{\omega_p^2}{\omega(\omega + \omega_{ce})} \qquad \text{and} \qquad N_R^2 = 1 - \frac{\omega_p^2}{\omega(\omega - \omega_{ce})}. \tag{3.24}$$

Using these expressions, one can evaluate the associated polarization states from the ratios in Equations 3.20, 3.21 and 3.22, yielding

$$\kappa_{x,y} = \mp i, \quad \kappa_{z,x} = 0, \quad \text{and} \quad \kappa_{z,y} = 0. \tag{3.25}$$

where the sign of $\kappa_{x,y}$ is positive in case the refractive index N_R is substituted. In both cases the wave is completely transverse.

The electric field components for the wave with $\kappa_{x,y} = -i$ and refractive index N_L are

$$E_x = \cos\omega t \qquad \text{and} \qquad E_y = -\sin\omega t. \tag{3.26}$$

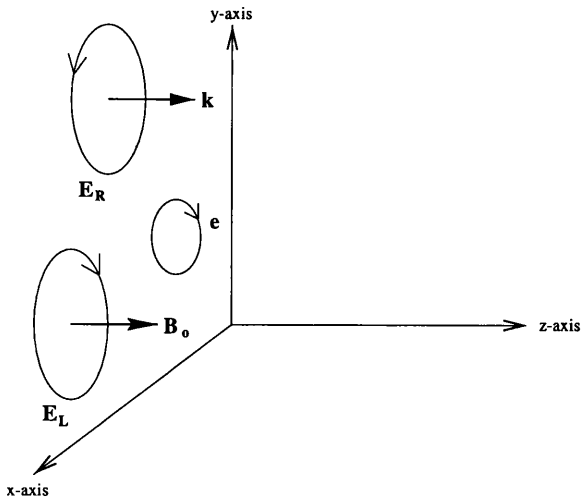

Figure 3.3: The circularly polarized principal characteristic waves.

Superposition of these wave components gives a characteristic wave with circular polarization. The direction in which the electric field describes the circle, the handedness, is clockwise for an observer looking towards the light source. In plasma wave theory, the wave is called left-handed and is sometimes referred to as the "slow" wave. Similarly, the characteristic wave with $\kappa_{x,y} = i$ and described by N_R has electric field components

$$E_x = \cos\omega t \qquad \text{and} \qquad E_y = \sin\omega t. \tag{3.27}$$

Again the polarization is circular, but the wave is now called the right-handed or "fast" wave. The electric field vector describes the circle in an anti-clockwise manner for an observer looking towards the light source. These polarizations are shown in Figure 3.3 and, included for comparison, is the direction of electron gyration. This corresponds to the direction of rotation of the right-handed wave.

Propagation Orthogonal to the Magnetic Field

Considering the case of wave propagation perpendicular to the external magnetic field, $\theta = 90°$, the Appleton-Hartree equation yields the refractive indices

$$N_o^2 = 1 - \frac{\omega_p^2}{\omega^2} \qquad \text{and} \qquad N_{ex}^2 = 1 - \frac{\omega_p^2(\omega^2 - \omega_p^2)}{\omega^2(\omega^2 - \omega_p^2 - \omega_{ce}^2)}. \tag{3.28}$$

The refractive index, N_o^2, also describes the propagation of an electromagnetic wave in the absence of a magnetic field ($\omega_{ce} = 0$) with the associated manner of propagation generally

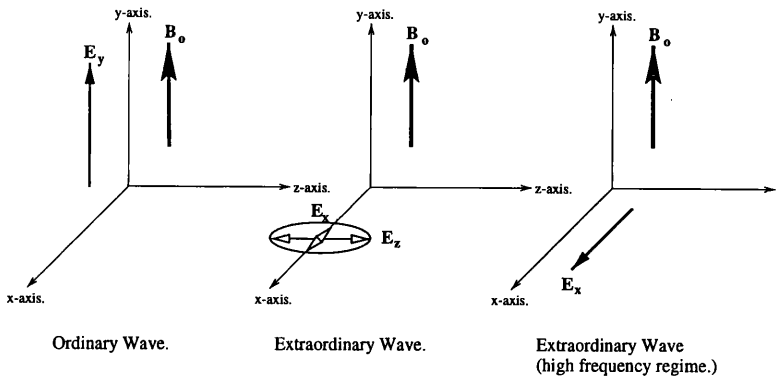

Figure 3.4: The Principal characteristic waves for propagation perpendicular to $\mathbf{B_o}$.

referred to as an ordinary mode or O-mode propagation. This leaves the extraordinary mode or X-mode for the propagation mode governed by N_{ex}.

Evaluating the polarization state for the O-mode propagation Equations 3.20, 3.21 and 3.22 yield the ratios

$$\kappa_{x,y} = 0, \quad \kappa_{z,x} = -i\frac{(\omega_{ce}/\omega)(\omega_p/\omega)^2}{1-(\omega_p/\omega)^2}, \quad \text{and} \quad \kappa_{z,y} = 0. \tag{3.29}$$

The characteristic wave is a linearly polarized transverse wave with the electric field along the y-axis, and therefore parallel to the external magnetic field.

In the case of X-mode propagation, the polarization ratios yield

$$\kappa_{x,y}\to\infty, \quad \kappa_{z,x} = -i\frac{(\omega_{ce}/\omega)(\omega_p/\omega)^2}{1-(\omega_p/\omega)^2(\omega_{ce}/\omega)^2}, \quad \text{and} \quad \kappa_{z,y}\to\infty. \tag{3.30}$$

There is no E_y component of the electric field, but there generally exists a z component. The characteristic wave is elliptically polarized in the x-z plane, as shown in Figure 3.4, with a plane perpendicular to the external magnetic field. That is, as such a wave propagates into a plasma it develops an electric field component E_x, thus becoming partly longitudinal and partly transverse.

In the high frequency regime with $\omega \gg \omega_p$ and $\omega \gg \omega_{ce}$ the longitudinal polarization coefficients $\kappa_{z,x}$, $\kappa_{z,y}$ are very small so that there is only a negligible longitudinal electric field component, see Figure 3.4. Thus the characteristic wave for X-mode propagation has now also become linearly polarized as in the O-mode case, but with the electric field vector perpendicular to the propagation direction and the external magnetic field.

3.2.2 The WKB Approximation of Geometrical Optics

The theory of electromagnetic wave propagation discussed so far assumes a homogeneous plasma throughout all space. It is important to consider what happens when there are spatial gradients in the electromagnetic properties. This implies that fields of the form $e^{i(kz-\omega t)}$ no longer separately satisfy Maxwell's equations.

If the properties of the plasma vary sufficiently slowly, then locally the wave can be thought of as propagating in an approximately uniform medium and, thus, the previous treatments apply, (see Budden, 1961). Thus, for any frequency and propagation direction, there is a locally a well defined **k**, propagation vector and refractive index N corresponding to the local values of the plasma parameters. This approximation of the wave amplitude as it propagates through the plasma for a given frequency can be expressed by

$$\mathbf{E} \simeq e^{i(\int \mathbf{k}\cdot\mathbf{dz}-\omega t)} \tag{3.31}$$

where z is the distance along the ray path and **k** is the solution of the homogeneous plasma dispersion relation for a given ω, based on the local plasma parameters. This is a good approximation provided that

$$\frac{|\nabla k|}{k^2} \ll 1 \tag{3.32}$$

implying that the fractional variation of **k** for one wavelength of the wave is small. Another viewpoint is that the refractive index scale length of the plasma is very much larger than the wavelength of the wave.

3.2.3 Faraday Rotation

The evolution of polarization experienced by an electromagnetic wave propagating through an inhomogeneous plasma , in a direction parallel to the external magnetic field, will be discussed in this section. The WKB approximation to geometrical optics and a high frequency regime are taken to be valid assumptions.

The progress of an electromagnetic wave of arbitrary polarization **E** is determined by resolving the electric field into two circular components, corresponding to a superposition of characteristic waves, and then allowing these two waves to propagate with their known refractive indices. The wave amplitude at any other position in the plasma is then determined by the superposition of the two waves there. Their phases will evolve differently as they propagate in the plasma because of the different refractive indices of each characteristic wave. Consider a wave linearly polarized in the x-direction as shown in Figure 3.5. The

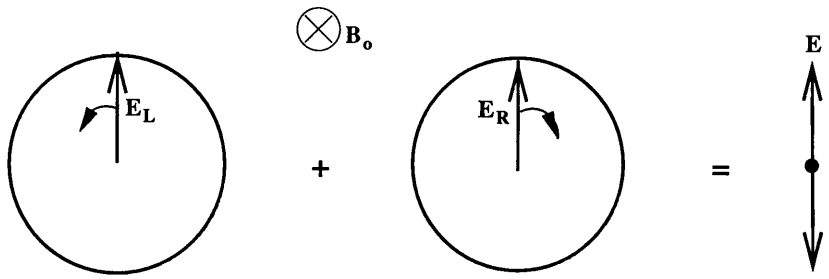

(a) A plane polarized wave as the sum of left- and right-handed circularly polarized wave.

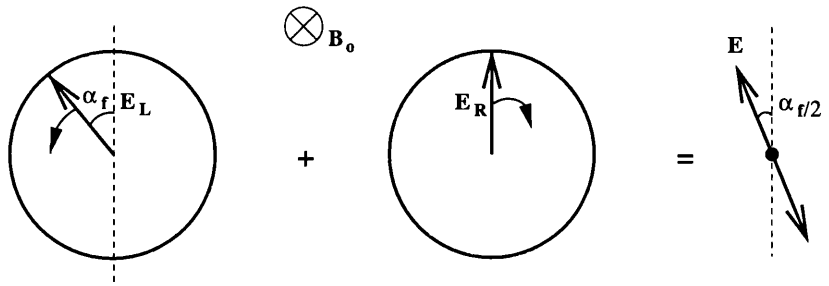

(b) After transversing the plasma, the L wave is retarded in phase relative to the R wave, and the plane of polarization is rotated.

Figure 3.5: The evolution of the plane of polarization in a refractive medium.

polarization can be written as the sum of a right-handed circularly polarized and left-handed circularly polarized wave, $\mathbf{E} = \mathbf{E_R} + \mathbf{E_L}$ where

$$\mathbf{E_R} = E_o(\widehat{\mathbf{e_x}} + i\widehat{\mathbf{e_y}})e^{i(\omega t)} \qquad \text{and} \qquad \mathbf{E_L} = E_o(\widehat{\mathbf{e_x}} - i\widehat{\mathbf{e_y}})e^{i(\omega t)}. \tag{3.33}$$

After propagating through the plasma along an optical path dz, this decomposition will then become

$$\mathbf{E_R} = E_o(\widehat{\mathbf{e_x}} + i\widehat{\mathbf{e_y}})e^{i(\omega t - k_R dz)} \qquad \text{and} \qquad \mathbf{E_L} = E_o(\widehat{\mathbf{e_x}} - i\widehat{\mathbf{e_y}})e^{i(\omega t - k_L dz)} \tag{3.34}$$

where $k_R = \frac{N_R c}{\omega}$ and $k_L = \frac{N_L c}{\omega}$. Recombining these two components gives the output polarization

$$\mathbf{E} = 2E_o e^{i[(\frac{N_R+N_L}{2})\frac{\omega}{c}dz]}\left[\cos\left(\frac{\alpha_f}{2}\right)\widehat{\mathbf{e_x}} + \sin\left(\frac{\alpha_f}{2}\right)\widehat{\mathbf{e_y}}\right] \tag{3.35}$$

where $\alpha_f = \int(N_L - N_R)\frac{\omega}{c}dz$ is the phase difference between the characteristic waves arising because of the difference in refractive index. The ratio of the electric field components is then given by

$$\kappa_{y,x} = \frac{E_y}{E_x} = \tan\left(\frac{\alpha_f}{2}\right). \tag{3.36}$$

Since N_L is greater than N_R, the phase velocity of the right-handed characteristic wave is greater than that of the left-handed, and thus the phase difference α_f is positive. The polarization of the wave after propagating a distance dz is still linear, but rotated by an angle $\frac{\alpha_f}{2}$ with respect to the initial polarization. This effect is known as Faraday rotation. Its magnitude, Ψ, is given by

$$\Psi = \frac{\alpha_f}{2} = \frac{1}{2}\int (N_L - N_R)\frac{\omega}{c} dz \tag{3.37}$$

which may be written as

$$\Psi = \frac{e}{2m_e c n_c}\int n_e \mathbf{B}\cdot\mathbf{dz} = 2.63\times10^{-13}\lambda^2 \int n_e |\mathbf{B_o}| \cos\theta dz. \tag{3.38}$$

The direction of rotation is in the same sense as the handedness of the faster characteristic wave, namely the right-handed circularly polarized wave. The Faraday rotation scales as the square of the wavelength, and is proportional to the line integral of the product of electron density and parallel component of the magnetic field.

Considering the case of wave propagation at a general angle θ to the magnetic field it is possible to evaluate the Faraday rotation angle by solving Equation 3.23. Provided that $\frac{\omega_{ce}}{\omega\cos\theta} \ll 1$ (and $1 - \frac{\omega_p}{\omega}$ is not too small), this may be approximated to lowest order as

$$\frac{E_x}{E_y} \simeq \pm i. \tag{3.39}$$

Therefore for weak magnetic fields, at all angles not too close to perpendicular, the characteristic polarizations are circular, as illustrated in Figure 3.6.

3.2.4 Birefringence

The theory of birefringence in an inhomogeneous magnetised plasma is similar to the theory of Faraday rotation. Birefringence, also called the Cotton-Mouton effect, (see Clarke and Grainger, 1971), arises from the anisotropy created by the magnetic field, and affects waves propagating in a direction perpendicular to the magnetic field. The characteristic waves are no longer approximately circularly polarized as is the case for propagation parallel to the magnetic field. A linearly polarized incident wave will generally acquire some degree of ellipticity.

Consider a plane electromagnetic wave propagating through a plasma in a direction perpendicular to the magnetic field as illustrated in Figure 3.7. This is a principal direction for which the characteristic waves are linearly polarized, with the electric field vector of the wave either parallel or orthogonal to the magnetic field. If the initial plane of polarization is

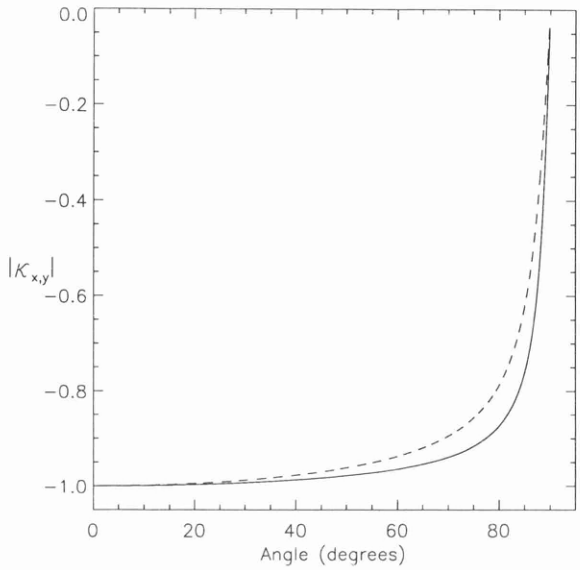

Figure 3.6: Transverse electric field ratio, $\kappa_{x,y}$, as a function of θ. The dashed line refers to the case where B = 2.1T and $n_e = 1{\times}10^{20}\mathrm{m}^{-3}$, whereas the solid line has B = 1.2T and $n_e = 1{\times}10^{19}\mathrm{m}^{-3}$.

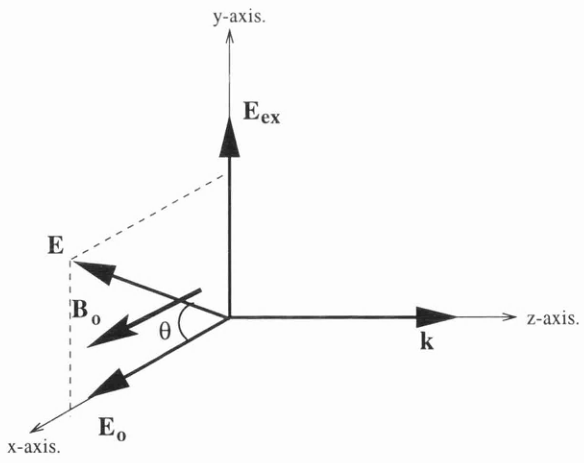

Figure 3.7: The two characteristic wave components for a wave propagating in a direction perpendicular to the magnetic field.

at an angle θ to the magnetic field direction, then the electromagnetic wave can be resolved into the electric field components corresponding to the ordinary and extraordinary principal characteristic waves, (see Muir, 1983), $\mathbf{E} = \hat{\mathbf{x}}E_o + \hat{\mathbf{y}}E_{ex}$ where

$$E_o = A_x e^{i(\omega t)} \qquad \text{and} \qquad E_{ex} = A_y e^{i(\omega t)} \tag{3.40}$$

with amplitudes

$$A_x = E\cos\theta \qquad \text{and} \qquad A_y = E\sin\theta \tag{3.41}$$

where $\mathbf{E}$ is the initial electric field vector, i.e. at $z = 0$. After propagating through the plasma, along a path dz, a phase difference between the characteristic waves arises due to the difference in refractive index. The electric field components are therefore

$$E_o = A_x e^{i(\omega t - k_o dz)} \qquad \text{and} \qquad E_{ex} = A_y e^{i(\omega t - k_{ex} dz)} \tag{3.42}$$

where $k_o = \frac{N_o c}{\omega}$ and $k_{ex} = \frac{N_{ex} c}{\omega}$. Eliminating ωt from the two equations above yields an equation describing the emergent electric field, (see Born and Wolf, 1964),

$$\left(\frac{E_o}{A_x}\right)^2 + \left(\frac{E_{ex}}{A_y}\right)^2 - \frac{2E_o E_{ex}\cos\alpha_b}{A_y A_x} = \sin^2\alpha_b \tag{3.43}$$

where $\alpha_b = \int (N_o - N_{ex})\frac{\omega}{c}\, dz$ is the phase difference between the characteristic waves. This equation describes an ellipse with the azimuthal angle, ψ, of the major axis given by, see Appendix(1),

$$\tan 2\psi = \tan 2\theta \cos\alpha_b \tag{3.44}$$

and with the ellipticity acquired described by

$$\epsilon = \tan\chi \tag{3.45}$$

where χ lies in range $(-\frac{\pi}{4} \geq \chi \leq \frac{\pi}{4})$ and is defined by

$$\sin 2\chi = \sin 2\theta \sin\alpha_b. \tag{3.46}$$

Considering the case where the phase difference, α_b, is small such that $\cos\alpha_b \cong 1$, the major axis of the resultant ellipse describing the emergent polarization will be parallel to the initial plane of polarization. However if α_b is not small, then only by having the initial plane of polarization at an angle of 0° or 90° to the external magnetic field will this also occur. If $\theta =$ 0° or 90°, from Equations 3.45 and 3.46, the ellipticity of the emergent electromagnetic wave is zero, whereas it has a maximum value when $\theta = 45°$. It can be inferred that the optimum input polarization for minimising the ellipticity is perpendicular or parallel to the external magnetic field, i.e. a characteristic wave.

The phase difference between the two characteristic waves, α_b, can also be expressed in terms of the plasma parameters by substituting the refractive indices for the ordinary and extraordinary waves, Equation 3.28

$$\alpha_b = \int (N_o - N_{ex}) \frac{\omega}{c} dz = \frac{\omega}{c} \int \frac{\omega_p^2 \omega_{ce}}{\omega^3} dz \tag{3.47}$$

$$= \frac{e^4 \lambda^3}{16\pi^3 \epsilon_o c^3 m_e^2} \int n_e \mathrm{B}_\perp^2 dz. \tag{3.48}$$

The ellipticity due to birefringent properties of the plasma are dependent on the cube of the wavelength, and scales with the line integral of the product of the electron density and the square of the magnetic field perpendicular to the direction of propagation.

3.3 Theory of Faraday Rotation and Birefringence

The coupling of Faraday rotation and Birefringence theories was first examined by Heald and Wharton (1965) for the particular case of wave propagation in a homogeneous plasma with a helical magnetic field. The more general case of wave propagation in an inhomogeneous plasma with a spatially varying magnetic field was however considered by Marco and Segre (1972). This work was further developed by Craig (1976) and Segre (1978). The work by Marco and Segre (1972) is reviewed assuming the WKB approximation and a high frequency regime.

The state of polarization of a plane electromagnetic wave propagating in a inhomogeneous plasma can be described by two angles ψ and χ. Every state of polarization can be uniquely defined by these two angles. It is convenient to refer to the Poincaré sphere, (see Born and Wolf, 1964), when discussing the evolution of the state of polarization. This is a sphere of unit radius where each state polarization is represented by a point P on the surface whose longitude and latitude are 2ψ and 2χ respectively, as shown in Figure 3.8. The Cartesian coordinates of the point P, also called the Stokes parameters, (see Clarke and Grainger, 1971), determine the polarization vector $\mathbf{s}$

$$\mathbf{s} = \begin{pmatrix} \cos 2\chi \cos 2\psi \\ \cos 2\chi \sin 2\psi \\ \sin 2\chi \end{pmatrix}. \tag{3.49}$$

Any polarized wave can be resolved into two orthogonally polarized waves. Consider two states of polarizations (ψ_1, χ_1), (ψ_2, χ_2) which are orthogonal only if the following conditions are met

$$\psi_2 = \psi_1 + \frac{\pi}{2}, \qquad \chi_2 = -\chi_1. \tag{3.50}$$

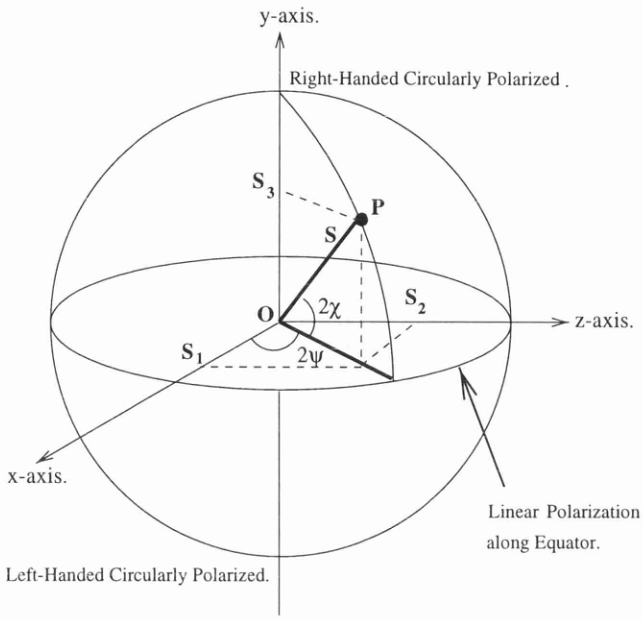

Figure 3.8: The Poincaré sphere.

These are represented by two diametrically opposite points on the Poincaré sphere.

The evolution in the polarization state of a plane electromagnetic wave propagating along the z direction in a plasma at an angle θ to the external magnetic field, see Figure 3.9, can be represented on the Poincaré sphere by a rotation of the point P, which represents the wave's initial polarization state, about an axis which joins the diametrically opposite points representing the orthogonally polarized characteristic waves. The angle of rotation is the phase difference between the two characteristic waves arising after propagating through the plasma. This change in the polarization state is described by the differential equation, (see Marco and Segre, 1972 and Segre, 1978),

$$\frac{d\mathbf{s}}{dz} = \mathbf{\Omega}(z) \times \mathbf{s}(z) \tag{3.51}$$

where

$$\mathbf{\Omega} = \frac{\omega}{c}(N_s - N_f)\,\mathbf{s_{cf}} \tag{3.52}$$

is the vector which describes the rotation of the Poincaré sphere, N_s and N_f are the refractive indices of the slow and fast characteristic waves respectively and $\mathbf{s_{cf}}$ is the direction of the vector which describes the fast characteristic wave. Equation 3.51 has an approximate

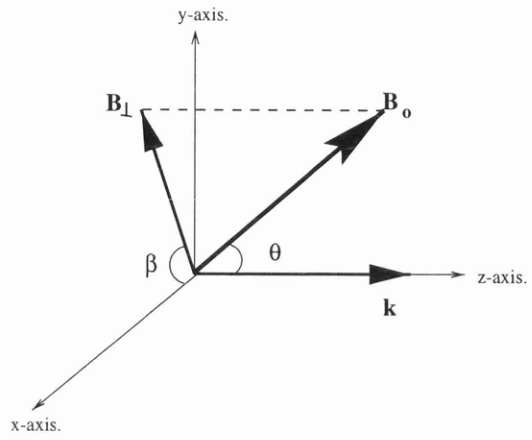

Figure 3.9: Coordinate system for an arbitrary wave propagating in a magnetised plasma.

solution when $\int|\mathbf{\Omega}|dz \ll 1$, (see Kamke, 1959), yielding

$$\mathbf{s}(z) = \mathbf{s_o} - \mathbf{s_o} \times \int_0^z \mathbf{\Omega}(z')dz' \tag{3.53}$$

where $\mathbf{s_o}$ is the initial polarization.

Referring to the geometry shown in Figure 3.9, the polarization of the fast characteristic wave is

$$\tan\chi_f = [(1+F^2)^{\frac{1}{2}} - 1]/F \tag{3.54}$$

where F is defined in Equation 3.19 and

$$\psi_f = -\beta. \tag{3.55}$$

Thus, from Equations 3.49, 3.54 and 3.55 it is possible to infer

$$\mathbf{s_{cf}} = \begin{cases} \cos 2\beta(1+F^2)^{-\frac{1}{2}} \\ -\sin 2\beta(1+F^2)^{-\frac{1}{2}} \\ F(1+F^2)^{-\frac{1}{2}} \end{cases}. \tag{3.56}$$

The difference of the refractive indices $N_s - N_f$ is obtained from Appleton's Equation, in the high frequency limit

$$N_s - N_f = \frac{\omega_p^2\omega_c^2}{2\omega^4}\sin^2\theta\frac{(1+F^2)^{\frac{1}{2}}}{(1-\frac{\omega_c^2}{\omega^2})}. \tag{3.57}$$

Introducing Equations 3.56 – 3.57 into Equation 3.52 yields

$$\mathbf{\Omega}(z) \equiv \begin{pmatrix} \Omega_1 \\ \Omega_2 \\ \Omega_3 \end{pmatrix} = \frac{\omega}{2c}\frac{\omega_p^2}{\omega^2}\frac{\omega_c^2}{\omega^2}\frac{\sin^2\theta}{(1-\frac{\omega_c^2}{\omega^2})}\begin{pmatrix} \cos 2\beta \\ -\sin 2\beta \\ \frac{2\omega}{\omega_c}\frac{\cos\theta}{\sin^2\theta} \end{pmatrix}. \tag{3.58}$$

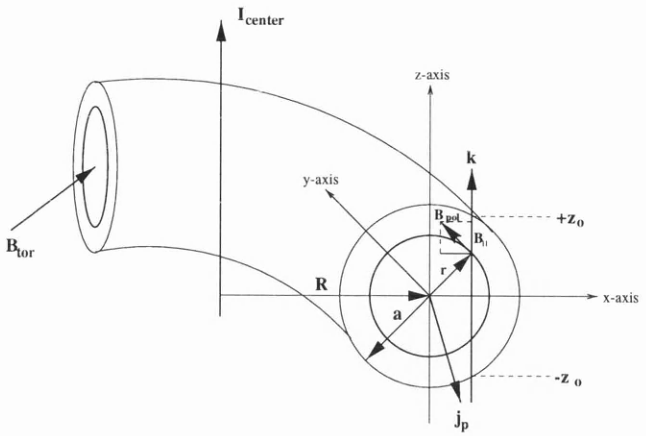

Figure 3.10: Coordinate system for plasma in a tokamak.

The solution of the propagation equation is therefore given by Equation 3.53, i.e.

$$\mathbf{s}(z) \equiv \begin{pmatrix} s_1 \\ s_2 \\ s_3 \end{pmatrix} = \begin{pmatrix} s_{10} + s_{30}\int_0^z \Omega_2(z')dz' - s_{20}\int_0^z \Omega_3(z')dz' \\ s_{20} + s_{10}\int_0^z \Omega_3(z')dz' - s_{30}\int_0^z \Omega_1(z')dz' \\ s_{30} + s_{20}\int_0^z \Omega_1(z')dz' - s_{10}\int_0^z \Omega_2(z')dz' \end{pmatrix} \tag{3.59}$$

provided

$$\int_0^z |\mathbf{\Omega}|dz' \ll 1. \tag{3.60}$$

3.3.1 Analytical Solution to the Propagation Equation

Consider a plane electromagnetic wave propagating along the z direction, parallel to the axis of symmetry of the torus, see Figure 3.10. Since $B_{tor} \gg B_{pol}$ in most tokamaks, to a good first approximation $\mathbf{B_o}$ is purely toroidal, nevertheless B_{pol} will be retained to first order.

Introducing simple parabolic models of the expected electron density $n_e(r)$ and the toroidal current density $j_p(r)$

$$\begin{aligned} n_e(r) &= n_o\left[1 - \left(\frac{r}{a}\right)^2\right] \\ j_p(r) &= j_o\left[1 - \left(\frac{r}{a}\right)^2\right] \end{aligned} \tag{3.61}$$

where n_o and j_o are respectively the electron density and current density at the center of the tokamak (i.e. $r = 0$) and "a" the radius of the plasma cross-section into Equation 3.58. The toroidal magnetic field is given by

$$B_{tor} = \frac{\mu_o I_{center}}{2\pi(R + x)} \tag{3.62}$$

where x is the distance from the plasma center to the beam chord, R the major radius of the plasma center and I_{center} the current flowing through the center of the tokamak inducing B_{tor}. The poloidal magnetic field is generated around the minor axis by a current caused to flow through the plasma by transformer action and can be determined from Ampere's Law (Equation 3.10). Taking account of the fact that since n, $\mathbf{B_o}$ and θ are even functions of z and β is odd, then $\Omega_1(z)$ and $\Omega_3(z)$ are even and $\Omega_2(z)$ is odd, and so

$$\int_{-z_o}^{z_o} \Omega_2(z)dz = 0 \tag{3.63}$$

where the integral is carried out over the entire chord of the plasma. Therefore for the general case of an initially elliptically polarized beam traveling through the plasma we have

$$s(z_f) = s_{of} \begin{pmatrix} \cos 2\chi_i \cos 2\psi_i - \cos 2\chi_i \sin 2\psi_i \int_{-z_o}^{z_o} \Omega_3(z')dz \\ \cos 2\chi_i \sin 2\psi_i + \cos 2\chi_i \cos 2\psi_i \int_{-z_o}^{z_o} \Omega_3(z')dz - \sin 2\psi_i \int_{-z_o}^{z_o} \Omega_1(z')dz \\ \sin 2\chi_i + \cos 2\chi_i \sin 2\psi_i \int_{-z_o}^{z_o} \Omega_1(z')dz \end{pmatrix} \tag{3.64}$$

where the subscripts f and i correspond to the emergent and initial polarization respectively. If the initial state of polarization is linear and aligned with either the x- or y-axis then solving Equation 3.64 the emergent state of polarization is again linearly polarized, i.e. ($s_{3f} = 0$), but the direction of polarization is rotated by a small Faraday rotation angle, $\Psi = \frac{s_{2f}}{2}$. The net effect of transversing the plasma in a characteristic mode with the initial electric vector aligned either parallel or perpendicular to the toroidal field is a pure Faraday rotation without a change of ellipticity. If the initial polarization vector is aligned arbitrarily to the toroidal magnetic field then birefringence causing a change in ellipticity of the polarization vector must be considered when analysing the emergent Faraday angle.

Evaluating Equation 3.64 with a range of typical COMPASS-D operating parameters as illustrated Figure 3.11, indicates the expected maximum Faraday rotation to be approximately 5°. Figure 3.12 shows the effect of birefringence on the ellipticity of the emergent wave as a function of the plasma minor radius.

The analysis carried out so far assumes that the condition in Equation 3.60 is fulfilled and that Equation 3.53 is a valid approximation to the propagation equation, i.e. Equation 3.51. Since the changes in polarization through the plasma are quite small in the case of the COMPASS-D operating regime, the series solution provides a very good approximation to the expected Faraday rotation angle and therefore a full numerical solution is unnecessary.

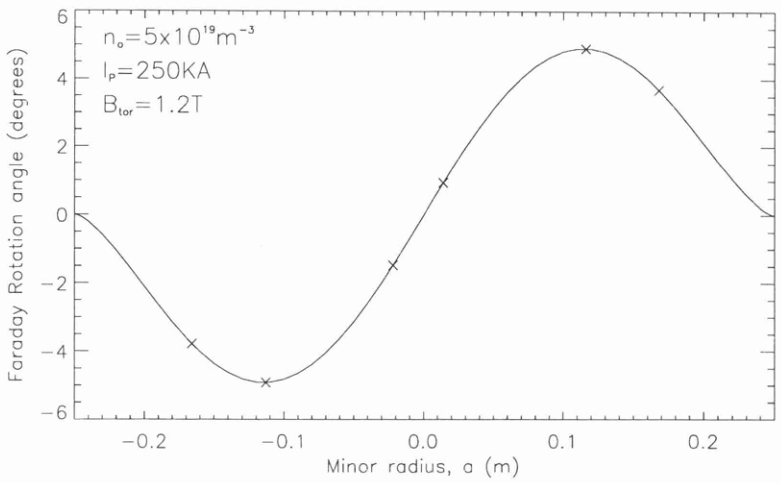

Figure 3.11: Expected Faraday rotation angle for a typical discharge on COMPASS-D. The crosses correspond to the position of the six chords used for polarimetry.

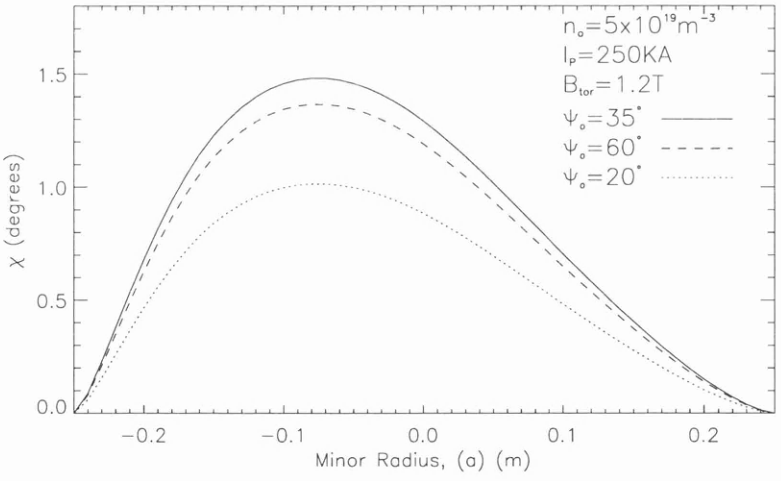

Figure 3.12: The effect of birefringence on linearly polarized waves as a function of the minor radius for three distinct input polarizations.

3.3.2 Physical Interpretation

The Faraday rotation effect offers a means to measure the poloidal magnetic field if the probing beam is injected perpendicular to the externally applied toroidal magnetic field. From Equation 3.38 it is possible to deduce that the poloidal magnetic field induced by the plasma current is solely responsible for the presence of a magnetic field component parallel to the propagation direction. Re-writing this in terms of the parameters in Figure 3.10 gives

$$\Psi = 2.63 \times 10^{-13} \lambda^2 \int n_e(z) \mathrm{B}_{||}(z) dz. \tag{3.65}$$

In order to determine the poloidal magnetic field it is necessary to simultaneously measure the electron density, n_e.

The most widely adopted method for determining the electron density is by interferometry, (see Veron, 1979). The application of interferometry is based upon the interaction between the electrons and an electromagnetic wave, passing through the plasma. This interaction can be expressed, through a refractive index N, and in the regime of weak interaction its deviation from unity is linearly dependent on the electron density. In an interferometric experiment, a probing beam passes through the tokamak vessel and its phase is determined by a heterodyne technique, (see Hutchinson, 1987), upon exiting the vessel. Once a plasma is created in the vessel the refractive index along the beam path is changed and therefore so is the optical path length. The resultant phase shift of the emergent beam can be monitored as a function of time and used to calculate the electron density, integrated along the beam path. According to Veron (1979) the phase shift is given by,

$$\Phi = \frac{\omega}{2cn_c} \int n_e(z) dz = 2.82 \times 10^{-15} \lambda \int n_e(z) dz. \tag{3.66}$$

A number of parallel lines of sight, usually between 5 and 20, can be utilised such that together they give a full-line integrated profile of the electron density. This is essentially a projection of the electron density profile in a single direction. The individual beams can be labelled by means of an impact parameter, which is defined as the shortest distance between the line of sight and the center of the cross-section.

By passing multiple parallel chords through the plasma cross-section the Faraday rotation and interferometry phase profile can be determined simultaneously. Knowing the electron density, the Faraday equation can be inverted to give the poloidal magnetic field and, by definition, the plasma current density. Assuming the electron density profile is known, an Abel inversion, (see Marco and Segre, 1972), or equivalent numerical inversion techniques are required to reconstruct a two-dimensional profile of the poloidal field, consult Section 3.3.3.

These mathematical procedures use assumptions regarding the plasma shape which along with the necessity of many chords through the plasma are the main disadvantages of the Faraday rotation technique.

Finally in the more general case of elliptical polarization, the rotation of the polarization angle will also be a function of the the linear birefringence, defined in Equation 3.48. This defines the change, caused by the plasma, in the ellipticity of the emergent beam. The quantity defined as $B_\perp$ is the component of the magnetic field perpendicular to the beam. Since in a tokamak the toroidal magnetic field, B_{tor}, is by far the largest component of $B_\perp$, the birefringence depends in practice on the toroidal field,

$$\alpha_b = 1.26 \times 10^{-18} \lambda^3 \int n_e(z) B_{tor}^2(z) dz. \tag{3.67}$$

3.3.3 The Abel Inversion

Interferometry and polarimetry share with many other diagnostic techniques the ability to measure the average value of some property along a chord through the plasma. A recurrent problem is the deduction of local values of the property under consideration from the available chordal measurements. However, most plasmas are invariably cylindrically symmetric. Using this fact it is possible to deduce the radial distribution from the chordal measurements using the known properties of the Abel inversion.

Consider the case of a plasma with cylindrical symmetry carrying a toroidal electrical current. The induced poloidal magnetic field lines also have cylindrical symmetry. Superimposing a toroidal magnetic field results in field lines that are helical. Under these circumstances a wave directed along the torus will not in general travel along a principal direction. However, Faraday rotation will occur due to the component of the field parallel to the wave path. A wave propagating in the poloidal plane, as illustrated in Figure 3.13, allows the Faraday rotation, Equation 3.65, to be expressed in terms of the impact parameter x_o,

$$\Psi(x_o) = 2A\lambda^2 \int_{x_o}^{a} n_e(r) B_{pol}(r) (r^2 - x_o^2)^{-\frac{1}{2}} dr \tag{3.68}$$

where B_{pol} is the poloidal field and $A = 2.63 \times 10^{-13}$. This assumes that the wave is not refracted by the plasma. If refraction is important, the line integral must be taken along the wave path. The Faraday rotation equation is of the form of an Abel integral, specifically of the Volterra type,

$$F(x_o) = 2 \int_{x_o}^{a} f(r) (r^2 - x_o^2)^{-\frac{1}{2}} dr \tag{3.69}$$

with a solution

$$f(r) = -\frac{1}{\pi} \int_r^a \frac{dF}{dx_o} (x_o^2 - r^2)^{-\frac{1}{2}} dx_o. \tag{3.70}$$

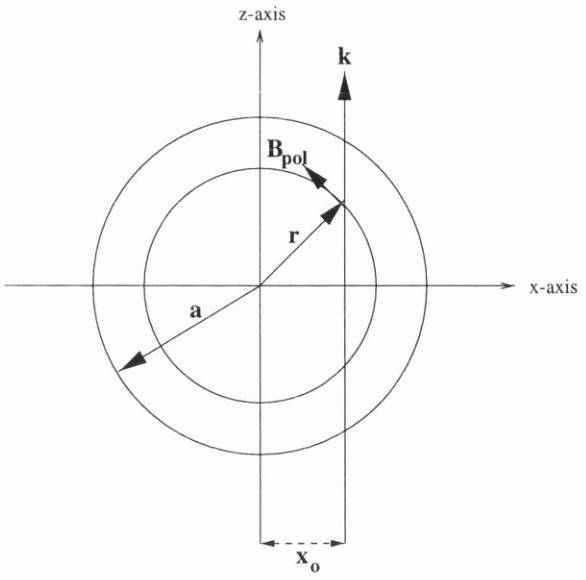

Figure 3.13: Chordal measurement in the poloidal plane of a tokamak.

It is possible to obtain the radial profile of f from measurements of chordal integral F.

Assuming cylindrical geometry and from Equation 3.68 it is possible to derive the following equation for the poloidal magnetic field

$$\mathrm{B}_{pol}(r) = -\frac{r}{\pi A \lambda^2 n_e(r)} \int_r^a \frac{d}{dx_o} \left(\frac{\Psi(x_o)}{x_o} \right) (x_o^2 - r^2)^{-\frac{1}{2}} dx_o \tag{3.71}$$

with $n_e(r)$ the spatial electron density distribution determined from a separate Abel inversion. Since measurements of Ψ are obtained only at a finite number of x_o values, some kind of interpolation scheme is required in order to perform the required integral. A small number of chord measurements, six chords in the case of COMPASS-D, will give only limited information about $\mathrm{B}_{pol}(r)$. If an effectively continuous $\mathrm{B}_{pol}(r)$ is deduced using interpolation, much of the detail of B_{pol} will depend on the assumptions inherent in the interpolation scheme.

The solution of Equation 3.71 is dependent on the spatial derivative of Ψ. Therefore, experimentally measurements of the Faraday rotation must be sufficiently precise for the derivative to be accurately determined, since the Abel inversion is sensitive to errors in Ψ. Deduction of $\frac{d\Psi}{dx_o}$ requires taking the difference ($\Delta\Psi$) of adjacent Ψ measurements. If these differences are such that $\Delta\Psi$ is considerably smaller than Ψ, as will usually be the case if Ψ is measured at a sufficient number of x_o values, then the fractional error $\Delta\Psi$ is much greater than that of Ψ. Fortunately this effect is compensated by the integration occurring which "smoothes out" some of the errors generated by the differentiation. However, it is beyond the

scope of this thesis to discuss or review the numerous and complicated numerical techniques used to invert chord integrated profiles.

3.4 Summary

The first sections of this chapter have been devoted to the derivation of the Appleton-Hartree equation and the associated eigenstates. Simplified expressions have been derived for the polarization eigenstates in the limiting cases of propagation parallel or perpendicular to the external magnetic field, yielding circularly and linearly polarized eigenwaves respectively. A numerical calculation, using COMPASS-D relevant parameter values, has been performed to demonstrate the transition behavior between the two limits, see Figure 3.6. This calculation showed that the eigenwave polarizations remained relatively close to circular for angles between $\mathbf{B}$ and $\mathbf{k}$ up to approximately 70°.

Next the theory has been simplified by restricting it to the domain where ω is much larger than both ω_p and ω_{ce}, a restriction that usually holds for interferometry and polarimetry. In this regime the eigenwaves are purely circular when considering propagation parallel to the external magnetic field. The plasma infiuence on the wave propagation may be described by three parameters: α_f, the ratio of the electric field components of the emergent wave in two orthogonal directions; ΔN, the difference between the refractive indices of the two modes and α_b the birefringence introduced into the propagating wave due to the toroidal magnetic field. The parameter α_f effectively represents the desired Faraday rotation. This quantity is related to a line-integrated measurement of the electron density and the product of electron density with the parallel magnetic field component.

In a subsequent section the Stokes matrix calculus technique used by Marco and Segre (1972) is presented to calculate the influence of the plasma on a beam. An analytical solution to the wave propagation equation is derived, incorporating parabolic models for the electron and toroidal current density. Using typical COMPASS-D operating parameters the expected Faraday rotation angles for each of the six chords is determined. A further calculation illustrating the ellipticity introduced into the propagating beam due to birefringence is also presented. Finally a few words are devoted to inversion techniques that allow the determination of local information from a set of line-integrated measurements.

Chapter 4

FIR Polarimetry on the COMPASS-D Tokamak

Plasma birefringence, resulting from the presence of a magnetic field component along the propagation direction of the beam, causes the linear or elliptical polarization of an incident probing wave to rotate. The rotation angle may be determined via a measurement of the polarization state of the emerging wave. The determination of the Faraday rotation may be achieved either by an amplitude or phase measurement. A conventional but robust polarization technique, the amplitude method, measures the relative intensity of two orthogonal linear waves polarized separately after passage through, or refiection from, a polarizer. Alternatively, phase sensitive technique utilising a single detector have been developed, where the incident polarization is modulated to generate an amplitude-modulation on the detected signal, from which the Faraday rotation can be derived. Both methods are examined and their suitability for commissioning onto COMPASS-D is discussed.

4.1 Determination of Faraday Rotation by a Phase Measurement

The phase measurement approach relies on a far-infrared beam with a continuously rotating elliptical polarization to probe the plasma, first proposed by Rice (1992). Measurement of the interferometric phase shift and the Faraday rotation is made with the same array of detectors. This circumvents the use of a second array of detectors, necessary in the amplitude method, or the need to use reproducible shots to measure the electron and current density alternatively. The rotating elliptical polarization method transforms the Faraday rotation measurement into a phase measurement which, to first order, is independent of variations in

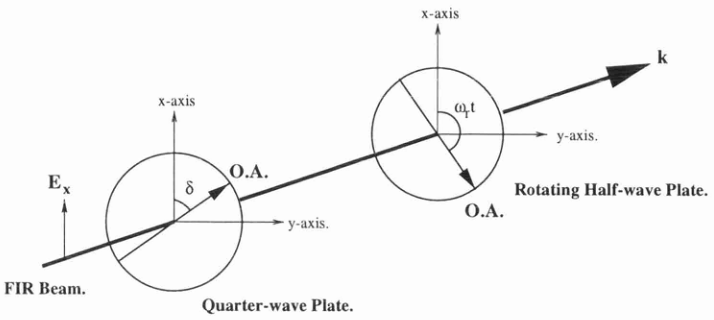

Figure 4.1: Arrangement of Quartz Wave Plates used to produce an elliptically polarized beam.

the signal amplitude.

4.1.1 Optical Arrangement

The method has a conventional Mach Zender geometry with two laser beams of differing frequency mixed to produce an intermediate frequency (I.F.) signal thereby allowing heterodyne detection. A rotating polarization ellipse is produced by the combination of a quarter-wave plate and a rotating half-wave plate. The quarter-wave plate introduces a degree of ellipticity into the initially linearly polarized beam and the rapidly rotating half-wave plate rotates the incident polarization ellipse at four times the angular frequency of the plate. The ellipticity is required so that the detected signal amplitude does not go to zero as the ellipse rotates.

The angle δ is defined as the angle between the optical axis and the vertical in the quarter-wave plate and ω_rt is the angle of rotation of the half-wave plate, see Figure 4.1. The resultant beam can be expressed in terms of Jones' matrices by

$$\mathbf{E} = \begin{bmatrix} \cos 2\omega_r t & \sin 2\omega_r t \\ \sin 2\omega_r t & -\cos 2\omega_r t \end{bmatrix} \begin{bmatrix} \cos^2\delta + i\sin^2\delta & \cos\delta\sin\delta(1-i) \\ \cos\delta\sin\delta(1-i) & \sin^2\delta + i\cos^2\delta \end{bmatrix} \begin{bmatrix} 1 \\ 0 \end{bmatrix} E_\circ e^{i\omega t}. \quad (4.1)$$

This can be represented as

$$\mathbf{E} = \begin{bmatrix} \frac{E_\circ}{\sqrt{2}}(1+\cos 2\delta\cos(4\omega_r t - 2\delta))^{\frac{1}{2}}\cos(\omega t + \chi_{ref,x}) \\ \frac{E_\circ}{\sqrt{2}}(1-\cos 2\delta\cos(4\omega_r t - 2\delta))^{\frac{1}{2}}\cos(\omega t + \chi_{ref,y}) \end{bmatrix} \quad (4.2)$$

where

$$\chi_{ref,x} = \tan^{-1}(\tan\delta\tan(2\omega_r t - \delta)) \quad (4.3)$$

$$\chi_{ref,y} = \tan^{-1}\left(\frac{\tan\delta}{\tan(2\omega_r t - \delta)}\right). \quad (4.4)$$

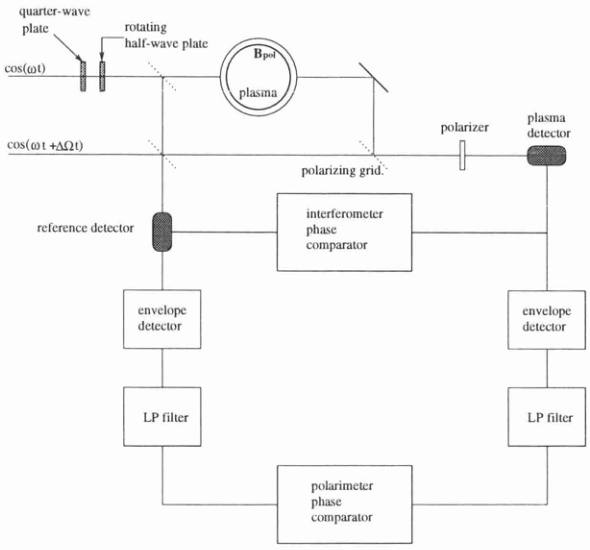

Figure 4.2: Illustration of the rotating ellipse polarimetry technique.

The magnitude of the beam is modulated by the rotating plate and the amount of modulation is determined by δ the fixed angle of the first plate. The modulation varies from zero when $\delta = \frac{\pi}{4}$ (circular polarization) to 100% when $\delta = 0°$ (linear polarization). It is not desirable to have complete modulation since the goal is carry out interferometry and polarimetry measurements simultaneously. If $\mathbf{E}$ is allowed to go to zero, then the interferometer will lose track of the phase. Typically a modulation of 50% is used with $\delta = 35°$.

This rotating elliptically polarized beam is then split in two, one part going through the plasma the other onto a reference detector, shown schematically in Figure 4.2. Both beams are also individually superimposed with a beam linearly polarized along the x-direction with an offset frequency $\omega + \Delta\Omega$

$$\mathbf{E} = \begin{bmatrix} E\cos(\omega t + \Delta\Omega t) \\ 0 \end{bmatrix} \tag{4.5}$$

and passed through a horizontal polarizer just before the detectors. This is the standard configuration for heterodyne detection.

The resultant signal on the reference detector is

$$\begin{aligned} S_{ref} =< & \frac{E_\circ^2}{2}(1 + \cos 2\delta \cos(4\omega_r t - 2\delta))\cos^2(\omega t + \chi_{ref,x}) + E^2\cos^2(\omega t + \Delta\Omega t) \\ & + \sqrt{2}E_\circ E(1 + \cos 2\delta\cos(4\omega_r t - 2\delta))^{\frac{1}{2}}\cos(\omega t + \chi_{ref,x})cos(\omega t + \Delta\Omega t) > . \end{aligned} \tag{4.6}$$

A bandpass filter at the difference frequency $\Delta\Omega$ will eliminate all D.C. and high frequency

terms, so the first and third terms above are zero. Also since $< \cos\omega t > = 0$ and $< \cos^2 \omega t >= \frac{1}{2}$,

$$S_{ref} = \frac{E_o E}{\sqrt{2}}(1 + \cos 2\delta \cos(4\omega_r t - 2\delta))^{\frac{1}{2}} \cos(\Delta\Omega t - \chi_{ref,x}). \tag{4.7}$$

This is an amplitude modulated signal, where the carrier signal $\cos(\Delta\Omega t - \chi_{ref,x})$ is modulated by the lower frequency $(1 + \cos 2\delta \cos(4\omega_r t - 2\delta))^{\frac{1}{2}}$ term.

The effect of the plasma, neglecting any additional ellipticity introduced by plasma birefringence, can be introduced into the second beam by adding a phase shift, Φ, in the rotating beam due to the plasma density, see Equation 3.66, and an additional rotation, the Faraday rotation Ψ see Equation 3.65, in the polarization ellipse due to the magnetic field. This yields

$$\mathbf{E} = \begin{bmatrix} \frac{E_o}{\sqrt{2}}(1 + \cos 2\delta \cos(4\omega_r t - 2\delta + 2\Psi))^{\frac{1}{2}} \cos(\Delta\Omega t + \Phi + \chi_{plasma,x}) \\ \frac{E_o}{\sqrt{2}}(1 - \cos 2\delta \cos(4\omega_r t - 2\delta + 2\Psi))^{\frac{1}{2}} \cos(\Delta\Omega t + \Phi + \chi_{plasma,y}) \end{bmatrix} \tag{4.8}$$

where

$$\chi_{plasma,x} = \tan^{-1}(\tan\delta \tan(2\omega_r - \delta + \Psi)) \tag{4.9}$$

$$\chi_{plasma,y} = \tan^{-1}\left(\frac{\tan\delta}{\tan(2\omega_r - \delta + \Psi)}\right). \tag{4.10}$$

This beam is also superimposed with the linearly polarized beam and passed through a horizontal polarizer. Following the same procedure as before and neglecting all D.C. and high frequency terms yields,

$$S_{plasma} = \frac{E_o E}{\sqrt{2}}(1 + \cos 2\delta \cos(4\omega_r t - 2\delta + 2\Psi))^{\frac{1}{2}} \cos(\Delta\Omega t - \Phi - \chi_{plasma,x}). \tag{4.11}$$

The plasma signal is then split to allow separate electronics to process the density phase shift and the polarimeter phase shift independently. The density can be determined by using a limiting amplifier to eliminate the modulation, followed by a zero crossing detector to measure the difference in phase Φ between the reference and plasma signal. The polarimeter data can be extracted by demodulating the signals. This is performed by passing the signals through a diode detector which is biased externally, resulting in signals proportional to

$$S_{ref} = A(1 + \cos 2\delta \cos(4\omega_r t - 2\delta))^{\frac{1}{2}} \tag{4.12}$$

$$S_{plasma} = A(1 + \cos 2\delta \cos(4\omega_r t + 2\Psi - 2\delta))^{\frac{1}{2}}. \tag{4.13}$$

The modulation of the amplitude signal, determined by the angle δ of the quarter-wave plate, is always less than one (usually about 0.5) so the square root can be expanded, giving

$$S_{ref} = A\left(1 + \frac{\cos 2\delta}{2} \cos(4\omega_r t - 2\delta) - \frac{\cos^2 2\delta}{8} \cos^2(4\omega_r t - 2\delta) + \ldots\right) \tag{4.14}$$

$$S_{plasma} = A\left(1 + \frac{\cos 2\delta}{2}\cos(4\omega_r t + 2\Psi - 2\delta) - \frac{\cos^2 2\delta}{8}\cos^2(4\omega_r t + 2\Psi - 2\delta) + \ldots\right). \quad (4.15)$$

These signals are then band-pass filtered about the frequency $4\omega_r t$ with a 1/e half-bandwidth to eliminate all higher harmonics of order $4\omega_r$, leaving

$$S_{ref} = A\left(\frac{\cos 2\delta}{2}\cos(4\omega_r t - 2\delta)\right) \quad (4.16)$$

$$S_{plasma} = A\left(\frac{\cos 2\delta}{2}\cos(4\omega_r t + 2\Psi - 2\delta)\right). \quad (4.17)$$

As with the interferometer, the Faraday rotation Ψ can be extracted by a zero-crossing technique.

4.1.2 Simulation of the Polarimetric Measurement

Due to the uniqueness of the proposed polarimetric technique it is necessary to ascertain the absolute phase resolution of the polarimeter and any factors that may influence it. Certain design features determine the absolute phase resolution of the polarimeter, these are:

- The degree of modulation introduced by the quarter-wave plate,
- The filtering method used to obtain the modulation envelope,
- The modulation frequency.

The temporal resolution of the polarimeter is limited by the rotation speed of the half-wave plate which rotates the polarization of the probing plasma beam. The maximum modulation frequency (which is four times the mechanical rotation frequency of the half-wave plate) is 6.7kHz for COMPASS-D. This is a limit of the air bearing which houses the half-wave plate. The maximum temporal resolution is therefore 0.15ms.

The expected reference and plasma signals at each detector were simulated numerically in order to ascertain the expected polarimetric precision at an intermediate frequency (I.F.) of 1MHz, the operating regime for the COMPASS-D interferometer, and at several half-wave plate rotation frequencies of 0.5kHz, 1kHz and 1.67kHz. The signals were polluted with a certain percentage of normally distributed noise, (see Park and Miller, 1988), (uncorrelated on either the reference or plasma detector). Both signals were then rectified and filtered in order to simulate the expected electronics setup. Four different filters were considered; Butterworth, Exponential, Bessel and an Ideal filter. The Butterworth filter operating characteristics closely match the intended electronics setup and was thus implemented in the analysis routine. The signals were band-pass filtered at $4\omega_r$ with a 1/e bandwidth, i.e. for a half-wave plate

rotation frequency of 1kHz this corresponded to a band-pass filter centered at 4kHz with a 1.2kHz bandwidth. The Faraday rotation angle was determined by detecting the zero crossings of the final signals by a simple cross-correlation routine.

The core of the program executed 10 cycles with loops producing 1000 independent simulated Faraday measurements, 10^4 values being generated overall, for each of the three modulation frequencies and the four distinct values of δ. The results from each loop were analysed to provide determinations of the Faraday rotation Ψ, and the variance of the distribution from which the standard deviation of a single measurement was obtained. Skewness and Kurtosis coefficients of the distribution were calculated, (see Wall, 1979), to determine if the underlying distribution was normal. By performing the exercise with 10 cycles of 1000 simulations each rather the 10^4 values from a single run, a standard error was calculated from the internal behavior for each of the investigated parameters. Finally, in order to check whether the conclusions might depend on the size of the data samples, the 10^4 simulated values were also generated with combinations of sample size and number of cycles respectively of [500,20], [2000,5], [5000,2], [10^4] for comparison with the chosen combination [1000,10]. No significant difference were found in the obtained values between all of these combinations, so providing confidence in the legitimacy of the adopted routine.

In Figure 4.3 the precision of the Faraday phase measurement is plotted against the imposed noise level for the defined I.F. of 1MHz, with half wave plate rotation frequencies of 0.5kHz, 1.0kHz, and 1.7kHz, and for four distinct values of δ, which determines the amount of modulation. Assuming a conservative noise level of 6% for the polarimeter, a precision of 0.4° can be obtained with a 1.67kHz half-wave plate rotation frequency (6.67kHz modulation frequency) provided δ is smaller than 20°. The precision increases for lower modulation frequencies. With a 6% noise level, a rotation frequency of 1kHz (4kHz modulation frequency) the polarimetric precision is 0.33° provided δ is smaller than 20°. The greatest precision is achieved with high degrees of modulation (i.e. small δ). Therefore a single pass through the plasma will allow the polarimeter to observe changes in the Faraday rotation of order 0.4° for the higher modulation frequency and provided that δ is smaller than 20° and a noise level of 6%.

A simple investigation of the distribution's asymmetry was also performed by examining the confidence levels. Skewness was barely detectable from inspection of the coefficients and no hint of kurtosis was found.

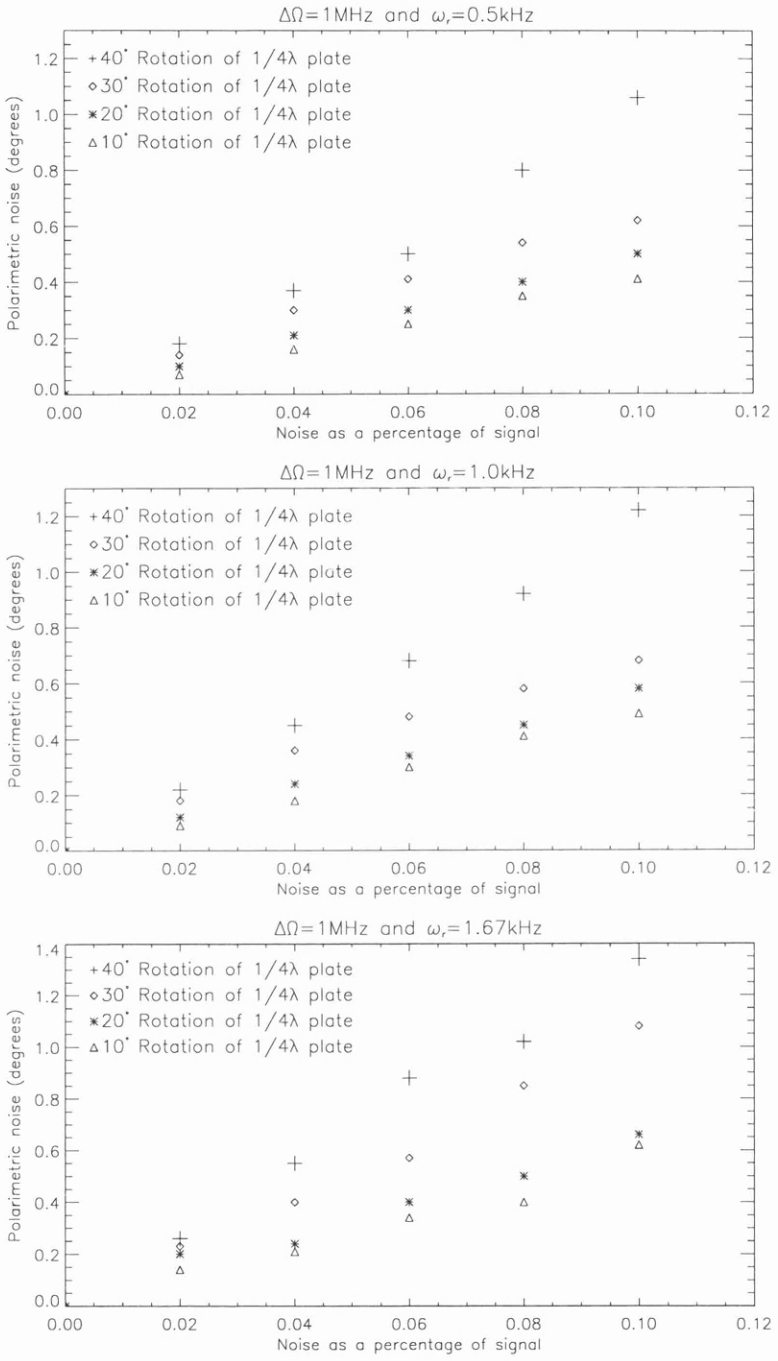

Figure 4.3: The uncertainties in determining the Faraday rotation for three distinct modulation frequencies as a function of the imposed noise level for various positions of the quarter-wave plate.

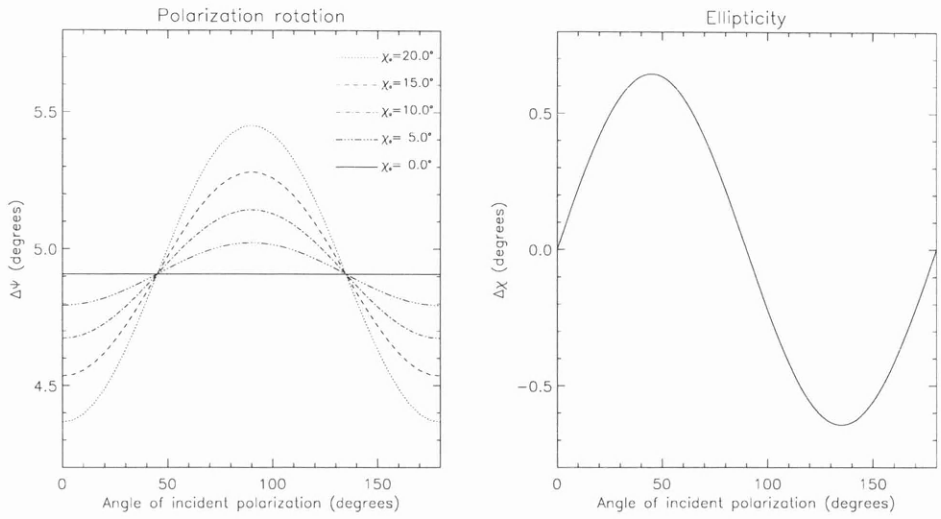

Figure 4.4: The effect from elliptical polarizations in Ψ and χ as a function of initial polarization angle ψ for various probing beam ellipticities. The solid lines refer to the case of linear polarization.

Analytical Simulation of Expected Faraday Results.

Using the analytical approach set out in Section 3.3.1 it is also possible to simulate the expected Faraday rotation angles at the plasma detector. The parameters used were for a typical COMPASS-D discharge, I_{plasma} = 250kA, B_{tor} = 1.2T, $n_e = 5\times10^{19}\mathrm{m}^{-3}$ and a parabolic density profile. Consider the plots in Figure 4.4 where both quantities (Ψ, χ) are plotted versus the input ellipse rotation angle, ψ. The first plot illustrates how the plasma birefringence affects both quantities Ψ, χ in the case of an elliptically polarized wave as a function of the incident polarization angle ψ for different values of χ_o. In the case of linear polarization the change is entirely due to the Faraday rotation provided the input polarization is aligned parallel to or perpendicular to the toroidal field. For elliptically polarized waves, the birefringence effects induce a periodical variation in the difference between the pure Faraday rotation angle and $\Delta\Psi_o$ shown. The deviation from pure Faraday rotation at $\chi_o = 20°$ is up to 10%. The birefringent effects may be avoided by either transmitting a linearly polarized beam through the plasma or by removing the birefringent effects from the signal with a bandpass filter centered at the rotating frequency of the beam. For small angles of χ_o, the second plot illustrates that the change in ellipticity is less than $\pm$ 0.7° and hence of little importance for experimental considerations.

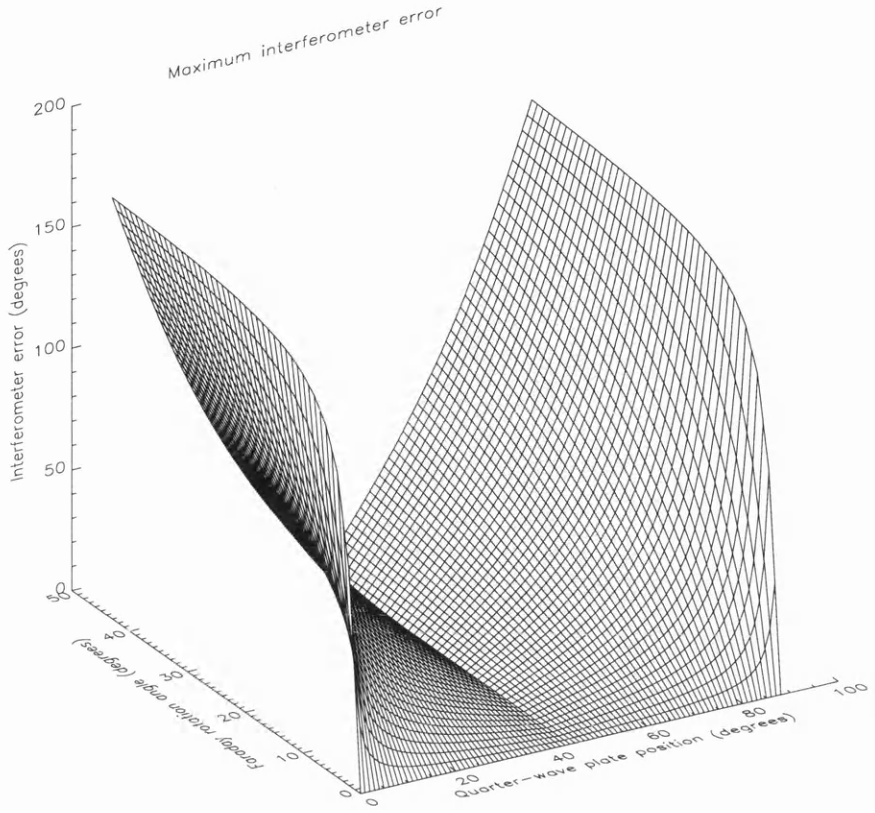

Figure 4.5: Maximum interferometer error as a function of the Faraday rotation angle and the optical axis of the quarter-wave plate which determines the polarization of the initial beam.

4.1.3 Influence of the Polarimeter on the Interferometer Measurements

One limitation of the proposed method is the introduction of phase errors into the data recorded by the interferometer as a result of the amplitude modulation of the 1MHz intermediate frequency, (see Geck et al., 1995). These phase errors have been analysed and their significance considered. The maximum phase error was calculated as a function of the Faraday rotation and the angle of δ, see Figure 4.5. Incorporating this extra phase shift into Equation 3.66 yields,

$$\Phi = 2.82\times10^{-15}\lambda\int n(r)dr + \delta\phi \tag{4.18}$$

where

$$\delta\phi = \chi_{plasma} - \chi_{ref} = \arctan[\tan\delta\tan(2\omega_r t + \Psi)] - \arctan[\tan\delta\tan(2\omega_r t)]. \tag{4.19}$$

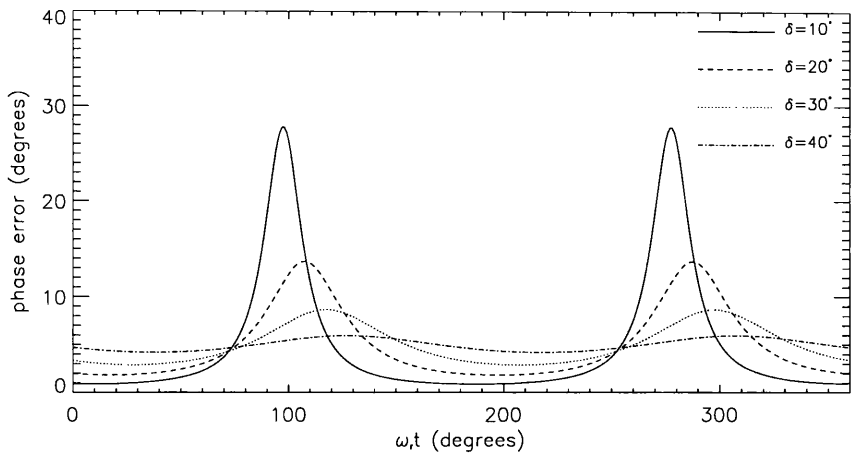

Figure 4.6: Time-varying interferometer phase contribution for a Faraday rotation angle of 5°.

This additional phase, $\delta\phi$, is a direct result of the rotating ellipse measurement technique which produces a time-varying phase contribution as shown in Figure 4.6. The magnitude of the phase $\delta\phi$ is a function of the degree of modulation of the received FIR beam, the modulation frequency and the Faraday rotation angle. This extra term can be removed by low-pass filtering the interferometer data with the subsequent loss of time resolution where necessary. The dual beam interferometer on COMPASS-D has a temporal resolution of 1MHz determined by the intermediate frequency of the two lasers. This excellent temporal resolution may be lost by the necessity of low-pass filtering at a frequency close to the rotating elliptical polarization frequency usually of the order of some kHz. Alternatively it is possible to reconstruct the interferometer data using computational methods once the Faraday rotation angle and the ellipticity of the polarization have been determined. In practice, however, this is extremely difficult because of uncertainties in these parameters.

Assuming a modulation of the FIR beam of 50%, i.e. $\delta = 35°$, and a typical plasma discharge resulting in a Faraday rotation angle of 6° will yield a phase contribution to the interferometer signal of 4.4°. With a high density discharge and an expected Faraday angle of 8° the phase contribution will be 5.9° to the interferometer signal. However, the phase resolution of the interferometer system is approximately $\frac{1}{60}$ fringe, 6°, corresponding to a density modulation for the central channel of approximately $0.6 \times 10^{17}\mathrm{m}^{-3}$. This implies that for the COMPASS-D tokamak the phase error introduced into the interferometer data

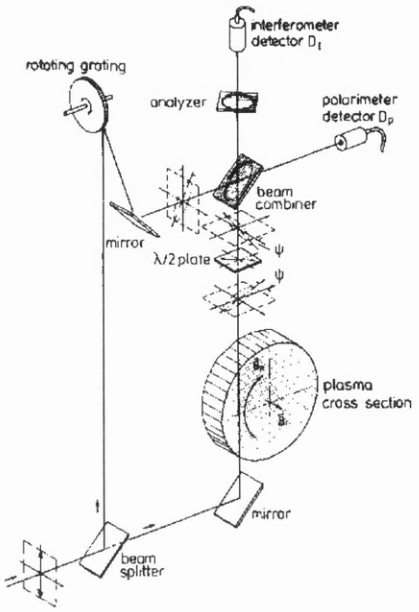

Figure 4.7: Optical arrangement for a single chord amplitude measurement of the Faraday rotation angle (Taken from Soltwisch, 1986).

by the polarimeter setup is comparable to its phase resolution and can therefore be neglected in the data reconstruction of the interferometer phase signal.

4.2 An Amplitude Measurement of the Faraday Rotation

The conventional polarimeter measures the change in orthogonal polarization before and after passage through the plasma. The Faraday rotation can be determined by taking the ratio of these orthogonal signals. The first polarimeter system to operate routinely was constructed by Soltwisch (1987) at Textor. This system utilised nine chords through the plasma and performed interferometry and polarimetry simultaneously.

4.2.1 Optical Arrangement

The basic configuration for simultaneous interferometric and polarimetric measurements by means of a heterodyne detection method is illustrated in Figure 4.7. After passage through the plasma the probing wave, which is initially linearly polarized, has become slightly elliptical ($\epsilon \ll 1$) due to the linear birefringence. The major axis of the vibrational ellipse is rotated by the angle Ψ relative to the initial plane of polarization. Hence, using the coordinate system in

Figure 4.7, the initial electric field is given by $(E_o e^{iwt}, 0)$ whereas the new state of polarization is

$$E = \frac{E_o}{\sqrt{1+\epsilon^2}} e^{(i\omega t - \Phi)} \begin{pmatrix} \cos\Psi & \sin\Psi \\ -\sin\Psi & \cos\Psi \end{pmatrix} \begin{pmatrix} 1 \\ \epsilon \end{pmatrix} \tag{4.20}$$

where Φ is the phase shift due to the plasma density. The wave then passes through a half-wave plate that acts as a calibrator whose purpose will be discussed subsequently.

The probing wave is then combined with a frequency offset reference wave at a polarizing beam splitter yielding

$$E = \begin{bmatrix} \frac{E_o}{\sqrt{1+\epsilon^2}}(\cos\Psi + i\epsilon\sin\Psi)e^{i\omega t - \Phi} \\ \frac{E_o}{\sqrt{1+\epsilon^2}}(-\sin\Psi + i\epsilon\cos\Psi)e^{i\omega t - \Phi} \end{bmatrix}. \tag{4.21}$$

The polarization of this reference wave is $\frac{E_{or}}{\sqrt{2}} e^{i(\omega t + \Delta\Omega t)}$; $-\frac{E_{or}}{\sqrt{2}} e^{i(\omega t + \Delta\Omega t)}$. The recombination is made by a beam combiner made of thin tungsten parallel to the plane of incidence, which yields a beat wave on each detector of the form

$$S_I = C_I + A_I \sin(\Delta\Omega t + \Phi + \Phi_I) \tag{4.22}$$

$$S_P = C_P + A_P \sin(\Delta\Omega t + \Phi + \Phi_P) \tag{4.23}$$

where

$$A_I = \frac{2|E_o||E_{or}|}{\sqrt{1+\epsilon^2}}(\cos^2\Psi + \epsilon^2\sin^2\Psi)^{\frac{1}{2}} \tag{4.24}$$

$$A_P = \frac{2|E_o||E_{or}|}{\sqrt{1+\epsilon^2}}(\sin^2\Psi + \epsilon^2\cos^2\Psi)^{\frac{1}{2}} \tag{4.25}$$

$$\tan\Phi_I = \frac{\cos\Psi}{\epsilon\sin\Psi} \tag{4.26}$$

$$\tan\Phi_P = \frac{\sin\Psi}{\epsilon\cos\Psi} \tag{4.27}$$

giving

$$\Phi_{biref} = \Phi_I - \Phi_P = \arctan\left(\frac{1}{\epsilon\tan\Psi}\right) - \arctan\left(\frac{\tan\Psi}{\epsilon}\right). \tag{4.28}$$

In normal operating conditions, assuming $\Psi \ll 1$ and $\epsilon \ll 1$

$$\begin{aligned} A_P &\simeq 2|E_o||E_{or}|(\Psi^2+\epsilon^2)^{\frac{1}{2}} \\ A_I &\simeq 2|E_o||E_{or}|. \end{aligned} \tag{4.29}$$

The signal S_I, whose large amplitude is almost insensitive to polarization changes, lends itself to determining the plasma-induced phase shift Φ in the usual way by comparing it with a sinusoidal reference signal of equal frequency $\Delta\Omega$ and fixed phase. The amplitude of signal

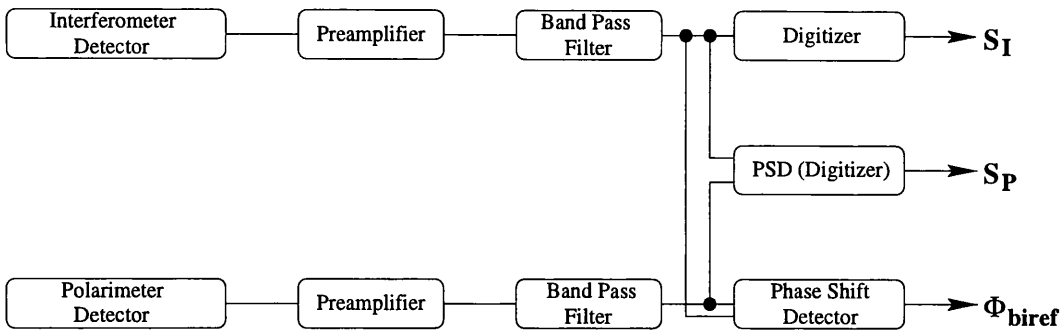

Figure 4.8: Schematic of polarimeter signal processing.

S_P is roughly proportional to the wave polarization Ψ. Knowing Ψ, the wave ellipticity can be determined by the phase measurement $\Phi_{biref} = \Phi_I - \Phi_P$ as

$$\epsilon \simeq -\Psi \tan(\Phi_P - \Phi_I). \tag{4.30}$$

Knowledge of the phase shift between both measured signals makes possible the determination of the plasma birefringence and can be used to correct the measurement of the Faraday angles if ϵ is too large. The temporal resolution is 1–10ms, determined by the integration time of the electronic system. The lower limit on the time resolution is set by the 1MHz modulation frequency of the polarimeter–interferometer. The amplitude of S_p is proportional to the Faraday angle but its sensitivity is very poor when Ψ becomes very close or smaller than the wave ellipticity. However, the phase difference $\Phi_P - \Phi_I$ is very sensitive to Ψ particularly when Ψ becomes smaller than the wave ellipticity. In order to extract the Faraday rotation angle, the signal S_p is processed as shown in Figure 4.8. Efficient noise filtering is achieved by a bandpass filter discriminating against slowly varying D.C. and high frequency components and by a phase sensitive detector (PSD) consisting of an analogue multiplier and a low-pass filter. In general a PSD selects a narrow band of a test signal at a frequency fixed by a sinusoidal control signal. Its output voltage is proportional to $A_I A_P \cos\Phi_{IP}$. In this case the PSD is controlled by S_I which matches both the intermediate frequency $\Delta\Omega$ and the shift Φ_{biref} of the test signal S_P. Thus, the processing circuit using the PSD multiplies the two signals S_P and S_I in order to improve the sensitivity for small values of Ψ. The output voltage, U_{PSD}, of the multiplier is given by

$$\begin{aligned} U_{\mathrm{PSD}} = \tfrac{1}{2}|A_x A_y| \cos(\Phi_P - \Phi_I) &= 2|E_o|^2 |E_{or}|^2 (\Psi^2 + \epsilon^2)^{\frac{1}{2}} \cos(\Phi_P - \Phi_I) \\ &\simeq 2|E_o|^2 |E_{or}|^2 \Psi. \end{aligned} \tag{4.31}$$

There is, however, still a dependence on the beam intensities $|E_o|^2|E_{or}|^2$ which may vary due to changes in the source power or refraction effects which are discussed in Section 4.2.2. This influence may be eliminated by normalising U_{PSD} to the square of the root mean square of A_I. The quantity

$$\frac{U_{\mathrm{PSD}}}{|A_I|^2} = C\Psi \tag{4.32}$$

is thus a measurement proportional to the Faraday angle, where C is a constant depending on the conversion factor of the electronic and detector responsitivity. This constant must be determined by a calibration routine. This is achieved in the absence of the plasma by rotating the half-wave plate in the probing beam path and monitoring the output voltage.

4.2.2 Refraction

There is a fundamental difficulty with the conventional polarimetry method proposed by Soltwisch (1981). Considering Equation 3.60 and neglecting ellipticity, the polarimeter signal may be described as

$$S_P = \Psi A_P \sin(\Delta\Omega t). \tag{4.33}$$

As the density gradients build during a plasma discharge, refraction causes the FIR beam to deflect and, depending on the detector geometry, the intensity $\mid A_P \mid^2$ to change. This effect can be eliminated in principle by dividing Equation 4.33 by the interferometer signal which is proportional to $\mid A_I \mid^2$. This works fairly well with the pyroelectric detector used by Soltwisch because it has a relatively large surface area so that refraction effects are small. Recently constructed interferometers use corner cube Schottky diode detectors which have a significantly improved noise-equivalent power (NEP) compared with the pyroelectric detector. The corner-cube antenna structure is, however, quite sensitive to beam deflections caused by refraction. Due to manufacturing limitations, each detector has a slightly different antenna pattern, so it is not reliable to use the interferometer detector to correct for amplitude variations on the polarimeter detectors.

Consider the situation where a wave is propagating at an angle ξ with respect to the refractive index gradient. By applying Snell's Law at two slightly displaced positions of the trajectory, it is possible to derive an expression for the change in the angle ξ between the propagation direction and the plasma density gradient:

$$\begin{aligned} N\sin\xi &= \left(N + \tfrac{dN}{dr}\delta r\right)\sin\left(\xi + \tfrac{d\xi}{dr}\delta r\right) \\ &\simeq N\sin\xi + \tfrac{dN}{dr}\sin\xi\delta r + N\tfrac{d}{dr}(\sin\xi)\delta r \end{aligned} \tag{4.34}$$

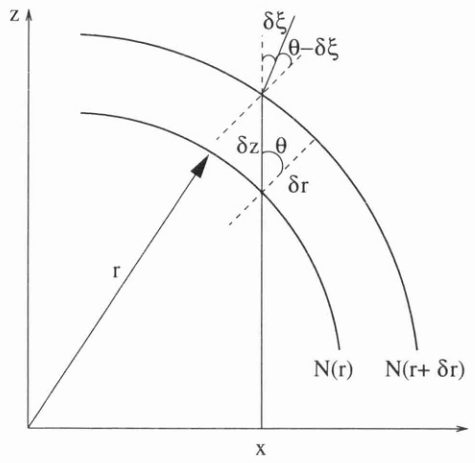

Figure 4.9: Coordinate system for refraction calculation.

which can be simplified as

$$\frac{d\xi}{dr} = -\frac{1}{N}\frac{dN}{dr}\tan\xi. \tag{4.35}$$

The derivative is taken along the wave trajectory and δr is the distance along the trajectory between the two points under consideration.

The amount of refraction depends on the derivative of the refractive index resulting in the wave trajectory being different for the two eigenmodes of propagation. However, for wavelengths appropriate for interferometry, the difference between the two refractive indices is at its maximum still approximately two orders of magnitude less than the derivative of the indices from unity, and for ray tracing can be discarded.

Equation 4.35 can be used straightforwardly in a numerical integration to calculate the path in the plasma of an incident electromagnetic wave. In order to get an idea of the significance of refraction effects, it is possible to calculate the change of the angle of propagation of an emerging ray with respect to the propagation angle of the same ray at incidence. More specifically, it is possible to calculate an "angular deviation" profile in the case of a wide, parallel beam incident on the plasma covering its entire cross-section. If the plasma has a circular shape, and the refractive index profile is assumed to be parabolic, it is also possible to derive an analytical expression for this angle of deviation ξ, (see Shmoys, 1961),

$$\xi(b) = \arcsin\left(2\left(\frac{\omega_{po}}{\omega}\right)^2\left(\frac{b}{a}\right)\sqrt{\frac{1-\left(\frac{b}{a}\right)^2}{4\left(\frac{b}{a}\right)^2\left(\frac{\omega_{po}}{\omega}\right)^2+\left(1-\frac{\omega_{po}^2}{\omega^2}\right)^2}}\right). \tag{4.36}$$

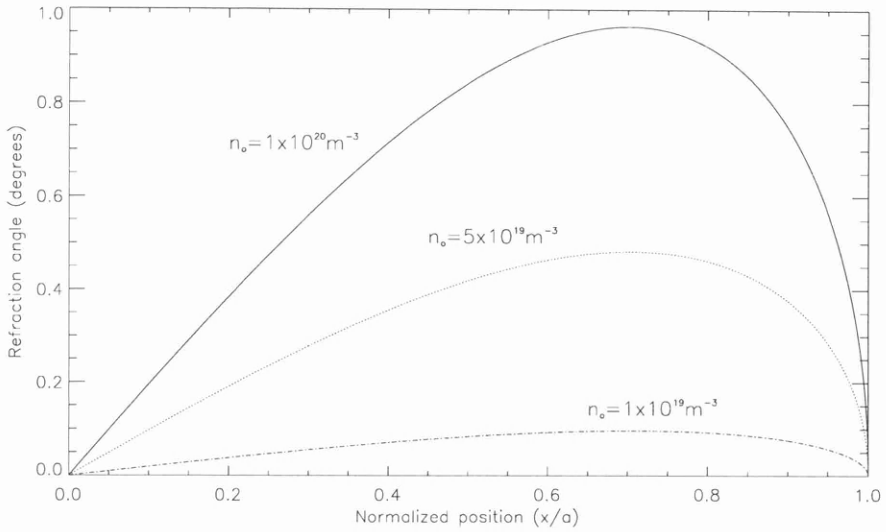

Figure 4.10: Angular deviation of FIR beam due to refraction as a function of the normalised plasma cross section, (x/a), calculated using Equation 4.36 for three distinct peak plasma densities.

Here $\left(\frac{b}{a}\right)$ is the normalised impact parameter of each ray, i.e. the minimum distance between the ray and the plasma center, b, normalised to the plasma minor radius, and ω_{po} is the angular plasma frequency at the center. Using this equation a calculation has been performed for the COMPASS-D geometry under realistic high density plasma conditions. The results are depicted in Figure 4.10. In the COMPASS-D case, the detectors necessarily have to be positioned quite a distance ($\simeq$ 1m) above the equatorial plane of the tokamak, both for geometrical reasons and to avoid electrical pick-up from the large magnetic fields confining the plasma. As a result, an angular deviation of only 0.5° will be sufficient to cause a beam displacement of approximately 0.5cm at the position of the detectors, even though the change of the path followed by the beam inside the plasma is negligible. The beam displacement at the detector may in that case be over 1cm for high density discharges. For pyroelectric detectors this displacement is not too troublesome due to their large detector surface area. However, for Schottky detectors this displacement will lead to erroneous readings on both detectors. The refraction effect is a more limiting problem for the amplitude method than for the phase measurement. Any drop off in power has severe consequences for an amplitude measurement which can interpret this diminution falsely as a result of Faraday rotation whereas the phase measurement has no such restrictions since it is independent of signal

variation to a first order.

4.2.3 Bench Test

A test bench was constructed to ascertain the feasibility of a polarimetric amplitude measurement on the COMPASS-D system as shown in Figure 4.11a. Unfortunately, due to time constraints, it was only possible to determine a polarimetric measurement along one chord. The optical components were mounted on a vibrationally stable table. An overview of the whole interferometer/polarimeter system is illustrated in Figure 4.11b.

Experimental Implementation

In the COMPASS-D interferometer/polarimeter system, a single high power ($\geq$ 160W) CO_2 laser is used to pump two separate far-infrared laser cavities. The CO_2 laser wavelength of 9.27μm is suitable for pumping the 432.6μm line of formic acid (CHOOH), the lasing medium. Each FIR laser cavity produces a vertically polarized TEM_{00} Gaussian mode at a power level of approximately 50mW. The probing beams were transported towards the bench setup by means of a series of curved elliptical mirrors. The laser beam was then focussed onto a rotating half-wave plate, in order to minimise truncation and diffraction effects associated with Gaussian propagation, (for clarification see the next section). The half-wave plate essentially acts as a chopper modulating the beam at four times the frequency of rotation of the plate, and thus enabling detection by the two pyroelectric detectors. The modulation frequency was set at 2kHz to coincide with the maximum frequency response of the pyroelectric detectors. A diode detection scheme consisting of an LED and a detector were installed on the half-wave plate allowing the stability of the rotation frequency to be ascertained. The beam then encountered a series of wire grid polarizers which divide the laser power equally between six channels, (see Edlington and Wylde, 1992). The test bench setup has a modified single pass configuration different to that described in Edlington and Wylde (1992), with only a single probing beam passing through the tokamak for detection. Therefore only polarimetric data may be obtained during the plasma discharges. This novel approach to beam splitting nevertheless has a drawback. Each channel has a different input polarization with respect to the toroidal magnetic field as shown in Table 4.1. In the case of the second chord through the plasma, the polarization is set at 35° to the toroidal field direction. After propagating through the tokamak each channel encounters a polarizing beam splitter or analyser where the two orthogonal polarization components are split and propagate onto two detectors, D_I and D_P. The data acquisition system included a PC based package

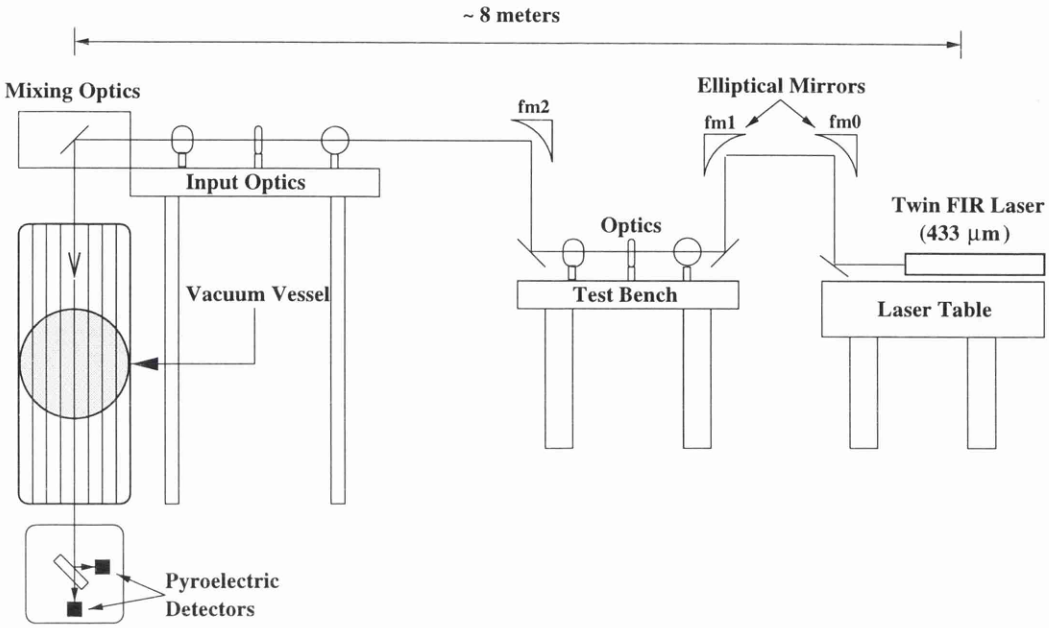

(a) Overview of the COMPASS-D interferometer/polarimeter.

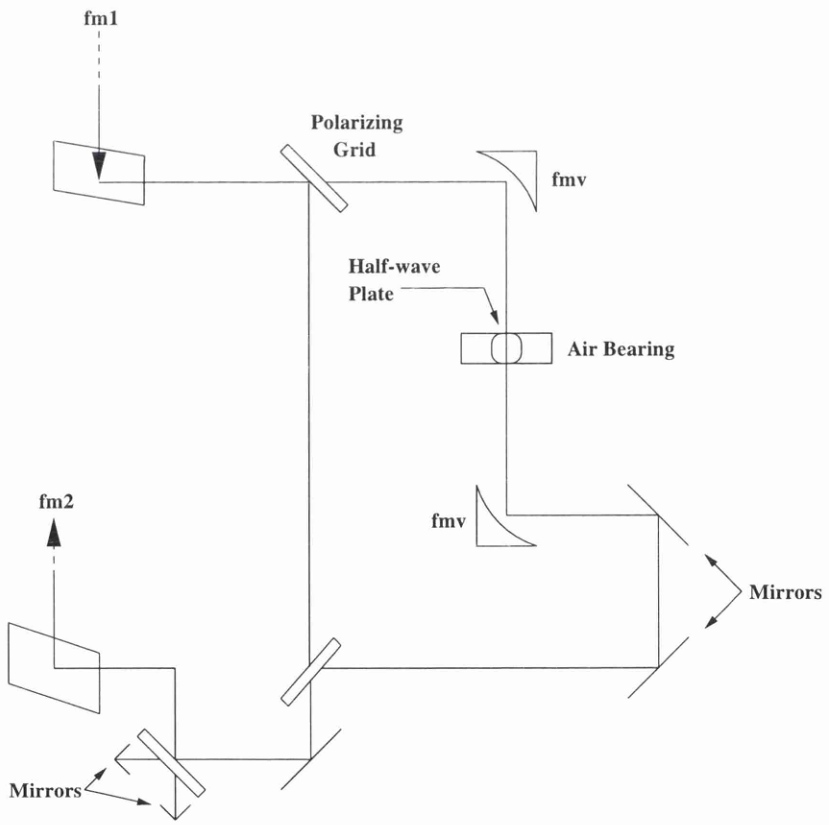

(b) Optical layout on the test bench.

Figure 4.11: Schematic depiction of the interferometer/polarimeter setup at COMPASS-D.

Channel	Radial Position x (m)	Input Polarization, Ψ_o (degrees)
1	0.168	20.0
2	0.116	35.0
3	0.014	60.0
4	-0.022	35.0
5	-0.113	0.0
6	-0.166	90.0

Table 4.1: The input polarization with respect to the toroidal magnetic field for each of the six channels.

called Labview and an oscilloscope. The amplified detector signals were filtered and digitised onto hard disk by Labview directly from the oscilloscope trace for both detectors.

In order to calibrate the electronics and determine the constant C in Equation 4.32 a half-wave plate needs to be inserted before the polarizing beam splitter. The calibration process involved rotating the half-wave plate through 1° steps in the absence of the plasma and measuring the detector outputs at each half-wave plate position. The resolution is of the order of 0.5° for the current configuration. This can be dramatically improved by the introduction of tailor made electronics and data acquisition systems. The signals were then Fourier analysed and the results plotted in Figure 4.12. The data points were subjected to a least square fit in order to calculate the conversion factor between the measured signal and polarization angle. This fit could then be used to compute the Faraday angle during plasma discharges.

The Optical Components

The wave plates used in the far infrared are often made of crystal quartz due to their negligible absorption losses and are invariably anti-reflection coated. Since the refractive index difference is rather small ($N_e = 2.1599$ and $N_o = 2.1162$ at a wavelength 432.6μm), relatively thick wave plates are needed to obtain a 180° phase difference. At 432.6μm the thickness of the half-wave plate is 4.47mm and it is held in place at the end of a hollow shaft air bearing spindle. The unit requires water cooling and filtered air at a rate of 1000 liters per minute at 80psi for the air bearing. The bearing is driven by an induction motor with a top rated speed of 100,000rpm. To reduce the chance of failure, the motor is usually operated at 60,000rpm. This produces the necessary modulated signal waveform at four times the rotation frequency. Unfortunately, due to slight non uniformities in the half-wave plate thickness, along with an absorption which varies depending on plate angle, there are

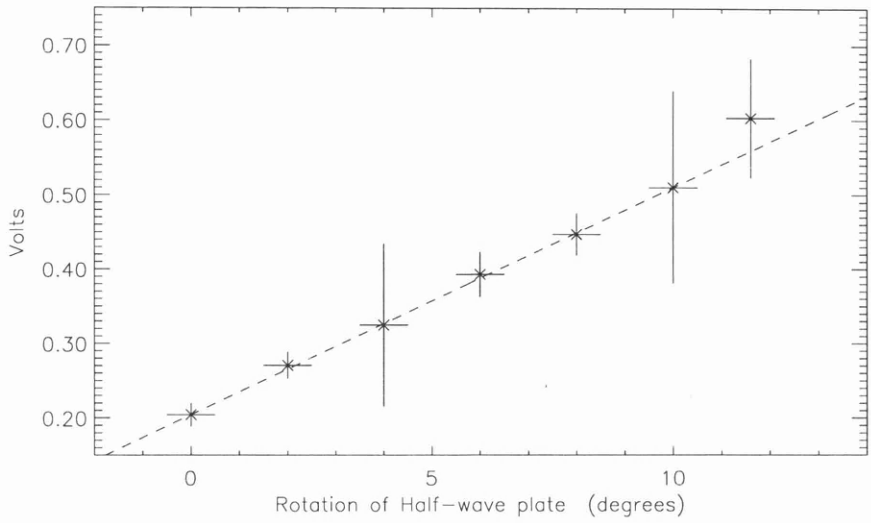

Figure 4.12: Variation of signal as a function of half-wave plate rotation.

frequency components in the detected signal at one or two times the fundamental motor frequency. These must be filtered out, thereby limiting the bandwidth to less than 1kHz.

Wire grids or meshes are used at several locations in the polarimeter system, acting either as beam splitters or polarizers. A detailed theory of waves incident on wire grids has been developed by Markuvitz (1951). The wire polarizers located in front of the Schottky detectors are free-standing grids made of 10μm diameter tungsten wire with a wire spacing of 25μm (1000lpi). The theoretical transmission for the undesired polarization ($\mathbf{E} \parallel$ wires) is about 0.5%.

A number of high quality plane and elliptical mirrors were utilised throughout the optical circuit. The plane mirrors themselves were 50mm diameter round flats, formed from a low expansion borosilicate glass (LEBG) with an aluminium coating on one side as a reflecting surface. The elliptical mirrors were also formed from aluminium with a variety of focal lengths as illustrated in Table 4.2

Wave Propagation

The wavelengths utilised in tokamak interferometric and polarimetric experiments are sufficiently large that the theory of geometrical optics is not adequate to describe the wave propagation. The use of Gaussian beam theory, (see Veron, 1979), is required which takes

Elliptical Mirror	Focal Length (mm)
fmv	228
fm0	1443
fm1	1325
fm2	-2773

Table 4.2: A list of the elliptical mirrors utilised in the test bench.

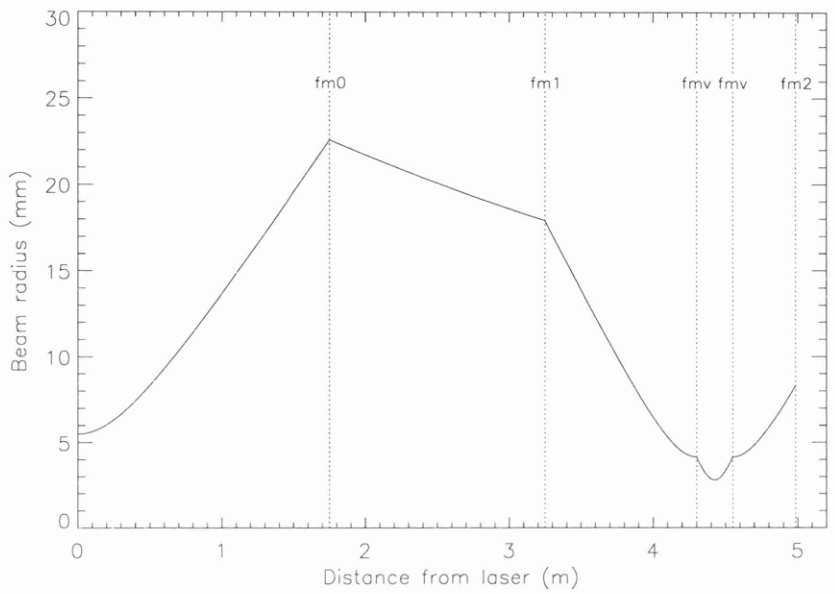

Figure 4.13: Calculated Gaussian propagation of the probing beam through the system. The x-axis is chosen such that the laser output coupler is at zero. The location of the beam forming mirrors are also indicated.

into account the finite size of the focal spot. The beam waist diameter ($\frac{1}{e}$ amplitude) upon exiting the laser is 11mm. A series of elliptical mirrors (fm0 $\rightarrow$ fmv) enable the beam waist to be minimised upon entrance to the half-wave plate and the torus mid plane. Utilising a Gaussian ray-tracing code, a model for the free space propagation of the laser beam through the system is presented in Figure 4.13.

If the size of the optical elements is not sufficiently large, the Gaussian beam will be truncated and diffraction effects will both deform the shape of the beam profile and disturb the phase front of the wave. Diffraction is considered negligible if the truncation occurs at an intensity level below 1% of the maximum. Assuming a Gaussian beam, this sets a safe

limit to the size D for the optic used:

$$D > 2.2d \tag{4.37}$$

where d is the beam $\frac{1}{e}$ diameter at the position of the optical element. Two further criteria needing consideration are the spot size and the maximum throw distance of the beam. The spot size, d_o, is defined as the smallest possible beam size after propagation through an optic of focal length f,

$$d_o \simeq \frac{2f\lambda}{d}. \tag{4.38}$$

For a given beam width, ω_L, intercepting an ideal lens no choice of focal length of the lens can give a beam waist at a greater distance than the maximum throw distance, d_{max}, defined as

$$d_{max} = \frac{k\omega_L^2}{4}. \tag{4.39}$$

Results

The rotation frequency of the half-wave plate may be determined by Fourier transforming the complete LED data array containing the time intervals for each complete rotation of the wave plate. Figure 4.14 illustrates the raw LED data for plasma shot 22118 clearly indicating a period of $\tau = 0.00207$ seconds between successive maxima, and the Fourier transform of the LED data resulting in a modulation frequency of 1928Hz and the corresponding harmonics. In order to determine the stability of the rotation frequency, the LED data array may be divided into a number of time intervals and a Fourier transform performed on each interval separately. However, during the length of a typical discharge, $\tau = 0.5$ seconds, the rotation frequency is stable to a high degree.

A series of high density plasma discharges were run on the COMPASS-D tokamak with the outlined configuration installed. Figure 4.15 shows plots of the integrated electron density from a 2mm interferometer diagnostic, the plasma current and the signals from both pyroelectric detectors for plasma shot 22118. The detector signals were then filtered using a Butterworth bandpass filter centered on 2kHz with a bandwidth of 200Hz. The bandwidth was chosen narrow enough to avoid low frequency magnetic power supply noise and higher frequency noise spikes. The filtered signals are also shown in Figure 4.15. A 50Hz A.C. supply voltage is visible in detector 2 signal and is subsequently removed via filtering.

Unfortunately, due to pickup from the magnetic coils surrounding the tokamak and the detectors, the signals from both detectors were affected, severely in the case of the second

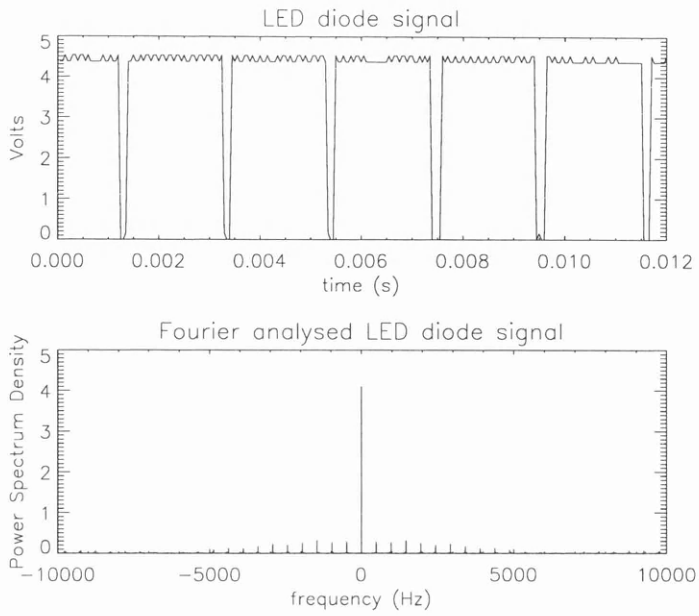

Figure 4.14: The LED diode signal indicating the rotation speed of the half-wave plate with the Fourier transform of the signal below.

detector. However, the amplitude of the signal detector clearly diminishes as the electron density peaks at time $\tau = 0.3$ seconds. During an amplitude measurement the orthogonal signal components measured by the two detectors varies as a function of the electron density and poloidal magnetic field and therefore the Faraday angle. However, no valuable information can be ascertained without the introduction of magnetic shielding and further vibrational isolation to the detectors.

Certain other instrumental considerations affected the accuracy of the Faraday measurement. The effects due to laser instability presented a significant problem, the overall power level drift increasing significantly with time (up to 20% in only 5 minutes). The problems were undoubtedly due to the age of the laser. Vibration of optical components, which can never be completely eliminated, causes a phase distortion of the measured signal that pollutes the measurement of the line-integrated density. This distortion has been kept small by selecting a wavelength that is large compared to the amplitude of vibrations.

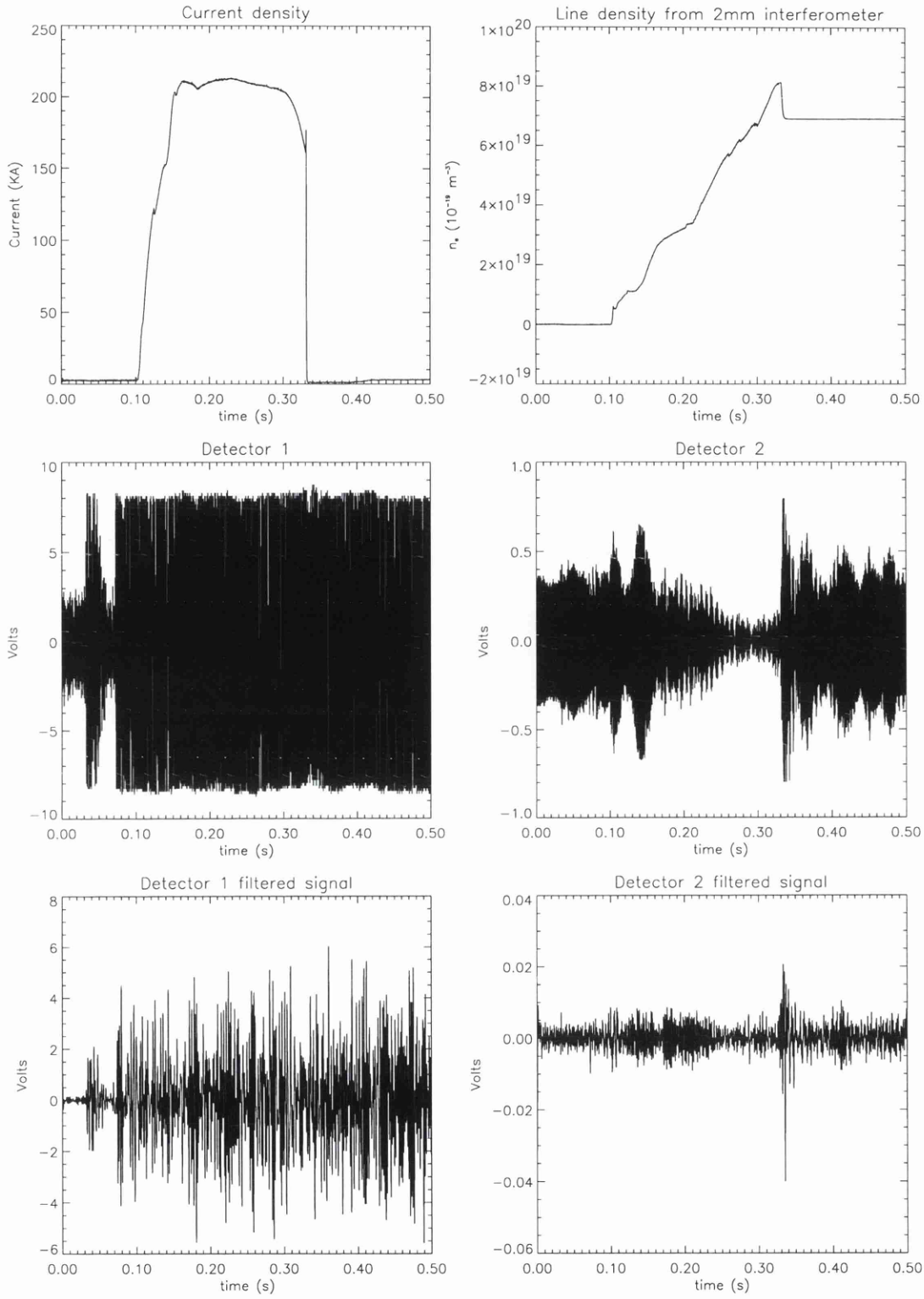

Figure 4.15: Evolution of the current and electron density as a function of time for a 250kA, 1.2T Ohmic discharge (shot 22118). The two detector signals in their raw and filtered form are also plotted below.

4.2.4 Simulation of the Amplitude Method

In order to ascertain the effect of the plasma on the initially linearly polarized beam, the signals of both detectors D_I and D_P were simulated for each of the six channels. The birefringent nature of the plasma introduces a certain degree of ellipticity in the propagating beam which can be detected as small changes of amplitude by the two detectors and which appear primarily as a phase shift, Φ_{biref}, of the polarimeter signal with respect to the interferometer signal. This small amplitude change could be interpreted incorrectly as a Faraday rotation by the system. It is imperative, therefore, to determine the accuracy of the Faraday measurement as a function of the ellipticity of the FIR beam for each of the six channels. In order to determine the pollution of the Faraday angle by the ellipticity, the following procedure is followed

- For each of the six chords through the plasma, the appropriate input linear polarization Ψ_o is selected from Table 4.1.
- The signals at both detectors are simulated for a typical discharge. The phase shift detector is also reconstructed in software and a value of Φ_{biref} determined.
- For small angles, Equation 4.28 can be written as

$$\epsilon \simeq -\Psi_{sim} \tan(\Phi_P - \Phi_I) \tag{4.40}$$

  allowing a determination of the plasma birefringence, ϵ. Ψ_{sim} is the expected Faraday rotation angle deduced from the analysis outlined in Section 3.3.1.
- Using Equation A.1 from Appendix (1) it is possible to infer the corrected Faraday rotation angle Ψ, from measured angle $\widetilde{\Psi}$. For small angles this can be expressed as

$$\Psi = \arctan \sqrt{\tan^2 \widetilde{\Psi} - \epsilon^2}. \tag{4.41}$$

- Comparing both the corrected and measured Faraday rotation angle, an estimation of the uncertainty in determining the angle may be achieved for each chord and for a particular discharge, illustrated in Figure 4.16.

The two outer chords, 5 and 6, have their input polarization either parallel or perpendicular to the toroidal magnetic field and thus are not influenced by the birefringence of the plasma. The measured Faraday angle therefore does not need any correction. The two inner chords, 1 and 2, have a large expected Faraday angle and a small expected ellipticity due to birefringence. This implies that the uncertainty in determining the Faraday angle is approximately $\pm$ 0.05°,

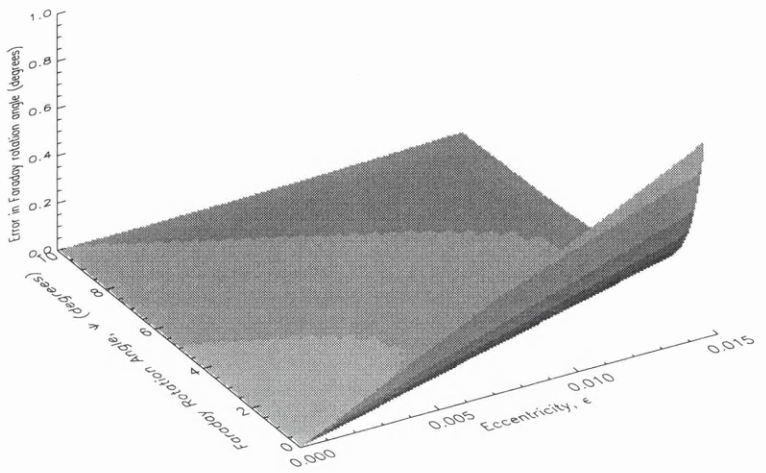

Figure 4.16: The uncertainty in determining the Faraday rotation angle as a function of the ellipticity introduced by the plasma birefringence and the Faraday rotation angle.

much less than the expected resolution of the system. The remaining chords, 3 and 4, suffer from low expected Faraday rotation angles and high ellipticity. This combination leads to significant uncertainties in the Faraday rotation angle of the order of $\pm$ 0.6° which is clearly undesirable. If an amplitude measurement were to be installed on COMPASS-D it is imperative, therefore, to adjust the input polarization of the middle two chords so that they are either parallel or perpendicular to the toroidal magnetic field.

In order to determine the polarimetric precision of the amplitude measurement, the two signals S_P and S_I at each detector were simulated numerically. The signals were then filtered through a Butterworth band-pass filter and the Faraday rotation angle determined. The signals were each polluted with a certain percentage of normally distributed noise in order to simulate the noisy electronic systems. The results are plotted in Figure 4.17. The polarimetric precision achieved with the bench test setup is $\pm$ 0.5° corresponding to an imposed noise level of approximately 8%. With a conservative imposed noise level of 5%, a precision of $\pm$ 0.3° can be achieved.

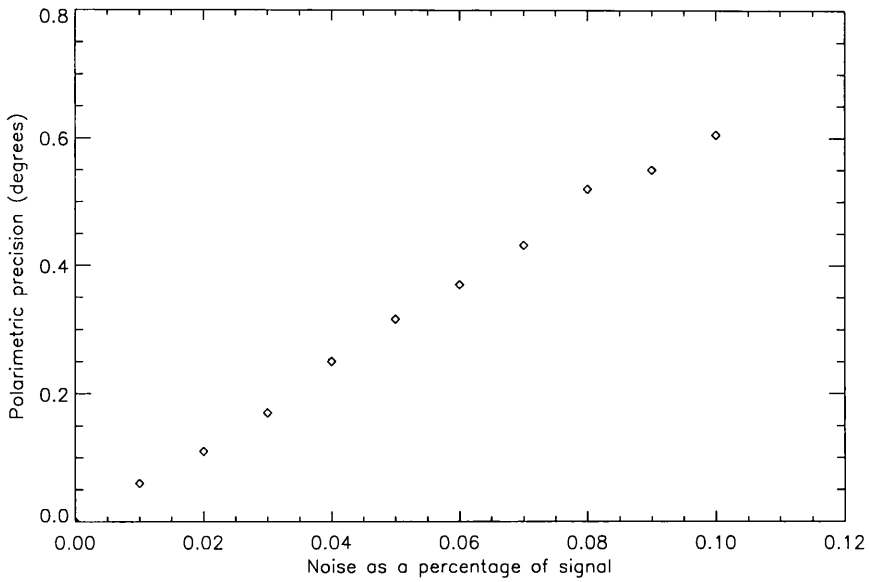

Figure 4.17: The polarimetric precision as function of imposed noise level for an amplitude measurement.

4.3 Discussion

Both polarimetric methods rely on the rotation of a well-defined incident polarization state as it propagates through the plasma. The rotation angle can be determined through a measurement of the relative power levels at two detectors, each sensitive to one of the two orthogonal linear polarization states. In single detection schemes, the orientation of the incident polarization state is modulated in time, resulting in an amplitude modulation of the detected signal. From the phase lag of this modulation with respect to a reference signal, the Faraday rotation angle may be deduced. The polarimeter measurement is independent of the signal amplitude, provided the signal remains large enough to stay above the noise level.

The present six channel interferometer installed on the COMPASS-D tokamak has a two pass configuration signifying that the FIR beam transverses the plasma twice along identical paths. The laser power is split equally between the six channels and recombined with a reference beam after passage through the tokamak by a series of wire grid beam splitters. This configuration must be adapted for a polarimetric measurement with the removal or re-alignment of the wire grid beam splitters and the adoption of a single pass of the laser beam through the tokamak. In the case of an amplitude measurement, the wire grid beam splitter must be re-aligned such that the input polarization into the tokamak must be parallel to or

Description	Phase Measurement	Amplitude Measurement
Temporal Resolution	maximum 6.7kHz (0.15ms) nominal 4kHz (0.25ms)	1ms determined by integration time of electronics.
Spatial Resolution	mm's	mm's
Detectors Required	one per channel (Schtokky)	two per channel (Pyroelectric)
Accuracy of Measurement	6% noise, 4kHz, $\delta \leq 20°$, 0.33° 6% noise, 4kHz, $\delta = 40°$, 0.45° 6% noise, 6.7kHz, $\delta \leq 20°$, 0.40° 6% noise, 6.7kHz, $\delta = 40°$, 0.85°	3% noise, 0.16° 5% noise, 0.30° 7% noise, 0.50°
Any Cross Coupling Problems?	$\delta = 35°$ (50% modulation) $\Psi = 6°$, $\delta\phi = 4.4°$ $\Psi = 6°$, $\delta\phi = 5.9°$	Error due to birefringence channel 5 & 6: $\Delta\Psi = 0°$ channel 1 & 2: $\Delta\Psi = \pm 0.05°$ channel 3 & 4: $\Delta\Psi = \pm 0.6°$
Other Comments	Calibration of electronics necessary. Refractive effects not important to first order. Major overhaul of present installation is necessary.	Determination of constant C, Equation 4.32, necessary daily. Refraction important in any amplitude measurement. Realignment of grid beam splitter and conversion to a single pass configuration required.

Table 4.3: Advantages and disadvantages of the two polarimetric measurement schemes.

perpendicular to the toroidal magnetic field. This configuration minimises the elliptisation of the emerging beam. With phase measurements, the wire grid splitter must be replaced with a mylar beam splitter so that a rotating polarized beam may propagate into the tokamak.

The advantages and disadvantages of each of the two measurement systems are tabulated in Table 4.3. Clearly the spatial resolution of both measurement techniques are comparable, though the phase measurement technique has a significantly better temporal resolution. When studying the evolution of fast moving plasma phenomena, such as magnetic islands and sawtooth activity, a high temporal resolution is desirable. The phase measurement technique requires only one detector per channel which is a significant advantage in the spatially restrictive regime of a tokamak. In terms of phase resolution of the Faraday rotation angle both methods are comparable assuming the phase technique has a modulation of the signal amplitude of 50% ($\delta = 35°$) and a 6% signal-to-noise level. The cross-coupling problems inherent in the phase measurement technique produce an additional phase contribution to the interferometer. However, this additional phase error is comparable or smaller than the phase resolution of the interferometer and may thus be discarded in the final analysis. The cross-coupling problems associated with the amplitude measurement technique produce an

elliptisation of the emerging polarization which may be misinterpreted as an additional Faraday rotation angle. This effect may be eliminated by the re-alignment of the polarizing grid splitters such that the incident polarization is parallel or perpendicular to the toroidal magnetic field. The amplitude measurement technique is maintenance intensive, requiring daily calibration and a high degree of laser stability. Refraction effects may also cause deleterious effects which to first order may be neglected in the phase method.

In conclusion, the phase measurement technique is clearly desirable in order to fulfill the basic aims of the physics programme on the COMPASS-D tokamak. This involves determining the temporal evolution of magnetohydrodynamic plasma phenomena and the effect of additional radio and neutral beam heating on plasma stability. The phase measurement has a high degree of temporal and spatial resolution, a good phase accuracy which greatly simplifies the mathematical inversion required to yield the poloidal magnetic field and hence the current density.

Chapter 5

Hα Polarimetry of the Solar Surface

5.1 Introduction

Numerous studies of broadband and line polarization variation from the solar center to limb have been conducted over the years, (see Section 1.2), utilising polarimetric instruments that have selectively sampled regions of the Sun using a small aperture, $\sim$ 5 arcseconds. This approach necessitated long exposure times to achieve the required photon accuracy, with the constant repositioning of the polarimeter's aperture to allow sequential scanning of the center-to-limb polarization variation (CLV). These two requirements are the main disadvantages of this observational technique introducing cumbersome positional uncertainties and the assumption that no global polarization change occurred during the course of the exposure. It is therefore desirable to conduct observations of the line polarization CLV using an imaging polarimetric technique with a large area, $\sim$ 10 $\times$ 5 arcminutes, of the solar surface may be observed simultaneously.

Polarimetric observations of the solar disk recorded in Hα ($\lambda = 6562.5$Å) during the Summer 1997 with the prototype imaging polarimeter are presented and discussed within the framework of the following aims:

I An investigation of the behavior of the polarization across the solar disk from center to limb with the aim of exploring an intriguing result by Leroy (1972), suggesting that the solar equatorial polarization is approximately ten percent larger than at the poles. This issue has been re-examined with new observations, utilising an imaging polarimetric technique, to explore the diagnostic potential in the context of the Hanle depolarization effect and identify problem areas that need to be addressed, rather than to present definite quantitative results on field strength and line parameters.

II The investigation of surface features exhibiting linear polarization associated with solar magnetic activity such as sunspots, surface mottling and prominences. Such studies are useful in exploring the magnetic field structure.

The experiment involved observations of the Hα line-center and the wings of the Hα line (i.e. $\Delta\lambda \pm 0.3$Å). Section 5.3 describes the measurements made during July and August 1997 across the Hα line.

Measurement of solar magnetic fields are generally deduced from direct observations of polarization in spectral lines. For the correct diagnostic of solar magnetic fields it is fundamental to have a detailed understanding of the physical mechanisms that are able to generate polarized radiation and those that are effective in modifying its properties in the transfer through the solar atmosphere.

5.2 Instrumental Polarization

Most telescopes and instruments polarize radiation to some small extent and distort any polarimetric measurements; this property is generally called instrumental polarization, (see Section 2.3). When observing a source of zero polarization, invariably some significant output in q, u, and v is obtained. As long as this polarization is small, it may be vectorially added to the true polarization signal when observing any other source, and therefore it may be vectorially subtracted during the reductions. Such vector zero points are determined by observing sources of zero polarization if these are available.

For reasons of symmetry and scattering geometry, the polarization is zero at disk center and increases towards the solar limb, and the plane of linear polarization is normally oriented tangential to the nearest limb. Any q or u signal seen in such (disc center) recordings is therefore due to instrumental polarization or the Zeeman effect. Measurements of the solar center can be used to provide a calibration for the instrumental polarization which affects all other results. Therefore, to correct the data for this fixed-pattern background, q recorded at solar disc center (calibration) is subtracted from limb recordings (the actual measurement), so that, in theory

$$(q_{pol} + q_{inst})_{\text{limb}} - (q_{inst})_{\text{center}} = q_{pol}. \tag{5.1}$$

A similar argument may equally be applied to the u parameter. Therefore, the disk center observations may act as a calibration for the true zero level.

Close to the solar limb at the position angle of celestial north or south (which is not far from the heliographic north or south poles), where some of the observations have been

made, Stokes V and U are usually intrinsically small, so that instrumental cross-talk ($V \rightarrow Q$ and $U \rightarrow Q$) is a minor problem. Sometimes significant Stokes V signals due to magnetic fields can infiltrate the Stokes Q spectrum through instrumental polarization, but this may be eliminated by taking a differential measurement. Cross talk from Q to the other Stokes parameters can in principle reduce the Q amplitudes and thus affect the polarization scale.

The rationale for this method of data acquisition may be summarised as follows. The degree of polarization for measurement will be very small (about 0.5%) and the precision, at best, will be a few times 0.01%. Also, the instrumental polarization of the instrument is not known to sufficient accuracy and and may well vary from day to day. Therefore it is advantageous to measure the difference of the measured polarization at two solar positions, and to monitor the variations of this difference. This differential approach negates the need to know the true polarization as it will be cancelled out in taking the difference, and knowledge of the position angle of a polarized source can be deduced from a measurement position in the q, u plane.

Finally it is desirable to ascertain the relationship between the instrumental polarimetric frame and the equatorial frame, the standard reference frame in polarimetry. This may be achieved by placing a Polaroid, weighted by a plumb-bob in order to keep its axis at a constant orientation with respect to the Earth (see Gehrels and Teska, 1960 for a fuller explanation), prior to the telescope aperture. Measurements were attempted on 24 September 1997 with the Polaroid alternately set with face in and face out. In the q,u plane the bisector of a pair of such measurements corresponds to a position angle of an equivalent Polaroid set with its axis parallel to the vertical. At local noon this corresponds to the north-south axis of the equatorial frame. This method requires no wind around the telescope and dome, unfortunately the weather conditions were adverse in this regard, causing the Polaroid to wobble constantly during integrations and therefore reducing the effectiveness of the results. A preliminary reduction of the data suggests that the instrumental frame is set at a 45° clockwise position to the $+q$ direction, i.e the N/S direction in equatorial coordinates. This result was expected since care was taken in the polarimetric design to align the edges of the Savart plate to the equatorial frame. Therefore the resolved orthogonally polarized components will be at 45° to the prism edge and to the frame of reference. The data obtained by the plumb-bob method confirmed this arrangement with an accuracy commensurate with the stellar measurements. Previous observations taken with the Hα filter removed, as outlined in Section 2.2.7, also suggest that the instrumental reference axis is offset by 45° ± 1° with respect to the equatorial reference frame.

5.3 Center to Limb Observations

Observations were recorded of the Sun's polar and equatorial regions during the course of three days in July 1997 in order to study the center-to-limb variation with the prototype imaging polarimeter. On the 9 July, observations were taken of the north polar region and the western limb of the Sun in the core of the Hα resonance line, as shown in Figure 5.1. The north polar region was investigated further on 19 July, again in Hα, see Figure 5.8. The next day, 20 July, the north polar and western limb regions were observed in the red-wing and the blue-wing of Hα, see Figure 5.12. A total of 10 exposures were recorded with μ values ranging between 0.09 and 0.65 at the northern and western limb. An additional 4 recordings were also made at disc center. Generally the full CLV of q and u was recorded. The aim in this case was to search for variations in q and u at different positions along the two limbs. Exposure times were typically 1 second at disc center and 3 seconds at the limb, $\mu = 0.09$. Hence the total time needed to record and store a full set of measurements (i.e. an image pair near the limb and at disc center) ranged between 100 seconds and 200 seconds (including moving the telescope and confirming the limb position), depending on the observed μ. Image motion, seeing and guiding errors limit the exact reproduction of the observed position between the two exposures to 5 arcseconds (depending mainly on seeing).

The Sun's axis of rotation is inclined at 7.25°, and the Earth's axis of rotation at 23.5° to the vertical to the plane of the ecliptic; hence the direction of the Sun's axis as viewed from the Earth varies considerably throughout the year. The position angle of the north pole of the Sun during the three days of observations, on 9, 19 and 20 July was 0.94°, 5.39° and 5.82° respectively. Another intrinsic consequence that needs to be considered is the differential rotation of the solar surface; the sun rotates faster at the equator than at the pole. The integration time for a complete set of observations is approximately 45 minutes as compared to the solar rotation period of 27 days suggesting that the change in the portion of the solar surface under investigation, as a result of rotation, is of no consequence.

Figures 5.1, 5.8 and 5.12 illustrate the regions of the Sun under investigation by the imaging polarimeter. The larger image is an Hα exposure of the Sun taken at the Observatoire de Paris while the smaller images are those taken in Glasgow by the double beam polarimeter with their characteristic ordinary and extraordinary exposures. The small rectangle superimposed on the whole Sun image represents the area under investigation by the imaging polarimeter. Figures 5.2, 5.9, 5.13 and 5.19 show the intensity variation for a half-wave plate position of $\psi = 0°$ for the regions under investigation on each of the three days. The intensity profiles of the ordinary and extraordinary images as a function of distance from the limb show slight

enhancements and depressions over the solar surface which may be explained by intensity fluctuations due to granulation and mottling effects. The ordinary and extraordinary beam profiles show excellent correlation across the solar surface. The limb of the Sun is recognisable but not clearly defined when inspecting the orthogonal beam intensities at the western and northern limbs. This leads to registration errors when the $p(\mu)$ curves are compared, this is discussed in greater detail in Section 5.3.1.

5.3.1 Shapes of the Polarized CLV

The center-to-limb polarization variation in q and u for the wavelengths under investigation are presented for the the north polar and western limb regions of the Sun. In order to quantify the differences in behaviour between the core and the wings of the Hα resonance line the following three parameters of the q and u profile are introduced: These are the q and u value in the blue-wing (i.e. at $\lambda = 6562.2$Å), in the red-wing ($\lambda = 6562.8$Å) and in the line-center ($\lambda = 6562.5$Å). In the following discussion it will be convenient to refer to these parameters as blue-wing, red-wing and line-center q and u, or q_b, q_r, q_c, and u_b, u_r, u_c, respectively.

The plotted CLV curves for q_c and u_c along the northern and the western limbs recorded in Hα on 9 July are shown in Figure 5.3 and Figure 5.4 respectively. Figure 5.10 has the CLV curve for q_c and u_c recorded on 19 July in Hα for the northern limb of the Sun. Observations taken on 20 July were in both the red- and blue-wing of the Hα resonance line. The blue-wing CLV polarization curves taken in Hα, q_b and u_b, along the northern and western limbs are plotted in Figure 5.14 and Figure 5.15, while the plots for the red-wing are shown in Figure 5.20 and Figure 5.21 respectively.

The CLV of the q amplitude increases from the center to the limb as expected, reaching a maximum at the limb. This is the case for all three wavelengths. Inspection of the CLV q plots shows that the curve falls off to background signal levels at about 40 arcseconds from the limb or $\mu \sim 0.3$ so offering ~ 10 good data points for the curve fitting determination. This is consistently the case for the three wavelengths under investigation. Beyond 40 arcseconds distance, the data points level off and fluctuate around the scaled zero point of polarization, determined from observations of the disk center.

In many or even most spectral regions, the magnitude of the continuum polarization is comparable to that of the line polarization. Thus, by measuring the line polarization from the polarization zero level, the results would be affected to variable degree by the behaviour of the continuum rather than of the lines alone. In addition, the amount of continuum

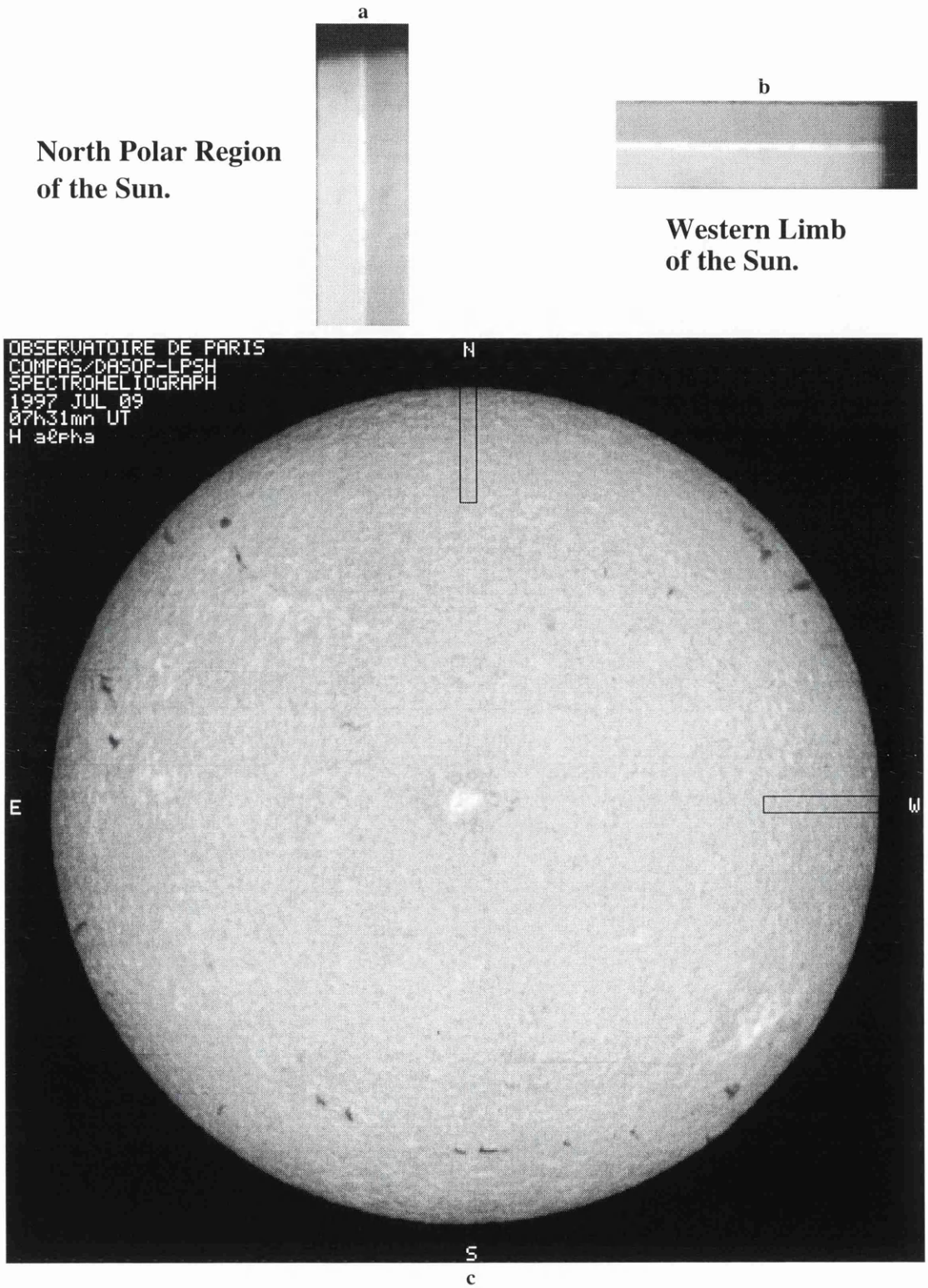

Figure 5.1: Three Hα core exposures of the Sun taken on 9 July 1997: (a) North polar region, (b) western limb and (c) whole solar disk taken at the Observatoire de Paris. The rectangles correspond to the polarimeter's field of view on the solar disk.

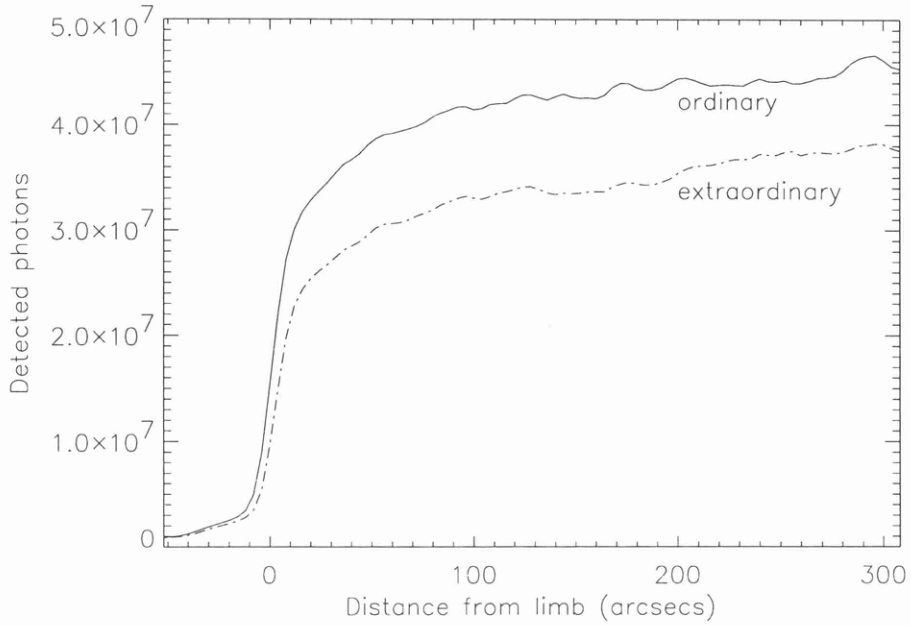

(a) The intensity variation of the western limb.

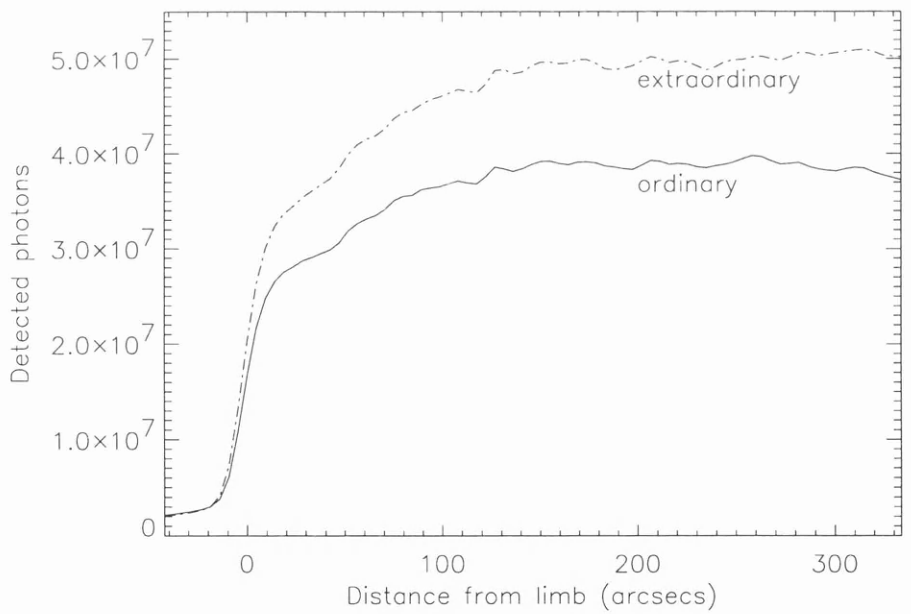

(b) The intensity variation of the north polar region.

Figure 5.2: The center-to-limb intensity variation at a half-wave plate position of $\psi = 0°$ for the north polar and western limb regions of the Sun on the 9 July 1997.

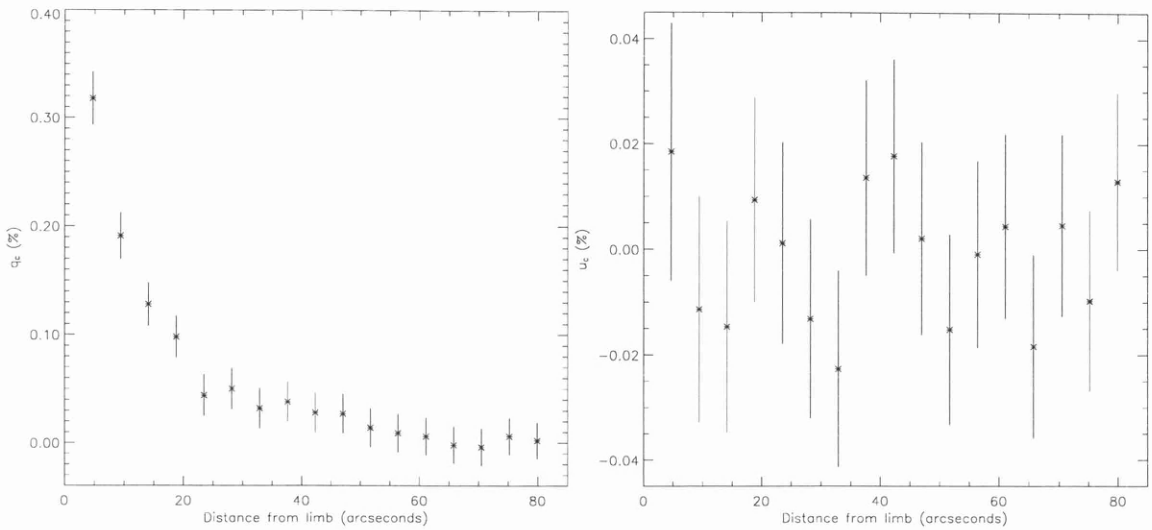

Figure 5.3: The center to polar limb variation of q and u polarization at the Hα core on 9 July 1997.

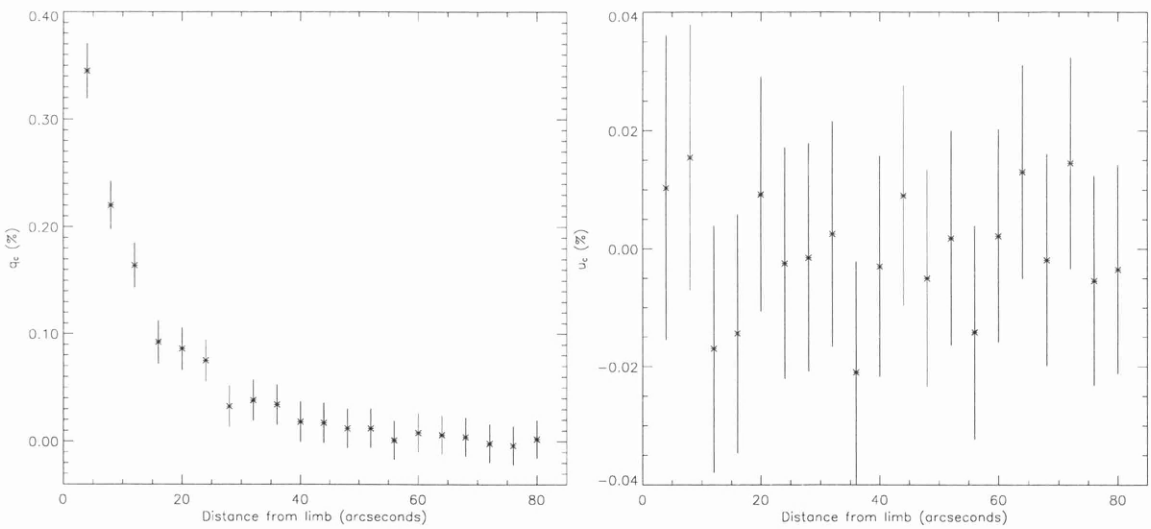

Figure 5.4: The center to equatorial limb variation of q and u polarization at the Hα core on 9 July 1997.

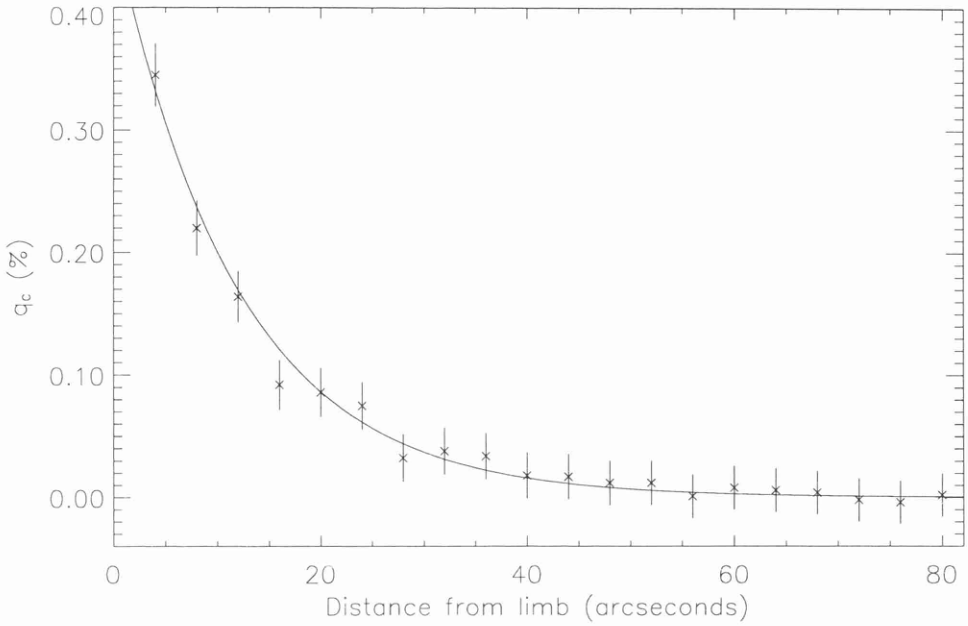

(a) The center to equatorial limb variation of q polarization.

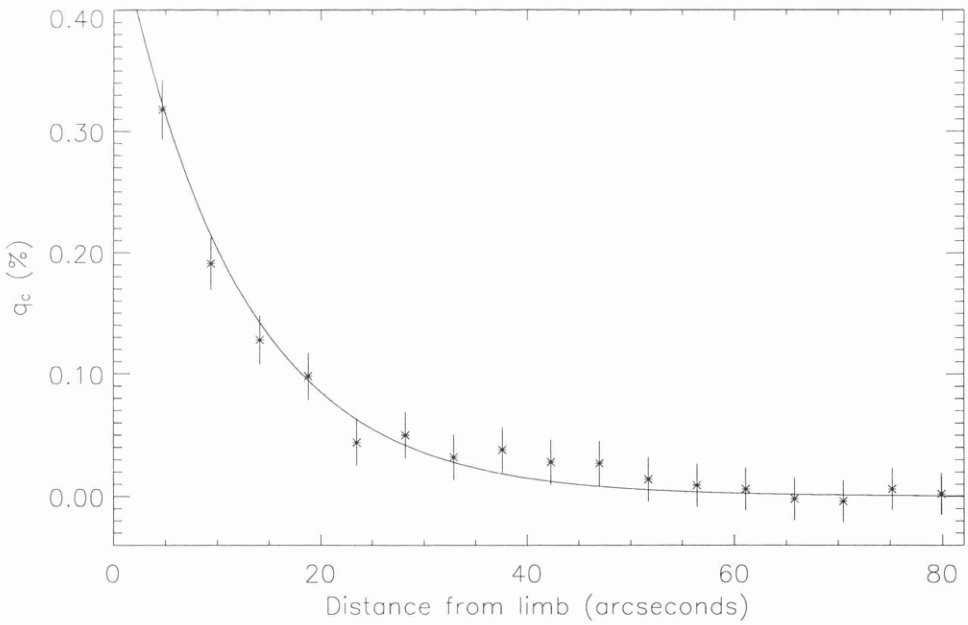

(b) The center to polar limb variation of q polarization.

Figure 5.5: Two plots illustrating the Hα core center-to-limb variation in the q polarization for the equatorial and polar regions of the Sun taken on 9 July 1997. A non-linear least squares fit of the form $q = Ce^{(-D\varpi)}$ has been calculated for each plot.

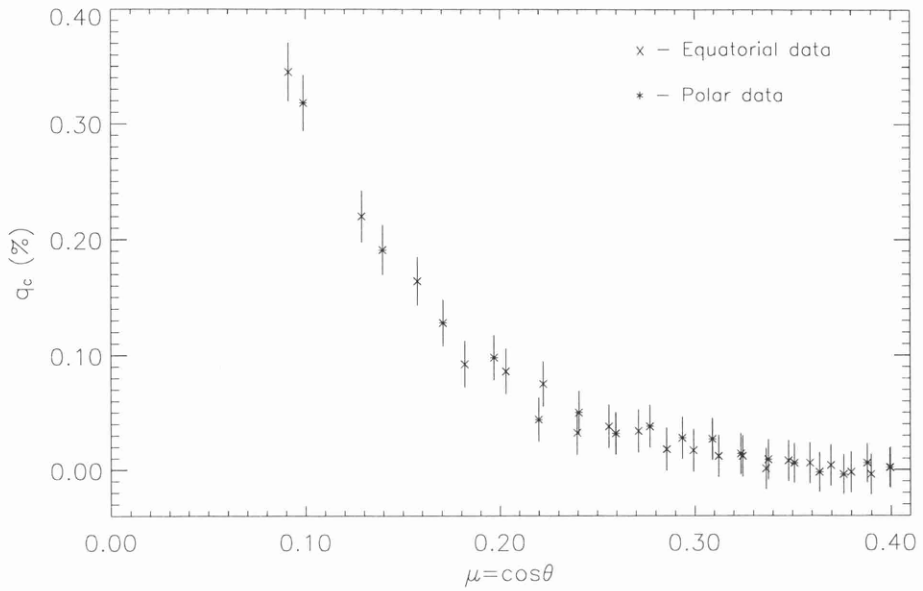

Figure 5.6: The center-to-limb polar and equatorial q polarization plotted versus the heliocentric angle taken on 9 July 1997.

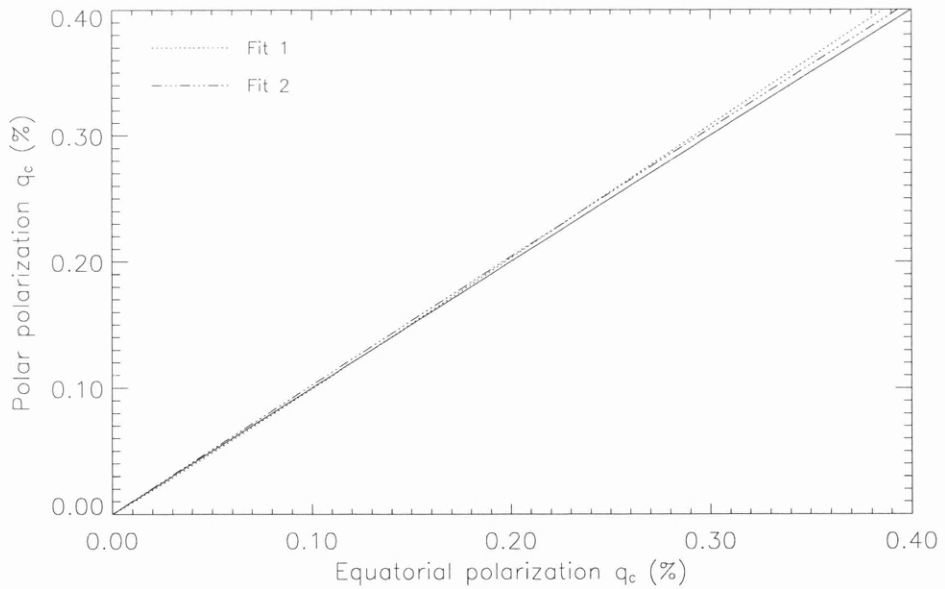

Figure 5.7: The center to pole q polarization versus the center to equator q polarization. The solid line corresponds to the case of identical polarization for the polar and equatorial regions at the same solar position. The dashed lines are the computed least squares fits to the data.

polarization cannot be determined well in regions with no well-defined depolarizing lines, as is unfortunately the case for most spectral regions. The magnitude of the continuum polarization is less than 4% of the maximum polarization amplitude of the Hα line, (see Stenflo et al., 1983a), and consistently much smaller than the measured q values for a limb distance $\mu \leq 0.3$. This illustrates that the measured polarization is significant and not a product of continuum and line mixing.

A semi-analytical expression, Equation 1.17, first introduced by Stenflo and Keller (1997) to describe the center-to-limb behaviour of the Sr I 4607Å resonance line was fitted to the recorded q data for all three wavelengths under consideration. This procedure was unsuccessful due to the steep CLV of the optically thick Hα line. This semi-analytical expression provides a good explanation for optically thin lines but is not applicable to optically thick lines, whose CLV is governed by more complex radiative-transfer effects.

Unfortunately the pixels of the CCD detector were not square but rectangular in shape. This meant that images recorded at the northern limb had a different scale length to those recorded at the western limb. Therefore, to facilitate a direct comparison of the shapes of the various curves at the northern and western limbs, it is necessary to introduce the following empirical expression which provides a good fit to the observed values for the polarization maximum and curve of the line:

$$q = \mathrm{A}e^{(-\mathrm{B}\mu)} \qquad \text{and} \qquad q = \mathrm{C}e^{(-\mathrm{D}\varpi)} \tag{5.2}$$

where A, B, C and D are the parameter values chosen to fit the data, The latter equation expresses the variation of q across the solar surface in arcseconds, ϖ, while the former expresses the variation in terms of μ, the heliocentric angle. This form is the commonly accepted representation in solar physics with μ being the cosine of the angle between the solar radius vector to the scatterer and the line of sight. The curve fitting routine utilises a gradient-expansion algorithm to compute a non-linear weighted least squares fit to the empirical expression with an arbitrary number of parameters, two in this case. Iterations are performed until the chi square values changes by 0.1% or less, or until 20 iterations have been performed. Table 5.1 lists the parameter values for each of the curves with the relevant Figure numbers for reference.

Comparison of the q polarization amplitude CLV for the northern and western limb of the Sun at Hα line may be determined by plotting the q_c(western limb) versus q_c(northern limb) as illustrated in Figure 5.7. The two dashed lines represent the two computed least squares fits to the data, see Figure 5.2, whose parameters are tabulated in Table 5.1, with the solid line corresponding to the case of identical polarization for the polar and equatorial regions at

Date	Wavelength	Region	A	B	C	D	Figure N^o
09 July	6562.5Å	North pole	1.167	13.090	0.485	0.087	5.5 and 5.6
09 July	6562.5Å	Western limb	1.154	13.151	0.466	0.084	5.5 and 5.6
19 July	6562.5Å	North pole	1.093	13.169	0.464	0.091	5.11
20 July	6562.2Å	North pole	0.980	13.640	0.380	0.092	5.16 and 5.17
20 July	6562.2Å	Western limb	0.891	13.820	0.352	0.091	5.16 and 5.17
20 July	6562.8Å	North pole	0.924	13.226	0.367	0.084	5.22 and 5.23
20 July	6562.8Å	Western limb	0.897	13.219	0.340	0.085	5.22 and 5.23

Table 5.1: The parameters A, B, C and D for the empirical expression introduced in Equation 5.2 in a tabulated form.

the same solar position. This plot indicates a small difference in the two polarization profiles, suggesting that the polar polarization is slightly greater than the equatorial polarization towards the limb. However, by shifting the polar curve with respect to the equatorial curve along the limb distance and minimising the residual or difference function defined by,

$$\Delta_{residual} = \sqrt{\frac{[q(\varpi)_{polar} - q(\varpi)_{equatorial}]^2}{n}} \tag{5.3}$$

it is possible to determine whether this enhancement is intrinsically a solar effect or a systematic positional error. This digitisation problem is due to the finite size of the detector pixel and may contribute to differences in the two curves. However, it may be removed by shifting the polar curve 0.82 arcseconds with respect to the equatorial curve thus minimising the function $\Delta_{residual}$ and making it is possible to infer that no significant difference exists between the polarization CLV of the two regions under investigation to a precision exceeding 0.5%. However, the spatial resolution of the imaging polarimeter during excellent seeing conditions does not exceed 4 arcseconds and hence this small corrective factor may not be investigated by shifting the actual solar images and recalculating the q polarization amplitudes accordingly. The q_c amplitude CLV recorded on 9 and 20 July is shown in Figure 5.25. The two data sets show good reproducibility well within the observational uncertainties. The main source of uncertainty is the determination of the limb position and hence even if μ does not suffer from systematic errors, some scatter is introduced by image motion into q. The μ value may change significantly in an exposure close to the limb lasting several seconds. The comparison between the different data sets shows that it is possible to obtain consistency after very careful corrections for the effects of limb position and transparency problems. The spread of the data points illustrates the degree of reproducibility of the results.

Conducting a similar analysis comparing the polar and equatorial polarization for the two other wavelengths under consideration yields similar results to Hα. Initially, inspection of the

q_b and q_r CLV's in Figure 5.18 and Figure 5.24 respectively yields the surprising result that the polar polarization is significantly greater than the equatorial polarization, 13% greater in the blue-wing and 9% in the red-wing. However, by shifting the polar curve with respect to the equatorial curve and minimising the residual function the apparent polarization enhancement disappears. A shift of 1 arcsecond for the blue-wing data and 0.2 arcseconds for the red-wing data minimises the residual function accordingly.

Inspection of Figures 5.6, 5.17 and 5.23 reveals that the line core and the line wings exhibit a similar CLV but with differing polarization amplitudes. The difference in behaviour between line-center and wings is much clearer by eliminating μ by plotting q_r, q_c vs q_b. The top plot in Figure 5.26 shows red-wing q_r vs blue-wing q_b. The relationship between the q of the two wings remains remarkably linear over a large range of μ values. It may be described by the linear regression passing through the origin (in units of % polarization)

$$q_r = 0.99 q_b, \tag{5.4}$$

which is also plotted. Increasingly, q_r is of approximately the same magnitude as q_b. Even more remarkable is the small scatter exhibited by the data points. The standard deviation of the points around this regression is 0.010 and is a measure of the total uncertainty in the line parameters. This value is half the value expected from the photon and instrumental noise, which suggests that the profile shape in the wings is extremely stable.

The line-center q_c plotted vs blue-wing q_b, bottom plot in Figure 5.26, shows a different picture. The relationship between the q of the center to the wings may be described by the linear regression passing through the origin (in units of % polarization)

$$q_r = 0.79 q_c, \tag{5.5}$$

at least a 2σ difference. The standard deviation of the points around the regression is 0.017. The scatter is large, much larger than that which any observational uncertainties could be expected to introduce. The two most obvious trends are the expected increase of q towards the limb, and the increase of the scatter of a prior unknown origin. An analysis of the noise and uncertainties in the line profiles suggests that this increased scatter is not just due to instrumental noise. A major observational uncertainty is the value of μ, which due to the steep CLV of q near the limb leads to a larger scatter there. Another consideration for this scatter may be a solar source, the most likely is the Hanle effect, since it acts almost exclusively on the line core, while leaving the wings unaffected. In the presence of a magnetic field the Hanle effect depolarizes the line core and rotates the direction of linear polarization. The depolarization depends on the strength and direction of the magnetic field. Therefore a

magnetic field that varies spatially in strength or direction can produce a scatter in the core-to-wing q ratio, since solar locations were randomly sampled with different field strengths or directions.

Inspection of the two plots in Figure 5.27 where the ratios q_c to q_b and q_r to q_b are plotted versus μ shows a tight relationship up to a limb distance of $\mu = 0.3$. Thereafter there is a significant amount of scatter which is related to the diminishing signal-to-noise ratio. The upper plot shows the tight relationship of the q_r to q_b ratio around unity up to a limb distance of $\mu = 0.3$. The q_c to q_b ratio lies around 1.3 but with a larger amount of scatter tending to increase towards the center, also illustrated in the lower plot of Figure 5.26.

Recent observations of the Hα line by Stenflo et al. (1997), as illustrated in Figure 1.7, and Keller (1998) in November 1994 yield the following polarization amplitude values for three northern limb positions (in units of % polarization),

$$\left.\begin{array}{l} \frac{p(\mu_{0.10})}{p(\mu_{0.15})} = \frac{0.299}{0.148} = 2.02 \\ \frac{p(\mu_{0.15})}{p(\mu_{0.20})} = \frac{0.148}{0.075} = 1.97 \\ \frac{p(\mu_{0.10})}{p(\mu_{0.20})} = \frac{0.299}{0.075} = 3.99 \end{array}\right\} \tag{5.6}$$

with an uncertainty of 0.002%. The corresponding ratios recorded in Glasgow on the 9 July in Hα for comparison (in units of % polarization) are as follows,

$$\left.\begin{array}{l} \frac{p(\mu_{0.10})}{p(\mu_{0.15})} = \frac{0.313}{0.162} = 1.93 \\ \frac{p(\mu_{0.15})}{p(\mu_{0.20})} = \frac{0.162}{0.084} = 1.94 \\ \frac{p(\mu_{0.10})}{p(\mu_{0.20})} = \frac{0.313}{0.084} = 3.73 \end{array}\right\} \tag{5.7}$$

with an uncertainty of 0.02%, a factor of 10 worse than the previous observations. A comparison of the previous data recorded in November 1994 with recent observations recorded in July 1997 illustrates the good agreement, to within 7%, in the recorded q polarization values between the different data sets. The data obtained by Stenflo et al. (1997) were taken using a small aperture running from the limb to the center in order to record the CLV. This accounts for the high photon accuracy, i.e. long integration times at each μ position, but this method introduces erroneous positional uncertainties.

Earlier observations of the solar disk in Hα were conducted by Stenflo et al. (1983b) at a limb distance of 10 arcseconds, $\mu = 0.144$, from the heliographic north pole recording a polarization $p = 0.17\% \pm 0.01\%$. This is in good agreement with the present observations which yield $p = 0.18\% \pm 0.02\%$.

There is no significant polarization in the u parameter at or across the solar limb in any of three wavelengths selected for investigation. Inspection of the u curve profiles in Figure 5.15

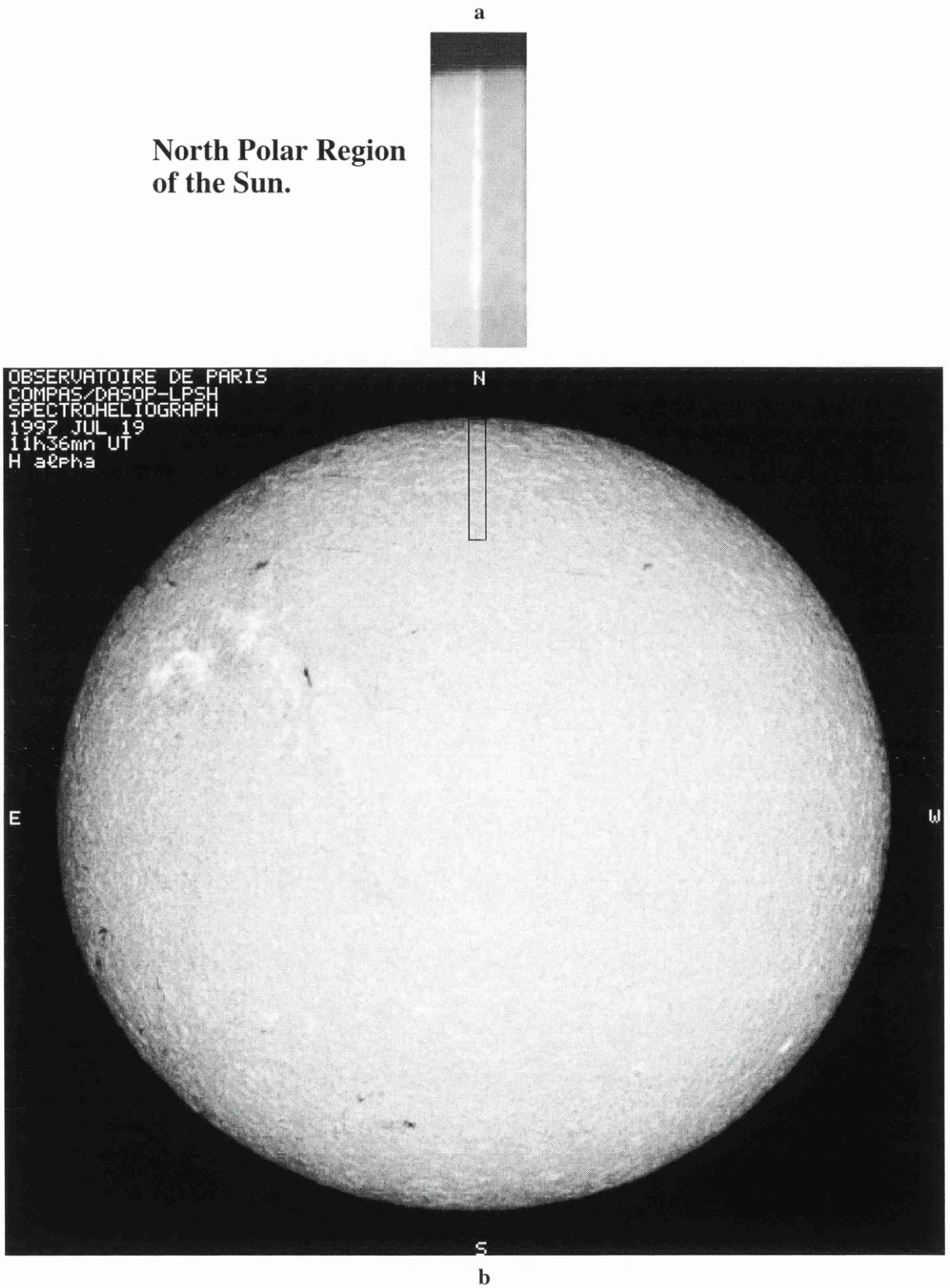

Figure 5.8: Two Hα core exposures of the Sun taken on 19 July 1997: (a) North polar region, (b) whole solar disk taken at the Observatoire de Paris. The rectangle corresponds to the polarimeter's field of view on the solar disk.

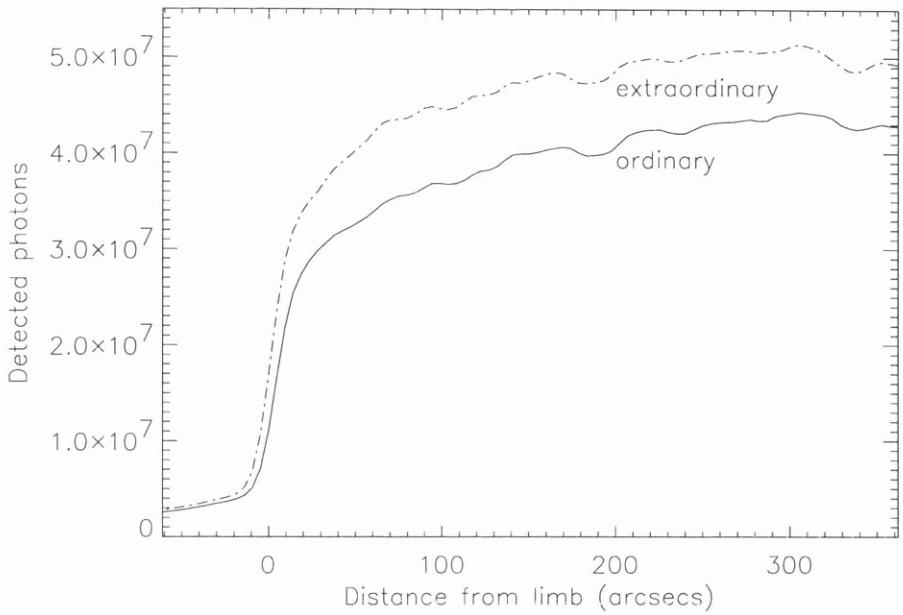

Figure 5.9: The center-to-limb intensity variation at a half-wave plate position of $\psi = 0°$ for the north polar region of the Sun taken on the 19 July 1997.

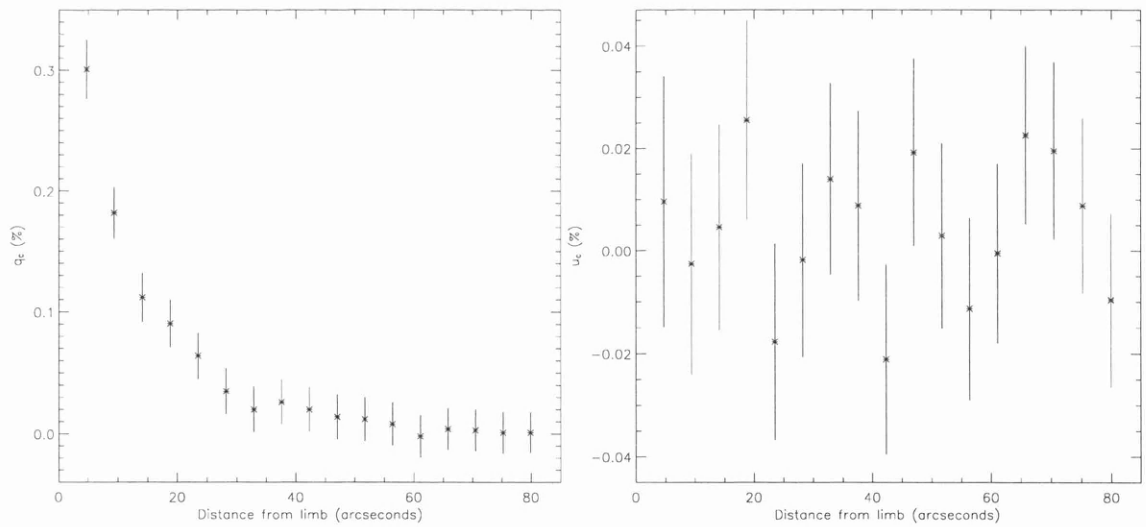

Figure 5.10: The center to polar limb variation of q and u polarization at Hα core taken on 19 July 1997.

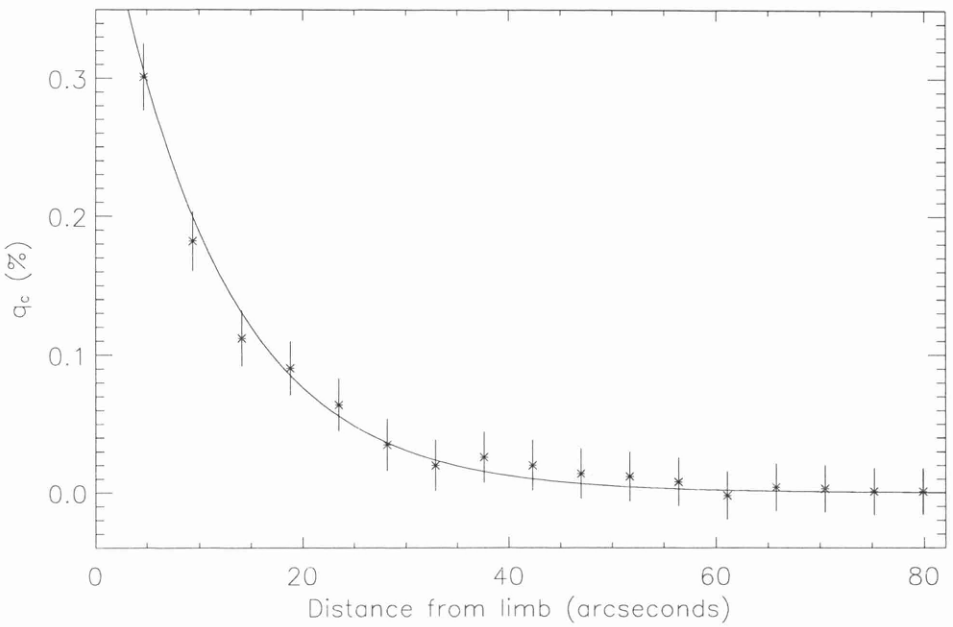

(a) The center to polar limb variation of q polarization.

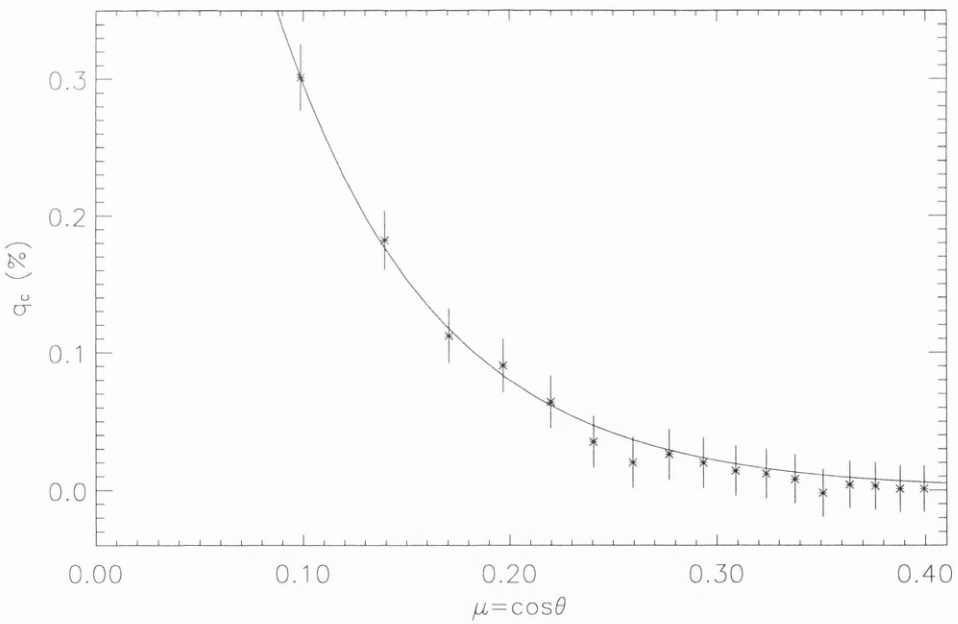

(b) The center to polar limb variation of q polarization.

Figure 5.11: Two plots illustrating the Hα core center-to-limb variation in the q polarization for the polar regions of the Sun on the 19 July 1997. A non-linear least squares fit of the form $q = Ce^{(-D\varpi)}$ has been calculated for each plot.

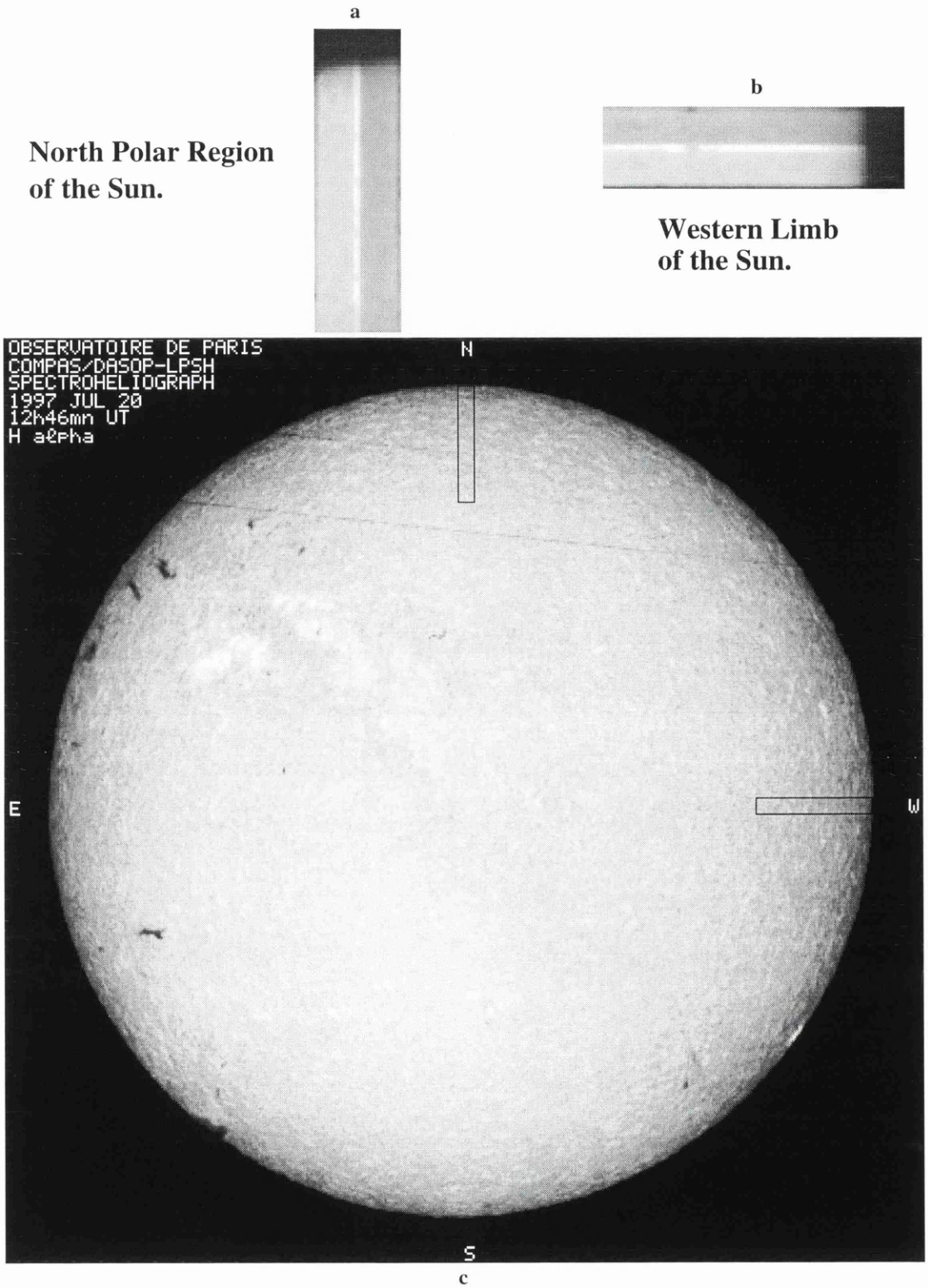

Figure 5.12: Two Hα blue-wing exposures of the Sun taken on 20 July 1997: (a) North polar region, (b) western limb and (c) a Hα whole solar disk image taken at the Observatoire de Paris. The rectangles correspond to the polarimeter's field of view on the solar disk.

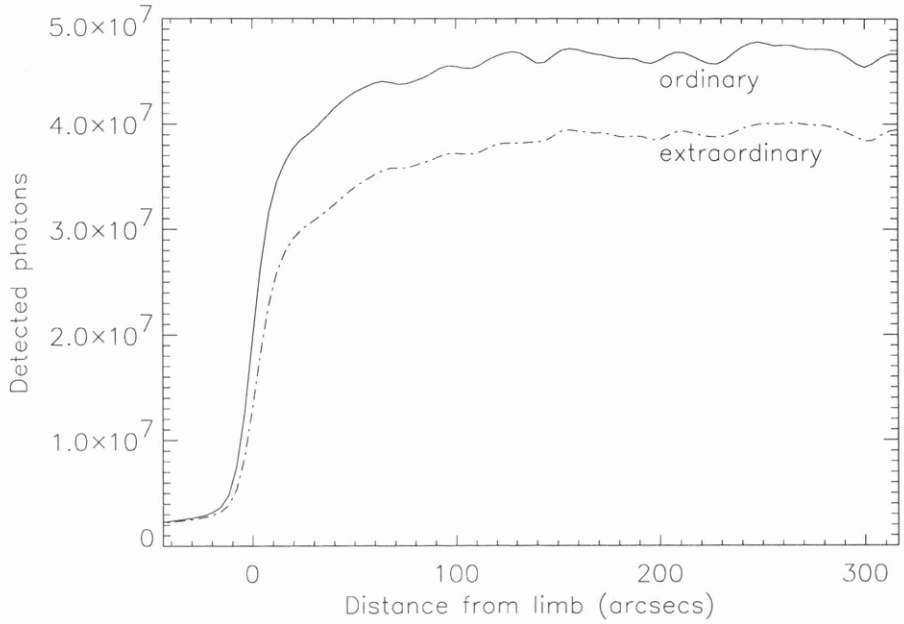

(a) The intensity variation of the western limb.

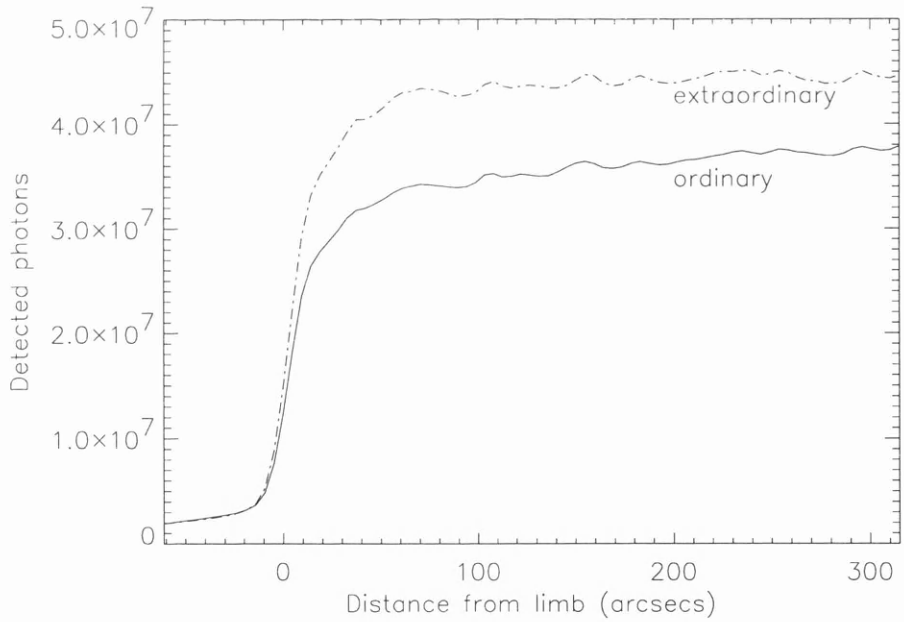

(b) The intensity variation of the north polar region.

Figure 5.13: The center-to-limb intensity variation at a half-wave plate position of $\psi = 0°$ for the north polar and western limb regions of the Sun taken on the 20 July 1997.

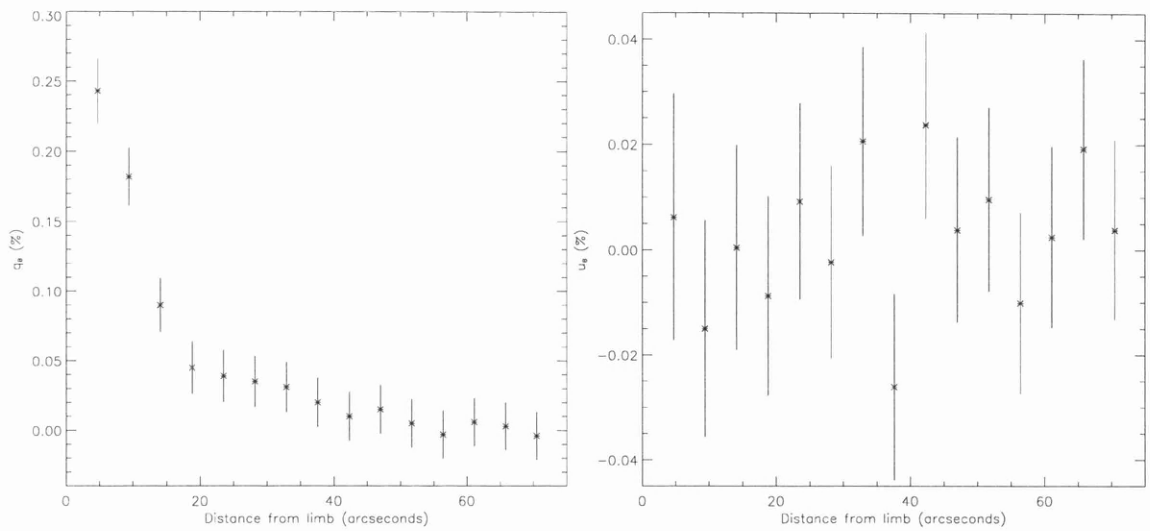

Figure 5.14: The center to polar limb variation of q and u polarization at the Hα blue-wing taken on the 20 July 1997.

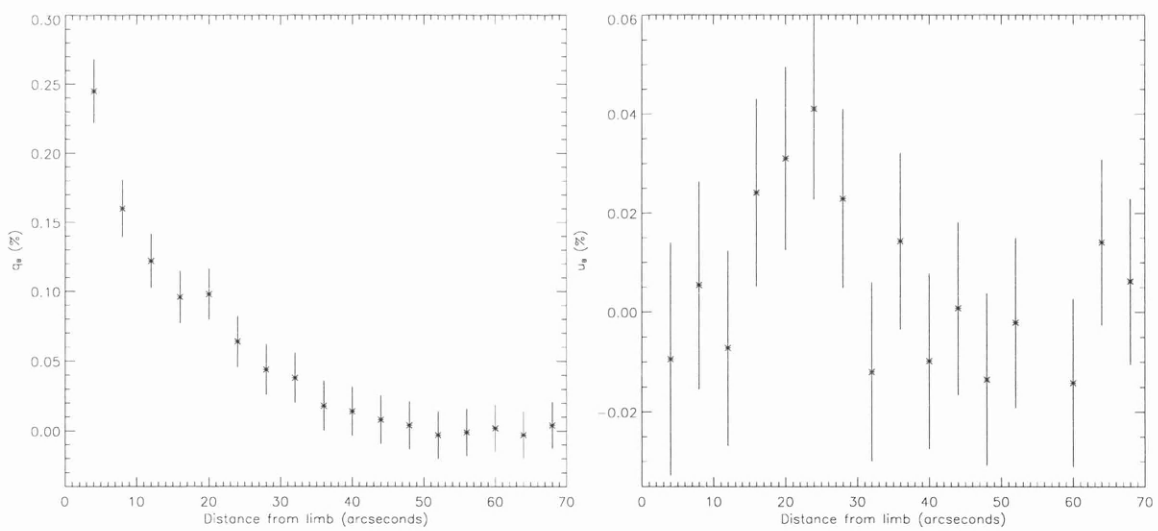

Figure 5.15: The center to equatorial limb variation of q and u polarizaton at the Hα blue-wing taken on 20 July 1997.

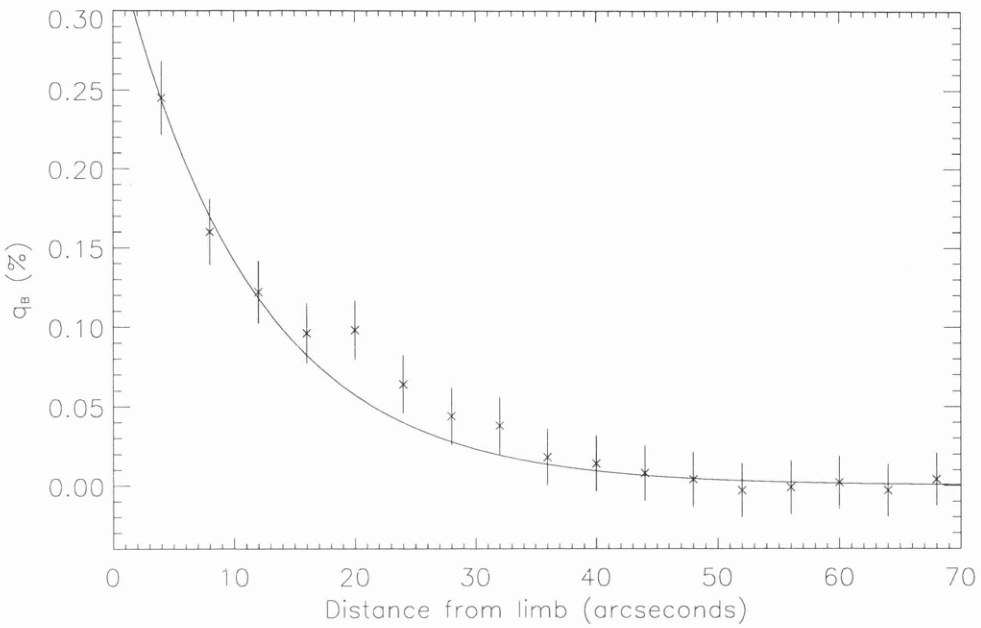

(a) The center to equatorial limb variation of q polarization.

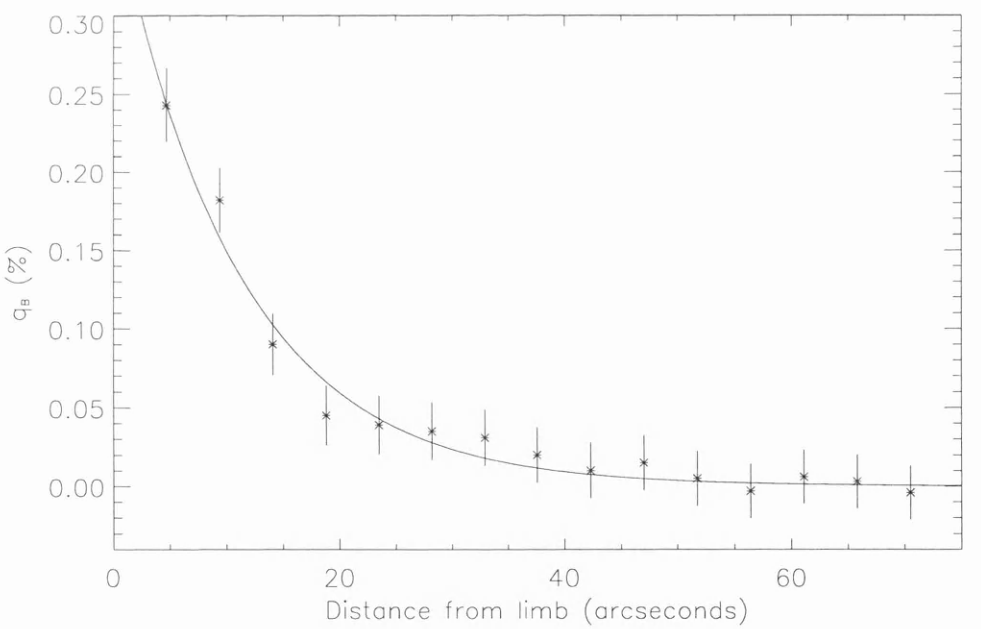

(b) The center to polar limb variation of q polarization.

Figure 5.16: Two plots illustrating the Hα blue-wing center-to-limb variation in the q polarization for the equatorial and polar regions of the Sun. A non-linear least squares fit of the form $q = Ce^{(-D\varpi)}$ has been calculated for each plot.

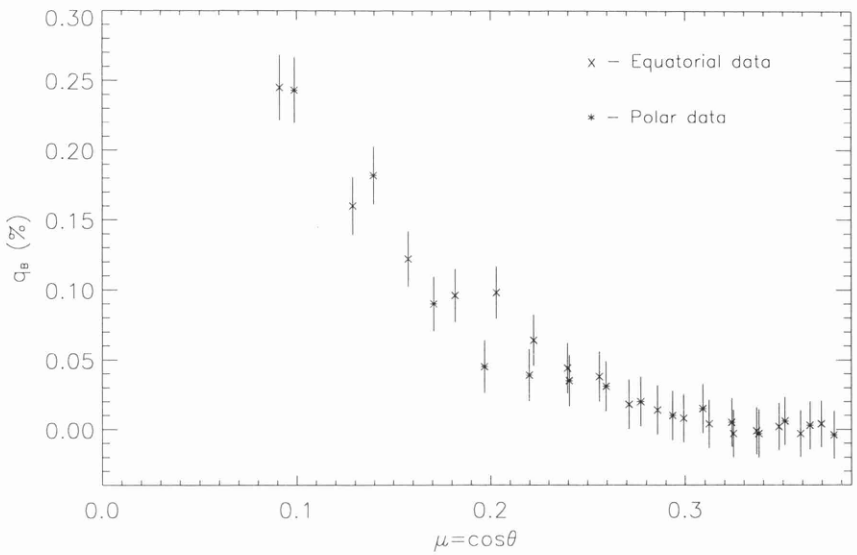

Figure 5.17: The center-to-limb polar and equatorial q polarization plotted versus the heliocentric angle taken on the 20 July 1997.

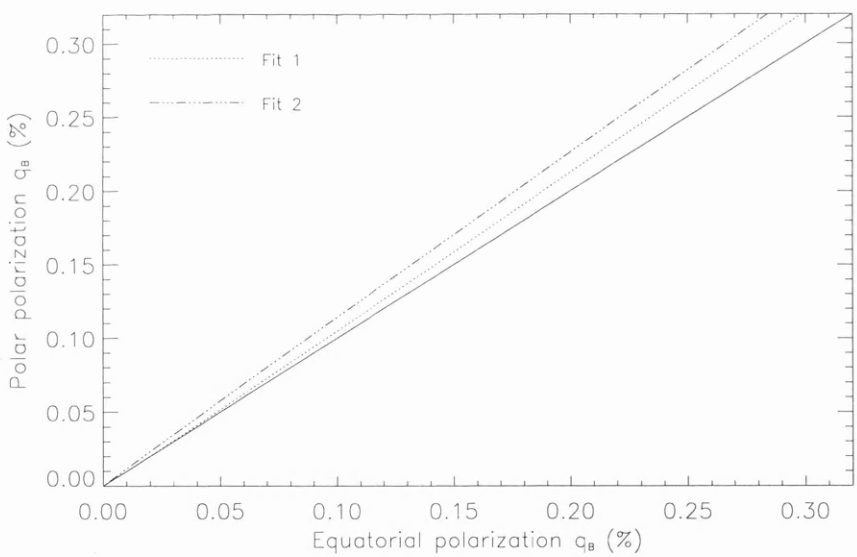

Figure 5.18: The center to pole q polarization versus the center to equator q polarization. The solid line corresponds to the case of identical polarization for the polar and equatorial regions at the same solar position. The dashed lines are the computed least squares fits to the data.

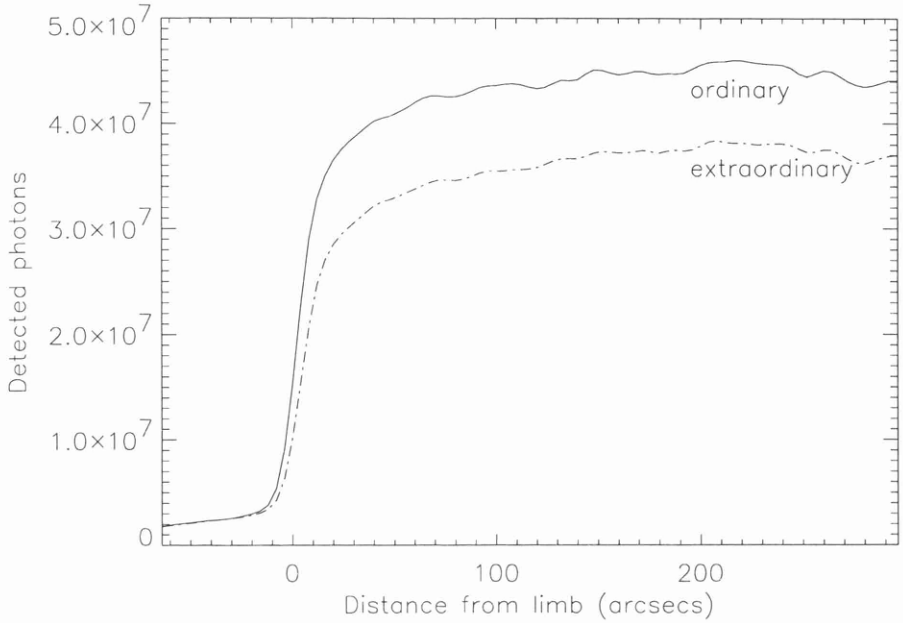

(a) The intensity variation of the western limb.

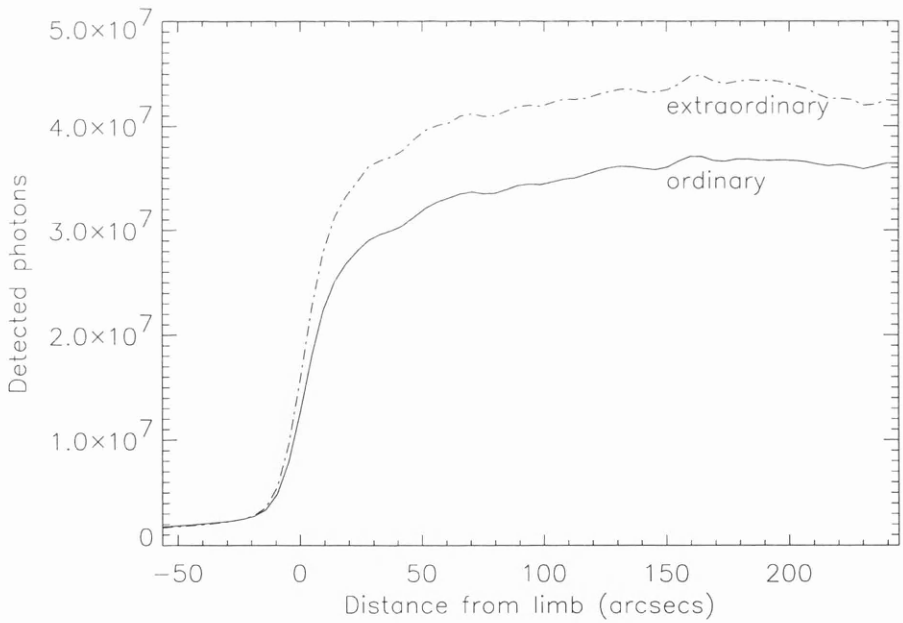

(b) The intensity variation of the north polar region.

Figure 5.19: The center-to-limb intensity variation at a half-wave plate position of $\psi = 0°$ for the north polar and western limb regions of the Sun on the 20 July 1997.

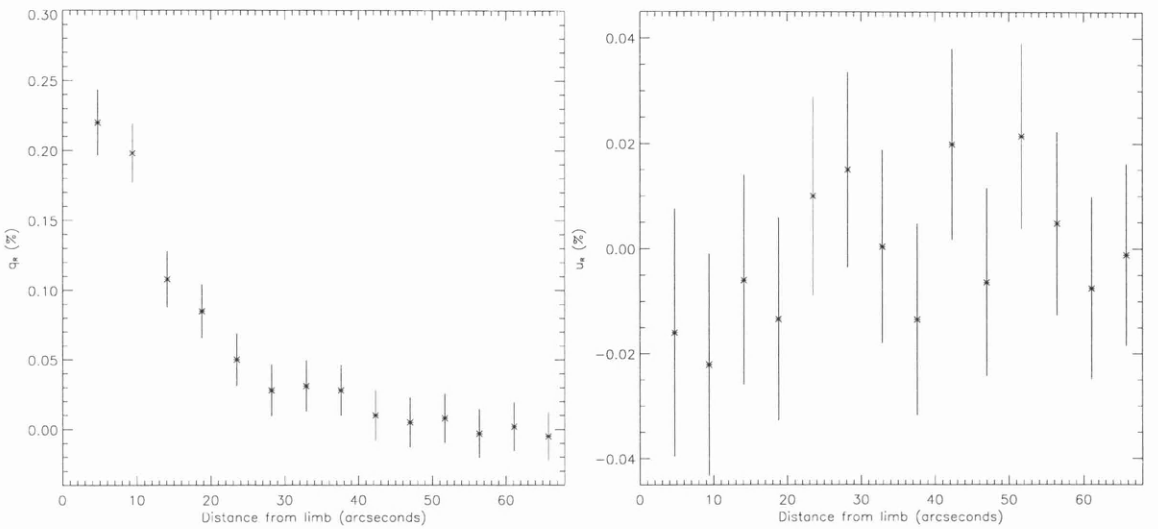

Figure 5.20: The center to polar limb variation of q and u polarization at the Hα red-wing taken on 20 July 1997.

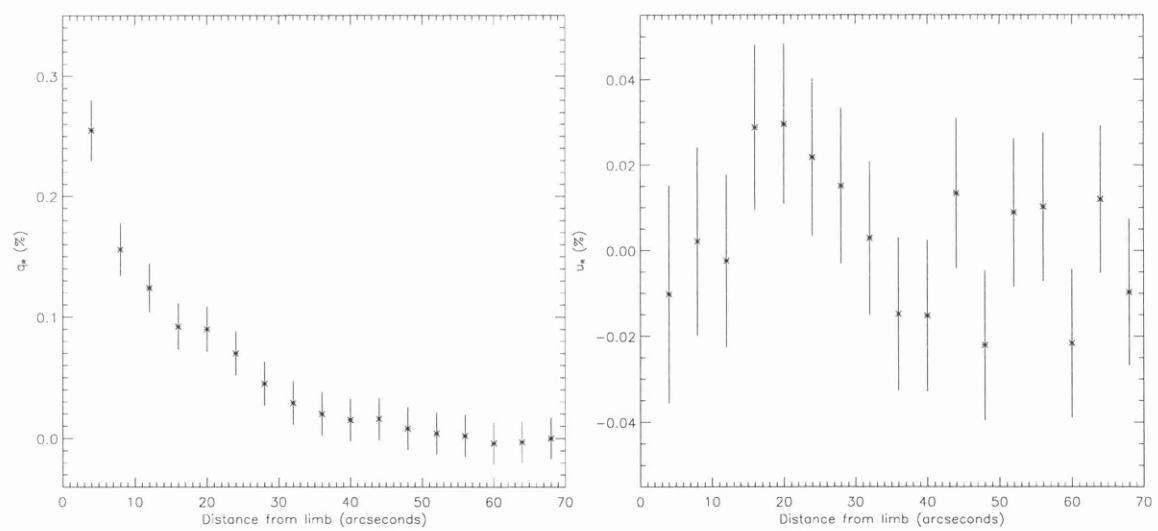

Figure 5.21: The center to equatorial limb variation of q and u polarization at the Hα red-wing taken on 20 July 1997.

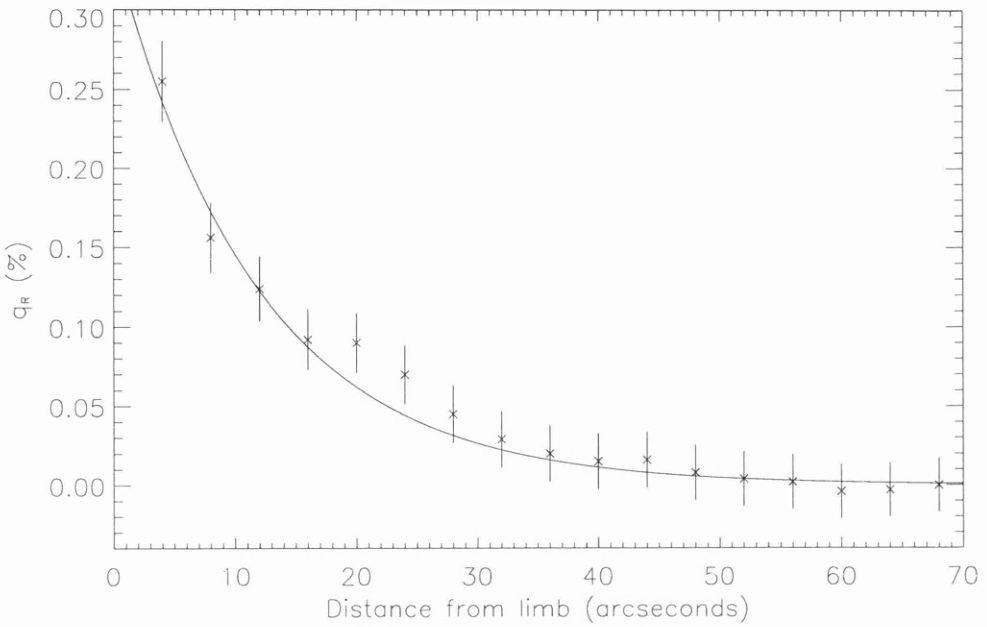

(a) The center to equatorial limb variation of q polarization.

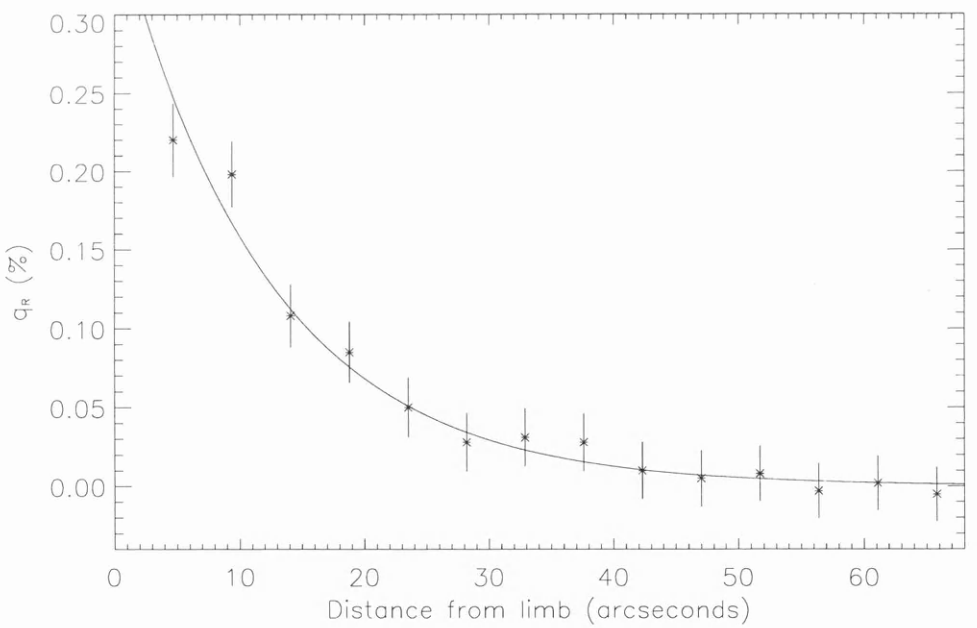

(b) The center to polar limb variation of q polarization.

Figure 5.22: Two plots illustrating the Hα red-wing center-to-limb variation in the q polarization for the equatorial and polar regions of the Sun. A non-linear least squares fit of the form $q = Ce^{(-D\varpi)}$ has been calculated for each plot.

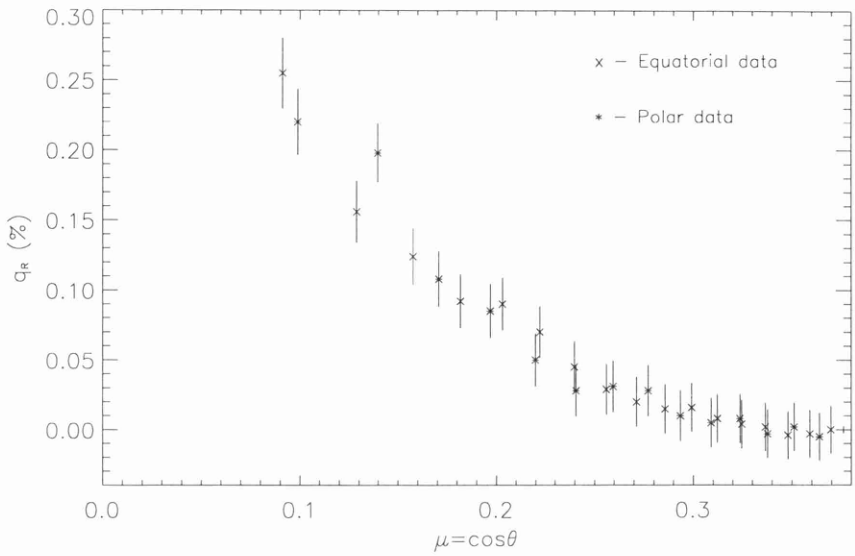

Figure 5.23: The center-to-limb polar and equatorial q polarization plotted versus the heliocentric angle taken on 20 July 1997.

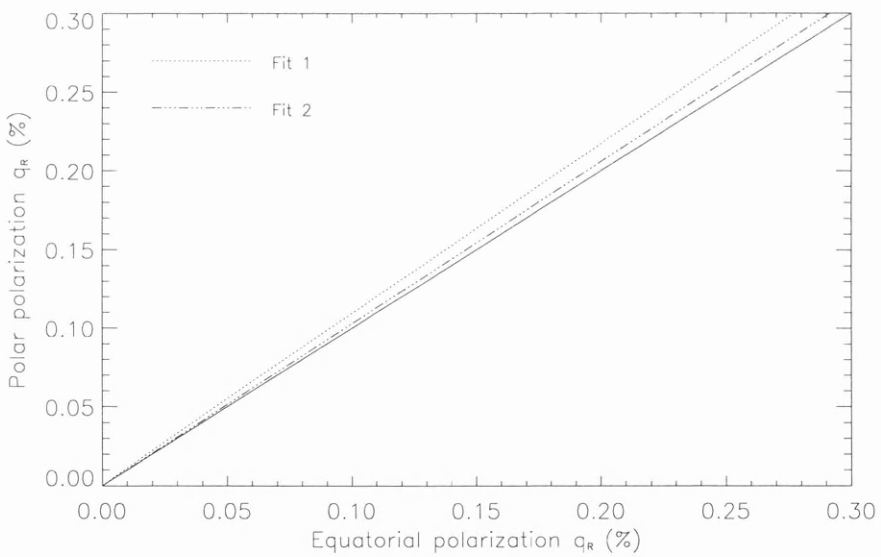

Figure 5.24: The center to pole q polarization versus the center to equator q polarization. The solid line corresponds to the case of identical polarization for the polar and equatorial regions at the same solar position. The dashed lines are the computed least squares fits to the data.

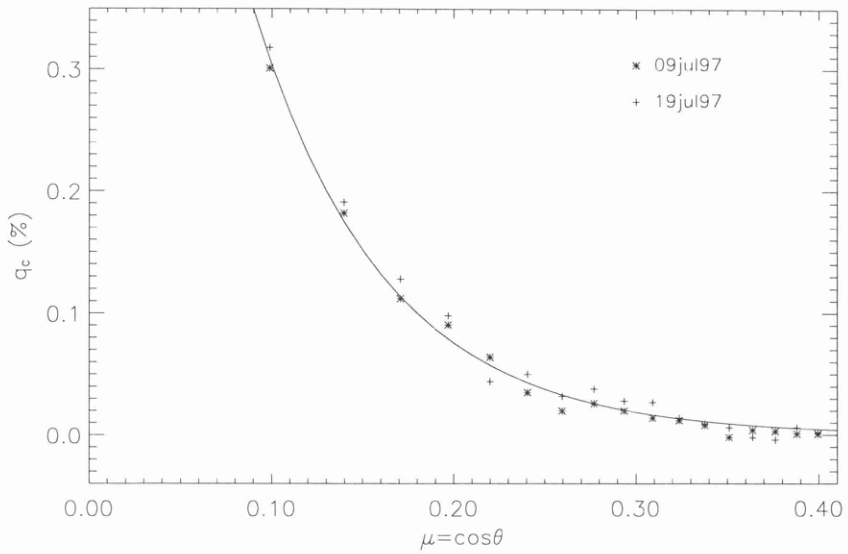

Figure 5.25: The center to polar limb q polarization at the Hα core for the 9 and 19 July. The solid curve corresponds to the best fit to the two data sets.

and Figure 5.21 reveal slight enhancements in polarization above the background level and this will be discussed further in Section 5.3.2. These results confirm that the polarization vector is generally aligned tangential to the limb. The small spread of the data points indicates the degree of reproducibility of the results. Although some of this spread may be of instrumental origin, there is clear evidence that part of the variation is intrinsically solar. This is evident in the CLV q curves where the amplitude is measured from the zero point of the polarization scale, which has been determined from observations of the solar center. The true zero of the polarization scale would have to be determined with respect to the neighbouring continuum line at the disk center.

5.3.2 Discussion

New low noise (0.02%) observational data for the center-to-limb variation (CLV) of the scattering polarization for the Hα line are presented at two locations, the northern and western limbs, on the quiet Sun. Although some information of the slope of the CLV curve is available for Hα at certain values of μ (see Stenflo et al., 1983a and Stenflo and Keller, 1997), and a number of different spectral lines, the only two lines for which the full CLV curve has been investigated in detail (apart from a few CLV curves from 1978 observations by Stenflo

et al., 1980) are the Sr I 4607Å and Ca I 4227Å lines. The Hα line is an optically strong line extending over a 4Å wavelength range and is surrounded by a clean continuum and formed in the lower regions of the chromosphere.

The polarization at the solar limb was found to be much higher in Hα than in the nearby continuum for the three wavelengths under investigation. No distinction in the general behaviour of the center-to-limb variation could be found between equatorial and polar regions for all three wavelengths. The polarization was found to decline by a factor of four when going from $\mu = 0.1$ to $\mu = 0.3$, a much steeper decline than other lines studied previously, as illustrated in Figure 1.7. The polarization in the core of Hα was found to be higher by at least 2σ with respect to the off-band measurements in the red- and blue-wings. The polarization decreases when moving out into the wings, because the ratio between the line and continuum opacities decreases, and the continuum is less polarized than the line. The CLV in polarization recorded in the blue- and red-wings were similar in amplitude and general behaviour as illustrated in the analysis presented in Section 5.3.1. The ratio of the blue- to red-wing polarization remains strictly constant, the line core shows a slightly larger scatter relative to the wings. This scatter is marginally larger than expected from the error budget. It may be interpreted in terms of either the Hanle depolarization of the line core by a weak field or due to positional uncertainties on the solar disk.

Observations recorded by Leroy (1972) infer a contentious result that the solar equatorial polarization is approximately ten percent larger than at the poles at a wavelength of 3820Å, in the UV. A number of instrumental and data reduction effects must be considered before the astrophysical implication of these results may be discussed. Foremost is the differential refraction effect in the Earth's atmosphere which introduces an apparent different scale length along the polar axis with respect to the equatorial axis. This effect is dependent on the Sun's altitude during observations, as shown in Figure 2.18 and may become dominant at low altitudes. Another important factor is the positioning of the instrument on the solar disk. The analysis conducted in Section 5.3.1 demonstrates that a slight misalignment or uncertainty in positioning has a great effect upon the polarization value recorded, especially near the limb where the CLV is varying most rapidly. The final factor, (see Leroy, 1997), is the possible contamination or mixing of the continuum (scattering) and the line (magnetic intensification) opacities and the extraction of the observed polarization of the line, especially in the UV. A likely physical explanation for the greater polarization at the equator with respect to the pole is the Hanle effect, which acts on the line core. Assuming the Sun has a classical dipole magnetic field suggests a greater magnetic field strength at the poles where the magnetic flux

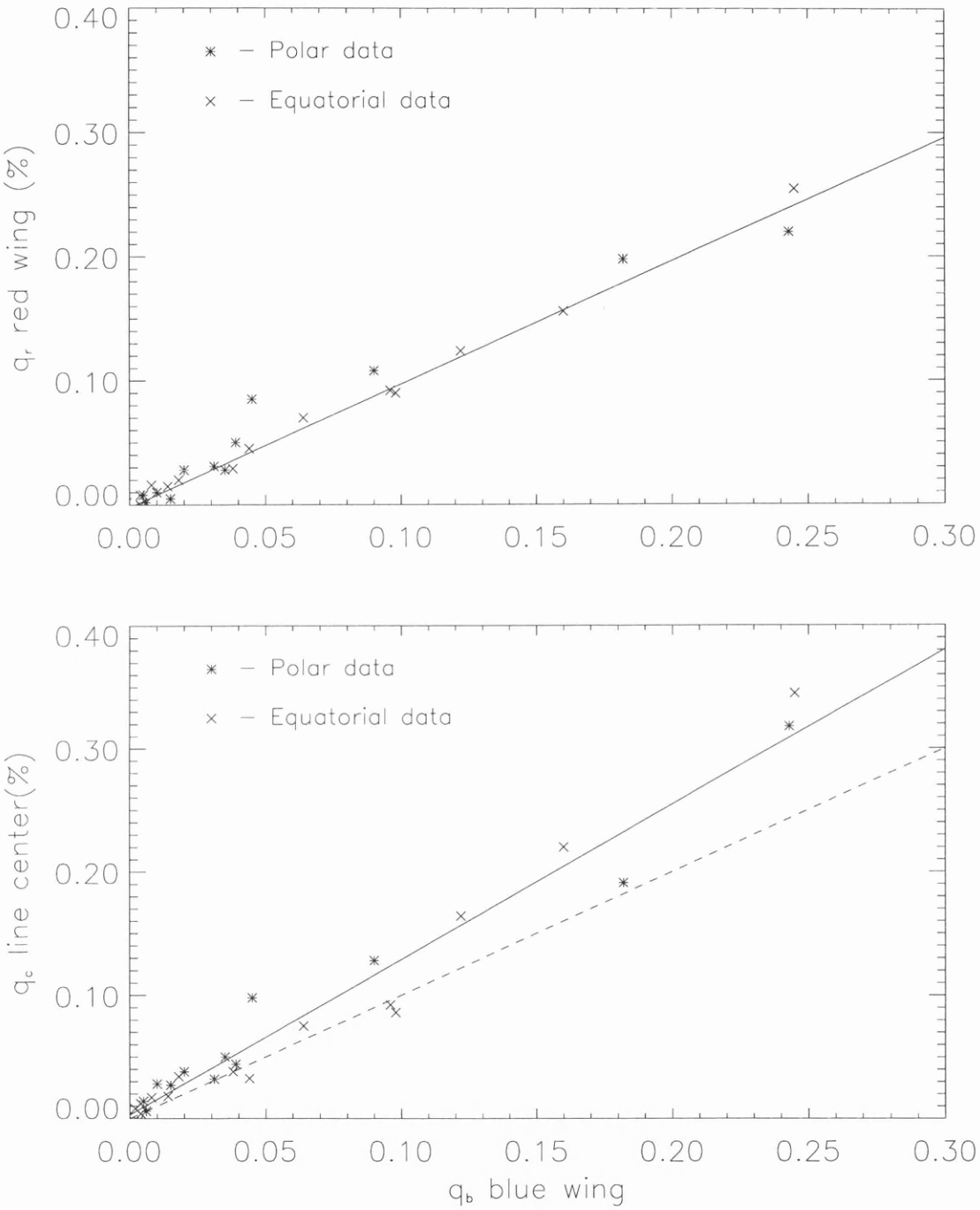

Figure 5.26: Red-wing q (top) and line-center q (bottom) versus blue-wing q. The straight line in the top plot is a linear fit to the data. The dashed line in the bottom plot corresponds to the case of identical polarization for the line-center and blue-wing.

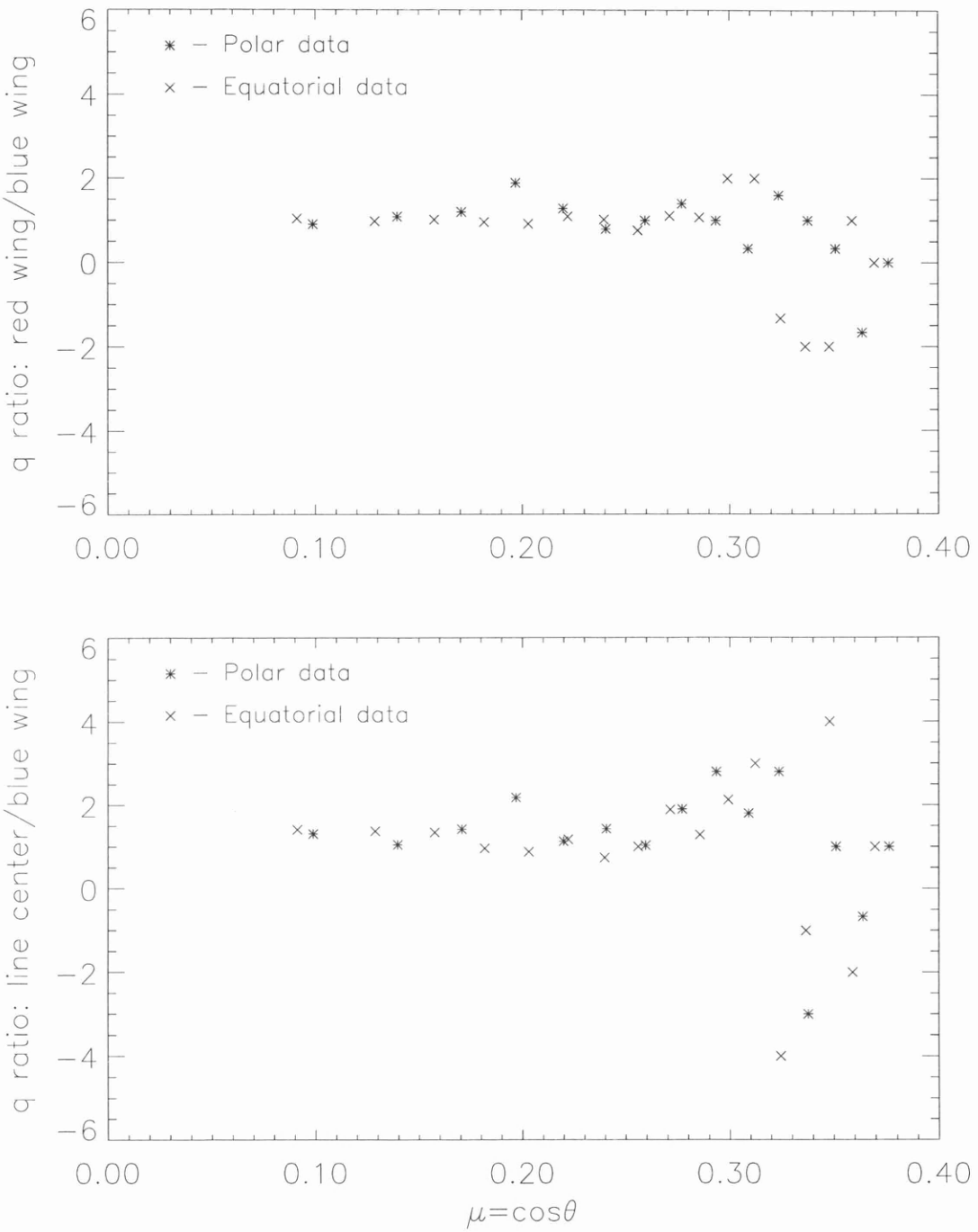

Figure 5.27: Top: CLV of the red-wing to blue-wing q ratio. Bottom: CLV of the line-center to blue-wing q ratio. The error associated with each data point is comparable to size of the plotted symbol.

is greatest. This increased field strength may cause a decrease of polarization with respect to a region of lower magnetic flux, i.e. the equator, and a rotation of the plane of polarization. The depolarization depends on the strength and direction of the magnetic field. Another likely physical explanation is that the 1972 polar observations cut across a region that had more of Hanle-depolarizing magnetic fields inside limb zone as compared with the case for the equatorial region.

As stated previously the lack of spread of the data points indicates the high degree of reproducibility of the results. There is clear evidence on the 20 July of a statistically significant intrinsically solar variation at a distance of 20 arcseconds in the u and q Stokes parameters in both the blue- and red-wings of the Hα line. This evidence is directly seen in Figure 5.15 and Figure 5.21 for the u and q normalised Stokes parameters. The CLV of the u and q amplitude shows a very pronounced kink near $\mu = 0.2$ indicating the parameter has a non-zero value, which means that the plane of polarization is not parallel to the limb. These kinks are present in both the blue- and red-wing data sets and indicate a general increase in polarization in the region of the solar limb centered on $\mu = 0.2$. Unfortunately due to the prevailing weather conditions at the observing site it was not possible to record the Hα core CLV, and therefore no comparison may be made. Calculations from the Stokes parameters show that the direction of vibration of linear polarization in the line has been rotated by 16° in the blue-wing and 10° in the red-wing. There is no possibility that such kinks in the curves could be produced by instrumental effects, concluding therefore that they must be intrinsically solar. Without any further analysis it is possible to state that the field whose influence is observed is relatively weak (since it does not completely destroy the resonance polarization), and that it is chromospheric (since the core of Hα is formed in the lower or middle chromosphere). These enhancements from the smooth CLV curve may be related to a variety of factors including the spatially varying Hanle effect on the Sun.

A possible mechanism that could enhance the polarization is related to the presence in the chromosphere of accelerated motions. Their effect on the line formation process is not simply equivalent to a convolution of the profile by a Gaussian distribution, because the absorption profile varies along a given line of sight. This kind of effect is analogous to the so-called Doppler-dimming which has been investigated for some coronal emission lines (see for example Beckers and Chipman, 1974). For chromosphere absorption lines it certainly yields an enhancement of the anisotropy of the radiation field and, as a consequence, an enhancement of the resonance polarization. However such an effect should be observed close to the solar limb as well as on the solar disk.

It is not in the scope of the present discussion to study this kind of phenomenon, but rather to examine the Hanle effect due to a weak magnetic field in the chromosphere. It is possible to enhance the line polarization observed on the disk, provided the magnetic field has a horizontal component located below the depth where the line is formed and which then vanishes in the line forming region. It has been shown by Faurobert-Scholl (1994) that the Hanle effect due to a magnetic canopy lying below the height where the line core is formed actually causes an increase in line core polarization as compared to its non-magnetic value. This surprising effect is a consequence of multiple scattering of line photons in the chromosphere. In the case of the Ca I 4227Å the line core polarization goes through a positive maximum between 700km and 900km and becomes negative (parallel to the solar limb) at higher altitudes, where it does not change anymore. The Hanle effect of a weak magnetic field located in the region of the positive maximum locally decreases the positive contribution, so that the emergent negative polarization gets enhanced as compared to the non-magnetic situation. This phenomenon disappears if the magnetic field lies too deep in the chromosphere, in regions where the polarization source function is very small, or if it lies too high, in regions where it is negative. This explains why the enhancement of the polarization appears only where the altitude of the canopy base lies between 700km and 1000km.

Another method for understanding the effect of the canopy base is to consider the following argument. The linear polarization of the Ca I 4227Å line is close to zero in the photosphere and it reaches a quite high positive maximum in the region between 700km and 1000km. It becomes negative when the line optical depth, τ_o, becomes smaller than unity. The Hanle effect in the region of the positive maximum moves the whole curve down and so it increases the emergent polarization (in absolute values). In other words, in the absence of a magnetic field, the line radiation field in the region where $\tau_o \sim 1$ has a quite large positive polarization. The effect of scattering in the line forming regions (between $\tau_o \sim 1$ and the surface) is to reduce the polarization and to produce a change of sign. A weak magnetic field lying slightly below the region where $\tau_o = 1$ decreases the positive polarization of the radiation field which reaches the line forming region. After scattering it emerges with a negative polarization which is larger, in absolute value, than in the absence of a magnetic field.

It is noted that the existence of a positive maximum of the polarization source function in the optical depth range 1 to 10 is found also for lines formed in isothermal atmospheres with depth-independent properties. Actually, it is a general feature for optically thick spectral lines, such as Hα, and it is due to the properties of multiple Rayleigh scattering. This physical argument may be relevant to the polarization enhancements observed in Hα since the line

core is formed where a canopy base might be present, specifically at an altitude between 1000km and 1600km. The line wings are formed at an altitude between 100km to 400km, (see Foukal (1990)).

5.4 Analysis of Solar Prominence Data

Observations were made of three prominences positioned at the western limb of the Sun during the course of three days in August 1997 in the Hα wavelength. The three prominences are shown in Figure 5.28: Figure 5.28a,b is a prominence recorded on 5 August 1997 at a position of $-54.2°$W on the solar limb, Figure 5.28c,d was recorded on 10 August 1997 at a position $+42.5°$W latitude, and finally Figure 5.28e was taken on 7 August 1997 at a latitude of $+15.5°$W. Unfortunately due to adverse weather conditions, the data for the prominence recorded on 5 August was poor and discarded. Data for the other two prominences were analysed and the polarization maps are shown in Section 5.4.1.

The aim of this study was to ascertain the feasibility of recording accurate polarization maps with the imaging polarimeter and to attempt an interpretation of the prominence structure in strictly a qualitative manner. The linear polarization measurements were obtained by the imaging polarimeter with exposure times of typically several seconds sufficient to image the prominences clearly on the CCD detector and to saturate the the nearby limb. Exposures of the disk center were also recorded in order to ascertain the zero polarization standard. The total time to record and store a full set of measurements (i.e. a prominence and at disc center) ranged between 150 seconds and 200 seconds.

5.4.1 Results

Figure 5.29 illustrates the ordinary and extraordinary intensity images of the prominence recorded on 7 August along with the corresponding contour plot. The solar limb in the images is saturated, i.e. the recorded intensity is beyond the dynamic range of the detector. The linear polarization map illustrating the vectors and the angle of polarization is shown in Figure 5.30. The prominence extends approximately 61 arcseconds along the solar limb and 56 arcseconds normal to it, i.e. the height above the limb is about 40,000km. The degree of polarization is approximately 0.8% in the lower regions of the prominence near the solar limb rising to 1.2% towards the outer regions. Due to the low intensity levels the uncertainty of these polarization values is of the order 0.15%. The orientation of the vectors is generally aligned tangential to the solar limb direction with some rotation towards the

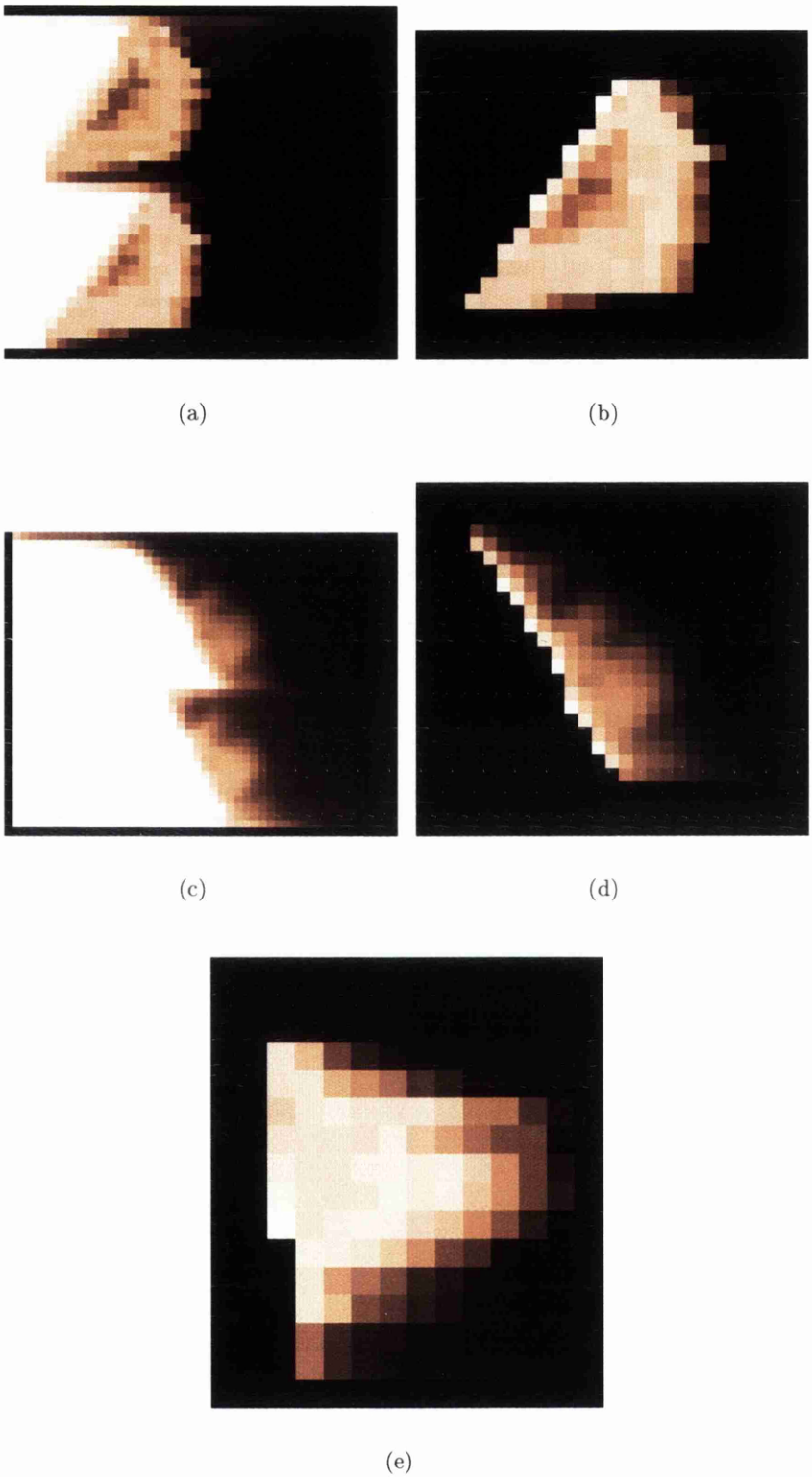

Figure 5.28: Three Solar prominences recorded during the Summer 1997 at the Cochno Observatory, Glasgow. Images (a) and (b) were recorded on 5 August 1997 at a position of $-54.2°$W on the solar limb showing a prominence in both the Ordinary and Extraordinary rays. Similarly images (c) and (d) were taken on 10 August 1997 at a solar latitude of $+42.5°$W and finally image (e) was recorded on 7 August 1997 at a solar latitude of $+15.5°$W.

edge of the prominence. Due to seeing effects and inaccurate registration between frames, the pixels close the solar limb cannot be utilised and thus produce erroneous polarization values. Finally Figure 5.31 shows the linear polarization data superimposed on the grey-scale intensity image.

Similarly Figure 5.32 shows the ordinary and extraordinary intensity images of the prominence recorded on 10 August along with the corresponding contour plot. The polarization map is illustrated in Figure 5.33 while the superposition of the grey-scale intensity image and polarization map is shown in Figure 5.34. The prominence under investigation extends beyond the available detector area along the solar limb, however it is approximately 43 arc-seconds in height or 31,000km. The degree of polarization is approximately 0.5% in the lower regions of the prominence near the solar limb rising to 0.8% towards the outer regions, somewhat lower than the prominence observed 7 August. The orientation of the polarization vectors is, again, generally aligned tangential to the solar limb direction. However, there is significant rotation of the polarization vectors in the center and towards the lower right regions of the prominence indicating areas of either differing plasma properties or magnetic field structure.

5.4.2 Discussion

The linear polarization of spectral lines observed in prominences is due to scattering of the anisotropic photospheric radiation, modified by the Hanle effect due to the local magnetic field, which leads to a depolarization and a rotation of the polarization direction. The linear polarization of Hα is also sensitive to the depolarizing effect of collisions with electrons and protons of the medium owing to the long range of the $H–H^+$ interaction potential and, moreover, it is modified by multiple scattering inside the prominence, because this line is not optically thin ($\tau_o \sim 1$).

The strength of the magnetic fields in a prominence may be inferred from measurements of linear polarization in Hα as characterised in the Figures 5.30 and 5.33. The small arrows represent the direction of polarization in Hα. The degree of polarization was estimated to be 0.8% for the prominence recorded on the 10 August. The angle through which the direction of polarization is rotated from tangency to the limb allows the inference of the strength of the fields in the prominence. The strength of the field, inferred from the 20°–25° angle of rotation, was between 45 and 60 gauss, (see Hyder, 1964). The direction of rotation of the polarization vector from tangency allows the direction of the line-of-sight component of the magnetic field.

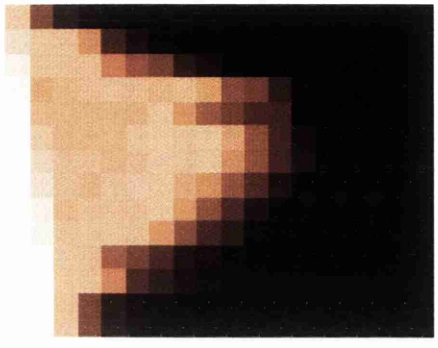

(a)

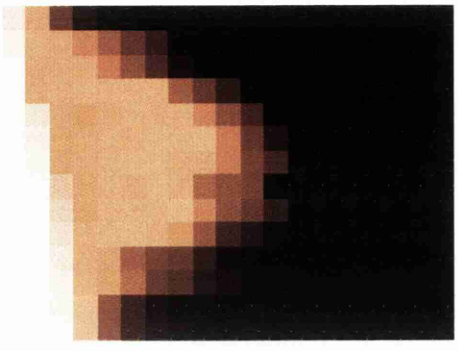

(b)

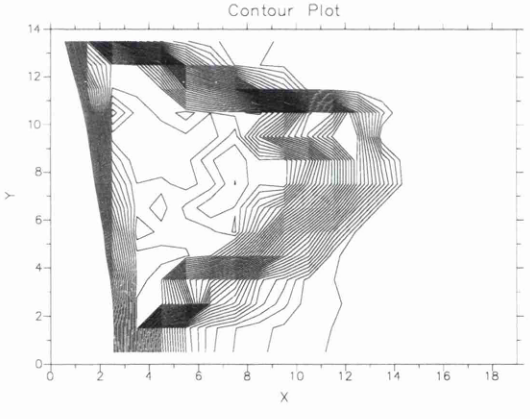

(c)

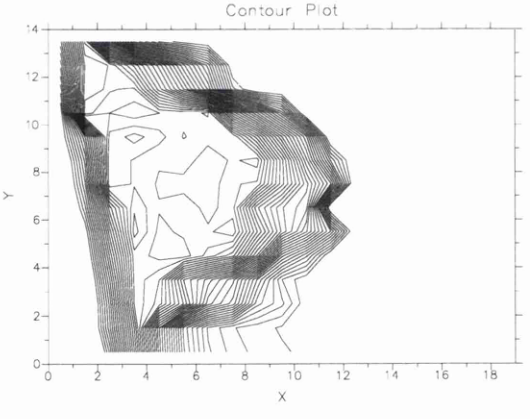

(d)

Figure 5.29: The (a) Ordinary and (b) Extraordinary images of the prominence recorded on 7 August 1997 at a solar latitude of +15.5°W. The contour plots of the alternatively polarized images are shown in (c) Ordinary and (d) Extraordinary.

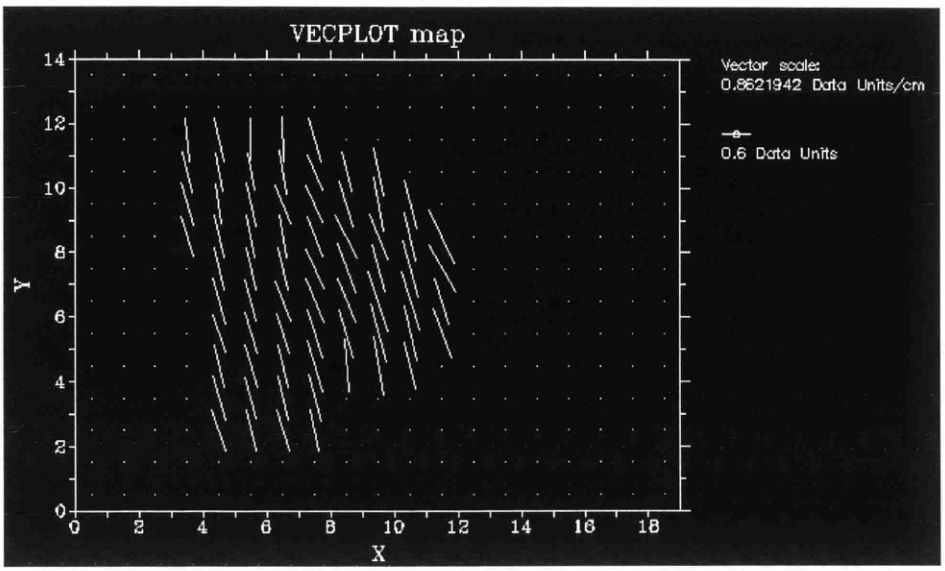

Figure 5.30: Polarization map of the prominence recorded on 7 August 1997. The data units are in percentage of polarization, p, (%).

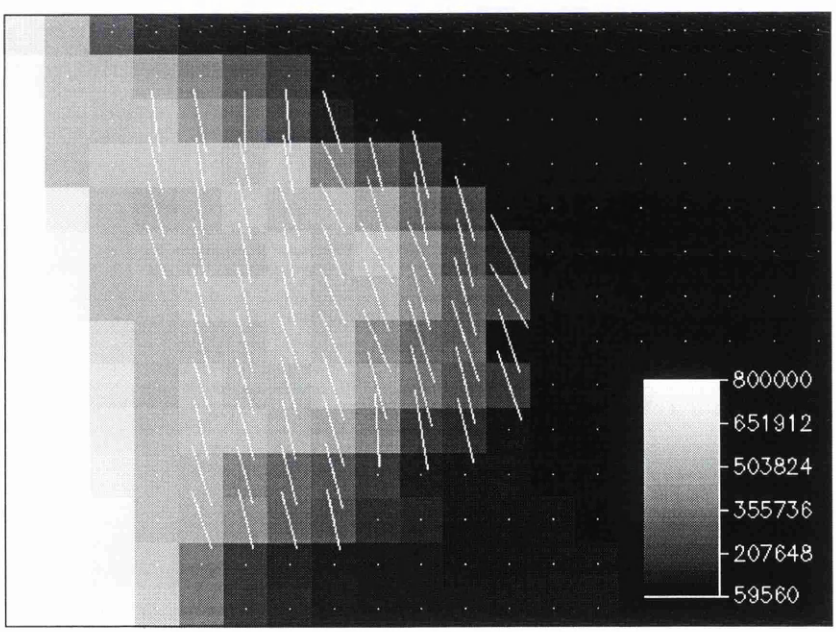

Figure 5.31: The linear polarization data of Figure 5.30 superimposed on a grey-scale intensity image. The grey-scale image shows the solar limb and prominence in high contrast. The key relates the number of detected photons to the intensity level of the image. The polarization orientations are generally tangential to the solar limb direction.

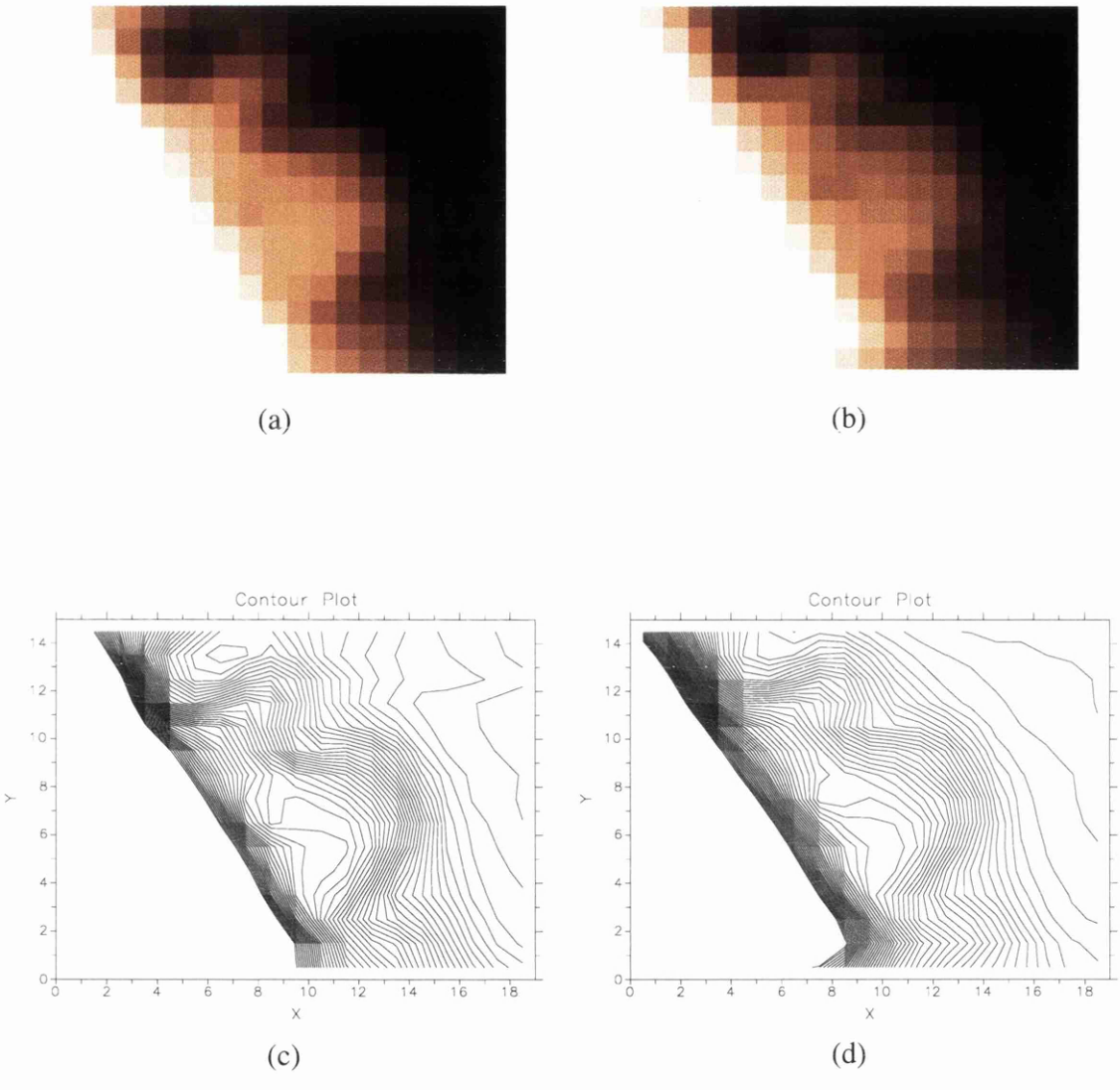

Figure 5.32: The (a) Ordinary and (b) Extraordinary images of the prominence recorded on 10 August 1997 at a solar latitude of +42.5°W. The contour plots of the alternatively polarized images are shown in (c) Ordinary and (d) Extraordinary.

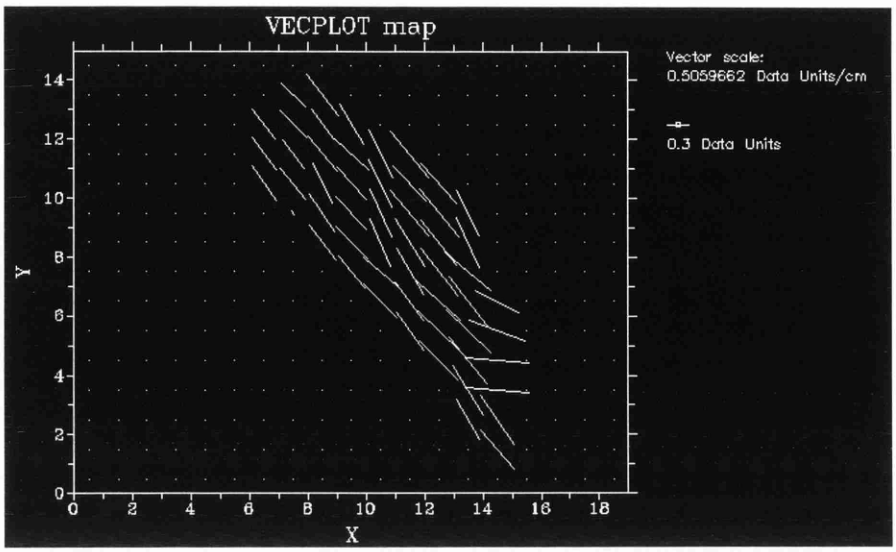

Figure 5.33: Polarization map of the prominence recorded on 10 August 1997. The data units are in percentage of polarization, p, (%).

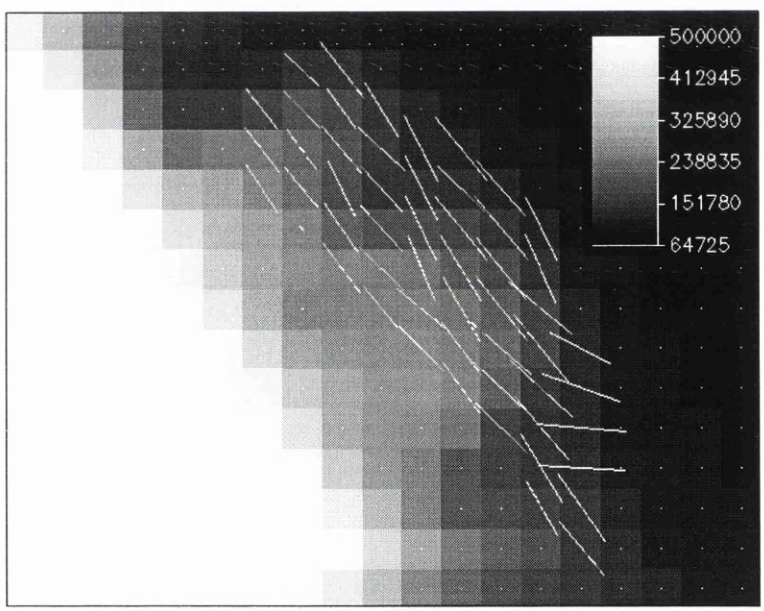

Figure 5.34: The linear polarization data of Figure 5.33 superimposed on a grey-scale intensity image. The grey-scale image shows the solar limb and prominence in high contrast. The key relates the number of detected photons to the intensity level of the image. The polarization orientations are generally tangential to the solar limb direction but with some structure towards the lower right.

However, it is impossible to determine completely the magnetic field vector from linear polarization measurements in one single line - namely Hα - because two parameters are measured, the linear polarization degree and direction (or the two linear polarization Stokes parameters q and u), whereas 3 components of the field vector need to be determined. Therefore measurements of two lines of differing optical depth are necessary for the determination of the three components of the field vector. A commonly used pair are He I D_3 and Hα, these providing the 3 magnetic field components and one extra parameter, the electron density (see Bommier and Sahal-Bréchot, 1978 and Bommier, 1980).

The principle of the two-line measurement and analysis is summarised as follows. In the case of simultaneous observations in one optically thin and one optically thick line a difference in the scattering geometries exists. This difference can be suitably exploited to remove the ambiguity concerning the two-fold degeneration of the solution in one line only: two field vectors are indistinguishable because they have the same effect on the linear polarization of the line. Therefore, the scattering geometry is not the same for Hα and He I D_3, owing to the prominence internal Hα radiation and to the absorption of the incident photospheric radiation by the prominence matter in the optically thick Hα line; by comparing the solutions provided by the optically thin He I D_3 line and the optically thick Hα line, it is possible to solve the fundamental ambiguity in individual cases, because the optically thin line provides two solutions symmetrical with respect to the line of sight, whereas the optically thick line provides two solutions also, which are not symmetrical with respect to the line of sight. By comparing the two pairs of solutions, it is possible to determine which is the "true" solution and which is the symmetrical "pseudo-solution" and to solve the fundamental ambiguity.

Chapter 6

Conclusion and Future Work

This chapter splits easily into three parts. The first part describes the results and conclusions obtained in the solar polarimetry work relating to the center-to-limb variation (CLV) of the Hα polarization, and the results obtained observing two prominences on the solar limb. The second part concerns the Faraday rotation polarimetry work and the two different polarimetric techniques under consideration for application to the COMPASS-D tokamak. Some system properties are discussed, both on a general level and focussing on the COMPASS-D situation with possible improvements suggested. In the final summary, the directions in which both these works could be extended are addressed.

6.1 Solar Polarimetry

Many phenomena in the solar atmosphere have their origin in magnetic fields. Magnetism is responsible for the structural richness of the solar atmosphere, for solar activity, and it is also thought to play an important role in the chromosphere, investigated here via the Hα spectral line.

It has been demonstrated that a 2-D polarimeter can be used for precision polarimetry needed for quantitative research of solar magnetic fields. The principle of using a masking grid in conjunction with a polarizing prism, such as a Savart plate, to eliminate atmospheric transparency effects and the need for flatfielding of the detector has been shown to be feasible for solar observations. A noise level of 0.1% in a single exposure is achieved with an angular resolution of 4 arcseconds. By frame averaging and averaging over rows oriented parallel to center-to-limb direction, the noise level could be reduced to the 0.02%. This value was chosen pragmatically so that the required number of exposures to achieve this precision was not excessive, taking into account the variable nature of the meteorology in Glasgow. It

allowed a good signal-to-noise ratio to be obtained within a reasonable time frame. The spectral resolution achieved with the narrow band (FWHM $\Delta\lambda = 0.3$Å) Hα tunable filter was $\pm$ 0.33Å. For reasons of symmetry and scattering geometry the polarization of the solar radiation is zero at the disk center allowing the instrumental offset to be estimated. However, the instrumental polarization of the instrument is not known to a sufficient accuracy such that the uncertainty is smaller that the random errors associated with the q and u measurements. Therefore, it is advantageous to measure the difference of the measured polarization at two solar positions. This differential approach negates the need to know the true polarization as it will be cancelled out in taking the difference. The instrumental polarization of the polarimeter was investigated using a novel monochromatic depolarizing technique outlined in Chapter 2. This was the first time this technique was experimentally tested. Unfortunately this attempt was unsuccessful for various practical reasons. However, an error analysis provided a useful insight on constraints of use particularly the effectiveness of the depolarizer arrangement at different wavelengths.

Low noise observations of q and u at the north polar region and the western limb of the quiet Sun were recorded at the University of Glasgow Cochno station. From these observations it was possible to derive the CLV polarization of the Hα line-center and at the two wings. Although some information on the slope of the CLV curve is available for a number of different spectral lines, the only lines for which the full CLV has been investigated in detail are the Sr I 4607Å and Ca I 4227Å. The analysis of the Hα line is more complicated due to its non-negligible optical thickness which causes a lower degree of polarization (a partial lowering of the radiation field anisotropy). Also the Hα line is formed over a much larger height range suggesting that the line profile is more dependent on scale variations.

The present observations give the detailed CLV of the Hα line for the polarization amplitude. The comparison between the data sets taken during three days in July 1997 shows that it is possible to obtain consistency after careful data reduction. The lack of spread of the data points illustrates the degree of reproducibility of the results, but there is evidence that at least some of the deviation must be intrinsically solar. The polarization at the solar limb was found to be much higher in Hα than in the nearby continuum for the three monitored wavelengths. No distinction in the general behaviour of the CLV could be found between equatorial and polar regions for all three wavelengths. Furthermore the polarization was found to decline by a factor of four when going from $\mu = 0.1$ to $\mu = 0.3$, a much steeper decline than the Sr I 4607Å and Ca I 4227Å. The polarization in the core of Hα was found to be higher by at least 2σ with respect to the off-band measurements in the red- and blue-wings. This phenomenon

was explained in Section 5.3.2 in terms of the ratio between the line and continuum opacities. It was also found that while the ratio of the blue- to red-wing polarization remains strictly constant, the line core shows a marginally larger scatter relative to the wings. This scatter is however comparable to the error budget and therefore this result should not be over emphasised, but it may be interpreted in terms of either the Hanle depolarization of the line core by a weak magnetic field or most likely due to positional uncertainties on the solar disk.

Leroy (1972) inferred the conflicting result that the solar equatorial polarization is approximately ten percent larger than at the poles. A likely physical explanation for this measurement is the Hanle effect. Assuming the Sun has a classical dipole magnetic field suggests a greater magnetic field strength at the poles where the magnetic flux is greatest. This increased field strength at the poles may cause a decrease of polarization with respect to a region of low magnetic flux and a rotation of the of the polarization direction. Another explanation is that the area of observation cut across a region that had more Hanle-depolarizing magnetic fields causing the observed depolarization. However, when dealing with a quantity that changes rapidly with position on the solar disk, much like the Hα CLV polarization, exact determination of observing position is very important. The analysis conducted in Section 5.3.1 demonstrated that a slight misalignment or uncertainty in positioning greatly affects the assigned polarization value recorded especially near the limb where the CLV is varying most rapidly. This is the most likely explanation for the conflicting results recorded by Leroy (1972).

Observation taken on 20 July 1997 clearly indicate a statistically significant intrinsically solar variation at a distance of 20 arcseconds in the u and q Stokes parameter in both the blue- and red-wings of the Hα line. This evidence is directly seen in Figure 5.15 and Figure 5.21. The CLV of the u and q amplitudes show a very pronounced kink near $\mu = 0.2$ that indicating the parameters have non-zero values, which means that the plane of polarization is not parallel to the limb. These kinks are present in both the blue- and red-wing data sets. Calculations from the Stokes parameters show that the direction of vibration of linear polarization in the line has been rotated by 16° in the blue-wing and 10° in the red-wing. These surprising enhancements of the q and u profiles from the smooth CLV curves near $\mu = 0.2$ may be explained in terms of the Hanle effect due to a magnetic canopy lying below the height where the line core is formed. This effect is a consequence of multiple scattering in the solar chromosphere and is discussed in a comprehensive manner in Section 5.3.2.

The linear polarization of two prominences observed during August 1997 was recorded by the imaging polarimeter thus illustrating the versatility and suitability of the instrument

for solar work. The degree of polarization is approximately 1% for the two prominences illustrated in Section 5.4.1. Unfortunately due to the low intensity levels the uncertainty of these polarization values is of the order 0.15%. The vectors are generally aligned tangential to the solar limb direction with some rotation of the vectors at certain locations. This rotation of the polarization vectors from tangency to the limb along with information concerning the degree of polarization allows the strength of the magnetic field to be determined. The degree of polarization was estimated to be 0.8% for the prominence recorded on the 10 August. The strength of the field, inferred from the 20°–25° angle of rotation, was between 45 and 60 gauss. The direction of rotation of the polarization vector from tangency allows calculation of the direction of the line-of-sight component of the magnetic field.

The basic mechanism of the prominence line emission is the resonance scattering of the incident photospheric and chromospheric radiation. This irradiation of prominences is highly anisotropic and the anisotropy increases with increasing prominence height above the solar surface. Resonance scattering of anisotropic radiation then leads to linear polarization of the emitted photons. However, the presence of a weak magnetic field generally decreases the amount of linear polarization and rotates the polarization direction with respect to the solar limb.

6.2 Faraday Rotation Polarimetry

Conventional polarimetric methods are based upon a classical picture, where a well defined polarization state of an incident electromagnetic wave is actually rotated by the plasma. The rotation angle can then be determined through a measurement of the relative power levels of two detectors, each sensitive to one of two orthogonal linear polarization states, this is the amplitude method. Alternatively in single detector schemes or phase method, the orientation of the incident polarization state is modulated in time, resulting in an amplitude modulation of the detected signal. From the phase lag of this modulation with respect to a reference, the Faraday rotation angle can then be deduced. The polarimetric measurement is independent of the signal amplitude, provided the signal remains large enough to stay above the noise level.

In the course of the research presented in this thesis, the two polarimetric methods, phase and amplitude, were evaluated with commissioning onto the COMPASS-D tokamak in mind. Using typical COMPASS-D operating parameters and an analytical solution to the wave propagation equation, the expected Faraday rotation angles for each of the six chords is determined. Since the maximum expected Faraday rotation angle is small, approximately 5°,

it is imperative to minimise the noise in the proposed system. The advantages and disadvantages of each of the two measurement systems are tabulated in Table 4.3. Clearly the spatial resolution of both measurement techniques are comparable, however the phase measurement technique has a significantly better temporal resolution. The phase measurement technique requires only one detector per channel which is a significant advantage in the spatially restrictive regime of a tokamak. In terms of phase resolution of the Faraday rotation angle both methods are comparable assuming the phase technique has a modulation of the signal amplitude of 50% ($\delta = 35°$) and a 6% signal-to-noise level. The cross-coupling problems inherent in the phase measurement technique produce an additional phase contribution to the interferometer which may thus be discarded in the final analysis. The cross-coupling problems associated with the amplitude measurement technique produce an elliptisation of the emerging polarization which may be misinterpreted as an additional Faraday rotation angle. This effect may be eliminated by the re-alignment of the polarizing grid splitters such that the incident polarization is parallel or perpendicular to the toroidal magnetic field. Refraction effects may also cause deleterious effects which to first order may be neglected in the phase method.

In conclusion the phase measurement technique is clearly desirable in order to fulfill the basic aims of the physics programme on the COMPASS-D tokamak. This involves determining the temporal evolution of magnetohydrodynamic plasma phenomena and the effect on plasma stability of additional radio and neutral beam heating. The phase measurement has a high degree of temporal and spatial resolution, and a good phase accuracy which greatly simplifies the mathematical inversion required to yield the poloidal magnetic field and hence the current density.

6.3 Future Work

There are several aspects which remain to be discussed in this final section but the following is a summary of the main points of the research undertaken

- The development and construction of an imaging polarimeter to observe, for the first time with this technique, the linear polarization of surface solar phenomena in Hα.
- The polarization at the solar limb was found to be much higher in Hα than in the nearby continuum. No distinction in the general behaviour of the CLV could be found between the equatorial and polar regions. Off-band Hα polarization measurements were found to be reduced by at least 2σ with respect to on-band measurements.

- Deviations from the smooth CLV curve were observed in the form of enhancements of polarization with an associated rotation in the **E** vector. These may be related to the Hanle effect and provide means of exploring magnetic fields involving small turbulent structures.

- A direct comparison of the two leading Faraday rotation techniques with a special emphasis on the COMPASS-D tokamak parameters.

- The construction of a test bench to study the feasibility of the amplitude method and the numerical simulation of each technique to determine the polarimetric precision.

It has been demonstrated here that, despite the problems encountered with image overlap in the imaging polarimeter, high polarimetric accuracy can be achieved by careful calibration. This is a very encouraging result and a great motivation for further improvements to the system.

Diagnostic methods based on the Hanle effect are at a formative stage. They require, as a first step, reliable calculations of the resonance polarization in the absence of a magnetic field. As resonance polarization appears only in lines formed under non-LTE conditions a good knowledge of the physical processes which play a role in the line formation is required. This has been done essentially for two resonance lines namely Ca I 4227Å and Sr I 4607Å lines. To understand the scattering physics on the Sun better and to exploit it for various diagnostic purposes, it is necessary to systematically observe the CLV behaviour of many more lines in a similar, rather complete way. The CLV of the scattering polarization is a sensitive function of the height variations of temperature and density in the chromosphere and it thus provides novel constraints for atmospheric modelling. A better understanding of the physics of the Hα line would greatly aid the interpretation of the results obtained and more progress in this regard is necessary.

The Faraday rotation work was successful in determing the accuracies and illustrating the problems that required solutions. However due to budgetary and time constraints no progress was possible in commissioning the proposed method onto the COMPASS-D tokamak and unfortunately has now been abandoned.

Perhaps the most important improvement to this thesis may have been achieved by observing at a better site. The adverse weather conditions in Glasgow make it a challenging site to observe the Sun and on numerous occasions curtailed promising observing runs.

Appendix A

Polarized Light

A.1 Detection of Elliptically Polarized Light

In relation to determining the Faraday rotation angle with any arbitrary polarized beam the following analysis is instructive. The electric field vector of an electromagnetic wave of arbitrary position may be written as, (see Fowles, 1975 and Wolf, 1993)

$$\mathbf{E} = \begin{pmatrix} E_x \\ E_y \end{pmatrix} = \begin{pmatrix} |E_x|e^{i\delta_x} \\ |E_y|e^{i\delta_y} \end{pmatrix} e^{i(kr-\omega t)} \tag{A.1}$$

The real part of this vector describes an ellipse at a given point in space (see Figure A.1). It follows that

$$\frac{E_y}{E_x} = \tan\widetilde{\Psi} e^{i(\delta_y - \delta_x)} \tag{A.2}$$

where

$$\tan\widetilde{\Psi} \equiv \frac{|E_y|}{|E_x|}. \tag{A.3}$$

Using a beam splitters resolving both polarization components aligned along the x- and y-axes, the apparently measured polarization angle, given by the transmitted intensities of the respective beam splitter I_x and I_y is equal to $\tan\widetilde{\Psi}$

$$\tan\widetilde{\Psi} = \sqrt{\frac{I_x}{I_y}}. \tag{A.4}$$

In the frame of the ellipse (x',y') the electric field vector is given by

$$\mathbf{E} = \begin{pmatrix} E'_x \\ iE'_y \end{pmatrix} e^{i(kr-\omega t)}, \tag{A.5}$$

where both E'_x and E'_y are real. The ellipticity then can be defined as

$$\epsilon \equiv \frac{E'_x}{E'_y} = \sqrt{\frac{I_{min}}{I_{max}}}. \tag{A.6}$$

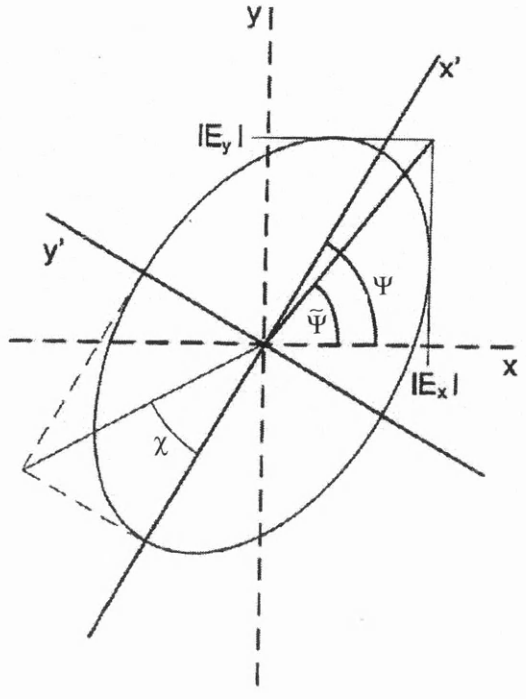

Figure A.1: Notation used in calculation of elliptically polarized light.

where I_{min} and I_{max} are the minimum and maximum intensities trasmitted by an ideal analyser. The quantity of interest is the polarization orientation Ψ, which is the actual inclination of the ellipse in the system (x,y). The apparent polarization angle $\tan\widetilde{\Psi}$ expressed in terms of Ψ will now provide information concerning the error introduced into the measurement due to the use of elliptical polarization rather than linear polarization.

$$\tan^2\widetilde{\Psi} = \frac{\epsilon^2 + \tan^2\Psi}{1 + \epsilon^2\tan^2\Psi} \tag{A.7}$$

In Figure A.2 this function is shown for different ϵ. For purely linear polarization ($\epsilon = 0$) $\widetilde{\Psi} = \Psi$, whereas for completely circular polarization ($\epsilon = 1$) $\tan\widetilde{\Psi}$ becomes independent of Ψ.

Linear polarization is transformed into elliptical polarizaton by applying a relative phase changer, which may be written as a matrix operation as,

$$\begin{pmatrix} e^{i\delta_x} & 0 \\ 0 & e^{i\delta_y} \end{pmatrix} \begin{pmatrix} |E_x| \\ |E_y| \end{pmatrix} = \begin{pmatrix} |E_x|e^{i\delta_x} \\ |E_y|e^{i\delta_y} \end{pmatrix} \tag{A.8}$$

It can be shown that the resultant ellipticity obtained by applying several phase changers of the same orientation, is simply the sum of the individual ellipticities, provided $\epsilon \ll 1$ and $\delta_y - \delta_x \ll \frac{\pi}{2}$.

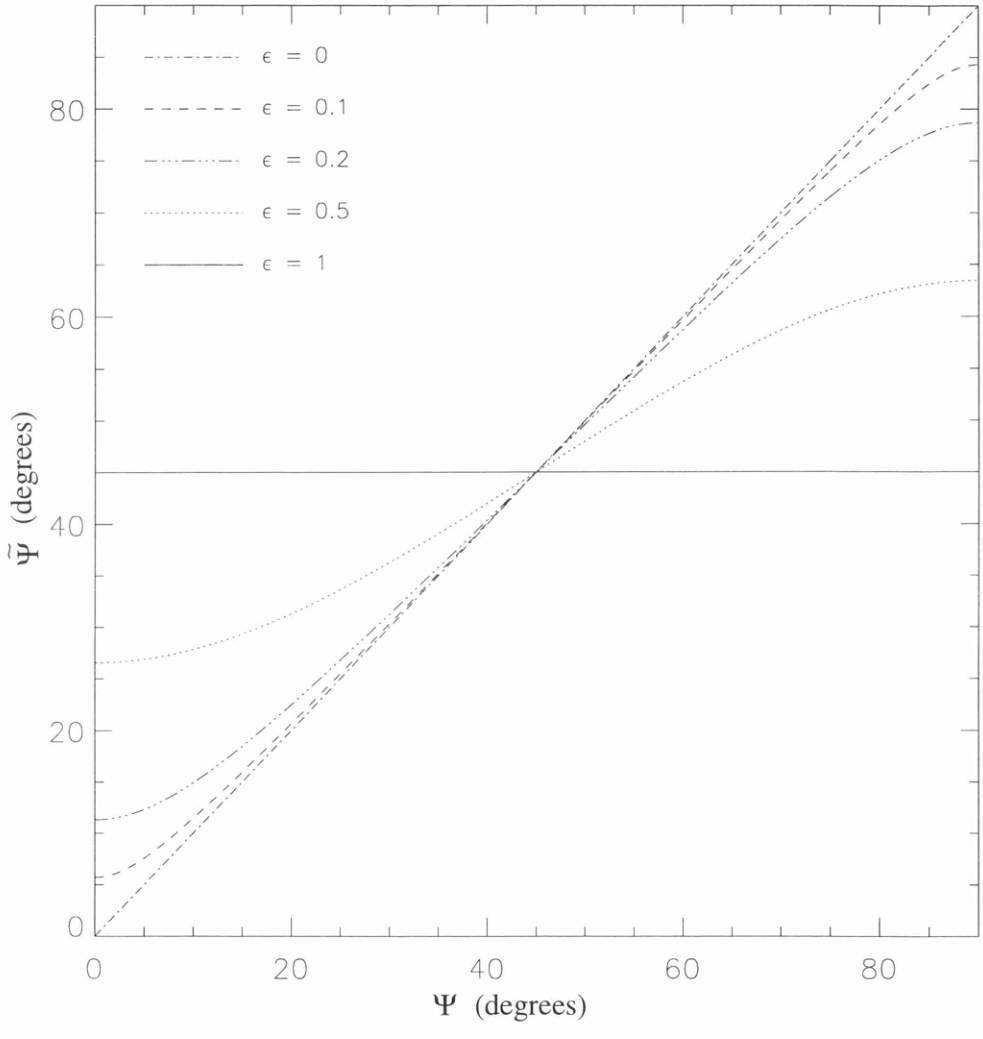

Figure A.2: $\tilde{\Psi}$ as a function of Ψ for varying ellipticities ϵ.

Bibliography

Allen, C. W.: 1973, *Astrophysical Quantities*, Athlone Press

Almeida, J. S. and Pillet, V. M.: 1992, *Astronomy and Astrophysics* **260**, 543

Appenzeller, I.: 1967, *Publication of the Astronomical Society of the Pacific* 136

Appleton, E. V.: 1932, *Proceedings of the Physical Society* pp 642–650

Barry, S., Nieswand, C., Bühlmann, F., Prunty, S. L., and Mansfield, H. M.: 1996, *Review of Scientific Instruments* **67(5)**, 1814

Baur, T. G.: 1981, *Optical Engineering* **20(1)**, 2

Beckers, J. M. and Chipman, E.: 1974, *Solar Physics* **34**, 151

Bianda, M., Solanki, S. K., and Stenflo, J. O.: 1998, *Astronomy and Astrophysics* **331**, 760

Billings, B. H.: 1951, *Journal of the Optical Society of America* **41(12)**, 966

Bommier, V.: 1980, *Astronomy and Astrophysics* **87**, 109

Bommier, V. and Sahal-Bréchot, S.: 1978, *Astronomy and Astrophysics* **69**, 57

Born, M. and Wolf, E.: 1964, *Principles of Optics*, Pergamon Press

Braithwaite, G., Gottardi, N., Magyar, G., O'Rouke, J., Ryan, J., and Veroné, D.: 1989, *Review of Scientific Instruments* **60(9)**, 2825

Breit, G.: 1925, *Journal of the Optical Society of America* **10**, 439

Brower, D. L., Zeng, L., and Jiang, Y.: 1997, *Review of Scientific Instruments* **68(1)**, 419

Budden, K. G.: 1961, *Radio Waves in the Ionosphere*, Cambridge University Press

Buil, C.: 1991, *CCD Astronomy: Construction and Use of an Astronomical CCD Camera*, Willmann-Bell, Inc

Chou, B. R.: 1991, *Astronomie* **19(7)**, 66

Clarke, D.: 1989a, *Practical Electronics* **October**, 12

Clarke, D.: 1989b, *Practical Electronics* **November**, 48

Clarke, D.: 1991, *Vistas in Astronomy* **34**, 303

Clarke, D. and Grainger, J. F.: 1971, *Polarized Light and Optical Measurement.*, Pergamon Press

Clarke, D. and Naghizadeh-Khouei, J.: 1994, *The Astronomical Journal* **108(2)**, 687

Coyne, G. V.: 1974, *Ricerche Astronomiche* **8(13)**, 311

Craig, A. D.: 1976, *Plasma Physics* **18**, 777

Degl'Innoncenti, E. L.: 1982, *Solar Physics* **79**, 291

Dodel, G. and Kunz, W.: 1978, *Infrared Physics* **18**, 773

Dollfus, A.: 1974, in T. Gehrels (ed.), *Planets, Stars and Nebulae Studied with Photopolarimetry*, p. 695, The University of Arizona Press, Tucson

Donné, A. J. H.: 1995, *Review of Scientific Instruments* **66(6)**, 3407

Dumont, S., Omont, A., and Pecker, J. C.: 1973, *Solar Physics* **28**, 271

Dumont, S. and Pecker, J. C.: 1971, *Astronomy and Astrophysics* **10**, 118

Edlington, T. and Wylde, R.: 1992, *Review of Scientific Instruments* **63(10)**, 4968

Faurobert-Scholl, M.: 1992, *Astronomy and Astrophysics* **258**, 521

Faurobert-Scholl, M.: 1993, *Astronomy and Astrophysics* **268**, 765

Faurobert-Scholl, M.: 1994, *Astronomy and Astrophysics* **285**, 655

Faurobert-Scholl, M., Feautrier, N., and Machefert, F.: 1995, *Astronomy and Astrophysics* **298**, 289

Feldman, U., Seely, J. F., Jr, N. R. S., Suckewer, S., and Title, A. M.: 1984, *Journal of Applied Physics* **56(9)**, 2512

Foukal, P.: 1990, *Solar Astrophysics*, John and Wiley & Sons, Inc

Fowles, G. R.: 1975, *Introduction to Modern Optics*, Holt, Reinehart and Winston Inc.

Geck, W. R., Qin, X., and Liao, J.: 1995, *Review of Scientific Instruments* **66(1)**, 860

Gehrels, T. and Teska, T. M.: 1960, *Proceedings of Astronomical Society of the Pacific* **72**, 115

Hanle, W.: 1924, *Z. Phys.* **68**, 49

Heald, M. A. and Wharton, C. B.: 1965, *Plasma Diagnostics with Microwaves*, New York: Wiley

Hutchinson, I. H.: 1987, *Principles of Plasma Diagnostics*, Cambridge University Press, ISBN 0-521-32622-2

Hyder, C. L.: 1964, *Astrophysical Journal* **140(2)**, 817

Janesick, J. R., Elliot, T., Collins, S., Marsh, H., Blocke, M. M., and Freeman, J.: 1984, in *Proceedings of the Society of Photo-Optical Instrumentation Engineers*, Vol. 501, pp 2–31

Kamke, E.: 1959, *Differentialgleichungen*, Chelsea, New York

Keller, C. U.: 1998, *Private Communication*

Kunz, W. and Dodel, G.: 1978, *Plasma Physics* **20**, 171, Research Note

Leroy, J. L.: 1972, *Astronomy and Astrophysics* **19**, 287

Leroy, J. L.: 1990, *Astronomy and Astrophysics* **237**, 237

Leroy, J. L.: 1997, *Private Communication*

Leroy, J. L., Ratier, G., and Bommer, V.: 1977, *Astronomy and Astrophysics* **54**, 811

Lyot, B.: 1928, *Ann D'Astroph* **8(1-2)**, 103

Mackay, C. D.: 1986, *Annual Review of Astronomy and Astrophysics* **24**, 255

Marco, F. D. and Segre, S. E.: 1972, *Plasma Physics* **14**, 245

Markuvitz, N.: 1951, *Waveguide Handbook*, McGraw Hill, New York

Mickey, D. L. and Orrall, F. Q.: 1974, *Astronomy and Astrophysics* **31**, 179

Mitchell, A. C. G. and Zemansky, M. W.: 1961, *Resonance Radiation and Excited Atoms*, Cambridge University Press

Moruzzi, G. and Strumia, F.: 1991, *The Hanle Effect and Level Crossing Spectroscopy*, Plenum Press

Muir, D. G.: 1983, *Ph.D. thesis*, Royal Holloway College

Öhman, Y.: 1939, *Monthly Notices of the Royal Astronomical Society* **99**, 624

Park, K. and Miller, S.: 1988, *Communications of the ACM* **31(10)**, 1192

Pickering, E. C.: 1873, *American Academy of Arts and Science* **9**, 1

Pospergelis, M. M.: 1965, *Soviet Astronomy* **9**, 313

Querfeld, C. W., Smartt, R. N., Bommier, V., Degl'Innocenti, E. L., and House, H. H.: 1985, *Solar Physcis* **96**, 277

Ramaprakash, A. N., Gupta, R., Sen, A. K., and Tandon, S. N.: 1997, *Astronomy and Astrophysics Supplement Series* **127(1)**, 369

Redman, R. O.: 1941, *Monthly Notices of the Royal Astronomical Society* **101**, 226

Rees, D. E. and Saliba, G. J.: 1982, *Astronomy and Astrophysics* **115**, 1

Rice, B. W.: 1992, *Review of Scientific Instruments* **63(10)**, 5002

Ridpath, I.: 1989, *Norton's 2000.0 Star Atlas and Reference Handbook*, Longman Scientific & Technical

Rommers, J. H., Donné, A. J. H., Karelse, F. A., and Howard, J.: 1997, *Review of Scientific Instruments* **68(2)**, 1217

Röser, H. J.: 1981, *Astronomy and Astrophysics* **103**, 374

Sahal-Bréchot, S., Bommier, V., and Leroy, J. L.: 1977, *Astronomy and Astrophysics* **59**, 223

Saliba, G. J.: 1985, *Solar Physcis* **98**, 1

Scarrott, S. M.: 1983, *Monthly Notices of the Royal Astronomical Society* **204**, 1163

Scarrott, S. M.: 1991, *Vistas in Astronomy* **34**, 163

Segre, S. E.: 1978, *Plasma Physics* **20**, 295

Serkowski, K.: 1970, *Publications of the Astronomical Society of the Pacific* **82**, 908

Serkowski, K.: 1974a, in N. Carleton (ed.), *Methods in Experimental Physics*, pp 361–414, Academic Press, New York, Volume 12A

Serkowski, K.: 1974b, in T. Gehrels (ed.), *Planets, Stars and Nebulae Studied with Photopolarimetry*, pp 135–174, The University of Arizona Press, Tucson

Shmoys, J.: 1961, *Journal Applied Physics* **32(4)**, 689

Shurcliff, W. A.: 1962, *Polarized Light*, Harvard University Press, Boston

Soltwisch, H.: 1981, *Infrared Physics* **21**, 287

Soltwisch, H.: 1986, *Review of Scientific Instruments* **57(8)**, 1939

Soltwisch, H.: 1987, in *Course and Workshop on Basic and Advanced Diagnostics Techniques for Fusion Plasmas*, Vol. II, pp 343–360, Varenna, Sept 1986 CEC Brussels EUR 10977EN

Stenflo, J. O.: 1974, *Solar Physics* **37**, 31

Stenflo, J. O.: 1981, in R. Dunn (ed.), *Solar Instrumentation. What's Next?*, pp 266–275, Sacramento Peak National Observatory, Sunspot, New Mexico

Stenflo, J. O.: 1982, *Solar Physics* **80**, 209

Stenflo, J. O.: 1994, *Solar Magnetic Fields: Polarized Radiation Diagnostics*, Kluwer, Dordrecht

Stenflo, J. O., Baur, T. G., and Elmore, D. F.: 1980, *Astronomy and Astrophysics* **84**, 60

Stenflo, J. O., Bianda, M., Keller, C. U., and Solanki, S. K.: 1997, *Astronomy and Astrophysics* **322**, 985

Stenflo, J. O. and Keller, C. U.: 1997, *Astronomy and Astrophysics* **321**, 927

Stenflo, J. O., Keller, C. U., and Gandorfer, A.: 1998, *Astronomy and Astrophysicss* **329**, 319

Stenflo, J. O. and Nagendra, K. N.: 1996, *Solar Polarization*, Kluwer, Dordrecht

Stenflo, J. O. and Povel, I.: 1985, *Applied Optics* **24(2)**, 3893

Stenflo, J. O., Twerenbold, D., and Harvey, J. W.: 1983a, *Astronomy and Astrophysics Supplementary Series* **52**, 161

Stenflo, J. O., Twerenbold, D., Harvey, J. W., and Brault, J. W.: 1983b, *Astronomy and Astrophysics Supplementary Series* **54**, 505

Stokes, G. G.: 1852, in *Transactions of the Cambridge Philosphical Society*, pp 399–425, Cambridge University, Volume IX

Veron, D.: 1979, in K. J. Button (ed.), *Infrared and Millimeter Waves*, pp 67–135, Academic, New York, Volume 2

Wall, J. V.: 1979, *Quarterly Journal of the Royal Astronomical Society* **20**, 138

Wiehr, E.: 1978, *Astronomy and Astrophysics* **67**, 257

Wiehr, E.: 1981, *Astronomy and Astrophysics* **95**, 54

Wolf, R. C.: 1993, *MSc. Thesis*, JET Joint Undertaking, Abingdon, (JET-IR(93)08)

Wróbleski, D., Huang, L. K., and Moos, H. W.: 1988, *Review of Scientific Instruments* **59(11)**, 2341

Wróbleski, D. and Lao, L. L.: 1992, *Review of Scientific Instruments* **63(10)**, 5140